



Universiteit
Leiden
The Netherlands

A Laboratory Route to Interstellar Ice

Broekhuizen, F.A. van

Citation

Broekhuizen, F. A. van. (2005, June 29). *A Laboratory Route to Interstellar Ice*. Retrieved from <https://hdl.handle.net/1887/2710>

Version: Corrected Publisher's Version

License: [Licence agreement concerning inclusion of doctoral thesis in the Institutional Repository of the University of Leiden](#)

Downloaded from: <https://hdl.handle.net/1887/2710>

Note: To cite this publication please use the final published version (if applicable).

A Laboratory Route to Interstellar Ice

PROEFSCHRIFT

ter verkrijging van
de graad van Doctor aan de Universiteit Leiden,
op gezag van de Rector Magnificus Dr. D.D. Breimer,
hoogleraar in de faculteit der Wiskunde en
Natuurwetenschappen en die der Geneeskunde,
volgens besluit van het College voor Promoties
te verdedigen op woensdag 29 Juni 2005
klokke 16.15 uur

door

Fleur Antoinette van Broekhuizen
geboren te Amsterdam in 1976

PROMOTIECOMMISSIE

Promotor : Prof. dr. E. F. van Dishoeck
Prof. dr. S. Schlemmer (Universität zu Köln)

Co-promotor : Dr. H. J. Fraser (University of Strathclyde)

Referent : Dr. M. Bonn (AMOLF, Amsterdam)

Overige leden : Dr. B. Brandl
Prof. dr. P. Ehrenfreund
Dr. M. Hogerheijde
Prof. dr. P. T. de Zeeuw

Cover:
The northern sky,
Atlas Coelestis sen Harmonica Macrocosmica,
A. Cellarius, Amsterdam 1661.

Artistic idea and design by Lux Buurman and Ab van Overdam

Contents

1	Introduction	1
1.1	The Interstellar Medium	2
1.1.1	The observation of molecules	2
1.1.2	Interstellar clouds and star formation	2
1.1.3	Ices and dust grains	3
1.1.4	UV in the interstellar medium	8
1.2	Laboratory Astrophysics	9
1.2.1	Interstellar ice analogs	9
1.2.2	A simulated interstellar environment	10
1.2.3	CRYOPAD	12
1.2.4	Limitations to the simulation of interstellar ice chemistry	13
1.3	Thesis Outline	14
1.4	Outlook	16
2	Infrared spectroscopy of solid CO-CO₂ mixtures and layers	21
2.1	Introduction	21
2.2	Experimental Procedure	23
2.3	Results	25
2.3.1	CO ₂ -bending mode	25
2.3.2	CO ₂ asymmetric stretching vibration	27
2.3.3	CO-stretching vibration	28
2.4	Discussion	31
2.5	Astrophysical Implications	36
2.6	Conclusion	38
3	The physical behaviour of CO and CO₂ in mixed and layered ices	43
3.1	Introduction	43
3.2	Experimental Procedure	47
3.3	Results and Discussion	48
3.3.1	CO spectroscopy	48
3.3.2	CO ₂ spectroscopy	49
3.3.3	Desorption of CO	51
3.3.4	Overview model(s) of the CO-CO ₂ ice systems	55
3.4	Concluding Remarks and Astrophysical Implications	57

4	Competition between CO and N₂ desorption from interstellar ices	61
4.1	Introduction	61
4.2	Experimental Procedure	63
4.3	Results	64
4.4	Discussion	67
5	Photodesorption of solid CO	73
5.1	Introduction	73
5.2	CRYOPAD	75
	5.2.1 Description of the apparatus	75
	5.2.2 Analysis techniques	80
5.3	First Results of CRYOPAD: CO Photodesorption	83
	5.3.1 Experimental procedure	83
	5.3.2 Model for UV-induced CO desorption	84
	5.3.3 Coverage dependence	86
	5.3.4 Temperature dependence	90
5.4	Discussion	95
	5.4.1 Photodesorption model	97
	5.4.2 Photodesorption mechanisms	97
	5.4.3 Temperature dependence	99
	5.4.4 Future experiments	99
	5.4.5 CO ₂ photolysis and photodesorption	103
5.5	Concluding Remarks	104
6	A quantitative analysis of OCN⁻ formation in interstellar ice analogs	111
6.1	Introduction	111
6.2	Experimental Methods	113
6.3	Results	114
	6.3.1 Band strengths	114
	6.3.2 Thermal formation of OCN ⁻	115
	6.3.3 UV photoprocessing of HNCO-containing ices	117
	6.3.4 UV photoprocessing of H ₂ O/CO/NH ₃ ices	118
	6.3.5 UV photoprocessing of H ₂ O/CH ₃ OH/NH ₃ ice	125
6.4	Astrophysical Implications	126
	6.4.1 UV photoprocessing: CO	128
	6.4.2 UV photolysis: Methanol	129
	6.4.3 UV photolysis or thermal processing: HNCO	130
6.5	Conclusion	132
7	A 3-5μm VLT spectroscopic survey of young low mass stars II: solid OCN⁻	137
7.1	Introduction	138
7.2	Observations	140
	7.2.1 Observational details	140
	7.2.2 The XCN band	141
	7.2.3 H ₂ O-ice column densities	141

7.3	Laboratory Experiments on OCN^- Pertinent to the Analysis of the XCN Band	142
7.3.1	Spectroscopy	142
7.3.2	Band strength	145
7.3.3	Formation mechanisms	146
7.4	Decomposition of the XCN Profile	146
7.5	Results	149
7.5.1	Results of the fitting procedure	149
7.5.2	Correlations with H_2O	150
7.5.3	Correlations with CO	150
7.6	Discussion	152
7.6.1	The OCN^- abundance	152
7.6.2	OCN^- abundance variations	155
7.6.3	OCN^- formation toward low-mass YSOs	156
7.7	Conclusion	158
Nederlandse samenvatting		161
Curriculum Vitae		165
Acknowledgements		167

Chapter 1

Introduction

The formation of snow and ice has always intrigued humans and challenged them to study these phenomena. The oldest text known that touches on the fundamental structure of a snow-crystal was written around 135 B.C. by the ancient Chinese philosopher Han Ying. In his book on the Moral Discourses of the Han Text, he was probably the first to recognise its hexagonal form, clearly stating that the 'flowers of snow are always six-pointed' (Mason, 1966). However, water was already suggested to exhibit a star-like geometry by the Greek philosopher Philalaos (460–400 B.C.), a Pythagorean follower who assumed that 'the particles of water are made of icosahedra', based on the universal theory of the five elements of nature (earth, water, fire, air, and ether) (Stillman, 1960). About 1100 years later, around 1000 A.D., the snow-crystal appears in the European literature in a manuscript of one of the first European students and writer Albertus Magnus. Every snowflake has its own unique history of formation, but although they all share the six-pointed symmetry, no two are alike. This is nicely visible in one of the first images found (see previous page), carved on wood by Olaus Magnus around 1555 A.D., which shows a beautiful reproduction of the many different forms of snowflakes that exist in nature. It is obvious from these clearly imaginative carvings, showing a moon, a hand and a flower shape, that people found them fascinating.

Like snow-crystals, interstellar ices consist predominantly of water (H_2O), but also contain significant fractions of other molecules such as carbon monoxide (CO), carbon dioxide (CO_2), and methanol (CH_3OH), and traces of dinitrogen (N_2) and ammonia (NH_3). The presence, or absence, of a molecule in the ice strongly depends on the environmental conditions. Vice versa, these molecules have an influence on their environment as well. Hence, the chemical composition and the structure of interstellar ices are thought to contain valuable information about the past and the future of interstellar regions, and it is for this reason that interstellar ices are simulated and studied under laboratory conditions. The present thesis contains a study of laboratory analogs of interstellar ices and presents a newly developed apparatus that provides a novel laboratory route to investigate the properties of these ices in more detail than has previously been possible.

1.1 The Interstellar Medium

Stars and their constellations were studied long before it was realised that the dark regions in between were not just ‘empty space’ (Herschel, 1785). Evidence that these ‘dark patches’ were actually composed of some kind of material was found by Hartmann (1904), who was the first to observe an absorption line from the calcium ion in the direction of a bright star whose line of sight passes through a region which was later interpreted to be an intervening interstellar cloud. In the following years, observations of additional small volatiles like hydrogen, helium and sodium from photographs of diffuse nebulae (e.g. Barnard, 1919) and in absorption on stellar spectra (e.g. Henroteau, 1921) became an accepted fact (McCrea, 1950; Plaskett & Pearce, 1930).

1.1.1 The observation of molecules

Molecules, radicals, ions and atoms are either observed in emission, or in absorption against a background radiation source. In the gas phase, they are mainly observed in the optical- and the millimetre-wavelength range of the electromagnetic spectrum, with only few in the infrared (IR) range. In contrast, in the solid state these compounds are observed mainly from their IR-absorption spectra, at wavelengths typically between 2–20 μm .

The first interstellar multi-atomic species were detected in the optical in absorption: CH and CN, two radicals that can only survive in the gas phase (McKellar, 1940; Swings & Rosenfeld, 1937). This observation, in combination with theoretical evidence for the presence of clouds led to the now generally accepted viewpoint that a considerable part of these clouds is in a molecular form. Since then, over 137 different molecules have been detected in the interstellar medium. Most of them are associated with cloudy regions of intensive star-formation. They range in complexity from the simplest diatomic (H_2), through familiar ones like H_2O , CO, CO_2 , NH_3 , nitrous oxide or “laughing gas” (N_2O), ethanol ($\text{CH}_3\text{CH}_2\text{OH}$), to exotic carbon-chains (“cyano-polyynes”) like HC_{11}N , and strong evidence exists for even larger aromatic molecules (polycyclic aromatic hydrocarbons, PAHs), although specific assignments have not yet been possible (e.g. Ruiterkamp et al., 2005).

1.1.2 Interstellar clouds and star formation

The most chemically rich areas of the interstellar medium are represented by hot cores (HCs) (e.g. Cazaux et al., 2003). They are characterised as warm (100–200K), dense ($n_{\text{H}} = 10^7 \text{cm}^{-3}$) regions (see also Table 1.1), that are in most cases associated with high mass star-formation, i.e typically 10 times more massive than our Sun, although solar-mass stars are now also known to have hot cores. Internal heating and UV-radiation that may be present inside HCs cause processing and evaporation of ice mantles, which initiate a rich chemistry, both in the gas-phase and in solid, and lead to the formation of a wide range of complex organics. As most molecules are observed in these regions of a cloud, the process of star-formation

Table 1.1: *Temperature and density of interstellar clouds*

Interstellar cloud	Density $n_{\text{H}} \text{ cm}^{-3}$	Temperature K
Diffuse molecular cloud	~ 100	40–80
Dense molecular cloud	$\sim 10^4\text{--}10^6$	10–50
Hot cores	$\sim 10^7$	100–200

will be shortly addressed to sketch the environment in which these molecules are thought to form.

A brief and oversimplified view of the evolutionary sequence of a star is as follows (see also Fig 1.1): at the appropriate temperature and density conditions, gas and dust contract to form concentrations, called clouds (see Table 1.1 for an overview on their typical temperatures and densities). In most cases, though, the gas and dust are not homogeneously distributed along this cloud, but situated in regions of lower and higher density. The higher density regions, so-called clumps, may contract further forming stars, possibly surrounded by a planetary system.

How this star-forming process is initiated is not yet fully understood. Possibly shocks, turbulence and magnetic fields play a role. The current understanding is that, provided that the temperature is low enough, a clumpy region of a cloud collapses under its own gravitational force to produce a young stellar object (YSO), surrounded by an envelope of gas and dust material. As the YSO evolves into a pre-main sequence star, part of this material settles in a rotating disk around the central star where the coagulation of gas and dust produces small bodies and planetesimals, which in turn can form planets. Eventually, when the star blasts away the remaining part of the disk, it enters the main-sequence into a stable life cycle.

The typical lifetime of a dark cloud is on the order of 10^5 to 10^7 yr and one can expect that during this time the molecular composition of the cloud changes tremendously due to a wide variety of chemical reactions induced by thermal-, UV- and particle-irradiation originating from stars. It is therefore very likely that the molecules observed in the initial cloud, and those observed in circumstellar disks or planets, may not be similar but are coupled via a complex network of chemical reactions. Knowing the (chemical) link between these molecules observed at different stages of the clouds life cycle is key in understanding the evolutionary process from clouds to stars.

1.1.3 Ices and dust grains

The interstellar dust grain

Interstellar dust grains are thought to be composed of primarily silicate and carbonaceous material probably enriched with elements such as iron, aluminium and magnesium (Jones & Williams, 1987; Krishna Swamy & O'Dell, 1967; Merrill et al.,

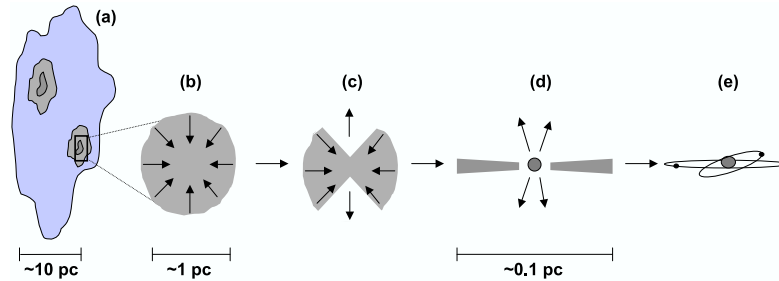


Figure 1.1: Simplified scheme of the star-formation process occurring in a dense cloud. (a) Clumped regions in a dense cloud. (b) A collapsing clump forms a pre-stellar core. (c) The pre-stellar core evolves into a young stellar object (YSO). (d) The YSO evolves to form a pre-main sequence star surrounded by a disk of gas and dust. (e) The star enters the main-sequence, possibly surrounded by one or more planets. The arrows point to the direction of material falling onto the core, or moving outwards via bipolar outflows on opposite sides of the stellar core, perpendicular to the disk. The typical dimensions of the star-complex are indicated in parsec where $1 \text{ pc} \approx 3 \times 10^{16} \text{ m}$.

1976; Tielens et al., 1996), although, their exact composition and morphology is still under debate (Dunne et al., 2004). It is known by now that interstellar dust grains cover a wide range of sizes from $0.01\text{--}1 \mu\text{m}$, and that even larger grains are likely to exist in circumstellar disks in which planets are forming. The size of these dust grains is of the same order of magnitude as that of the dust particles in cigarette smoke, of natural air pollutants, of metallic dust, or that of viruses, but about 100 times smaller than the floating raindrops of a foggy cloud on earth.

Interstellar ices

Many dust grains residing in cold dense interstellar cloud regions are covered by icy mantles of molecules. Water (H_2O) was the first ice-phase, or solid state, molecule as such detected, identified by its $3.1 \mu\text{m}$ IR-absorbance feature (Gillett & Forrest, 1973). However, its absorbance spectrum was somewhat puzzling as it was not perfectly reproduced by a laboratory based absorbance spectrum of a single pure H_2O -ice and seemed to indicate different ice-environments. The observed band profile was therefore proposed to be either due to mixtures with other molecules such as NH_3 (Merrill et al., 1976), or due to the presence of various different H_2O -ice structures (Léger et al., 1979). Justification for the possible presence of mixed ices was found soon afterwards, when more molecules were discovered in the solid state (e.g. Boogert & Ehrenfreund, 2004; Gerakines et al., 1999; Keane et al., 2001; Schutte et al., 1999; Schutte & Khanna, 2003; Willner et al., 1982).

Interstellar ices are found in the dense regions of interstellar clouds (e.g. Gibb et al., 2004), in the mid-plane of disks around young stars (e.g. Pontoppidan et al.,

Table 1.2: Molecules detected in interstellar ices towards protostars

Molecule	Abundance % w.r.t. H ₂ O	Molecule	Abundance % w.r.t. H ₂ O
H ₂ O	~100 ^a	CO	~3–50 ^a
CO ₂	~7–25 ^a	NH ₃	<10 ^a
CH ₃ OH	2–25 ^a	CH ₄	0.9–1.9 ^b
H ₂ CO	3–7 ^b	OCS	0.1 ^b
C ₂ H ₆	≤0.4 ^b	OCN [−]	≤1.9 ^c
NH ₄ ⁺	3–17 ^d	HCOOH	≤1.7 ^e

^a Gibb et al. (2004), ^b Ehrenfreund et al. (1997), ^c Chapter 7, ^d Schutte & Khanna (2003), ^e Keane et al. (2001)

2005), on satellites (e.g. Buratti et al., 2005; Jewitt & Luu, 2004; Nussbaumer, 2005; Ostro & Pettengill, 1978), and in comets (e.g. Crovisier et al., 2004; Kawakita et al., 2004). These ices can contain a large fraction (more than 50%) of all the condensible material and are consequently an important sink and source of volatile molecules. The molecules detected to date in ices towards protostars are summarised in Table 1.2. As H₂O appears to be always the dominant ice constituent, the abundances of the other molecules are listed with respect to the amount of H₂O-ice observed. Particularly interesting is the observation of an absorption feature at 4.62 μm (Soifer et al., 1979). First, this feature was thought to be due to solid CO, but later it was ascribed to OCN[−], an ion which is readily produced by ultraviolet and particle irradiation of “simple” H₂O, CO and NH₃-containing interstellar ice analogs in the laboratory (e.g. Grim & Greenberg, 1987, and Chapter 6), and which consequently provided the first observational evidence for the presence of complex ice chemistry.

The formation of ice mantles

Similar to snowflakes on earth, interstellar ices grow when gas phase molecules crystallise around a nucleation-core in the form of thin icy mantles (typically 40–100 molecular layers thick, Pontoppidan et al., 2003). This condensation process is initiated by high gas-densities ($n_{\text{H}} = 10^3\text{--}10^5$ atoms cm^{−3}) and low temperatures (10–50 K). When the sticking probability of the molecules is close to unity, a value that is assumed to apply to many gases under dense cloud conditions (because for most, the surface temperature of the grains is below their sublimation point), chemical models of dense cloud regions (e.g. Willacy & Millar, 1998) show that all molecules, except H₂, are removed from the gas phase within $\sim 10^9/n_{\text{H}}$ years. This implies that all gas phase molecules condense as ice mantles around dust grains within the lifetime of such a cloud. However, since for each molecule the critical temperature required for condensation is different, one can imagine that in the presence of a temperature gradient different molecules freeze-out in different regions of a cloud or disk, or at different stages in time in a cool-down or heating

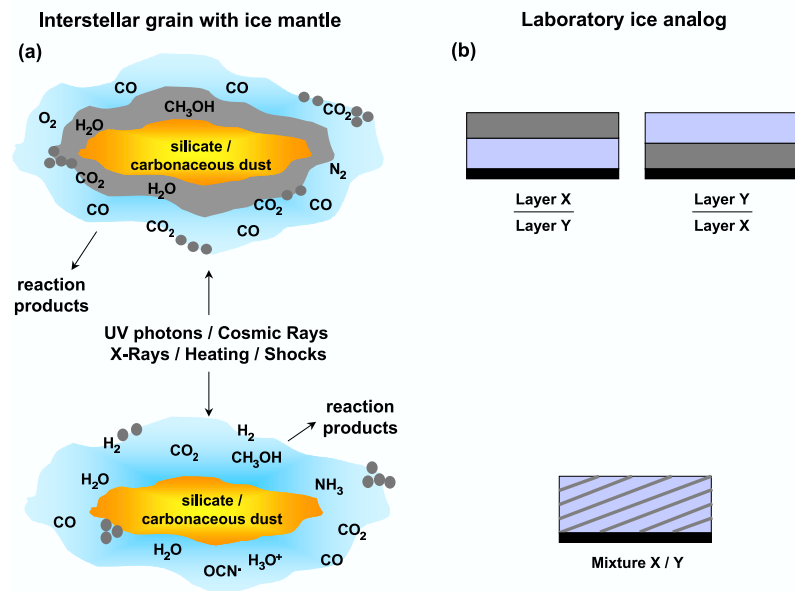


Figure 1.2: (a) Two possible models for the structure of an interstellar ice mantle. (top) An ice as formed from the condensation of gases, thermal distillation or via surface reactions, and (bottom) resulting from thermally induced diffusion of molecules and chemical reactions induced in the bulk of the ice. The grey dots represent molecules. The different external energy sources that may affect the ice are shown and desorbing reactants and products are indicated. (b) The laboratory model of (top) a layered, and (bottom) a mixed interstellar ice analog composed of molecules X and Y.

phase.

Consequently, the differential accretion of species from the gas phase will have a large influence on the eventually formed ice structure. However, the ice structure is also determined by the in-situ production of molecules: either at the grain or ice surface via surface reactions, or by chemical and physical processes that are induced at the surface or in the bulk of the ice by various external energy sources that affect the ice as it is evolving over time.

One model to describe the morphology of these ice mantles is therefore that of an onion-shell, shown schematically at the top in Fig. 1.2a for the strongly simplified scenario of two layers dominated by H₂O and CO, respectively. Such a structure is either produced via differential accretion, or via “thermal distillation” when initially mixed ice components segregate into different ice phases due to thermal warming (see Schutte & Greenberg, 1997, for a review). Thermal segregation is seen for example for mixtures of CO₂ and H₂O under laboratory conditions (Sandford & Allamandola, 1990). Molecules produced in-situ via surface reactions can further enhance this layered structure, in this case leading to small amounts

of CO₂ residing at the CO-ice surface. However, as surface reactions occur during the different stages of the ice mantle growth provided that the precursor molecules are present, CO₂ can also form prior to any major CO freeze-out (forming the CO-ice layer) resulting in a CO₂-ice layer at the interface between CO and H₂O.

Alternatively, the ice morphology can be described by a model of a mixture (Fig. 1.2a, bottom). Ever since the first observational indication that complex chemistry could be occurring in interstellar ice mantles (Soifer et al., 1979), it has been proposed that irradiative processes induced by cosmic-rays, energetic particles or ultraviolet (UV)-photons may be key in the formation of molecules in dense molecular clouds (e.g. Gerakines et al., 1996; Greenberg et al., 1980; Hudson & Moore, 1993; Muñoz Caro et al., 2004). These induce the formation of the next generation molecules in the bulk of the ice, which naturally gives rise to a more mixed structure instead of clearly segregated layers. In addition, a mixed ice morphology can be produced by thermally induced mixing of layered ices due to the diffusion of molecules, a process that is observed, for example, for CO and H₂O, where initially segregated CO migrates into the H₂O-ice layer (Collings et al., 2003).

Observational evidence suggests that most ices consist of rather pure ice environments, i.e. different layers (or domains) of segregated molecules. However, the different factors affecting the ice morphology clearly indicate that this does not imply that the ices must be formed as such. Instead, because the ice morphology observed is the result of an unknown combination of freeze-out, surface reactions, and thermal- and irradiative processing, a thorough understanding of the possible interstellar formation and destruction mechanisms of the observed molecules, and their physical interactions as a function of temperature, is required when one wants to propose a possible scenario for the formation and evolution of the observed interstellar ices. Chapters 2 and 3 of this thesis present such a study for the CO-CO₂ ice system conducted under laboratory conditions. This work shows that mixed and layered CO-CO₂ ices behave significantly different upon thermal warming, suggesting that based on a laboratory comparison, their interstellar spectra can serve to constrain the initial formation mechanisms of CO₂ from the presence (or absence) of an interstellar CO-CO₂ ice environment.

Chemical differentiation

As more molecules are being detected in an increasing variety of environments, it appears that the solid-state abundances of molecules can show very different trends from one environment to another. Some showed a surprisingly constant abundance toward different sources, for example the amount of CO₂-ice with respect to that of H₂O-ice (Boogert & Ehrenfreund, 2004; Boogert et al., 2004; Gerakines et al., 1999; Gibb et al., 2004; Nummelin et al., 2001; Whittet et al., 1998), whereas other abundances, such as those of CO-ice (Pontoppidan et al., 2003) and solid OCN⁻ (Chapter 7) vary from source to source by at least one order of magnitude. It is also observed that going from the outside into the centre of an interstellar cloud, the ices are composed of a different set of molecules (van Dishoeck et al., 1999). This chemical differentiation is obviously due to the physical or chemical

processes at work, and it was therefore proposed that the formation, destruction, freeze-out and desorption of molecules should depend on the local conditions. Vice versa this implies that solid-state molecules (possibly in combination with those present in the gas-phase) can be used as chemical probes to characterise the physical conditions of a certain environment. These conditions are studied by astrochemical models that use the chemical and physical characteristics of molecules determined in the laboratory to describe the evolution of the chemical composition of a certain environment with time as a function of physical parameters such as temperature, density and radiation field (e.g. Bergin et al., 2001; Pontoppidan et al., 2005; Rodgers & Charnley, 2001; Tafalla et al., 2004).

New telescopes built to observe ices, such as the ground based VLT-ISAAC spectrometer on Paranal (Chile), the Spitzer Space Telescope, and in the future the mid-infrared instrument MIRI on the James Web Space Telescope, (will) bring large progress to the understanding of the chemical distribution of molecules. Their significantly improved observational sensitivity and spectral resolution, compared to their predecessor ISO, allow to probe regions toward much fainter background stars than was previously possible. This opens up the possibility to look for the same cloud at many lines of sight to YSOs and background stars that are spatially only hundreds of AU apart ($1 \text{ AU} \approx 1.5 \times 10^{14} \text{ m}$). In this way, one can “map” small scale abundance variations of molecules to resolve the chemical structure of interstellar cloud environments in high detail (Pontoppidan et al., 2005, 2004), which consequently will provide new information to refine the astrochemical models and improve our understanding of cloud evolution.

1.1.4 UV in the interstellar medium

This thesis focuses on the effects of UV-irradiation on the chemical and physical behaviour of the most abundant molecules observed in various interstellar ice analogs under simulated conditions in the laboratory, and compares these effects to those induced by thermal warming. UV-photons are either produced in the vicinity of a young star, or induced by cosmic ray excitation of H_2 . The first gives rise to a broad range of UV-photons contributing to an interstellar radiation field (ISRF) on the order of $10^8 \text{ photons cm}^{-2} \text{ s}^{-1}$ at the outer edge of a molecular cloud (Mathis et al., 1983), although this can be higher when the young star is in close proximity to the cloud. However, the penetration of interstellar UV-photons into a cloud is limited as they get absorbed by the dust present. This causes the attenuation of the interstellar UV-field inwards (i.e. at a cloud extinction of $A_V = 5 \text{ mag}$ the ISRF is reduced to about $10^4 \text{ photons cm}^{-2} \text{ s}^{-1}$) and may eventually lead to the absorption of all interstellar UV-photons in the outer regions of a cloud if this cloud is sufficiently dense. Cosmic rays do, however, penetrate a dense cloud without being absorbed and thereby create a cosmic ray induced UV-field in the interior of the cloud. This UV-field is much weaker than that of the ISRF, typically 10^3 – $10^4 \text{ photons cm}^{-2} \text{ s}^{-1}$ (Shen et al., 2004), although X-ray induced UV-photons may have an additional contribution in some cloud regions (Stäuber et al., 2005), and its photons are somewhat less energetic, being dominated by the Lyman and Werner emission bands of H_2 . Because of this less intense, less energetic cosmic ray in-

duced UV-field, the contribution of UV-photoprocessing to the chemical evolution in dense clouds is still a topic of debate (Bourdon et al., 1982; d’Hendecourt et al., 1982; Gerakines et al., 1999; Tielens & Hagen, 1982; van Broekhuizen et al., 2004). UV-photons are, however, expected to play an important role in the (clumpy) photon dominated regions (PDR’s) (Bergin et al., 1995; Gorti & Hollenbach, 2002; Jansen et al., 1995; Spaans et al., 1995; Störzer & Hollenbach, 1999; Turner, 2000), in the upper layers of circumstellar disks (Aikawa et al., 2002; van Zadelhoff et al., 2003; Willacy & Langer, 2000), and in the outer regions of dark clouds (Shen et al., 2004).

In addition to the potential of UV-photons to induce an active ice-chemistry, they may also mediate in the desorption of molecules (Chapter 7). Photodesorption is the process in which the absorption of a photon by a solid state molecule induces the ejection of this molecule into the gas-phase. Chemical models of some of the regions mentioned above predict that UV-photodesorption can be an effective route to return condensed molecules from interstellar grains back into the gas phase, if the photodesorption of the molecules is sufficiently efficient (Watson & Salpeter, 1972a,b; Willacy & Langer, 2000).

1.2 Laboratory Astrophysics

The observation of emission and absorption spectra of a large variety of (initially unknown) interstellar molecules in the millimetre, sub-millimetre, near-, and far-infrared wavelength range, triggered laboratory astrophysics because it required a database of known molecular spectra to use as a comparison to facilitate their identification. At the time when the first observational spectra were obtained, a lot of spectral information was already at hand as physicists and chemists had studied the spectroscopy of many gases and solids. Most of these studies, however, applied to atmospheric conditions, which vary significantly from those of the ISM, especially from those environments where most ices are found. As these differences can give rise to distinct molecular characteristics, solid state laboratory astrophysics has been devoted to study the different spectral properties of astronomically relevant condensed molecules under simulated interstellar conditions as a function of the ice composition, the temperature, and processes such as UV- and particle irradiation (e.g. Bernstein et al., 1997; d’Hendecourt et al., 1986; Ehrenfreund et al., 1999; Elsila et al., 1997; Gerakines et al., 1996; Grim et al., 1989; Hagen et al., 1979; Hudson & Moore, 1999; Palumbo, 1997; Roser et al., 2001; Schutte et al., 1992; van Broekhuizen et al., 2004; Watanabe & Kouchi, 2002; Whittet et al., 1998; Wu et al., 2003).

1.2.1 Interstellar ice analogs

The scenarios that apply to the formation of ices in interstellar clouds (Sect. 1.1.3) logically give rise to two different morphologies that simulate these ices in the laboratory, i.e. a mixed ice analog, and one composed of different layers of either pure or mixed molecules, shown schematically in Fig. 1.2b.

Unravelling the interstellar ice composition

Using the models in Fig. 1.2b as a starting point, the spectral characteristics of interstellar ice analogs are studied to find the correct combination of ices that reproduces the interstellar case. Though relatively effective in providing a possible identification of the ices observed, this mix-and-match approach can easily give rise to degenerate results (e.g. Boogert et al., 2004; Léger et al., 1979; Merrill et al., 1976; Pendleton et al., 1999). This is in the first place because the interpretation of interstellar spectra is complicated by the possible presence of the many different ice-environments in the line of sight between the telescope and the radiation source. Although a detailed analysis of observations often can put constraints on the number of environments present, one can never be 100% certain if the molecules observed in a single spectrum are condensed on the same dust grain, or if the spectrum is a superposition of spectra of many different ice mantles. Furthermore, observations often contain only a limited set of spectral features, which complicates the ice analysis as a laboratory spectrum arising from a mixture of molecules does not necessarily result in a unique interpretation, especially not if only one or two absorption bands are observed. A third complication arises as the observed spectral profile may be modified due to grain shape effects compared to the laboratory spectrum, which in some cases can produce similar band profiles as can be induced by thermal warming.

It is therefore very important not only to reproduce the interstellar spectrum, but also to establish a basic understanding of the physical behaviour of each molecule detected. Some of the questions that need to be addressed are: How does the spectrum of a single molecule in a pure ice change as a function of the temperature and the ice structure? How does this thermal behaviour change in the presence of a second molecule, and what happens if a third molecule is added to the ice? Is there a difference between the thermal behaviour of molecules in a mixed and layered ice configuration, and what spectroscopic changes do irradiative processes induce? At this moment, these problems are being studied in several different laboratories, which all aim for a better understanding of the processes underlying the ice-observations, such that from a combination of the band profiles of different molecules observed, the ice-environment of interstellar ices can be constrained (e.g. Alsindi et al., 2003; Ehrenfreund et al., 1999; Fraser et al., 2004; Sandford et al., 1988, and Chapters 2 and 3 of this thesis).

1.2.2 A simulated interstellar environment

The simulation of interstellar conditions to study interstellar ice mimics in an earth based laboratory is a tedious task, which needs to take into account the temperature and pressure in the ISM, the effects of the (partly unknown) interstellar grain surface, and the different time scales involved in the reactions. Most of the astronomically oriented laboratory work has been conducted under high vacuum (HV) conditions at typical pressures of 10^{-7} Torr (or $\sim 0.8 \times 10^{-7}$ mbar) and cryogenic temperatures that can be varied between 10–200 K (where 273 K = 0°C). Fig. 1.3 presents a schematic picture of the HV reaction chamber that has been used to study the physical interactions between solid CO and CO₂ in Chapters 2 and 3,

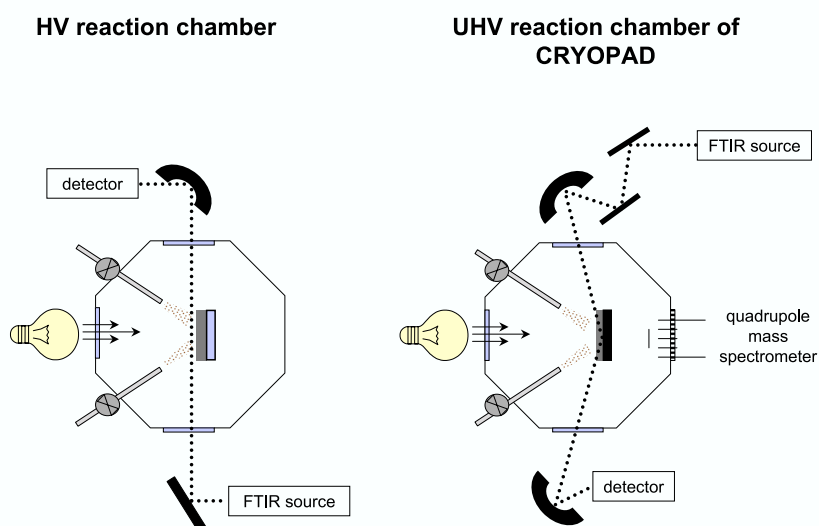


Figure 1.3: A schematic representation of (left) the HV reaction chamber and (right) the UHV reaction chamber of CRYOPAD, showing the analysis techniques, Fourier Transform infrared (FTIR) spectroscopy and quadrupole mass spectrometry, used to monitor the physical and chemical behaviour of the condensed molecules. Gas phase molecules are condensed via two deposition tubes at the surface of an infrared (IR)-transparent CsI window (in the HV) or a reflective Au-surface (in the UHV), positioned at the centre of the chamber. Both surfaces can be rotated 360° degrees to allow for transmission FTIR in the HV chamber, or for line of sight mass spectrometry in the UHV chamber. The ice formed can subsequently be heated thermally or irradiated by the UV light source (lamp).

and the UV-induced formation of OCN^- in Chapter 6 (see Gerakines et al., 1995, for a description).

However, although it can be assumed that the pressure regime at 10^{-7} Torr (or $\sim 10^{10}$ molecules cm^{-3} at 50 K) is such that no more than two gas phase molecules collide at once, it is still a factor of 10^3 – 10^6 higher than is to be expected in the densest regions of an interstellar cloud (Sect. 1.1.3). As this HV environment consists predominantly of H_2O , this gives rise to considerable amounts of H_2O accreting at the ice surface during an experiment of typically 2–24 hours: about one layer of H_2O molecules each 10–100 seconds. This is not so dramatic when H_2O -dominated ices are studied, but becomes significantly problematic when one wants to look at chemical (or physical) processes in the complete absence of H_2O . One way around this problem is to look at sufficiently thick ices, so that any H_2O

accretion in the course of the experiment is only a minor fraction of the total amount of ice. Still, to be conclusive about processes such as the questionable UV-induced formation of CO₂ from pure CO-ice (Cottin et al., 2003; Gerakines et al., 1996), it is important to remove this source of contamination by creating a better, “cleaner” vacuum. In addition, a better vacuum will relax the restrictions on the experimental conditions to study thick ices only, which does not apply to the interstellar ice thickness and may be a source of error (on the order of 100 molecular layers of ice, Pontoppidan et al., 2003).

Therefore, more and more laboratories in the astrochemistry community now start to develop ultra high vacuum (UHV) instruments (Roser et al., 2002; Watanabe et al., 2000, and Chapter 5). The improved vacuum conditions under which these UHV systems operate, i.e. on the order of 10^{-11} – 10^{-10} Torr, significantly decrease the H₂O contamination and consequently allow for the study of thin films of condensed molecules relevant to interstellar ice mantles in dense clouds at an increase sensitivity.

1.2.3 CRYOPAD

The Cryogenic Photoproduct Analysis Device (CRYOPAD), a new instrument built in the Raymond and Beverly Sackler Laboratory for Astrophysics as part of this Ph.D.-project, is developed to simulate ‘hot core’ chemistry in the laboratory, but can alternatively be used to study processes under conditions that apply to the more quiescent regions of dense clouds. Fig. 1.3 (right) shows a sketch of the reaction chamber. Its settings are specified to study the effects of UV- and thermal processing on the solid state chemistry of interstellar ice analogs. UHV conditions (8×10^{-11} Torr) are applied to minimise contamination of the ice sample, which is essential for the analysis of the formation of trace products of the processing *and* the detection of possible photon-induced desorption of the condensed molecules or reaction products. Photodesorption is often neglected when UV-induced reactions of condensed molecules are studied in the laboratory (e.g. Cottin et al., 2003; Gerakines & Moore, 2001; Gerakines et al., 2000, 2004, 1996). However, experiments by Westley et al. (1995a,b) show that the photodesorption of H₂O-ice by UV-photons can be significant and high enough to be an effective means to return physisorbed molecules from interstellar grains to the gas-phase in those parts where there is major freeze-out due to high densities and low temperatures (see Sect. 1.1.4).

The physical interactions between the condensed molecules and the induced formation of reaction products are recorded by Fourier Transform reflective absorption infrared spectrometry (FT-RAIRS) in the 4000-400 cm⁻¹ region. In addition, the gas phase composition of the reaction chamber is monitored in-situ by a quadrupole mass spectrometer to allow for the detection of photodesorbing molecules. The quadrupole mass spectrometer is additionally used to study the physical interactions between molecules in the solid state via temperature programmed desorption (TPD). In a typical TPD measurement a constant heating rate is applied to the ice to desorb all condensed molecules. From the resulting desorption spectrum recorded molecule-selectively by the mass spectrometer, one

can derive the binding energies of the molecules in the ice and obtain information about the ice structure. The combination of FT-RAIRS and quadrupole mass spectrometry significantly improves the methodology of analysis, which provides for a much better understanding about the chemical and physical processes that are induced in the ice (see Chapter 5 for further details).

1.2.4 Limitations to the simulation of interstellar ice chemistry

Although laboratory experiments are essential for understanding the physical and chemical processes that possibly occur in interstellar ices, there are certain limitations to the application of the data (see Turner, 1974, for a somewhat dated though instructive overview). Apart from the uncertainties about the history of the observed interstellar ices, two other factors may have an influence on the laboratory results that cannot be accounted for. First is the actual grain surface, and second is the timescale involved in the evolution of an interstellar ice mantle.

The surface at which a molecule condenses can have a strong effect on the chemical and physical behaviour of this molecule. For example, due to surface-molecule interactions, the surface can change the ice structure, change the spectral profile of the molecule or mediate as a catalyst in chemical reactions. Most HV experiments that use transmission infrared spectroscopy to study the ices require an IR-transparent surface such as CsI, CaF₂, NaCl or MgF₂, but alternative surfaces such as carbonaceous material or Au can be adopted when different analysis techniques are used. It must be realised that none of these surfaces truly reflect the interstellar grain surface, nor come close to simulate their actual size, although attempts are being made to study condensed molecules at surfaces that are more astronomically relevant (e.g. Fraser et al., 2005, and references therein). However, as the exact grain surface is unknown, it is difficult to deduce its participation in ice-phase reactions. To a first approximation, it is therefore best to study interstellar ice analogs at an inert surface. This approach allows to study the interaction between the condensed molecules in isolation, before this interaction is being complicated by the additional influence of the underlying surface.

The time-span difference between a laboratory experiment and the age of a typical ice mantle in an interstellar cloud is often accounted for by astrochemical models. These models extrapolate the reaction kinetics obtained in the laboratory to the conditions (time, pressure and temperature) that apply to the interstellar case. However, the validity of such extrapolations is not at all obvious. The maximum duration of a single experiment in the laboratory is on the order of 24 hours, which can be extended to about 10 days under UHV conditions. However, the typical lifetime of a molecular cloud is on the order of 10⁵–10⁷ years. This means that there is a chance that extremely slow kinetic processes that do not happen on a laboratory time scale, do occur in space. As many reaction kinetics strongly depend on the temperature, one method to stimulate slow processes in the laboratory is to raise the temperature, although then different reaction pathways may become available that were previously inaccessible, something that should be checked for.

A second process where time plugs in, one that is especially relevant to consider for this thesis, is the UV-induced chemistry. The cosmic ray induced UV field

inside an interstellar cloud (10^3 – 10^4 photons $\text{cm}^{-2} \text{s}^{-1}$) is many orders of magnitude lower than that used in the laboratory (10^{13} – 10^{15} photons $\text{cm}^{-2} \text{s}^{-1}$), which is required to observe any significant effect of irradiation within a 24 hours experiment (see for example Chapter 6 of this thesis). With typical UV-absorption cross sections of $10^{-18} \text{cm}^2 \text{photon}^{-1}$ per molecule, this implies that in the laboratory, it takes about 1000 s on average before a UV-excited molecule gets excited by a second photon. In the interstellar case the time between a first and second photon excitation is much longer, but because most chemical reactions occur on pico- to milli-second time scales, one can safely assume that this does not give rise to significantly different chemical reactions, but only if the reaction rate and the UV-flux are linearly proportional. The difference in UV intensity can become of importance if the UV-induced processes studied are non-linear and depend on the photon-dose.

By knowing about the possible sources of error that can be introduced when interstellar conditions are simulated in the laboratory, control experiments can be setup such that the extent of their uncertainties can be investigated. Given these limitations, laboratory studies can therefore add to a better understanding of the physical and chemical processes between astronomically relevant molecules in the solid state.

1.3 Thesis Outline

This thesis presents a laboratory study on the physical and chemical behaviour of condensed molecules induced by thermal warming and UV-irradiation under simulated interstellar cloud conditions in the laboratory. Part of this work, i.e. that presented in Chapters 2, 3, and 6, has been conducted under HV conditions using FTIR spectroscopy to study the infrared characteristics of the solid state molecules. Chapters 4 and 5 present the work from CRYOPAD, the new UHV apparatus that has been developed and built as part of this thesis project, and is dedicated to quantitatively study UV-induced processes in ices (Sect. 5.2). The Chapters are ordered by increasing complexity of the physical and chemical processes induced in the solid, starting with a study on the thermal interaction between CO and CO₂ and closing with a quantitative study of the UV-formation efficiency of OCN⁻. Chapter 7 is not a laboratory investigation but presents a large set of observational data of the 4.62 μm band, ascribed to the OCN⁻ ion. This observational investigation forms a nice example of how the interstellar ice environment and formation mechanisms of a molecule can be constrained from a comparison of laboratory data and a large sample of observational spectra.

Chapter 2 presents the results of the first systematic study on the spectral characteristics of the physical interactions between CO and CO₂ in mixed *and* layered ices as a function of temperature. CO and CO₂ are two of the most abundant molecules observed in interstellar ices after H₂O. Under interstellar conditions, it is most likely that CO₂ forms via surface reactions involving CO, or alternatively via irradiative processes when CO resides in a H₂O-rich ice environment. CO, on the other hand, forms in the gas phase but is easily regenerated by the

same irradiative processes that formed CO₂. This interrelation suggests that CO and CO₂ are likely to be located in close proximity of each other in interstellar ices, which is expected to be visible from their IR-spectra. The improved spectral resolution (0.5 cm⁻¹) used in comparison to previous works, extends the existing Leiden database of laboratory spectra to match the spectral resolution reached by modern telescopes and to support the interpretation of the most recent data from the Spitzer Space Telescope. It is found that the spectroscopy and the desorption characteristics of mixed and layered ices are fundamentally different, implying that a combination of the spectral profiles of CO and CO₂ can be used to constrain the morphology and thermal evolution CO-CO₂ ices. Furthermore, the data suggest that the interstellar CO-CO₂ ice spectra likely reflect the initial formation conditions, and that CO₂ can act as a physical barrier to CO interacting with other molecules.

These results, together with additional data on the desorption kinetics of CO from CO-CO₂ ices, are used in **Chapter 3** to construct a model to describe the physical properties of CO and CO₂ under interstellar conditions. This model provides a more fundamental understanding of the CO-CO₂ system, and can be used to predict the physical interactions of these molecules in a variety of different condensed phases that may be present in interstellar ices.

Chapter 4 presents the first experimental report of the desorption of CO and N₂ from layered and mixed ices, studied in CRYOPAD using TPD. Millimetre observations of pre- and protostellar cores show that the abundances of the gas-phase tracer molecules, C¹⁸O and N₂H⁺, anti-correlate with each other and often exhibit "holes" where the density is greatest. Although these results are reasonably well reproduced by astrochemical models, experimental evidence found here shows that the relative difference between the CO and N₂ binding energies is significantly less than those adopted by the models. This result will decrease the anti-correlation of CO and N₂H⁺ in the gas-phase (once applied to the models), and is the first step to study the more complex, astronomically more relevant system of the desorption kinetics of CO and N₂ from H₂O-ice.

In **Chapter 5**, CRYOPAD has been used to study the desorption of CO from solid CO induced by UV-photons as a function of the surface coverage and the ice temperature. This is the first study conducted in CRYOPAD that makes use of the quadrupole mass spectrometer, the FT-RAIRS system and the UV-irradiation source together. The results indicate that this photodesorption is probably not very efficient under interstellar conditions, but may occur due to processes induced in the underlying grain or ice surface. This first set of results demonstrates that CRYOPAD can derive qualitative and quantitative information about photo-induced processes of condensed molecules, which will add to the current understanding of these processes under interstellar conditions.

Chapter 6 studies quantitatively the UV-formation efficiency of OCN⁻ in comparison to its thermal production. As the laboratory 4.62 μm feature of OCN⁻ fits well with the 4.62 μm absorption band observed along the line-of-sight towards various young stellar objects, this interstellar band became generally used as a qualitative tracer of energetic processing of interstellar ice mantles. However, the results presented here indicate that the UV-induced formation of OCN⁻ falls

short of reproducing the highest observed interstellar abundances. In contrast, the acid-base reaction between solid HNCO and NH_3 or H_2O is much more efficient in forming OCN^- and it is therefore concluded that the $4.62\ \mu\text{m}$ band is not necessarily a tracer of UV-processing.

The interstellar $4.62\ \mu\text{m}$ band, observed in the spectra of 34 deeply embedded young stellar objects by the VLT-ISAAC spectrometer, has been analysed in **Chapter 7** for the presence of OCN^- . These data provide the first opportunity to study the solid OCN^- abundance toward a large number of low-mass YSO's. It is found that at least two components underlie the $4.62\ \mu\text{m}$ band, of which only one can be ascribed to OCN^- . The results presented in Chapter 6 indicate that the inferred abundances quantitatively allow for a photochemical formation mechanism. However the large source-to-source abundance variations observed within the same star-forming cloud complex suggest that alternative routes, such as surface chemistry, should be considered.

1.4 Outlook

The applications of the newly built CRYOPAD are twofold. The first results obtained suggest that UV-induced desorption processes may substantially contribute to the desorption of ices in the coldest regions of interstellar clouds. Future work should therefore further investigate these processes to understand the underlying desorption mechanisms at work, including a detailed study of their photon-dose dependence, the relation between the photon-flux and the desorption rate, and the effect of the underlying (ice) surface. However, a second important feature of CRYOPAD is that it has the option to grow ices at different rates to produce different ice structures. A second line of research should therefore focus of the chemical and physical behaviour of molecules as a function of the ice structure. Given the accretion rate of gas-phase molecules in interstellar clouds, the ice morphologies that can be formed in CRYOPAD are much more likely to resemble the interstellar case than those produced under HV laboratory conditions. This will add significant new insights to the current understanding of UV- and thermally induced processes under interstellar conditions.

Bibliography

- Aikawa, Y., van Zadelhoff, G. J., van Dishoeck, E. F., & Herbst, E. 2002, *A&A*, 386, 622
- Alsindi, W. Z., Gardner, D. O., van Dishoeck, E. F., & Fraser, H. J. 2003, *Chem.Phys.Lett*, 378, 178
- Barnard, E. E. 1919, *ApJ*, 49, 1
- Bergin, E. A., Ciardi, D. R., Lada, C. J., Alves, J., & Lada, E. A. 2001, *ApJ*, 557, 209
- Bergin, E. A., Langer, W. D., & Goldsmith, P. F. 1995, *ApJ*, 441, 222
- Bernstein, M. P., Allamandola, L. J., & Sandford, S. A. 1997, *Advances in Space Research*, 19, 991
- Boogert, A. C. A. & Ehrenfreund, P. 2004, in *The Astrophysics of Dust*, In press
- Boogert, A. C. A., Pontoppidan, K. M., Lahuis, F., et al. 2004, *ApJS*, 154, 359
- Bourdon, E. B., Prince, R. H., & Duley. 1982, *ApJ*, 260, 909
- Buratti, B. J., Cruikshank, D. P., Brown, R. H., et al. 2005, *ApJL*, 622, L149
- Cazaux, S., Tielens, A. G. G. M., Ceccarelli, C., et al. 2003, *ApJL*, 593, L51
- Collings, M. P., Dever, J. W., Fraser, H. J., McCoustra, M. R. S., & Williams, D. A. 2003, *ApJ*, 583, 1058
- Cottin, H., Moore, M. H., & Bénilan, Y. 2003, *ApJ*, 590, 874
- Crovisier, J., Bockelée-Morvan, D., Colom, P., et al. 2004, *A&A*, 418, 1141
- d'Hendecourt, L. B., Allamandola, L. J., Baas, F., & Greenberg, J. M. 1982, *A&A*, 152, L12
- d'Hendecourt, L. B., Allamandola, L. J., Grim, R. J. A., & Greenberg, J. M. 1986, *A&A*, 158, 119
- Dunne, L., Morgan, H., Eales, S., Ivison, R., & Edmunds, M. 2004, *New Astronomy Review*, 48, 611
- Ehrenfreund, P., Boogert, A. G. A., Gerakines, P. A., et al. 1997, in *ESA SP-419: The first ISO workshop on Analytical Spectroscopy*, 3
- Ehrenfreund, P., Kerkhof, O., Schutte, W. A., et al. 1999, *A&A*, 350, 240
- Elsila, J., Allamandola, L. J., & Sandford, S. A. 1997, *ApJ*, 479, 818
- Fraser, H. J., Bisschop, S. E., Pontoppidan, K. M., Tielens, A. G. G. M., & van Dishoeck, E. F. 2005, *MNRAS*, 356, 1283
- Fraser, H. J., Collings, M. P., Dever, J. W., & McCoustra, M. R. S. 2004, *MNRAS*, 353, 59
- Gerakines, P. A. & Moore, M. H. 2001, *Icarus*, 154, 372
- Gerakines, P. A., Moore, M. H., & Hudson, R. L. 2000, *A&A*, 357, 793
- . 2004, *Icarus*, 170, 202

Bibliography

- Gerakines, P. A., Schutte, W. A., & Ehrenfreund, P. 1996, *A&A*, 312, 289
- Gerakines, P. A., Schutte, W. A., Greenberg, J. M., & van Dishoeck, E. F. 1995, *A&A*, 296, 810
- Gerakines, P. A., Whittet, D. C. B., Ehrenfreund, P., et al. 1999, *ApJ*, 522, 357
- Gibb, E. L., Whittet, D. C. B., Boogert, A. C. A., & Tielens, A. G. G. M. 2004, *ApJS*, 151, 35
- Gillett, F. C. & Forrest, W. J. 1973, *ApJ*, 179, 483
- Gorti, U. & Hollenbach, D. 2002, *ApJ*, 573, 215
- Greenberg, J. M., Allamandola, L. J., Hagen, W., van de Bult, C. E. P., & Baas, F. 1980, in *IAU Symp. 87: Interstellar Molecules*, 355–361
- Grim, R. J. A. & Greenberg, J. M. 1987, *ApJL*, 321, L91
- Grim, R. J. A., Greenberg, J. M., de Groot, M. S., et al. 1989, *A&AS*, 78, 161
- Hagen, W., Allamandola, L. J., & Greenberg, J. M. 1979, *Ap&SS*, 65, 215
- Hartmann, J. 1904, *ApJ*, 19, 268
- Henroteau, F. 1921, *J. Royal Astr. Soc. Canada*, 15, 62
- Herschel, W. 1785, *Philosophical Transactions Series I*, 75, 213
- Hoyle, F. & Wickramasinghe, C. 1979, *Ap&SS*, 66, 77
- Hudson, R. L. & Moore, M. H. 1993, *ApJL*, 404, L29
- . 1999, *Icarus*, 140, 451
- Jansen, D. J., van Dishoeck, E. F., Black, J. H., Spaans, M., & Sosin, C. 1995, *A&A*, 302, 223
- Jewitt, D. C. & Luu, J. 2004, *Nature*, 432, 731
- Jones, A. P. & Williams, D. A. 1987, *MNRAS*, 224, 473
- Kawakita, H., Watanabe, J., Ootsubo, T., et al. 2004, *ApJL*, 601, L191
- Keane, J. V., Tielens, A. G. G. M., Boogert, A. C. A., Schutte, W. A., & Whittet, D. C. B. 2001, *A&A*, 376, 254
- Krishna Swamy, K. S. & O'Dell, C. R. 1967, *ApJ*, 147, 937
- Léger, A., Klein, J., de Cheveigne, S., et al. 1979, *A&A*, 79, 256
- Mason, J. A. 1966, *Commentary on Kepler's essay: 'On the Six-Cornered Snowflake'* (Oxford:Oxford University Press)
- Mathis, J. S., Mezger, P. G., & Panagia, N. 1983, *A&A*, 128, 212
- McCrea, W. H. 1950, *The Observatory*, 70, 100
- McKellar, A. 1940, *PASP*, 52, 187
- Merrill, K. M., Russell, R. W., & Soifer, B. T. 1976, *ApJ*, 207, 763
- Muñoz Caro, G. M., Meierhenrich, U., Schutte, W. A., Thiemann, W. H.-P., & Greenberg, J. M. 2004, *A&A*, 413, 209
- Nummelin, A., Whittet, D. C. B., Gibb, E. L., Gerakines, P. A., & Chiar, J. E. 2001, *ApJ*, 558, 185
- Nussbaumer, J. W. 2005, in *36th Annual Lunar and Planetary Science Conference*, 1949
- Ostro, S. J. & Pettengill, G. H. 1978, *Icarus*, 34, 268
- Palumbo, M. E. 1997, *Advances in Space Research*, 20, 1637

- Pendleton, Y. J., Tielens, A. G. G. M., Tokunaga, A. T., & Bernstein, M. P. 1999, *ApJ*, 513, 294
- Plaskett, J. S. & Pearce, J. A. 1930, *MNRAS*, 90, 243
- Pontoppidan, K. M., Dullemond, C. P., van Dishoeck, E. F., et al. 2005, *ApJ*, 622, 463
- Pontoppidan, K. M., Fraser, H. J., Dartois, E., et al. 2003, *A&A*, 408, 981
- Pontoppidan, K. M., van Dishoeck, E. F., & Dartois, E. 2004, *A&A*, 426, 925
- Rodgers, S. D. & Charnley, S. B. 2001, *ApJ*, 546, 324
- Roser, J. E., Manicò, G., Pirronello, V., & Vidali, G. 2002, *ApJ*, 581, 276
- Roser, J. E., Vidali, G., Manicò, G., & Pirronello, V. 2001, *ApJL*, 555, L61
- Ruiterkamp, R., Cox, N. L. J., Spaans, M., et al. 2005, *A&A*, 432, 515
- Sandford, S. A. & Allamandola, L. J. 1990, *ApJ*, 355, 357
- Sandford, S. A., Allamandola, L. J., Tielens, A. G. G. M., & Valero, G. J. 1988, *ApJ*, 329, 498
- Schutte, W. A., Allamandola, L. J., & Sandford, S. A. 1992, *Advances in Space Research*, 12, 47
- Schutte, W. A., Boogert, A. C. A., Tielens, A. G. G. M., et al. 1999, *A&A*, 343, 966
- Schutte, W. A. & Greenberg, J. M. 1997, *A&A*, 317, L43
- Schutte, W. A. & Khanna, R. K. 2003, *A&A*, 398, 1049
- Shen, C. J., Greenberg, J. M., Schutte, W. A., & van Dishoeck, E. F. 2004, *A&A*, 415, 203
- Soifer, B. T., Puetter, R. C., Russell, R. W., et al. 1979, *ApJL*, 232, L53
- Spaans, M., Hogerheijde, M. R., Mundy, L. G., & van Dishoeck, E. F. 1995, *ApJL*, 455, L167+
- Stäuber, P., Doty, S. D., van Dishoeck, E. F., & Benz, A. O. 2005, *A&A*
- Störzer, H. & Hollenbach, D. 1999, *ApJ*, 515, 669
- Stillman, J. M. 1960, *The story of Alchemy and the Early Chemistry*, p.115 (New York, Dover Publications, INC.)
- Swings, P. & Rosenfeld, L. 1937, *ApJ*, 86, 483
- Tafalla, M., Myers, P. C., Caselli, P., & Walmsley, C. M. 2004, *A&A*, 416, 191
- Tielens, A. G. G. M. & Hagen, W. 1982, *A&A*, 114, 245
- Tielens, A. G. G. M., Wooden, D. H., Allamandola, L. J., Bregman, J., & Witteborn, F. C. 1996, *ApJ*, 461, 210
- Turner, B. E. 1974, *Ap&SS*, 29, 247
- . 2000, *ApJ*, 542, 837
- van Broekhuizen, F. A., Keane, J. V., & Schutte, W. A. 2004, *A&A*, 415, 425
- van Dishoeck, E. F., Black, J. H., Boogert, A. C. A., et al. 1999, in *ESA SP-427: The Universe as Seen by ISO*, 437
- van Zadelhoff, G.-J., Aikawa, Y., Hogerheijde, M. R., & van Dishoeck, E. F. 2003, *A&A*, 397, 789
- Watanabe, N., Horii, T., & Kouchi, A. 2000, *ApJ*, 541, 772
- Watanabe, N. & Kouchi, A. 2002, *ApJ*, 567, 651
- Watson, W. D. & Salpeter, E. E. 1972a, *ApJ*, 174, 321

Bibliography

- . 1972b, *ApJ*, 175, 659
- Westley, M. S., Baragiola, R. A., Johnson, R. E., & Baratta, G. A. 1995a, *Nature*, 373, 405
- . 1995b, *Plan. Space Sci.*, 43, 1311
- Whittet, D. C. B., Gerakines, P. A., Tielens, A. G. G. M., et al. 1998, *ApJL*, 498, L159+
- Willacy, K. & Langer, W. D. 2000, *ApJ*, 544, 903
- Willacy, K. & Millar, T. J. 1998, *MNRAS*, 298, 562
- Willner, S. P., Gillett, F. C., Herter, T. L., et al. 1982, *ApJ*, 253, 174
- Wu, C. Y. R., Judge, D. L., Cheng, B., et al. 2003, *Journal of Geophysical Research (Planets)*, 108, 13

Chapter 2

Infrared spectroscopy of solid CO-CO₂ mixtures and layers

Abstract

The spectra of solid CO and CO₂ have been studied under laboratory conditions using Transmission-Absorption Fourier Transform infrared spectroscopy in mixed and layered ice morphologies. This work aims to provide spectra at improved resolution (0.5 cm^{-1}) of the CO₂ bending and asymmetric stretching mode, as well as the CO stretching mode, extending the existing Leiden database^a of laboratory spectra to match the spectral resolution reached by modern telescopes and to support the interpretation of the most recent data from the Spitzer Space Telescope. It is shown that mixed and layered CO and CO₂ ices exhibit very different spectral characteristics, which depend critically on thermal annealing and can be used to distinguish between mixed, layered and thermally annealed CO-CO₂ ices. CO only affects the CO₂ bending mode spectra in mixed ices below 50 K, where it exhibits a single asymmetric band profile in intimate mixtures. In all other ice morphologies the CO₂ bending mode shows a double peaked profile, similar to that observed for pure solid CO₂. Conversely, CO₂ induces a blue-shift in the peak-position of the CO stretching vibration, in mixed ices to a maximum value of 2142 cm^{-1} and in layered ices to between $2140\text{--}2146\text{ cm}^{-1}$. As such, the CO₂ bending mode puts clear constraints on the ice morphology below 50 K, whereas beyond this temperature the CO stretching vibration can distinguish between initially mixed and layered ices. This is illustrated for the low-mass young stellar object HH46, where the laboratory spectra are used to analyse the observed CO and CO₂ band profiles and put constraints on the formation scenarios of CO₂.^{1,2}

2.1 Introduction

CO₂ is one of the most abundant components of interstellar ice after H₂O and CO (Boogert et al., 2004; Gerakines et al., 1999; Gibb et al., 2004; Nummelin et al., 2001; Whittet et al., 1998) and has been observed in the solid-state on lines-of-sight towards a variety of high- and low-mass stars, field stars and galactic centre sources.

¹F. A. van Broekhuizen, I. M. N. Groot, H. J. Fraser, E. F. van Dishoeck, and S. Schlemmer

²All the laboratory spectra are made available on the web at

http://www.strw.leidenuniv.nl/lab/mixed_layered_CO_CO2/

Surprisingly little variation in abundance exists between these objects, generally ranging from 10 to 23 % with respect to H₂O-ice, although values of 34 to 37 % have been reached for some low- and intermediate mass sources (Pontoppidan et al. in prep.; Boogert et al., 2004; Nummelin et al., 2001). In the gas phase, observations imply that the CO₂ abundance is a factor of ~ 100 less than in the solid state (Boonman et al., 2003; van Dishoeck et al., 1996), indicating that CO₂ forms in the solid-phase. The most popular formation mechanism is via energetically mediated reactions such as UV photolysis of mixed H₂O-CO ices (Watanabe & Kouchi, 2002). However, the fact that CO₂ ice is also observed towards the quiescent clouds in front of Elias 16, where there is little if any UV- or proton-induced chemistry, suggests that no energetic ice-processing is required for CO₂ formation, so surface reactions involving CO must play a key role (Roser et al., 2001; Whittet et al., 1998). Whichever formation route is invoked, a direct link is implied between the location of CO and CO₂ within interstellar ices.

Recent high resolution observations of solid CO towards a large sample of embedded objects using the VLT-ISAAC spectrometer show that 60-90 % of solid CO in interstellar ices resides in a nearly pure form, segregated from other molecules. In addition, a significant number of the sources show evidence for CO in a H₂O-rich environment, at a minimum abundance of 19 % with respect to the pure CO component (Boogert et al., 2004; Fraser et al., 2004; Pontoppidan et al., 2003). Given these constraints, a scenario can be imagined in which CO₂ forms via surface reactions on the pure CO-ice layer, resulting in a bi-layered ice-structure. Alternatively, if CO₂ forms from UV- and proton-induced reactions involving the CO in the H₂O-rich environment, one can envisage that CO₂ will reside in a H₂O-rich ice without being in direct contact with CO. The latter situation has been simulated in detail in the laboratory by, for example, Gerakines et al. (1995) and Ehrenfreund et al. (1999), who recorded infrared (IR) spectra of mixed ices.

The key aim of this paper is to establish the influence CO may have on the CO₂ spectral features and vice versa. In addition to the spectroscopic features of CO at 2139 and 2136 cm⁻¹ in pure and H₂O-rich ice environments respectively, a third component of the interstellar CO-ice band has been detected at around 2143 cm⁻¹ along many lines of sight. In the VLT-ISAAC and other surveys, this band was attributed to the TO-component, which arises due to LO-TO splitting of the pure ice feature, assuming that some of the CO-ice is actually crystalline, and that there is a degree of polarisation in the background source (Pontoppidan et al., 2003). Conversely, Boogert et al. (2002) assign this band to CO in a CO₂ dominated environment, implying that the 2143 cm⁻¹ band may be key in tracing the interplay between CO and CO₂. This paper therefore also analyses the presence or absence of the 2143 cm⁻¹ feature in the spectra of CO-CO₂ laboratory ices, as a function of the morphology (i.e., the configuration of CO and CO₂ in the CO-CO₂ ice system: either mixed, or separated in two pure layers) and temperature, to find the origin of this band.

Solid CO₂ can be observed in interstellar spectra by its asymmetric stretching (ν_3) and bending (ν_2) modes. The ν_2 mode is known to be very sensitive to the local ice environment but is weaker than the stretching mode. The higher sensitivity of the recently launched Spitzer Space Telescope, compared to that of its

predecessor the Infrared Space Observatory (ISO), has made it possible to conduct a detailed analysis of the $\nu_2(\text{CO}_2)$ band over a wider range of interstellar objects. First results show that the CO_2 abundances are similar to or higher than those deduced with ISO (Pontoppidan et al. in prep.; Boogert et al., 2004; Watson et al., 2004).

Thus, there is the possibility to combine the new observational data of solid CO_2 and CO to place constraints on the CO_2 ice environment. Previous laboratory studies have dealt with mixtures of binary ices composed of CO and CO_2 (Ehrenfreund et al., 1996, 1997; Elsila et al., 1997). These proved very useful for interpreting interstellar ice observations. However, systematic studies including layered ices are necessary to link the spectral characteristics to the interstellar environments mentioned above.

This work presents the effects of CO on the spectroscopy of the CO_2 -bending and stretching mode as well as the influence of thermal annealing in pure, mixed and layered ice systems. The data are taken at an increased spectral resolution of 0.5 cm^{-1} with respect to the previous laboratory studies mentioned above, aimed to resolve the CO_2 -bending mode and the CO -stretching vibration in detail in order to meet the accuracy of the VLT-ISAAC and Spitzer data as well as future mid-infrared spectra to be obtained with the James Webb Space Telescope. The experimental details are explained in Sect. 2.2. The spectroscopic behaviour of CO and CO_2 are presented and discussed in Sects. 7.5 and 5.4, respectively, as a function of the temperature and ice composition. In Sect. 6.4 the astrophysical implications are discussed and one example of a comparison of the new experimental data with observations is given.

2.2 Experimental Procedure

All experiments were conducted in a high vacuum (HV) chamber described in detail elsewhere (Gerakines et al., 1995), at a base-pressure below 2×10^{-7} Torr. Ices of $^{12}\text{C}^{16}\text{O}$ (Praxair 99.997% purity) and $^{12}\text{C}^{16}\text{O}_2$ (Praxair 99.997% purity) were grown on the surface of a CsI window, pre-cooled to 15 K, via effusive dosing at a growth rate of $\sim 10^{16} \text{ molec cm}^{-2}\text{s}^{-1}$, directed at 45 degrees to the surface normal. Transmission Fourier Transform Infrared spectra of the ice systems were recorded at 0.5 cm^{-1} at fixed temperatures between 15 to 100 K, using a total of 128 scans between $4000\text{--}400 \text{ cm}^{-1}$ and a Zero filling factor of 4. Each recording was started directly after the temperature had equilibrated, which took ~ 2 min, and lasted ~ 20 min.

The pure and layered ice structures were grown in situ from CO and CO_2 gas bulbs that were filled to a total pressure of 10 mbar, pre-prepared in a glass-vacuum manifold at a base-pressure of $\sim 10^{-5}$ mbar and deposited via single and sequential dosing, respectively. Mixed ices were prepared by dosing gas from pre-mixed CO and CO_2 bulbs.

The Full Width at Half Maximum (FWHM) and the peak-position of the CO -stretching, CO_2 -bending and CO_2 asymmetric stretching mode were determined using the Levenberg-Marquardt non-linear least square fitting routine within Ori-

Table 2.1: Ice compositions

Ice morphologies	Nomenclature	Conc. ratio		Exposure (s)	Approx. ice ^a thickness (L)
		CO	CO ₂		
pure	CO	1	-	60	600
	CO ₂	-	1	60	600
layered	1/1 CO/CO ₂	1	1	60 + 60	1200
	1/1 CO ₂ /CO	1	1	60 + 60	1200
	1/2 CO/CO ₂	1	2	60 + 120	1800
	2/1 CO ₂ /CO	2	1	120 + 60	1800
	3/1 CO ₂ /CO	3	1	180 + 60	2400
	10/1 CO ₂ /CO	10	1	600 + 60	6600
mixed	1:1 CO:CO ₂	1	1	120	1200
	2:1 CO:CO ₂	2	1	180	1800
	1:10 CO:CO ₂	1	10	660	6600

^a 1 L = 10¹⁵ molec cm⁻² ≈ 1 mono-layer.

gin 7.0. Uncertainties in the peak-centre position and FWHM were typically less than 0.05 cm⁻¹, except close to the desorption temperature where uncertainties may be larger.

Previous work on the spectroscopy of CO₂-ice has indicated that the ice structure (i.e. amorphous or crystalline) influences its spectral profile (Falck, 1986), although some uncertainty exists in the literature as to the extent of the crystallinity of low temperature vapour deposited CO₂-ice (Falck, 1986; Sandford & Allamandola, 1990; Sandford et al., 1988). Consequently, optical constants have not been derived for the ices studied here. Before doing so, a systematic study is required of the degree of crystallinity in pure, vapor-deposited CO₂ ices and the influence of these phases on the CO₂ spectroscopy, which will be the topic of future work.

The range of ices studied here are summarised in Table 2.1. The nomenclature adopted is as follows, *A:B* denotes a mixture whereas *A/B* will be used to indicate layered structures with *A* on top of *B*, with *A* and *B* as the deposited amounts of CO and CO₂. Aside from small deviations associated with the thermal behaviour of the ice, the band intensities correlate well with the deposited amounts of gas. The relative concentrations of CO and CO₂ range from 2 to 0.1 CO/CO₂, relevant for comparison with observations where high-mass YSO's show CO/CO₂ column density ratios varying from 0.1 to 1.3, with the lowest ratios found in sources with the highest temperatures, where most CO has been evaporated (Gibb et al., 2004). Only limited data exist for low-mass YSO's, showing CO/CO₂ column density ratios of ~0.25 (Gibb et al., 2004). All of the laboratory spectra discussed here have been made available through the Internet at http://www.strw.leidenuniv.nl/~lab/mixed_layered_CO_CO2/.

2.3 Results

2.3.1 CO₂-bending mode

In Fig. 2.1 the spectra of the CO₂-bending (ν_2) mode at 15 K are shown, from top to bottom, in pure, layered, and mixed ices, the latter with CO. In the pure ice, the ν_2 spectrum has two components, peaking at 654.7 and 659.8 cm⁻¹ (marked by two black lines) with FWHM of 1.8 and 3.1 cm⁻¹, respectively, showing the Davydov splitting of this mode, induced when its degeneracy is lifted due to a highly ordered ice structure (Decius & Hexter, 1977). In the bi-layered ice structures (below), the ν_2 spectrum exhibits an identical band profile, irrespective of whether CO₂ was deposited on top or underneath the CO-ice layer.

Conversely, when CO₂ is mixed with CO, the ν_2 spectrum changes drastically. In Fig. 2.1, the 2:1 and 1:1 CO:CO₂ show one broad asymmetric band without any sub-structure, peaking at between 655 and 657 cm⁻¹. In the 1:10 CO:CO₂ ice, however, the spectrum again exhibits two peaks centred at 654.7 and 659.8 cm⁻¹ (FWHM of 3.6 and 6.1 cm⁻¹), similar to pure CO₂-ice, but with somewhat larger FWHM.

In Fig. 2.2, the thermal evolution of the ν_2 mode is shown for four of the ices studied. The grey lines in each of the plots mark the position of the two ν_2 peaks at 15 K in pure CO₂-ice, and serve as reference for any thermally or morphologically induced spectroscopic changes. Pure CO₂-ice is shown in Fig. 2.2a. At $T \leq 40$ K, the spectrum is unchanged but beyond 40 K a gradual changing ice structure is apparent as the absolute band intensities of both peaks increase while their FWHM decrease until the point at which CO₂ desorbs. Consequently, the most narrow and intense bands are observed at 80 K, just prior to desorption, with FWHM of 1.3 and 1.0 cm⁻¹ at 654.7 and 659.8 cm⁻¹, respectively.

The thermal evolution of the ν_2 mode spectra of 1/1 CO/CO₂ layered ice in Fig. 2.2b, shows identical thermal behaviour to the pure CO₂-ice (Fig. 2.2a). Reversing the order of the bi-layers (CO₂/CO) leads to almost identical spectra.

Figs. 2.2c and 2.2d show the thermal evolution of the ν_2 in 2:1 and 1:1 CO:CO₂ mixtures, respectively. In both ices the first inklings of sub-structure become visible at 22 K, which subsequently evolve to a pure-like CO₂ spectrum beyond 40 K. The actual profiles though, are slightly broader and more asymmetric than the pure spectra, especially for the feature centred at 659.8 cm⁻¹.

Under the present experimental conditions, the CO₂ desorbs between 80 and 90 K in all the ices studied here. The one exception is 1:10 CO:CO₂ where desorption is retarded to 90–100 K, although the thermal evolution of its bending mode spectra (not shown in Fig. 2.2) is similar to that in pure CO₂-ice.

All four panels of Fig. 2.2 show evidence of a small artifact centred at 667.8 cm⁻¹. From the 90 K spectrum in Fig. 2.2a it is clear that this feature is not associated with CO₂ ice since CO₂ has fully desorbed yet the peak remains. This artifact is probably not real and as it does not influence any of the results it is not discussed further.

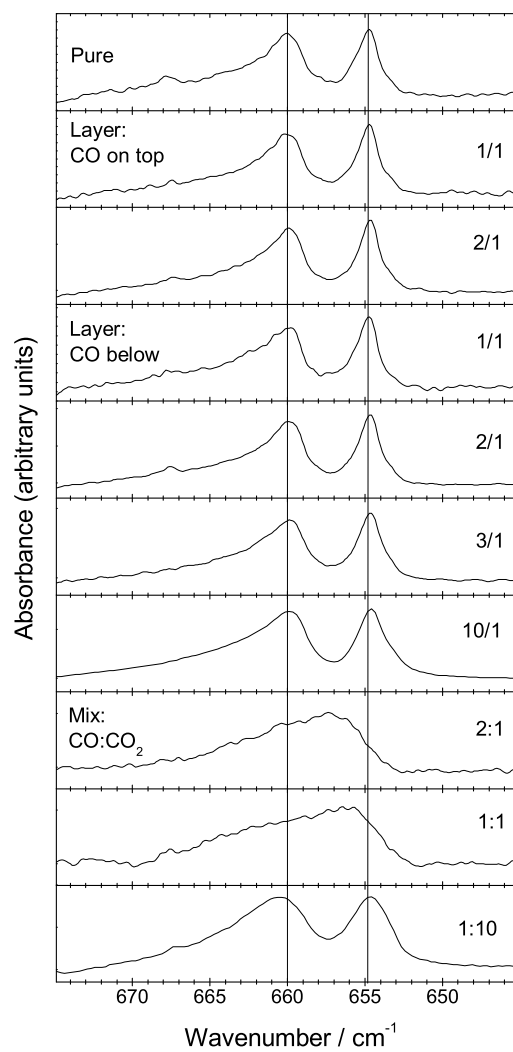


Figure 2.1: The spectral profile of the CO₂-bending mode at 15 K in pure ice and in various binary ice morphologies with CO. The two vertical black lines mark the positions of the two peaks observed in the bending mode spectra of pure CO₂.

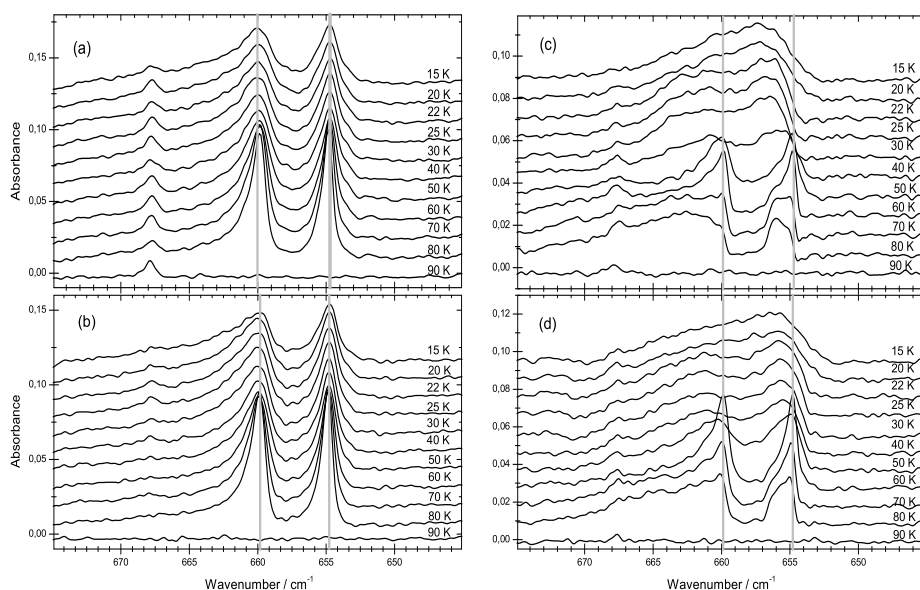


Figure 2.2: The thermal evolution of the CO_2 -bending mode for (a) pure CO_2 -ice, (b) a 1/1 CO/CO_2 layered ice, and (c) 2:1 $\text{CO}:\text{CO}_2$ and (d) 1:1 $\text{CO}:\text{CO}_2$ ice mixtures, from 15–90 K. The two vertical grey lines mark the positions of the two peaks of the bending mode at 15 K in pure CO_2 -ice.

2.3.2 CO_2 asymmetric stretching vibration

The thermal evolution of the CO_2 asymmetric stretching (ν_3) vibration is shown in Fig. 2.3 for the same four ice morphologies shown in Fig. 2.2. As with the ν_2 mode, the trend observed is that almost no spectral differences can be seen between the pure and layered ices (Fig. 2.3a and b), whereas peak-position changes and FWHM differences are observed between the pure and the mixed ices (Figs. 2.3a and 2.3c and d).

In pure CO_2 -ice (Fig. 2.3a), the ν_3 mode peaks at 2344.0 cm^{-1} (FWHM of 10.6 cm^{-1}), as indicated by the grey line in all panels. Its peak-centre position is independent of temperature. However, beyond 40 K the FWHM decreases gradually with increasing temperature, in a similar fashion as is observed for the ν_2 mode of CO_2 , reaching a minimum value of 5.2 cm^{-1} at 80 K, where the peak intensity is also at a maximum.

In the ν_3 spectra in 2:1 and 1:1 $\text{CO}:\text{CO}_2$ (Figs. 2.3c and 2.3d, respectively) at least three different spectral components are present between 15 and 80 K. At 15 K, in both ices the spectral profile is dominated by a broad asymmetric band, peaking at 2339.9 cm^{-1} (FWHM of 13.3 cm^{-1}), which exhibits a shoulder at around 2334 cm^{-1} in the case of 1:1 $\text{CO}:\text{CO}_2$. By 22 K, the spectrum has evolved into a much narrower feature, peaking at 2342.5 cm^{-1} , and beyond 50 K a third component starts to develop, which is most clearly visible at 80 K as a band at around 2351 cm^{-1} .

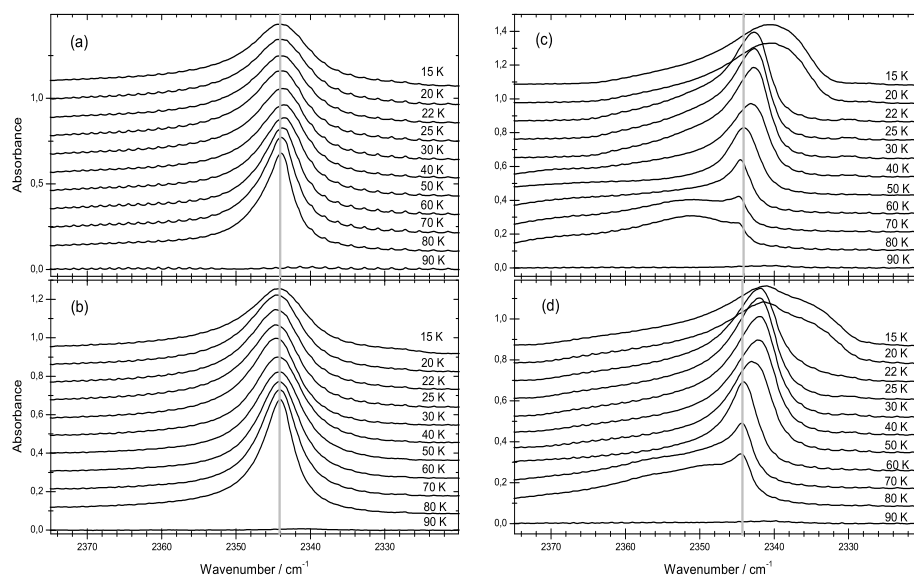


Figure 2.3: The thermal evolution of the asymmetric stretching mode of CO₂ in (a) pure, (b) 1/1 CO/CO₂, (c) 2:1 CO:CO₂ and (d) 1:1 CO:CO₂, from 15–90 K. The grey line marks the peak-centre position at 15 K in pure CO₂-ice.

2.3.3 CO-stretching vibration

The CO-stretching vibration is shown in Fig. 2.4, for pure, layered and mixed ices at 15 K. In pure CO-ice (the top spectrum) the spectrum peaks at 2138.7 cm^{-1} (FWHM of 1.6 cm^{-1}), with a shoulder visible at approximately 2141 cm^{-1} , as indicated by the black arrow. This has been observed previously by Sandford et al. (1988) and its source has been recently discussed by Fraser et al. (in prep.). Again, as with the CO₂ asymmetric stretching and bending modes, the spectrum of the CO-stretching mode in layered ices is almost identical to that of pure CO-ice, whereas the mixed ices show significant spectral deviations compared to the pure case.

All three mixed ice spectra in Fig. 2.4 have much broader CO-stretching bands, which are blue-shifted with respect to the pure CO-ice spectrum (marked by the grey line). The peaks are centred between 2140.3 and 2141.6 cm^{-1} , with FWHM extending from 5.6 to 9.0 cm^{-1} (see also Elsila et al., 1997). Equimolar mixtures induce the strongest blue-shifts from the pure CO-ice spectrum.

Thermal annealing of pure CO-ice induces no changes to the CO-spectrum, as emphasised by the grey line that indicates the peak centre position at 15 K (Fig. 2.5a). Pure CO desorbs between 25–30 K under the present experimental conditions. At up to 22 K in 1/1 CO/CO₂ (Fig. 2.5b), the thermal evolution of the CO-stretching vibration clearly resembles that of pure CO-ice. However, beyond 22 K

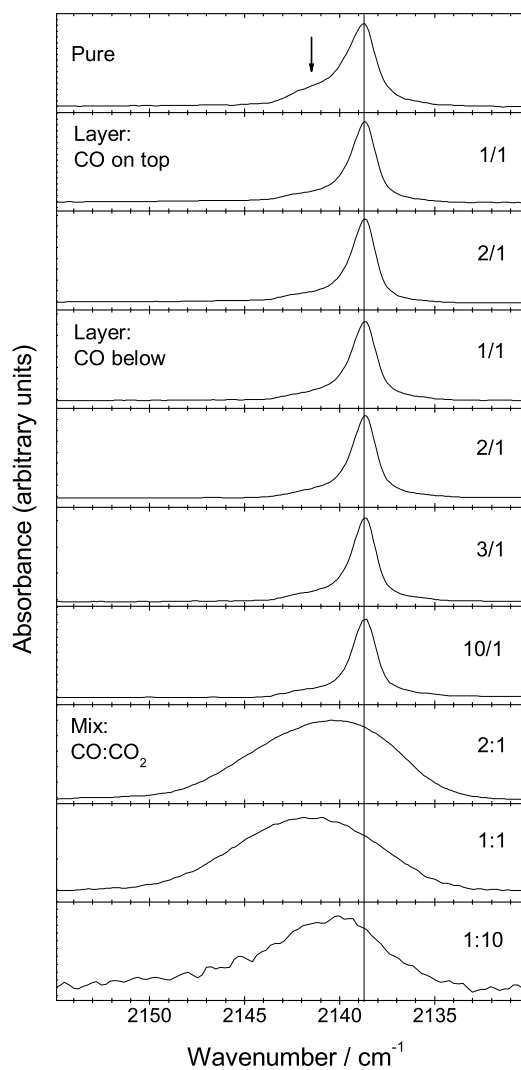


Figure 2.4: The spectra of the CO-stretch vibration at 15 K in pure ice and in layered and mixed ices with CO₂. The vertical line marks the peak-position of CO in a pure ice.

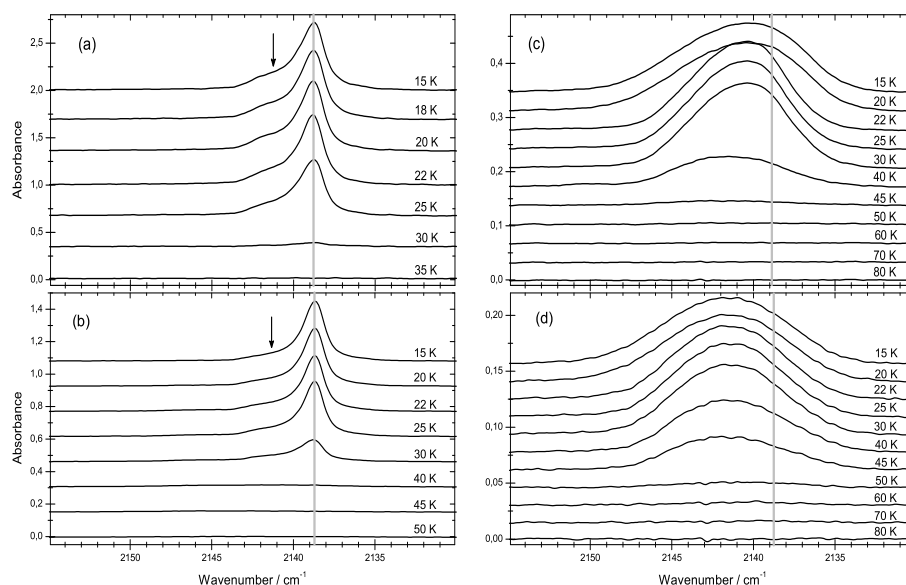


Figure 2.5: The thermal evolution of the CO-stretching vibration in (a) pure CO-ice, (b) 1/1 CO/CO₂, (c) 2:1 CO:CO₂ and (d) 1:1 CO:CO₂ from 15–80 K. The grey line marks the position of the main peak at 15 K in pure CO-ice.

the shoulder at $\sim 2141 \text{ cm}^{-1}$ is more pronounced than in the pure ice spectrum. This effect becomes more obvious with increasing thickness of the CO₂ layer and is best seen in Fig. 2.6 for the most extreme case of CO₂/CO studied here, 10/1. The intensity of the main peak (2138.9 cm^{-1}) clearly decreases with respect to 1/1 CO/CO₂ (Fig. 2.5b), while its ‘shoulder’ at 2141 cm^{-1} becomes relatively more intense and a third feature appears at around 2145.5 cm^{-1} , as indicated by the black arrows in Fig. 2.6. From 30 K onwards, CO starts desorbing and both features at 2141 and 2145.5 cm^{-1} decrease in intensity. The feature at 2141 cm^{-1} , however, reduces faster, leading to a further apparent blue-shift of the overall CO band. From 40–60 K as the 2145.5 cm^{-1} environment is lost, the overall band position starts shifting back to the red while this band also reduces in intensity, before the remaining CO finally desorbs (with the CO₂) above 80 K.

Figs. 2.5c and 2.5d show the thermal evolution of the CO-stretching vibration in 2:1 and 1:1 CO:CO₂ mixtures, respectively. Again the thermal behaviour is very different to pure or layered ices. The broad bands present at 15 K (Fig. 2.4) narrow between 20 and 22 K to a FWHM between 6.5 and 7.6 cm^{-1} , but the peak centre position does not change. The onset of CO desorption is around 30 K, similar to pure CO-ice, but continues up to about 50 K, in 2:1 CO:CO₂, and to about 60 K in the 1:1 CO:CO₂ mixtures. In the case of 1:10 CO:CO₂ (not shown) this desorption trajectory is extended even further as a small fraction of the CO codesorbs with the CO₂ between 90 and 100 K.

Neither the mixed nor layered ice morphologies show evidence for an isolated CO-feature centred at 2143 cm^{-1} , as was suggested for CO-CO₂ interactions in in-

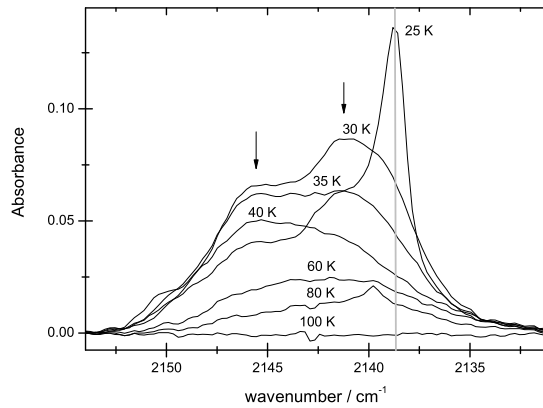


Figure 2.6: The thermal evolution of the CO-stretching vibration in a 10/1 CO₂/CO layered ice system, from 25–100 K. The thick grey line marks the peak-centre position of the main spectral feature in pure CO-ice. The two arrows indicate the two shoulders that evolve as the temperature increases.

terstellar ices by Boogert et al. (2002). However, mixed ices do show a broad band, blueshifted with respect to the pure ice component, which may explain the observation of an extended blue wing in the interstellar CO band. Under the present laboratory conditions, however, the peak of this band never extends further than 2142 cm⁻¹. In layered ices, CO gives rise to a spectral feature at around 2143 cm⁻¹ after thermal annealing beyond 20 to 22 K, when CO interacts with CO₂ at a ratio of ~ 1:10 (see Fig. 2.6, and van Broekhuizen et al. in prep.).

2.4 Discussion

The results described in Sect. 7.5 provide clear evidence that the morphology of CO and CO₂ containing ices affects their spectroscopy, which will be the focus of the following discussion. The actual ice structure and the processes that give rise to these spectra, such as matrix rearrangements, diffusion and desorption, will be the topic of discussion in an upcoming paper by van Broekhuizen et al. in prep.

Most obviously, the spectra of pure and layered ices differ widely from those of mixed ices. Further analysis was undertaken to disseminate additional information from these spectra. Peak positions and FWHM of the vibrational bands were determined as a function of the ice temperature, and are shown in Figs. 2.7 (CO₂-bending), 2.8 (CO₂-stretching) and 2.9 (CO-stretching). The associated uncertainties of these data have been calculated but error bars are omitted from these plots for clarity. These plots simplify the evaluation of spectral shifts and changes in FWHM as a function of temperature and ice morphology.

In addition to the significant spectral differences, which arise due to the various ice morphologies (Sect. 7.5), the thermally induced spectroscopic changes come about, in most cases, at specific temperatures, i.e. 22, 30 and 50 K. These tem-

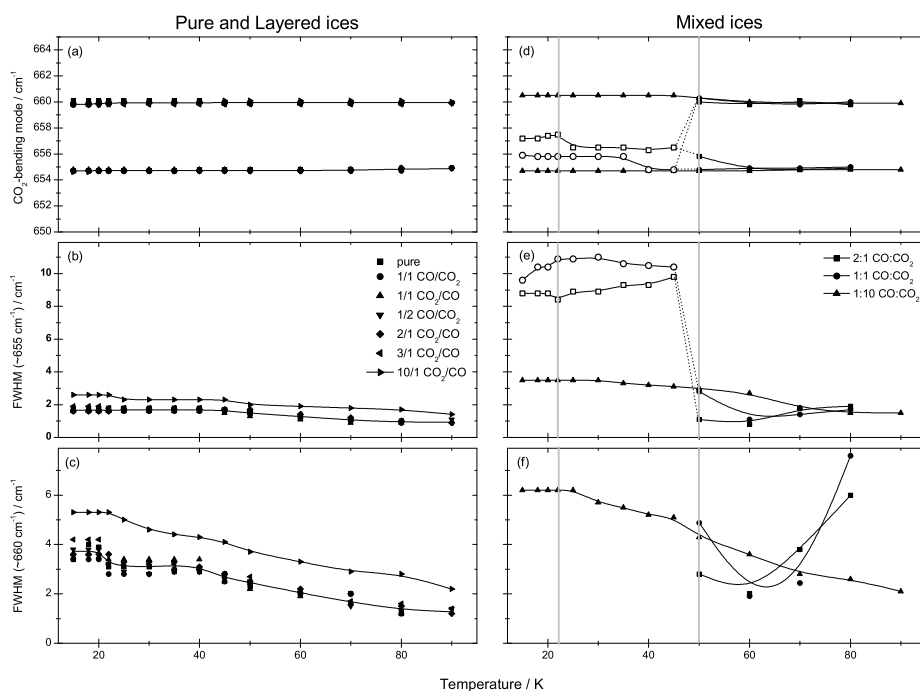


Figure 2.7: The peak-centre positions and FWHM of the main spectral features of the CO₂-bending mode, plotted as a function of ice temperature. (a) Peak-centre positions in the pure and layered ices with the corresponding FWHM of the feature centred at (b) 655 cm⁻¹, and (c) 660 cm⁻¹. (d) Peak-centre positions in the mixed ices with the corresponding FWHM of the peak at (e) 655 cm⁻¹, and (f) at 660 cm⁻¹. The legend in (b) gives the symbol assignment for all three left-hand panels, that in (e) for all three right-hand panels. Open symbols indicate the presence of only a single peak, whereas solid symbols mark the presence of the doublet. In each of the panels, spline-fits through the data points guide the eye. The two vertical grey lines enclose the temperature range between 22 and 50 K (see text for details)

temperatures are related to CO diffusion, the onset of CO desorption and the temperature at which most of the CO is desorbed, respectively (see for further discussion Collings et al., 2003, Fraser et al. in prep. and van Broekhuizen et al. in prep.), and are indicated in Figs. 2.7, 2.8 and 2.9 by vertical bars.

Much attention has been given to the spectra of the CO₂-bending mode as new observations from the Spitzer Space Telescope arrive. In pure and layered ices the bending mode is always split into two fully resolved peaks (Fig. 2.7a). In mixed ices this is true only beyond 50 K (Fig. 2.7c), with the exception of very dilute mixtures, i.e. 1:10, where CO₂ dominates the ice matrix and therefore a doublet profile exists even at low temperatures. It is interesting to note that in this case, the splitting of the bending mode is slightly greater than in pure and layered ices

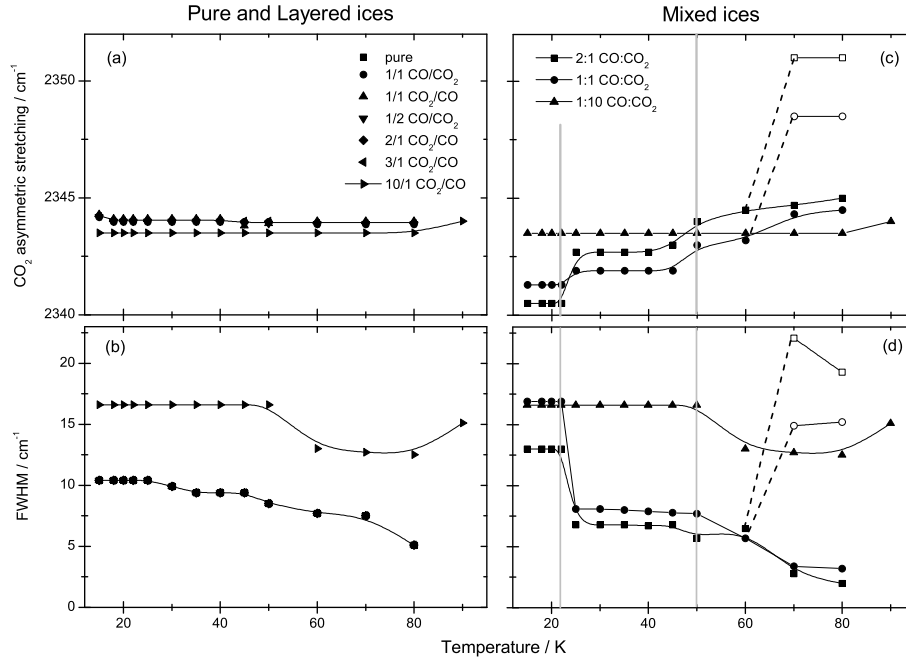


Figure 2.8: The peak-centre positions and FWHM of the main spectral features of the CO₂ asymmetric stretching vibration, plotted as a function of the ice temperature. (a) Peak-centre positions in pure and layered ice with (b) the corresponding FWHM. (c) Peak-centre positions in mixed ices with (d) the corresponding FWHM. The legend in (a) gives the symbol assignment for the two left-hand panels, that in (c) for the right-hand panels. Open and closed symbols are used to indicate independent peaks present at the same temperature. In each of the panels, spline-fits through the data points guide the eye. In (c) and (d), the two vertical grey lines enclose the temperature range between 22 and 50 K and the dashed lines connect two separate features that appear in the same spectrum (see text).

but reverts to the same value for $T \geq 50$ K. The FWHM also starts out larger than in any pure and layered ices but decreases from 22 K onwards, reaching values similar to pure and layered ices at $T \geq 60$ K (Fig. 2.7d and 2.7e).

The asymmetric stretching mode of CO₂ shows similar trends to the bending mode. In mixed ices the band position shifts significantly up to 50 K. Above this temperature the band position is commensurate with that of the pure CO₂-ice, but a second band appears, which is significantly broader than the pure ice feature. Consequently, pure CO₂ ice and mixed ices beyond 50 K have a different morphology, although this is hardly discernible from the spectra of the CO₂-bending mode. In the case of CO-CO₂ ices, the above indicates that also the CO₂ asymmetric stretching mode is very sensitive to its local environment and can provide additional information to constrain the interstellar ice morphology.

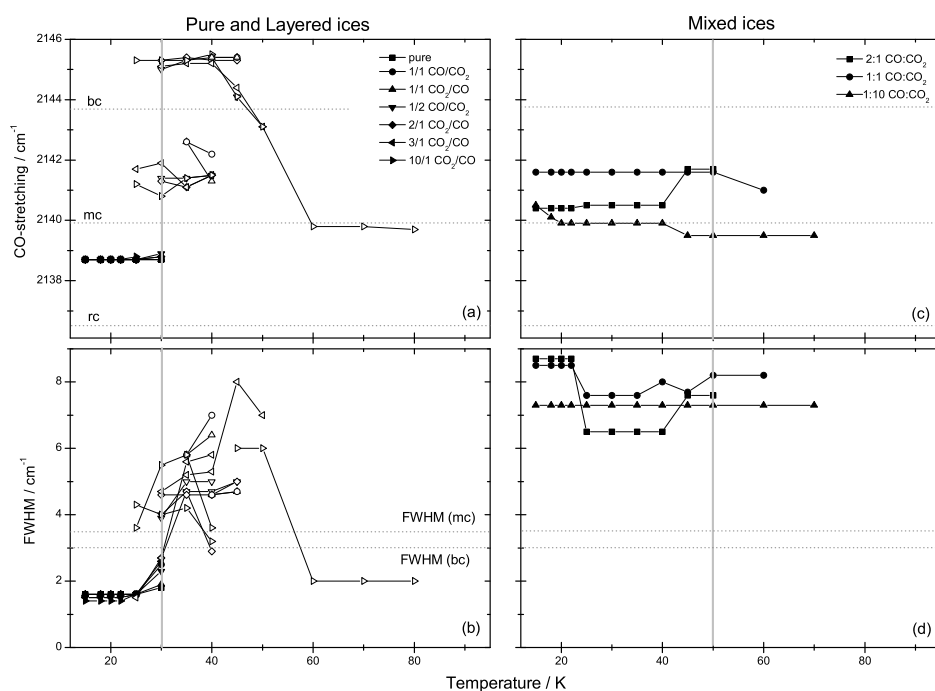


Figure 2.9: The peak-centre positions and FWHM of the CO-stretching vibration, plotted as a function of ice temperature. (a) Peak-centre positions in pure and layered ices with (b) their corresponding FWHM. (c) Peak-centre positions in mixed ices with (d) their corresponding FWHM. The legend in (a) gives the symbol assignment for the two left-hand panels, that in (c) for the right-hand panels. Solid symbols indicate strong bands, open symbols mark the more tenuous detections (see text). Symbols indicating the same feature are connected by lines to guide the eye. The vertical grey line in the left panels marks the temperature at which pure CO desorbs, that in the right panels marks the temperature at which the single peak profile of the CO₂-bending mode in a mixture converts to a doublet. The three horizontal (dotted) lines in (a) and (c) indicate the three line centres of the phenomenological fit to the interstellar solid CO-band observed by Pontoppidan et al. (2003) (see text). The two dotted lines in (b) and (d) give the FWHM of the mc and rc of the fitted components although it should be noted that that FWHM can be altered by grain shape effects.

The shift and broadening of the CO-stretching vibration appear in different temperature ranges compared to the significant effects in the CO₂ bands. The band positions in mixed ices are temperature independent from 15 K onwards (Fig. 2.9c), which is in agreement with the fact that CO is likely to remain bound in the CO₂ matrix over the full temperature range, leading to a constant matrix shift. Furthermore, the band position is significantly shifted with respect to the pure and layered ices below 30 K, because beyond this temperature the CO fea-

ture in pure and layered ices becomes almost indistinguishable from the noise, in agreement with the desorption of pure CO ice under the present laboratory conditions (Collings et al., 2003; Ehrenfreund et al., 1996; Sandford et al., 1988).

The fraction of CO that remains trapped or bound somehow in the CO₂ layer exhibits spectra that are significantly blue-shifted and broadened by a factor of 2 to 3. This trend sets in beyond 22 K (see Fig. 2.6) and leads to features that have band positions and FWHM similar to the mixed ices, although extended further into the blue to around 2145.5 cm⁻¹. This might suggest that CO and CO₂ are mixing. However, such a mixing is not apparent in the spectra of the CO₂ bending mode, where a minimum fraction of ~10% of CO mixed in with CO₂ should be visible in the case of a 1:10 mixture. The absence of mixing during thermal annealing of the layered ices has previously also been found for CO in layered CO-CH₄ ices (Alsindi et al., 2003).

The positions of the three main interstellar CO-ice components (Pontoppidan et al., 2003) are drawn as horizontal lines (Fig. 2.9). The red component (denoted as rc in Fig. 2.9), which is associated with CO in a H₂O-rich environment, is not relevant for the present study and is subsequently ignored. The middle component (mc), associated with a pure CO ice environment, lies within the peak-centre position of the CO spectrum in pure and layered laboratory ices. The blue component (bc) of the interstellar profile is often invoked as being indicative of the presence of CO:CO₂ mixtures in interstellar ice. However, from the peak positions indicated here no direct match is found between the position of this bc and the band positions of the ices studied here. Nevertheless both mixed and layered ices do contain a blue-shifted component, and even if the shift does not match the interstellar case, a blue wing on the CO interstellar profile might possibly be interpreted as a mixed CO:CO₂ ice, although a firm identification is complicated. However, given that the band strength of CO in CO₂ ice is similar to that in pure CO ice (Gerakines et al., 1995), a positive identification should be possible under interstellar conditions.

Evidence, or the lack thereof, for the assignment of the interstellar bc to CO-CO₂ interactions can also be found from the FWHM plot. The bluest layered and mixed ice components, found between 2141–2146 cm⁻¹ all have FWHM 1.5 to 3 times larger than the FWHM of the interstellar bc. Such evidence does question the assignment of a 2143 cm⁻¹ feature to CO:CO₂ ice mixes but cannot rule it out completely. Further work will be required on LO-TO splitting of the CO-stretching mode (a plausible alternative carrier of the 2143 cm⁻¹ feature, see Pontoppidan et al., 2003) on this same subset of ice morphologies in the laboratory. In addition, a detailed analysis is needed of young stellar objects that exhibit a strongly pronounced CO blue wing, e.g. L 1489, SVS 4–9, Reipurth 50 and RNO 91 (Pontoppidan et al., 2003), and a single profile for the CO₂ bending mode, together with polarisation measurements toward the same sources, before the assignment of the CO 2143 cm⁻¹ band can be fully resolved.

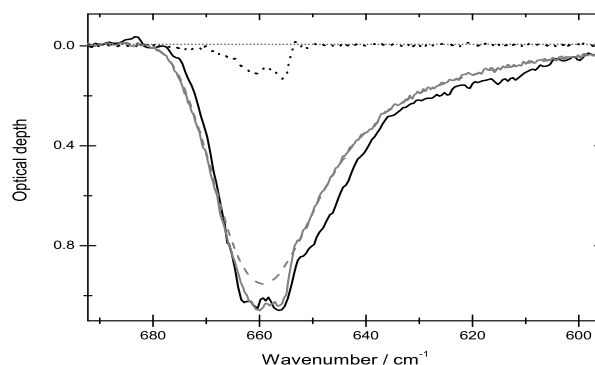


Figure 2.10: The CO₂-bending mode as observed toward HH 46 by Spitzer (black solid line, Boogert et al., 2004), reproduced by a combination of a laboratory spectrum of CO₂ at 10 K in 10:1 H₂O:CO₂ (light grey dashed line) and at 40 K in 1:1 CO:CO₂ (dotted line). The resulting match is shown by the dark grey line.

2.5 Astrophysical Implications

The laboratory results presented here have shown that combining CO- and CO₂-observational data could be a powerful tool to elucidate the local environment of both molecules in interstellar ices. This is illustrated here for the low-mass object HH 46, which is presumably less affected by thermal processing than the more massive YSO's observed with ISO, increasing the chance of observing evidence for CO in a CO₂ ice environment. Its CO₂-bending and CO-stretching mode were recently studied in detail by Boogert et al. (2004). There, the CO₂-bending mode was fitted by a laboratory spectrum of thermally annealed hydrogen-bonded ice (i.e. H₂O- and CH₃OH-rich CO₂ ice at $T = 115$ K), or alternatively by a combination of laboratory spectra of CO₂ in H₂O-rich ice at 10 K and 125 K, also containing CH₃OH. Both situations gave fits that compare reasonably well with the observation. In addition, the CO-stretching mode was fitted using the phenomenological decomposition into three components described by Pontoppidan et al. (2003). Abundances derived with respect to H₂O were 32 % CO₂, 15 % CO in a H₂O-rich ice, and 5 % CO in a pure CO-ice environment.

Here, the CO₂-bending mode of HH 46 has been re-analysed to establish the maximum possible contribution from a CO-CO₂ ice component. In addition, the CO-stretching mode of HH 46 has been analysed to see if both the CO and the CO₂ band profiles can be fitted consistently.

Fig. 2.10 shows the spectrum of the CO₂-bending mode of HH 46 observed with Spitzer (solid black line, Boogert et al., 2004). Close examination of this band shows a small substructure between 15.3 and 15.1 μm , which Boogert et al. (2004) fitted with a thermally annealed H₂O-CO₂ mixture. However, this feature coincides with the position of CO₂ in an equimolar mixture with CO at 40 K in the laboratory (Fig. 2.10, dotted line). Therefore, one can also match the CO₂-bending mode of HH 46 by combining two different laboratory spectra of CO₂, one at 10 K

Table 2.2: Results of the CO-CO₂ fit toward HH 46

Ice component	N (10^{17}) ^a molec cm ⁻²	$N/N(\text{CO}_2)_{\text{tot}}$ ^b	$N/N(\text{CO})_{\text{tot}}$ ^b	$N/N(\text{H}_2\text{O})$ ^c
CO ₂ (in CO)	1.05 ^d	0.04		0.013
CO (in CO ₂)	2.38 ^e		0.15	0.030
CO (2143-feature)	0.81 ^f		0.05	0.010

Maximum amounts in CO-CO₂ mixtures are consistent with data, ^a using a band strength $A_{\text{CO}_2} = A_{\text{CO}} = 1.1 \times 10^{-17}$ cm molec⁻¹ (Gerakines et al., 1995). ^b Total column densities, N_{tot} , of CO and CO₂, respectively, as derived by Boogert et al. (2004). ^c $N(\text{H}_2\text{O}) = 8.0 \times 10^{18}$ cm⁻² (Boogert et al., 2004). ^d Integrated area of CO₂ bending mode spectrum at 40 K in 1:1 CO:CO₂ is 1.16 cm⁻¹. ^e $\tau_{2141.4} = 0.30 \pm 0.01$, FWHM of 9 cm⁻¹. ^f $\tau_{\text{bc}} = 0.30 \pm 0.01$, FWHM of 3.0 cm⁻¹.

in a 10:1 H₂O:CO₂ mixed ice (Boogert et al., 2004, light grey dashed line) and one at 40 K in a 1:1 CO:CO₂ ice. It should be noted that the interstellar profile of the last laboratory spectrum might be affected by grain shape effects. However, as 1:1 CO:CO₂ ice at 40 K is no longer a homogeneous mixture (van Broekhuizen et al. in prep.), at present there are no optical constants available (to the best of our knowledge) to correct for these effects. The overall match in Fig. 2.10 (grey line) indeed shows that the small feature at the bottom of the CO₂-bending mode of HH 46 can be reproduced by CO₂ in a mixed ice environment with CO, although the small feature at 662 cm⁻¹ and the wing red-wards of 650 cm⁻¹ were less well matched. The column density of CO₂ in CO is listed in Table 2.2, together with its relative ice fraction with respect to all CO₂ present and its abundance with respect to H₂O ice. Clearly, this mix and match procedure can only provide a rough estimate of the (maximum) column density of the CO-CO₂ ice component contributing to the CO₂-bending mode and is only meant to illustrate how laboratory data of binary ices of CO and CO₂ can constrain the interstellar ice environment of CO₂.

Fig. 2.11 shows the spectrum of the solid CO stretching mode as observed toward HH 46 (solid line) by VLT-ISAAC. The spectrum is reduced and fitted using the same methods that were described in detail by Pontoppidan et al. (2003). In Fig. 2.11a, the CO ice band has been fitted using a laboratory spectrum of CO at 40 K in 1:1 CO:CO₂ ice (thick solid line) and one at 10 K in 1:10 CO:H₂O ice (dashed line). In addition, a pure CO ice component (the mc of interstellar CO-ice, dotted line) was required to obtain a good fit ($\chi^2 = 1.3$). The column density, fractional abundance with respect to all CO present, and abundance with respect to H₂O ice, of CO in a 1:1 CO:CO₂ ice environment is listed in Table 2.2. This abundance is approximately 2 × larger than that of CO₂ in a mixed ice with CO, suggesting a 2:1 rather than a 1:1 CO:CO₂ mixing ratio, which in fact exhibit very similar laboratory spectra (Fig. 2.2 and 2.5).

Fig. 2.11 shows that an equally good fit of the CO-stretching band toward HH 46 ($\chi^2 = 1.2$) is obtained by adopting the bc, mc, and rc components of the interstellar CO ice band, in which case the contribution of the bc component to the CO band is consistent with the presence of 1:1 CO:CO₂ ice at an abundance of 1 % (Table 2.2), if this component in fact is due to CO in CO₂ (see Sect. 5.4).

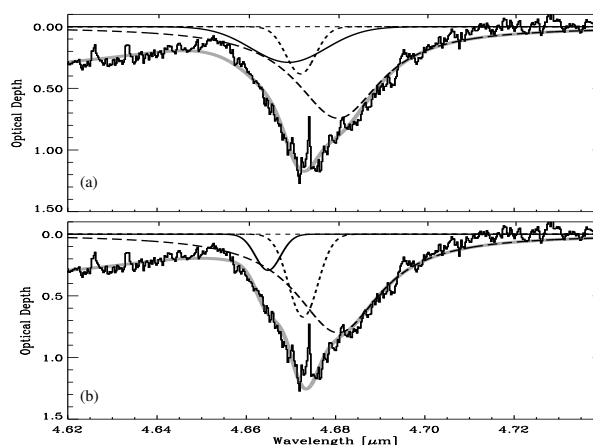


Figure 2.11: The CO stretching mode as observed towards HH 46 by VLT-ISAAC (solid line). Two different fits are shown, adopting (a) the CO laboratory spectrum at 40 K in 1:1 CO:CO₂ (thick solid line) and at 10 K in 1:10 CO:H₂O (dashed line), and the mc of solid CO (dotted line), $\chi^2 = 1.3$, and (b) the bc, mc, and rc component of solid CO, described by Boogert et al. (2004), $\chi^2 = 1.2$. In both plots, the total fit to the CO band is shown in grey, including a Gaussian fit to the XCN band to the blue of the CO stretching mode (not shown).

Despite the degeneracy of the fit, the above analysis of the HH 46 data shows that, based on laboratory data, the spectra of CO and CO₂ are consistent with a (maximum) abundance of 1–3% of an intimate CO:CO₂ ice mixture at 40 K with respect to H₂O-ice. Consequently, this fraction of CO₂ should have formed initially mixed with CO, suggesting reactions in the bulk of the ice, or surface reactions, to be responsible for its formation. However, as this fraction is only 4% of all CO₂ present (see Table 2.2), whereas the rest (96%) is in a cold H₂O-rich environment, this seems to imply that the fraction of CO₂ that forms directly from CO in a CO environment is very small. Thus, it is more likely that the formation of the majority of CO₂ involves chemical reactions that require CO in a H₂O based environment (Ruffle & Herbst, 2001). This is corroborated by the spectral profile of the CO-stretching mode, showing that only 15% of all CO is mixed with CO₂ (see Table 2.2). However, as noted in Sect. 5.4, further studies of those sources that show a strong blue wing on the CO band but no evidence of CO in H₂O are needed, in combination with an analysis of their CO₂ bending mode profiles, before one can be more conclusive.

2.6 Conclusion

In summary, the experimental work presented here shows that CO only affects the CO₂-bending mode in intimate mixtures below 50 K, where mixing of CO and CO₂ results in a single asymmetric band profile for the CO₂ bending mode. In all

other CO-CO₂ ice morphologies studied here the CO₂-bending mode shows the same doublet profile. Conversely, the CO-stretching vibration is blue-shifted to a maximum of 2142 cm⁻¹ in intimate mixtures with CO₂ and between 2140 and 2146 cm⁻¹ when CO interacts with a layer of initially pure CO₂. Consequently, a feature centred at 2143 cm⁻¹ may appear in interstellar spectra due to the interaction between CO and CO₂, but the laboratory bands have significantly larger FWHM than the interstellar feature so that its assignment remains inconclusive. Further constraints can be put on its assignment by analysis of the interstellar CO₂-bending mode spectra. Indeed, the laboratory data do indicate that the combined band profiles of CO and CO₂ can be used to distinguish between mixed, layered and thermally annealed CO-CO₂ ices. Ultimately, this can provide important constraints on the formation mechanism of CO₂, one of the most abundant interstellar ices.

Acknowledgements

This research was financially supported by the Netherlands Research School for Astronomy (NOVA) and a NWO Spinoza grant. The authors would like to thank Klaus Pontoppidan for helpful discussions and Adwin Boogert for kindly providing the Spitzer CO₂ data of HH 46.

Bibliography

- Alsindi, W. Z., Gardner, D. O., van Dishoeck, E. F., & Fraser, H. J. 2003, *Chem.Phys.Lett*, 378, 178
- Boogert, A. C. A., Blake, G. A., & Tielens, A. G. G. M. 2002, *ApJ*, 577, 271
- Boogert, A. C. A., Pontoppidan, K. M., Lahuis, F., et al. 2004, *ApJS*, 154, 359
- Boonman, A. M. S., van Dishoeck, E. F., Lahuis, F., & Doty, S. D. 2003, *A&A*, 399, 1063
- Collings, M. P., Dever, J. W., Fraser, H. J., McCoustra, M. R. S., & Williams, D. A. 2003, *ApJ*, 583, 1058
- Decius, J. C. & Hexter, R. M. 1977, *Molecular Vibrations in Crystals* (McGraw-Hill)
- Ehrenfreund, P., Boogert, A. C. A., Gerakines, P. A., et al. 1996, *A&A*, 315, L341
- Ehrenfreund, P., Boogert, A. C. A., Gerakines, P. A., Tielens, A. G. G. M., & van Dishoeck, E. F. 1997, *A&A*, 328, 649
- Ehrenfreund, P., Kerkhof, O., Schutte, W. A., et al. 1999, *A&A*, 350, 240
- Elsila, J., Allamandola, L. J., & Sandford, S. A. 1997, *ApJ*, 479, 818
- Falck, M. 1986, *J.Chem.Phys.*, 86, 560
- Fraser, H. J., Collings, M. P., Dever, J. W., & McCoustra, M. R. S. 2004, *MNRAS*, 353, 59
- Gerakines, P. A., Schutte, W. A., Greenberg, J. M., & van Dishoeck, E. F. 1995, *A&A*, 296, 810
- Gerakines, P. A., Whittet, D. C. B., Ehrenfreund, P., et al. 1999, *ApJ*, 522, 357
- Gibb, E. L., Whittet, D. C. B., Boogert, A. C. A., & Tielens, A. G. G. M. 2004, *ApJS*, 151, 35
- Nummelin, A., Whittet, D. C. B., Gibb, E. L., Gerakines, P. A., & Chiar, J. E. 2001, *ApJ*, 558, 185
- Pontoppidan, K. M., Fraser, H. J., Dartois, E., et al. 2003, *A&A*, 408, 981
- Roser, J. E., Vidali, G., Manicò, G., & Pirronello, V. 2001, *ApJL*, 555, L61
- Ruffle, D. P. & Herbst, E. 2001, *MNRAS*, 324, 1054
- Sandford, S. A. & Allamandola, L. J. 1990, *ApJ*, 355, 357
- Sandford, S. A., Allamandola, L. J., Tielens, A. G. G. M., & Valero, G. J. 1988, *ApJ*, 329, 498
- van Dishoeck, E. F., Helmich, F. P., de Graauw, T., et al. 1996, *A&A*, 315, L349
- Watanabe, N. & Kouchi, A. 2002, *ApJ*, 567, 651
- Watson, D. M., Kemper, F., Calvet, N., et al. 2004, *ApJS*, 154, 391
- Whittet, D. C. B., Gerakines, P. A., Tielens, A. G. G. M., et al. 1998, *ApJL*, 498, L159

Bibliography

Chapter 3

The physical behaviour of CO and CO₂ in mixed and layered ices

Abstract

*A systematic set of experiments on the thermal behaviour and desorption characteristics of pure, layered and mixed CO-CO₂ ices, are presented. From the results, it has been possible to construct a model to describe these physical properties under interstellar conditions. The data have shown that a combination of the spectral profiles of CO and CO₂ can be used to constrain the morphology and thermal evolution of condensed systems containing both molecules. Below 60 K, under high-vacuum experimental conditions, the spectroscopy and desorption characteristics of mixed and layered ices are fundamentally different, with no evidence for either segregation (in mixed ices) or mixing of the constituents (in layered ices) upon heating. Hence, morphological and phase information inferred from CO-CO₂ spectra of interstellar ice are likely to reflect the conditions under which the ice originally formed. However, the inability of CO to bulk-diffuse through either crystalline or amorphous CO₂ ice also implies that CO₂ can form a physical barrier to CO interacting with other molecules. It is found that between 40–60 K, ~5 % of CO with respect to CO₂, is retained at the surface of nano- to micro-sized crystalline CO₂ domains, a fraction of which become intercollated in the CO₂ matrix beyond 60 K due to the propagation of crystallisation fronts. This largely affects the probability for subsequent chemical reactions under interstellar conditions. The model presented provides a fundamental understanding of the CO-CO₂ system, from which the physical interactions of these molecules can be predicted in a variety of different condensed phases.*¹

3.1 Introduction

CO and CO₂ are two of the most abundant molecules in interstellar ices. Observational evidence and laboratory studies suggest that a close relationship exists between these molecules, whose solid-state interstellar chemistries are closely intertwined. In interstellar ices, it is most likely that CO₂ forms via atom (or radical) – molecule surface reactions involving CO (Alexander et al., 2003; Gerakines et al., 1999; Gibb et al., 2004; Nummelin et al., 2001; Roser et al., 2001; Ruffle & Herbst,

¹F.A. van Broekhuizen, H.J. Fraser, I.M.N. Groot, and S.Schlemmer

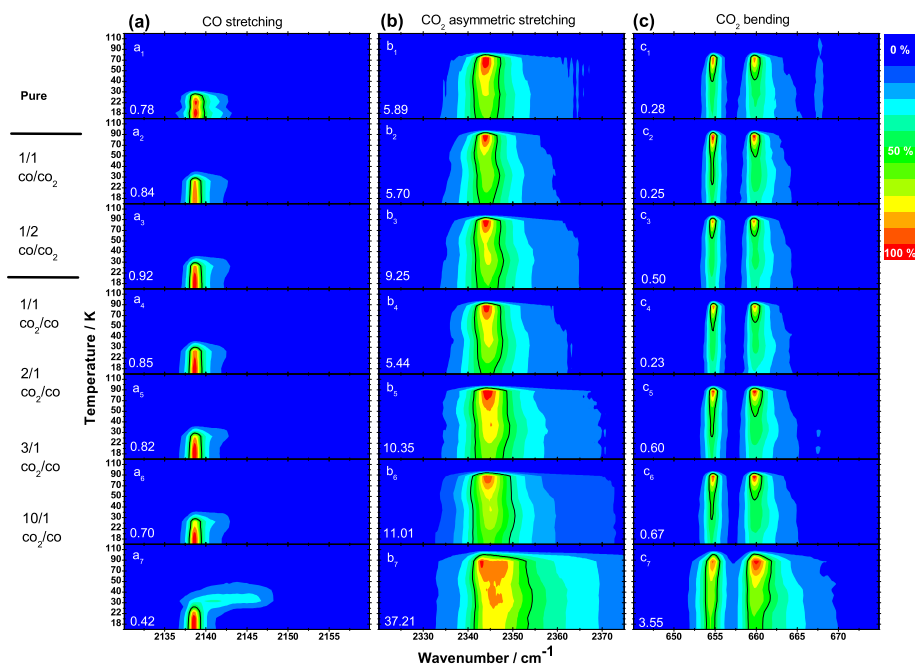


Figure 3.1: The absorbance (contours) of (a) the CO stretching, (b) the CO₂ asymmetric stretching, and (c) the CO₂ bending mode, as a function of wavenumber (x-axis) and temperature (y-axis) for the pure and layered ice morphologies studied. All spectra are background corrected and normalised with respect to the highest intensity peak within each matrix element, and scaled from 0–100% in steps of 10% with the 50% level marked by a black line. The integrated absorbance of each spectrum at 15 K, over the full spectral range shown, is given at the bottom left corner of each plot (cm⁻¹). The temperature scale is non-linear.

2001; van Dishoeck et al., 1996; Whittet et al., 1998). Irradiation processes (UV and electron mediated) can also produce CO₂ from ices containing CO and H₂O, or some other source of C and O (e.g. Loeffler et al., 2004; Palumbo, 1997; Watanabe & Kouchi, 2002). Conversely, CO, which forms in interstellar regions in the gas phase, is commonly re-generated in laboratory experiments by the same types of irradiation that can form CO₂ (e.g. Gerakines et al., 1999; Palumbo, 1997; Richey et al., 2004; Wu et al., 2003).

As a consequence of the intimate relationship between the formation and destruction of CO and CO₂, it is very likely that both molecular species will be located within close proximity of each other in interstellar ices. If CO₂ forms prior to- or subsequent to- the major CO freeze-out, it is likely that the two species will be spatially separated in the ice, i.e. in a layered morphology. For example, in regions where surface reactions involve the conversion of CO to CO₂, a layer of CO₂ ice will build up over the CO ice layer, probably until such a time as either all

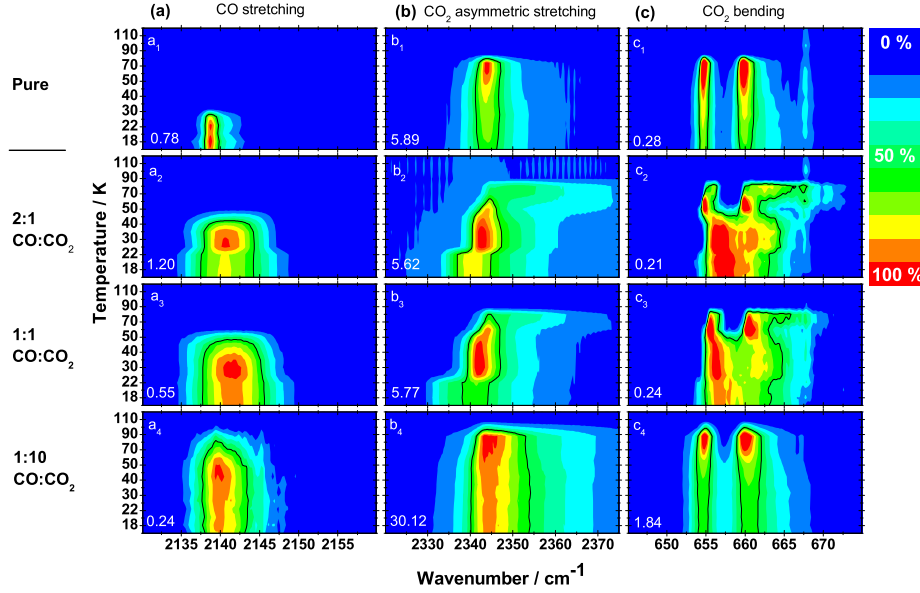


Figure 3.2: The absorbance (contours) of (a) the CO stretching, (b) the CO₂ asymmetric stretching, and (c) the CO₂ bending mode, as a function of wavenumber (x-axis) and temperature (y-axis) for the pure and mixed ice morphologies studied. All spectra are background corrected and normalised with respect to the highest intensity peak within each matrix element, and scaled from 0–100% in steps of 10% with the 50% level marked by a black line. The integrated absorbance of each spectrum at 15 K, over the full spectral range shown, is given at the bottom left corner of each plot (cm⁻¹). The temperature scale is non-linear.

the CO is converted to CO₂ (an unlikely scenario) or until the whole CO surface is covered by CO₂, at which point the reaction will be unable to proceed further. If the CO₂ is predominantly formed by irradiative processes, either by penetration of UV photons or electrons into the CO layer, or by photo-induced processes involving CO or other species trapped within H₂O ice layers, one would be inclined to predict that the resulting ice morphologies would be mixed CO-CO₂ ices. Based on these caveats, it is important to try to distinguish these two scenarios in the interstellar ice environment, since the actual ice morphology can have significant impact on the subsequent thermal evolution of the ice, affecting the diffusion, segregation and trapping of both molecules, thereby influencing their potential to participate in subsequent chemical reactions.

Van Broekhuizen et al. (A&A, submitted) (henceforth referred to as Paper I) have made a detailed study of the CO₂ bending and asymmetric stretching mode, and the CO stretching vibration, to characterise the effects of CO on solid CO₂ spectra, and vice versa, as a function of relative concentration, temperature and ice morphology. Prior to Paper I it had already been shown that mixing of

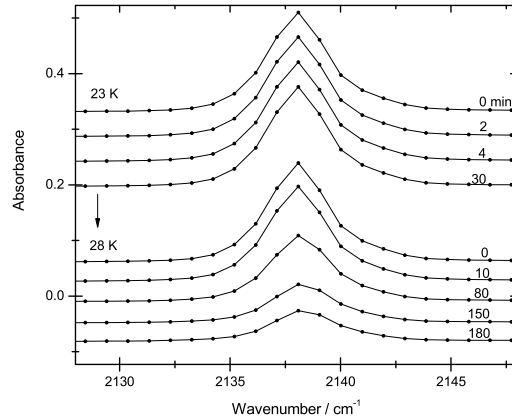


Figure 3.3: Example of a kinetic experiment. The CO-stretching mode spectra in pure CO ice recorded isothermally after various times of annealing (marked at the right hand side of each spectrum) at 23 K (top 4 spectra) and at 28 K (bottom 5 spectra). $t = 0$ at 23 K corresponds to the moment in time at which the ice temperature was raised from 20 to 23 K, $t = 0$ at 28 K to that from 23 to 28 K (indicated also by an arrow; see text).

CO and CO₂ induces significant changes to the spectra of both molecules (e.g. Ehrenfreund et al., 1996, 1997; Elsila et al., 1997), indicating that a combination of solid-state bands from both molecules can be used to constrain their interstellar ice environment(s) but only if it is assumed that CO and CO₂ are mixed. The systematic studies undertaken in Paper I extended the range of CO-CO₂ spectra available for comparison with astronomical spectra. In particular, Paper I showed that the spectra of CO and CO₂ in layered ices are significantly different to those of mixed CO-CO₂ ices, implying that a combination of CO and CO₂ spectra cannot only constrain their local ice environment but also the morphology and thermal history of the ice, as well as hinting at the chemical mechanisms leading to CO₂ formation. For completeness, these experimental methods and the results are summarised in Sect. 3.2 and Sect. 7.5. In Sect. 3.3.3, we extend the results outlined in Paper I to include isothermal kinetic studies of CO diffusion in CO-CO₂ matrices, and from a combination of all the data, present a model to describe the physical processes occurring during the thermal evolution of CO-CO₂ ices in the laboratory (see Sect. 3.3.4). On this basis, we have been able to obtain a clearer understanding of the physical behaviour of solid CO and CO₂ under interstellar conditions, and, in Sect.5, discuss the effects of morphology and thermal history on the spectra of CO and CO₂, and the relevance of our findings in constraining possible formation mechanisms for CO₂ in interstellar ices.

3.2 Experimental Procedure

The experimental methods and spectra obtained are described in detail in Paper I. Briefly, all the experiments were conducted in a high vacuum (HV) apparatus at $\leq 2 \times 10^{-7}$ Torr (base pressure) (Gerakines et al., 1995). Ices composed of $^{12}\text{C}^{16}\text{O}$ (Praxair 99.997% purity) and $^{12}\text{C}^{16}\text{O}_2$ (Praxair 99.997% purity) were grown via effusive dosing on the surface of a CsI window, pre-cooled to 15 K, at a growth rate of $\sim 10^{16}$ molec. $\text{cm}^{-2} \text{s}^{-1}$. FTIR spectra (128 scans, zero filling factor = 4, 0.5 cm^{-1} resolution) were recorded isothermally before and after deposition of each ice component, and at fixed temperatures between 15 and 100 K, in steps of between 3 and 10 K. The resulting spectra are shown in Figs. 3.1 and 3.2, for 0/1, 1/1, 2/1, 3/1 and 10/1 CO_2/CO , 0/1, 1/1 and 1/2 CO/CO_2 , and 1:1, 2:1 and 1:10 $\text{CO}:\text{CO}_2$, where the nomenclature $A:B$ refers to mixed ices, and A/B indicates a layered ice structure, with A on top of B . Henceforth, this set of experiments will be referred to as the stepwise warm-up experiments.

To provide key information on the diffusion of CO prior to its desorption, an additional set of kinetic experiments (not previously reported in Paper I) were made for a limited subset of the ices studied, namely pure CO-ice, 1/1, 2/1 and 3/1 CO_2/CO and 1:10 $\text{CO}:\text{CO}_2$. Identical experimental conditions and ice-growth methods were employed as in the stepwise warm-up experiments, except that at each fixed temperature, the ice was left to equilibrate while spectra were recorded every 2–4 min. using Fourier Transform Infrared spectroscopy (FTIR) at 2.0 cm^{-1} spectral resolution (16 scans, zero filling factor of 4). Only when no further spectral changes could be observed (i.e. the ice had reached a meta-stable configuration), was the temperature raised to the subsequent fixed temperature point.

An example of such a kinetic experiment is given in Fig. 3.3 for pure CO ice. Of all spectra of the CO-stretching band recorded between 15 and 28 K, only a small fraction of those taken isothermally at 23 and 28 K are shown because these temperatures appeared the most interesting for this particular ice-system. Before the ice was heated to 23 K, it had been 10 min. at 15 K and 15 min at 20 K without showing any spectral changes. The top four spectra in Fig. 3.3 are taken at 23 K, 0, 2, 4 and 30 min. after this temperature was set from the previous one at 20 K. As after 30 min. still no spectral changes were observed, the ice temperature was raised one step further to 28 K, as indicated by the arrow. Again every 2 min. a spectrum was recorded. Now, the intensity of the CO-stretching band is observed to decrease with time, indicating that CO is desorbing (see Sect. 3.3.3 for further analysis of these data). This desorption process was followed isothermally in time until all CO desorbed (no meta-stable state evolved in this particular case).

The results presented in the following sections will show that the physical behaviour of the ices is influenced by their structure and phase, especially the degree of crystallinity within the ice layers. In the remainder of this paper it is assumed that the CO_2 ices obtained in our laboratory are predominantly nano- or micro-crystalline, with large cracks and fissures between the crystalline domains, which are sterically accessible enough for CO to diffuse on / in them. The reasoning behind this conclusion is laid-out in detail in Sect. 7.5.

3.3 Results and Discussion

The results of the step-wise warm-up experiments are described in detail in Paper I, focusing separately on the CO-stretching, the CO₂-asymmetric stretching and the CO₂-bending mode as a function of ice morphology, i.e. layered or mixed, and temperature. The full data-set is summarised in Figs. 3.1 and 3.2, for all the layered and mixed ices respectively in the form of matrix contour plots. All spectra shown in these matrices have also been made available on the web at www.strw.leidenuniv.nl/~lab/mixed_layered_CO_CO2/.

3.3.1 CO spectroscopy

The first row of elements in Fig. 3.1 and 3.2 show the spectra of pure solid CO and CO₂, for comparison with the remaining data. The pure CO-ice spectrum (Figs. 3.1a₁ and 3.2a₁) peaks at 2138.7 cm⁻¹ (FWHM = 1.7 cm⁻¹), and no readily identifiable changes occur to the band profile below 25 K; beyond this temperature the band simply reduces in intensity as the CO desorbs.

In the layered ices (Figs. 3.1a₂ to 3.1a₇) the spectral profile of CO is indistinguishable from that of pure CO-ice up to 20 K. Beyond this temperature, a second feature evolves, whose peak position ranges from 2140 to 2146 cm⁻¹. This blue-shifted feature is clearly visible in Fig. 3.1a₇, but also present (though weaker) in all the spectra of the layered ices, irrespective of whether the CO is initially deposited above or below the CO₂ (see Paper I). This feature is interpreted as arising from CO-CO₂ interactions, because this is the temperature range at which, in the step-wise experiments, the CO becomes mobile at the interface between CO and CO₂. Consequently, the CO must be able to interact with a range of binding sites at the CO₂ ice-surface where it is energetically favourable for the CO to reside, as it is slightly more tightly bound to one or more CO₂ molecules than to the other CO molecules in the ice. This is indicated by the small blue-shift of the CO stretching vibration peak associated with this interaction, reflecting a slight strengthening of the CO bond. This effect is most pronounced in the 10/1 CO/CO₂ ice (Fig. 3.1a₇), possibly because of the large relative abundance of CO₂.

In CO:CO₂ mixtures, the peak position of the CO-stretching vibration is also blue-shifted with respect to the pure CO spectrum (see Figs. 3.2a₂ to 3.2a₄), and the FWHM is significantly broader, i.e. 5.6 to 9.0 cm⁻¹. These parameters simply reflect the morphology of the mixed ice sample, where CO and CO₂ molecules are in close proximity to each other, interacting over a range of intermolecular distances and orientations, not unexpectedly giving rise to a broad Gaussian line profile. The CO band position is shifted even at 15 K, with the maximum shift observed in 1:1 CO:CO₂ (Fig. 3.2a₃), which peaks at 2141.6 cm⁻¹ (FWHM of 9.0 cm⁻¹). When the mixing ratio deviates from the equimolar case, i.e. if CO is further diluted in CO₂, or if more CO is added to the mixture, this blue-shift is reduced as illustrated in Figs. 3.2a₂ and 3.2a₄. From Fig. 3.2a it is also clear that heating of the mixed ices does not induce any further blue-shift to the CO stretching mode peak position, unlike the layered ices, where on heating, a second CO band appears bluewards of the original one at 2138.7 cm⁻¹, centred between 2140–2146 cm⁻¹. From these

data it is therefore concluded that the bonding environment of the CO molecule within a CO₂ matrix (i.e. in the mixed ice) is not equivalent to the binding sites that the CO molecules occupy on the internal surface of the CO₂ in layered ices (see above).

With the exception of the 1:10 CO:CO₂ ice (Fig. 3.2a₄), the CO-stretching vibration band both narrows and increases in intensity beyond 22 K in the mixed ices, probably as a result of lateral interactions between neighbouring CO molecules, reflecting an increase in the orientational organisation of CO in the matrix. The absence of this effect in the 1:10 CO:CO₂ ice is most likely related to the degree of crystallinity of the CO₂ ice present in that ice matrix, evinced by the double peaked CO₂-bending mode (see Fig. 3.2c₄ and Sect. 3.3.2).

3.3.2 CO₂ spectroscopy

In contrast to the spectra of CO in pure or layered ices, there is no corresponding change, between 20 and 25 K, in the asymmetric-stretching or bending modes of CO₂ to indicate the existence of CO-CO₂ interactions (Figs. 3.1b₁-3.1b₆ and 3.1c₁-3.1c₆). This implies that either the fraction of CO₂ molecules interacting with CO is a relatively small percentage of the total number of CO₂ molecules in the ice matrix, or that the perturbation of the CO₂ bond is negligible compared to the strengthening of the CO bond described above. One may speculate that CO-CO₂ interactions at the surface involve donation of some electron density from the lone-pair of the O-atom in CO₂ into the conjugated bond system of the CO, as suggested by the gas phase CO dimer (Xu et al., 1996), whereas the weaker interaction in the mixture may only be quadrupolar or weakly electrostatic. Beyond 40-50 K, where almost all the CO has desorbed from the layered ices, the bending-mode spectra of the remaining CO₂ closely resembles that of pure CO₂ ice, with a doublet peak structure that narrows and intensifies, suggesting a continuous expansion of the crystallised phase within the ice layer, right up to the point where the CO₂ desorbs at 80-90 K (Decius & Hexter, 1977).

In fact, as is clear from Figs. 3.1b and 3.1c, the pure and layered ices all have very similar CO₂ spectra, with the asymmetric stretching vibration peaking at 2344.0 cm⁻¹ (FWHM = 10.6 cm⁻¹) and the bending mode split into a doublet, with peaks at 654.7 cm⁻¹ (FWHM = 1.8 cm⁻¹) and 659.8 cm⁻¹ (FWHM = 3.1 cm⁻¹), as is already well known (Yamada & Person, 1964). This doublet splitting of the CO₂ bending mode is indicative of Davidov splitting, which occurs when the ice is strongly ordered, as is the case in a purely crystalline CO₂ ice structure (Decius & Hexter, 1977; Falk, 1987). Such an observation suggests that the CO₂ ice layers grown here, either directly on the CsI window, or on-top of the CO-ice layer, must be predominantly crystalline. This interpretation is at odds with the previous analysis of mixed ice spectra by Sandford & Allamandola (1990), where the bending mode doublet is assigned to amorphous CO₂ ice, based on the band profile of the CO₂ asymmetric stretching mode. However, it is feasible that the experimental method used to grow the ice, both here and in the case of Sandford & Allamandola (1990) (i.e. relatively rapid vapour-deposition from the gas phase), would give rise to crystalline domains within the CO₂ ice layer. Since adsorption

is an exothermic process, the energy released as successive CO₂ molecules are adsorbed may be channelled into torsional and rotational motion of the molecules, such that they are not able to diffuse across the whole substrate surface, but are able to re-orientate to form localised crystalline domains. The issue of amorphous CO₂ ice will be re-addressed in Sect. 3.4.

At temperatures below 20 K in mixed ices, the CO₂-bending mode spectra exhibit a broad, asymmetric, single-line profile (Figs. 3.2c₂ and 3.2c₃), which peaks in a similar wavelength range as the double-peaked profile of pure CO₂-ice. At and beyond 20 K, the first inklings of a splitting reappear, superimposed on the broader single-peak profile. As the temperature increases, these peaks become more pronounced, coincident with the temperature range over which the majority of the CO desorbs from the ice matrix (see Sect. 3.3.3). Beyond 40–50 K, the doublet is fully resolved, although each peak is slightly broader than its companion in the pure CO₂ spectrum. Once again, the appearance of this doublet suggests that crystalline domains are being formed.

Additional information on the mixed CO-CO₂ ice structure is found in the CO₂-asymmetric stretching vibration spectra, Fig. 3.2b. Even at 15 K, the band profile of the asymmetric stretching vibration is both broadened (FWHM = 13 to 18 cm⁻¹) and shifted (to a maximum value of ~2340 cm⁻¹ in 2:1 CO:CO₂) with respect to the same feature in pure CO₂ ice (Fig. 3.2b₁), depending on the precise ice composition. At 22 K, coincident with changes to the CO stretching vibration and CO₂ bending mode spectra, the asymmetric stretching peak is blue-shifted, narrows and increases in intensity with respect to the band profile at 15 K: as such changes are not observed in the pure or layered ices, these effects must be related to changes in the local CO-CO₂ environment, most probably reflecting increasing structural order in the mixed ice matrix. However, segregation of the ice constituents towards pure domains can be ruled out because the CO-stretching vibration profiles (Fig. 3.2a₂–3.2a₄) do not revert to those of pure CO ice. Interestingly, between 50 and 80 K, a shoulder appears on the CO₂-asymmetric stretching peak, at around 2350 cm⁻¹, which becomes increasingly pronounced as the CO desorbs. A similar band is observed in the spectra of nano-sized CO₂ particles (Bonnamy et al., 2003; Ewing & Sheng, 1988), which suggests that as CO desorbs it leaves behind a strongly cracked structure with many small crystalline domains. Nobel gases are known to form micro-porous solids in a similar fashion, by first growing a mixed ice and then gently warming the sample to selectively desorb the noble gas from the matrix, (e.g. Givan et al., 1997; Manca et al., 2004). This interpretation is consistent with the fact that the 2350 cm⁻¹-feature is more pronounced in the spectra of the 2:1 CO:CO₂ ice compared with the 1:1 CO:CO₂. It is even consistent with the CO₂ bending mode spectra, which exhibit a double peaked band profile here and in nano-sized particles (Bonnamy et al., 2003). This does however also imply that CO₂ has very limited (if any) translational mobility under these experimental conditions, which might explain the formation of micro-crystalline CO₂ domains with cracks and fissures on deposition.

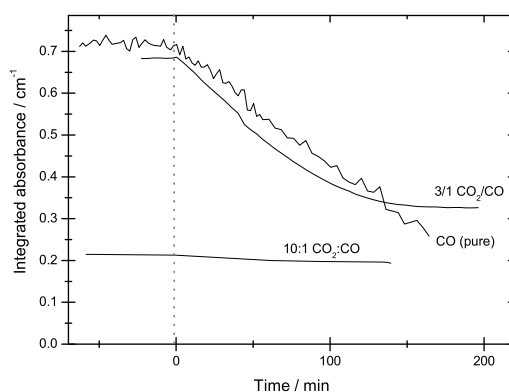


Figure 3.4: Examples of the time-evolution of the integrated absorbance of the entire CO-stretching band between $2130\text{--}2160\text{ cm}^{-1}$, shown for pure CO ice (at 28 K), 3/1 CO_2/CO ice (at 28 K), and 10:1 $\text{CO}_2:\text{CO}$ (at 45 K). Integrated absorbances were derived from spectra recorded during the kinetics experiments (see text for details). The vertical line indicates the “ $t=0$ ”, start-point for each experiment, where the temperature was raised from 23→28 K for the pure and layered ices, and 40→45 K for the mixed ice. The more noisy pure CO profile results from an instability in the He-Ne laser alignment which was replaced before completing the other kinetic experiments.

3.3.3 Desorption of CO

In addition to the influence of CO on the CO_2 spectroscopy at 15 K and visa versa, the most significant changes in the ice spectra are related to physical changes in the ices as they are heated. From the step-wise experiments it is difficult to ascertain whether such processes are diffusion limited or desorption limited. In the case of the pure and layered ices, it is evident that the onset of CO desorption is at or beyond 25 K, proceeding most dramatically between 28 and 30 K (Fig. 3.1). Prior to this, between 20 and 25 K, the CO spectroscopy is already changing, indicating the onset of some physical processes within the ice. Similarly, in the mixed ices, CO desorption is retarded with respect to the pure ice case, being most pronounced between 40 and 70 K, even though significant changes are observed in both the CO and CO_2 spectra at around 22 K. As all the evidence suggests that CO_2 has a very limited (if any) mobility in the CO- CO_2 ices, it follows that the spectral changes prior to the major CO desorption must be related to the mobility of the CO molecules, and / or the propagation of the crystallisation boundaries in the CO_2 ice.

Fig. 3.4 illustrates the integrated absorbances of the kinetic spectra from three ices, pure CO at 28 K, 3/1 CO_2/CO at 28 K, and 10:1 $\text{CO}_2:\text{CO}$ at 45 K, as a function of time. The temperature difference between the data displayed was chosen because, as can be seen from Fig. 3.1 and Fig. 3.2, the onset of CO desorption is not equivalent in the pure and layered ices as compared to the mixed ices - these just

happen to be the most interesting kinetic curves.

The dotted vertical line in Fig. 3.4 marks the $t = 0$ point in the time-domain at which the temperature of each ice system was raised from the previous value. Consequently, the slope of the curves reflect the rate at which CO is desorbing from the ice matrix at these specific ice temperatures. Similar curves can be derived at all the other temperatures at which kinetic experiments were conducted (13 isothermal points between 15 and 80 K for each ice) which gives interesting information on the rate and the amount of CO desorption from these ices as a function of temperature. In addition, those experiments that are conducted above the desorption onset temperature indicate something about the fate of any CO trapped in the matrix after the majority of the CO component has desorbed, those prior to the desorption onset temperature give more detailed information on the diffusion processes leading to matrix reorganisation prior to desorption. In reality even at very low temperatures some of the molecules do have sufficient energy to desorb from the matrix, which makes it harder to differentiate between diffusion and desorption processes as the ice temperature approaches the desorption onset temperature.

From Fig. 3.4 it is clear that the curves from the pure CO ice and the 3/1 CO₂/CO layered ice are almost identical; evidence that even in the case of layered ices with CO₂ on top, CO desorbs from a CO-dominated ice environment. If the CO had to diffuse through the bulk of the CO₂ ice prior to desorption, one would have expected the layered ice curve to have been offset with respect to the pure ice curve. As this is not the case, the CO₂-ice layer most certainly contains large cracks and fissures (indicative of a micro-crystalline CO₂ structure), or pores (indicative of an amorphous CO₂ ice structure), both open directly to the ice-vacuum interface. Consequently, CO desorption may involve a very rapid surface diffusion along the pore or crack surface, or simply a capillary flow of the desorbing gas from the CO ice layer to the vacuum.

At 28 K, eventually all pure CO ice desorbs. However, in case of a 3/1 CO₂/CO layered ice, some CO remains (Fig. 3.4). This fraction of CO is directly related to the presence of the 2140-2146 cm⁻¹ feature in the CO spectra (Sect. 3.3.1). This is shown in Fig. 3.5a, where the integrated absorbance of the CO band is plotted for a spectrum which lies on the asymptotic region of the desorption curve, i.e. in the region where no further changes to the integrated absorbance of the CO band were detected and it was assumed the ice had reached a meta-stable state at that surface temperature. It is clear that between 20 and 28 K the band composition changes prior to the desorption of CO. The integrated intensity of the overall band profile increases by about 10 % of its original value, evidence that the absorption coefficient of the CO-ice is a weak function of temperature, but in astronomical terms well within the 20–30 % uncertainty that is usually assumed when A-values are used to determine interstellar abundances. Closer inspection of Fig. 3.5a shows that the change in the integrated intensity of the overall CO-profile is coupled with a loss in intensity from the pure-CO ice component and a gain in the CO-CO₂ ice environment. Clearly the ice temperature is sufficient for the CO molecules to be mobile, and consequently they diffuse from the CO layer where they were deposited, along the surface cracks and fissures of the overlying

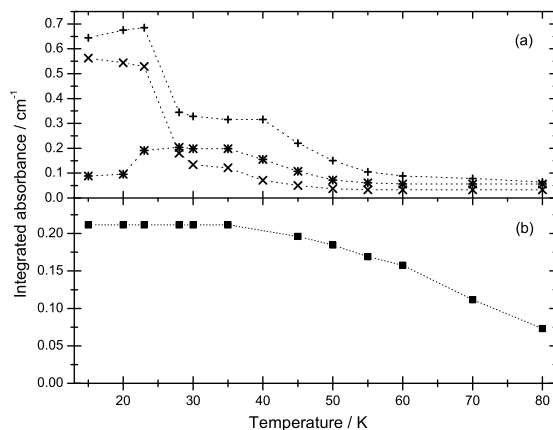


Figure 3.5: Differential evolution of the CO-stretching vibration band with temperature, showing (a) the integrated absorbance of the overall line profile (from 2130 to 2160 cm^{-1}), and that of the underlying components of the band from spectra recorded in the kinetic experiments on $3/1\text{ CO}_2/\text{CO}$ ice, and (b) the entire CO-stretching band in the kinetic experiments on $10:1\text{ CO}_2:\text{CO}$ ice. In (a), the overall band profiles are indicated by (+). For each spectrum of $3/1\text{ CO}_2/\text{CO}$ the CO-band was also decomposed into a contribution from pure-CO ice (\times), (a profile resembling that of pure CO ice spectra at 15 K) and a second band possibly related to CO-CO₂ interactions ($*$), lying between 2140 and 2146 cm^{-1} . The connecting dotted lines in (a) and (b) are included for guidance only.

CO₂ layer, until they find suitable binding sites on the CO₂ ice surface. Occupation of such sites would be energetically more favourable than for the CO to remain in the pure CO-ice layer. This is in agreement with previous laboratory experiments where CO diffusion was observed redistributing CO from multilayers to surface sites, (e.g. Collings et al. 2003, Manca et al. 2004, Fraser et al. 2004, and Fraser et al. in prep.). During these organisational changes within the matrix, no CO desorbs, as indicated by the integrated absorbance of the overall CO band.

It is important to establish that the assumption that CO cannot diffuse through the bulk of the CO₂ over-layer is valid. If the $2140\text{--}2146\text{ cm}^{-1}$ feature is not actually related to CO-CO₂ interactions at the *surface* of the CO₂ ice, but relates to interactions in the *bulk*, this would imply that when the $2140\text{--}2146\text{ cm}^{-1}$ component reaches its maximum contribution to the overall integrated absorbance, which is 30% at around 23 K (Fig. 3.5a), approximately 30% of the CO molecules would have had to be mixed into the CO₂ ice (for bulk diffusion to have occurred), if one is assuming similar band strengths for pure CO and CO:CO₂ mixed ices (Gerakines et al., 1995). In the $3/1\text{ CO}_2/\text{CO}$ ice, this mixing ratio equates to the formation of a $1:9\text{ CO}:\text{CO}_2$ mixed ice. Consequently, if these interactions were induced by mixing, one should observe peak broadening of the CO and CO₂ bands similar to those observed for $1:10\text{ CO}:\text{CO}_2$ in Fig. 3.2a₄–3.2c₄. The absence of such effects

in Figs. 3.1a–3.1c indicates that layered ices do not mix during thermal warming. The CO diffusion and spectral changes must therefore be related to surface diffusion of the CO. For the 1/1 CO₂/CO and 2/1 CO₂/CO layered ices it is found that 10% and 20% of the CO, respectively, is migrating into the CO₂ ice layer. Apparently, by reducing the amount of CO₂ one ends up with an equal ratio between CO in CO₂. This means that the total surface area of CO₂ accessible for CO to interact, is proportional to the thickness of the CO₂ ice layer, which implies that, under the present experimental conditions the surface-to-volume ratio of the CO₂ layer is a constant. This is consistent with the presence of a constant distribution of micro-crystalline domains and suggests that the CO₂ layer does not have a porous structure.

At temperatures higher than around 28 K, the majority of the CO desorbs. From Fig. 3.5a it is clear that CO molecules are lost more rapidly from the pure CO domains than from the surface of the CO₂ ice. This is consistent with the surface molecules being more tightly bound than the CO molecules in the multilayer (see Sect. 3.3.1). Beyond 30 K, both components of the CO-band gradually decrease in intensity, the pure-CO component more rapidly than the 2140-2146-component. However between 30 and 40 K very little if any change is observed in the overall integrated intensity of the band, suggesting that although some CO may be desorbing from the ice the loss rate is very slow, and in fact the ice system is again undergoing restructuring. It is likely that this reflects the diffusion of the last fraction of the remaining pure CO ice to surface sites on the CO₂. It should be emphasised here that also in these kinetic experiments there is no evidence for changes in the spectral profile of the CO₂ bands around these temperatures. Beyond 40 K, there is a gradual decrease in the overall integrated absorbance of the CO-band, coupled with similar decreases in the component features: the CO is continually desorbing, probably as it is forced off the surface by the propagation of the crystallisation fronts of solid CO₂, as the CO₂ component undergoes a phase change from a micro-crystalline to a bulk or polycrystalline layer, which would require the cracks and fissures to close up. Such changes in the structure of the CO₂ ice layer are implied from its spectroscopy (see Fig. 3.1).

The desorption of CO from the mixed ices (Fig. 3.5b) is understandably different to the layered case, mainly because the morphologies of the two systems are so different (compare Figs. 3.1 and 3.2). The CO₂ matrix is literally constraining the desorption process: evidence from the layered ice kinetic experiments clearly demonstrates that bulk diffusion of CO through CO₂ does not occur under these experimental conditions. Again, such findings are consistent with those of CO diffusion in other condensed solid systems, (Collings et al., 2003; Fraser et al., 2004; Manca et al., 2004) with the exception of CO:N₂ (Oberg et al., 2005) and CO:CH₄ (Alsindi et al., 2003) where both matrix elements are translationally mobile. Consequently, for the CO to desorb from the mixed ice system there must be a route via which the CO molecules can reach the ice-vacuum interface without migrating through the bulk. It seems that the onset of CO desorption from mixed ices is somewhere between 40 and 70 K. Interestingly, this corresponds to the same temperature at which bulk crystallisation was seen to occur in the pure and layered CO₂ ices. It seems that CO desorption from the mixed ices is related to the phase

change of the CO₂ matrix component, as cracks open to the ice-vacuum interface and CO is then forced out of the matrix.

Fig. 3.5b is a similar plot to Fig. 3.5a, showing the temperature dependence of the integrated intensity of the entire CO band from 2130–2160 cm⁻¹ for 10:1 CO₂:CO ice. Prior to 35–40 K the integrated intensity is unchanged: CO is not desorbing. By 60 K, 75% of the CO initially deposited on the substrate is still present in the ice matrix. Given that none of the CO₂ has desorbed, this corresponds to a new mixing ratio of 10:0.75 CO₂:CO, reducing to 10:0.5 CO₂:CO at 70 K. For comparison, the amount of CO residing at the internal surface of the 3/1 CO₂/CO layer at 60 K, corresponds to not more than 10% of all the CO (or a new ratio of 3/0.1 CO₂/CO) that was initially present at 15 K. Clearly prior to the bulk crystallisation threshold of CO₂, CO is more easily retained within the ice structure of mixed ices compared to layered ices. Beyond the crystallisation barrier, both ice systems have very similar trace concentrations of CO present.

3.3.4 Overview model(s) of the CO-CO₂ ice systems

From all the evidence presented here, it is possible to construct a consistent picture to describe the thermal evolution of CO- and CO₂-containing ices under pseudo-interstellar conditions. This is summarised in Fig. 3.6, which shows the key physical processes occurring in these ices. These can be subdivided in three apparently distinct processes, i.e. CO desorption, crystallisation of CO₂, and CO₂ desorption.

In layered CO-CO₂ ices (Fig. 3.6a) the two molecular ices are, after deposition, spatially separated from each other. The CO ice seems to form an amorphous ice film, but significant evidence exists that, at least under the experimental conditions described here, the CO₂ ice more closely resembles a micro-crystalline material with cracks and fissures. At 20 K, as the layered ices are heated, the CO molecules are sufficiently mobile to diffuse from the CO ice layer across the surfaces of the cracks in the CO₂ ice and fill the ‘pockets’ between the micro-crystalline domains. No desorption is observed at this stage, nor is bulk diffusion of CO into the CO₂ ice ever observed. At around 25–28 K CO starts to desorb. The desorption proceeds rapidly, such that even by 40 K not more than 5% of the original CO deposited remains somewhere in the ice. Experimental evidence suggests this CO is bound at the CO₂ ice surface, and gradually desorbs from this environment. The desorption of the remaining CO is accelerated beyond 50–60 K, as bulk crystallisation of the CO₂ ice occurs. With the propagation of the crystallisation fronts through the ice lattice, CO is forced out of the structure. A very small fraction may accidentally remain ‘trapped’ in the CO₂ ice, rather like an impurity, if it becomes sandwiched between two crystalline domains before it can desorb. This fraction co-desorbs with the CO₂.

In mixed CO-CO₂ ices (Fig. 3.6b) the two molecules are closely interacting from the start. Except in mixed ices of very high CO₂ concentrations (e.g. 1:10 CO:CO₂), the micro-crystalline structure of the CO₂ is disrupted by the presence of the CO molecules. Some structural rearrangement occurs in the mixed ices between 20 and 25 K, although this appears to be a reorientation of the molecules within the matrix, rather than any kind of diffusion process. Certainly no segregation of the

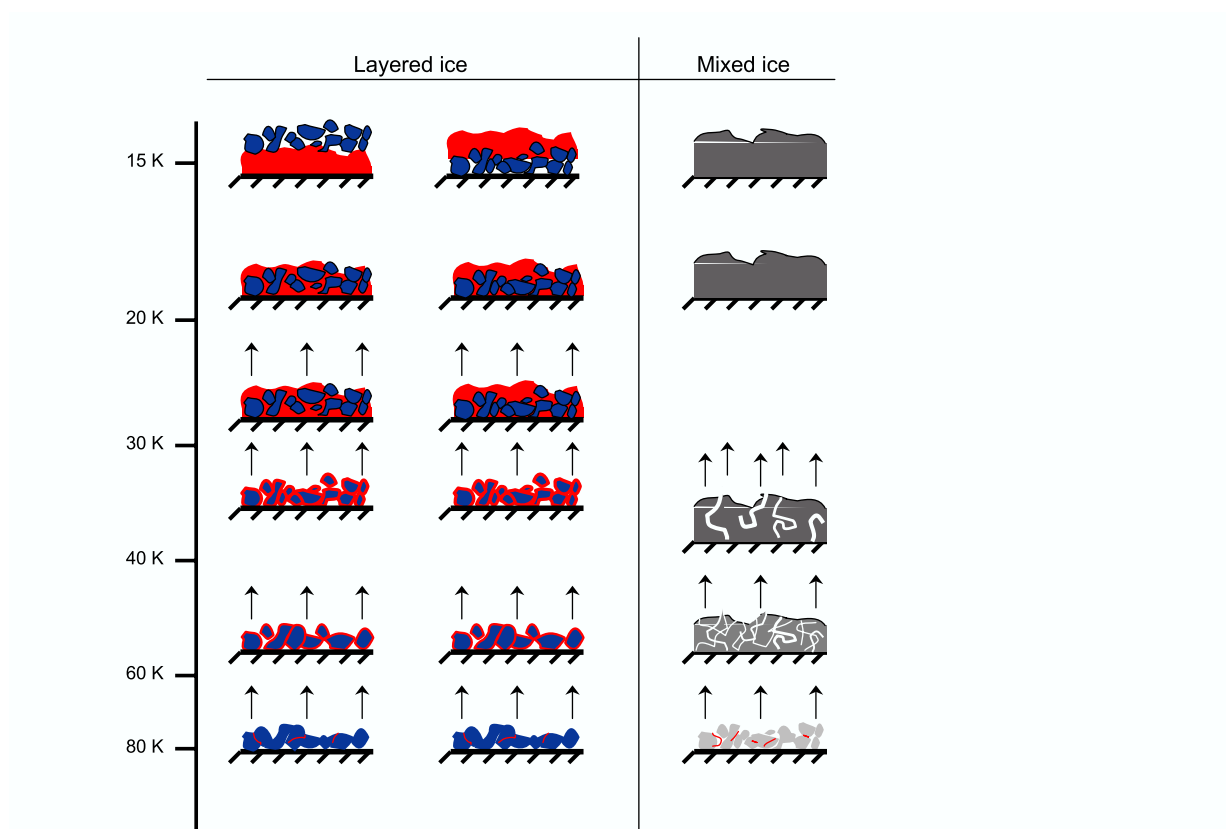


Figure 3.6: Summary of the physical behaviour of CO and CO₂ induced by thermal heating in layered and mixed ices. CO₂ is blue, CO is red, and mixtures are indicated by a grey scale, more dark when more CO is present. The key temperatures at which changes occur in the ice matrices are indicated on the left-hand (non-linear scale). CO desorption is indicated by straight arrows. See text for details.

components is observed. In fact CO is unable to diffuse through the bulk of the CO₂ ice, so CO desorption is not observed to occur from the mixed ices until at least 40–70 K, i.e. at 60 K in 1:10 CO:CO₂, 75% of all CO initially present is still mixed. The onset of CO desorption happens to coincide with the temperature range over which bulk crystallisation of CO₂ ice occurs. It is likely that the onset of crystallisation leads to cracks opening up in the CO₂ ice, along which the CO can escape to the ice-vacuum interface and subsequently desorb. As with the layered ices, by 70 K, only about 5% of CO with respect to CO₂ (i.e. a mixing ratio of 10:0.5 CO:CO₂) remains in the ice matrix. This small fraction co-desorbs with the CO₂ beyond 80 K.

3.4 Concluding Remarks and Astrophysical Implications

The spectroscopic evidence presented here and in Paper I, has shown that CO-CO₂ ices of mixed and layered morphologies are distinguishable from each other, using a combination of band profiles from the CO-stretching, the CO₂-asymmetric stretching and the CO₂-bending modes. Hence, it should be possible to constrain the morphology of the CO-CO₂ interstellar ices from IR-observations. The current spectra and the set of additional kinetic experiments, provide one consistent picture to describe the physical interactions between these two molecules in both ice-morphologies. The model constructed from these data allows for the prediction of the CO-CO₂ interplay in a variety of phases under interstellar conditions.

The differences observed between mixed and layered ices have major consequences not only for the physical, but also for the chemical properties of interstellar CO-CO₂ systems. As has been shown here, CO is unable to diffuse in, or through a CO₂ ice layer (i.e. no mixing), although CO does migrate on the CO₂ surface. Conversely, when CO and CO₂ are closely mixed in an amorphous like structure, its diffusion is also constrained prior to desorption (i.e. no segregation), until CO is forced out of the matrix, most probably due to the propagation of crystallisation fronts of CO₂. Hence, the phase and morphology as inferred from CO-CO₂ interstellar ice-spectra are likely to reflect the conditions under which the ice originally formed. Consequently, on lines of sight where ices containing CO and CO₂ are detected, some constraints can be placed on the CO₂ formation mechanism(s), simply from the detailed spectroscopy of both species (see Paper I for a more detailed discussion).

These results also imply that surface diffusion is needed for CO to move through the CO₂ matrix. Hence, in the absence of cracks and fissures, CO₂ ice may act as a barrier to CO migration. This has major implications on the reaction probabilities of CO under interstellar conditions because it implies that if CO accreted in a separate over-layer on CO₂, or when CO₂ formed as a layer on top of CO via surface reactions, CO₂ may literally block CO from interactions with other condensed molecules. This may be key in understanding the presence or absence of features like for example the 2152 cm⁻¹ signature of CO in H₂O (Fraser et al., 2004). Alternatively, when CO is formed via photo- or particle-induced reactions in the bulk of the CO₂, it is trapped and therefore strongly constrained in its interaction with other molecules until, beyond 40–50 K, the ongoing crystallisation in the CO₂ matrix forces CO out.

The present data do show evidence that between 40–60 K there is always a relative concentration of about 5% of CO on the CO₂-ice surface, available for chemical reactions. However, although this is a constant under the present laboratory conditions, the CO₂ matrix structure is meta-stable and it may be possible that in the interstellar case the crystallisation fronts of the CO₂ ice slowly propagate further due to the longer time scales involved. This will lower the effective surface-to-volume ratio of CO₂ over time, and consequently lead to a smaller relative concentration of CO at the surface.

The CO-CO₂ ice structure, i.e. crystalline or amorphous, may also effect the

spectral profiles and the amount of molecules that are observed. The current data showed that the micro crystalline CO₂ domains exhibit a doublet bending mode profile. Conversely, amorphous CO₂ layers are expected to exhibit a single broad band (Falk, 1987). As clearly the interplay between the CO₂ molecules in a pure solid depends on the ice structure, one may also expect that the interactions between CO and CO₂ change for a different CO₂ ice structure. Hence, the 2140–2146 cm⁻¹ feature observed here for CO at the crystalline CO₂ surface, may change in the presence of an amorphous surface. It is therefore needed to study the formation of amorphous CO₂ ices by using very slow deposition rates, and to investigate systematically the effects of crystalline versus amorphous ice on the diffusion and desorption characteristics of CO and CO₂ and the influence of their spectroscopy.

Acknowledgements

This research was financially supported by the Netherlands Research School for Astronomy (NOVA) and a NWO Spinoza grant. The authors would like to thank E.F. van Dishoeck for many useful discussions.

Bibliography

- Alexander, R. D., Casali, M. M., André, P., Persi, P., & Eiroa, C. 2003, *A&A*, 401, 613
- Alsindi, W. Z., Gardner, D. O., van Dishoeck, E. F., & Fraser, H. J. 2003, *Chem.Phys.Lett*, 378, 178
- Bonnamy, A., Georges, R., Boissoles, J., Canosa, A., & Rowe, B. R. 2003, *J.Chem.Phys.*, 118, 3612
- Collings, M. P., Dever, J. W., Fraser, H. J., McCoustra, M. R. S., & Williams, D. A. 2003, *ApJ*, 583, 1058
- Decius, J. C. & Hexter, R. M. 1977, *Molecular Vibrations in Crystals* (McGraw-Hill)
- Ehrenfreund, P., Boogert, A. C. A., Gerakines, P. A., et al. 1996, *A&A*, 315, L341
- Ehrenfreund, P., Boogert, A. C. A., Gerakines, P. A., Tielens, A. G. G. M., & van Dishoeck, E. F. 1997, *A&A*, 328, 649
- Elsila, J., Allamandola, L. J., & Sandford, S. A. 1997, *ApJ*, 479, 818
- Ewing, G. E. & Sheng, D. T. 1988, *J.Phys.Chem.*, 92, 4063
- Falk, M. 1987, *J.Chem.Phys.*, 86, 560
- Fraser, H. J., Collings, M. P., Dever, J. W., & McCoustra, M. R. S. 2004, *MNRAS*, 353, 59
- Gerakines, P. A., Schutte, W. A., Greenberg, J. M., & van Dishoeck, E. F. 1995, *A&A*, 296, 810
- Gerakines, P. A., Whittet, D. C. B., Ehrenfreund, P., et al. 1999, *ApJ*, 522, 357
- Gibb, E. L., Whittet, D. C. B., Boogert, A. C. A., & Tielens, A. G. G. M. 2004, *ApJS*, 151, 35
- Givan, A., Loewenschuss, A., & Nielsen, C. J. 1997, *Chem.Phys.Lett*, 275, 98
- Loeffler, M. J., Baratta, G. A., Palumbo, M. E., Strazzulla, G., & Baragiola, R. A. 2004, in *Lunar and Planetary Institute Conference Abstracts*, 2037
- Manca, C., Martin, C., & Roubin, P. 2004, *Chem.Phys.*, 300, 53
- Nummelin, A., Whittet, D. C. B., Gibb, E. L., Gerakines, P. A., & Chiar, J. E. 2001, *ApJ*, 558, 185
- Oberg, K. I., van Broekhuizen, F., Fraser, H. J., et al. 2005, *ApJL*, 621, L33
- Palumbo, M. E. 1997, *Advances in Space Research*, 20, 1637
- Richey, C. R., Underwood, R. A., & Gerakines, P. A. 2004, in *Lunar and Planetary Institute Conference Abstracts*, 1450
- Roser, J. E., Vidali, G., Manicò, G., & Pirronello, V. 2001, *ApJL*, 555, L61
- Ruffle, D. P. & Herbst, E. 2001, *MNRAS*, 324, 1054
- Sandford, S. A. & Allamandola, L. J. 1990, *ApJ*, 355, 357
- van Dishoeck, E. F., Helmich, F. P., de Graauw, T., et al. 1996, *A&A*, 315, L349

Bibliography

Watanabe, N. & Kouchi, A. 2002, *ApJ*, 567, 651

Whittet, D. C. B., Gerakines, P. A., Tielens, A. G. G. M., et al. 1998, *ApJL*, 498, L159

Wu, C. Y. R., Judge, D. L., Cheng, B., et al. 2003, *Journal of Geophysical Research (Planets)*, 108, 13

Xu, Y. J., McKellar, A. R. W., & Howard, B. J. 1996, *J.Mol.Spec.*, 179, 345

Yamada, H. & Person, W. B. 1964, *J.Chem.Phys.*, 41, 2478

Chapter 4

Competition between CO and N₂ desorption from interstellar ices

Abstract

Millimeter observations of pre- and protostellar cores show that the abundances of the gas-phase tracer molecules, C¹⁸O and N₂H⁺, anti-correlate with each other and often exhibit “holes” where the density is greatest. These results are reasonably reproduced by astrochemical models provided that the ratio between the binding energies of N₂ and CO, R_{BE} , is taken to be between 0.5 and 0.75. This paper is the first experimental report of the desorption of CO and N₂ from layered and mixed ices at temperatures relevant to dense cores, studied under ultra-high vacuum laboratory conditions using temperature programmed desorption. From control experiments with pure ices, $R_{BE} = 0.923 \pm 0.003$, given $E_b(N_2-N_2) = 790 \pm 25$ K and $E_b(CO-CO) = 855 \pm 25$ K. In mixed (CO:N₂ = 1:1) and layered ice systems (CO above or below N₂), both molecules become mobile within the ice matrix at temperatures as low as 20 K, and appear miscible. Consequently, although a fraction of the deposited N₂ desorbs at lower temperatures than CO, up to 50% of the N₂ molecules leave the surface as the CO itself desorbs, a process not included in existing gas-grain models. This co-desorption suggests that for a fraction of the frozen-out molecules, R_{BE} is unity. The relative difference between the CO and N₂ binding energies as derived from these experiments is therefore significantly less than that currently adopted in astrochemical models. ¹

4.1 Introduction

Dense molecular clouds are the starting point in our understanding of star formation. These regions evolve towards characteristically cold ($\lesssim 10$ K), centrally-concentrated, pre-stellar cores, which then collapse to form protostars. The fundamental properties of these cores are determined almost exclusively from observations of optically thin gas-phase tracers. However as cores evolve towards the collapse phase, densities increase and the time-scales for volatile gas-phase molecules to deplete onto grains become shorter than the age of the core (e.g., Caselli et al., 1999; Walmsley et al., 2004). Of the critical processes governing chemical differentiation in starless cores that are not yet well understood, a key

¹K. I. Öberg, F. A. van Broekhuizen, H. J. Fraser, S. E. Bisschop, E. F. van Dishoeck, and S. Schlemmer

issue is the relative freeze-out of CO and N₂ and their desorption rates (Bergin & Langer, 1997, henceforth BL97).

C¹⁸O accurately traces the distribution of material in cold, dense cores, except in regions of high extinction ($A_v \gtrsim 10$ mag) (e.g., Kramer et al., 1999). When CO becomes frozen out onto the surfaces of cold dust-grains, a corresponding drop is observed in the gas-phase C¹⁸O abundance (e.g., Bergin et al., 2001; Pagani et al., 2004; Tafalla et al., 2002), and solid ¹²CO is detected (e.g., Chiar et al., 1998; Whittet et al., 1998, and references therein). Unfortunately, N₂ is not directly observable in the gas-phase, and the vibrational band strength of solid ¹⁴N₂ is around 5 orders of magnitude lower than the corresponding band strength of ¹²CO, making its detection in interstellar ices impossible (Sandford et al., 2001). The N₂ gas abundance is therefore inferred from observations of its chemical “daughters”, such as N₂H⁺.

The chemical network of N₂H⁺ formation and destruction is described in detail by Jørgensen et al. (2004), showing that the chemistries of CO, N₂, N₂H⁺, HCO⁺ and H₃⁺ are intimately entwined. N₂H⁺ is considered a more suitable gas-phase tracer than C¹⁸O because its abundance can remain constant when CO is depleted (Bergin et al., 2001; Di Francesco et al., 2004; Jørgensen, 2004; Pagani et al., 2004; Tafalla et al., 2002). However depletion of N₂H⁺ (and thus N₂) has been detected within the densest regions of the pre-stellar B68 dark cloud (Bergin et al., 2002), around the Class 0 source IRAM04191 +1522 (Belloche & André, 2004), within starless cores in L183 (Pagani et al., 2004), and in a range of sources in Oph A (Di Francesco et al., 2004).

In gas-grain models, the relative abundances of gas-phase CO and N₂ are governed by the balance of the freeze-out timescales, which depend mostly on density and the desorption timescales, which in turn depend mostly on the grain temperature, binding energies, and desorption kinetics. Models reasonably assume that for both molecules, and at grain temperatures lower than 10–15 K, all sticking probabilities are very close to 1, so the freeze-out timescales are identical for a given grain density. By using first order desorption kinetics, with pre-exponential factors, $\nu_o \approx 10^{12} \text{ s}^{-1}$, models can reproduce the N₂H⁺ and CO observations by assuming that the difference between the desorption rates of CO and N₂ is a direct function of the ratios between their binding energies, $R_{BE} = E_b(\text{N}_2\text{-N}_2)/E_b(\text{CO-CO})$. For example, BL97 set R_{BE} at 0.65, based on the *ab initio* calculations of Sadlej et al. (2003), and assuming $E_b(\text{CO-CO}) = 960 \text{ K}$. Subsequently, Bergin et al. (2002) used an extension of the BL97 chemical model to reproduce their observations of N₂H⁺ in B68, with initial values for the binding energies of CO-CO and N₂-N₂ of 1210 and 750 K respectively ($R_{BE} = 0.62$), although best fits to the emission spectra were actually obtained with $E_b(\text{N}_2\text{-N}_2) = 900 \text{ K}$ ($R_{BE} = 0.75$). Conversely, Aikawa et al. (2003) assume that the value R_{BE} is even lower than that used in BL97. The range of binding energies applied in each case arises due to a lack of relevant laboratory data in the literature.

To accurately model the entire CO-N₂ gas-grain system a minimum of five binding energies need to be known, namely those for N₂-N₂, CO-N₂, H₂O-N₂, CO-CO, and H₂O-CO, together with a knowledge of the order of reaction and pre-exponential factor in the rate equations describing the desorption processes.

In light of these needs, the best laboratory analog mimicking the interstellar case would be the tertiary ice system, $\text{N}_2\text{-CO-H}_2\text{O}$, where CO and N_2 are sequentially or co-adsorbed on a pre-existing porous H_2O -ice layer. One such qualitative study has been made under high-vacuum conditions showing that, after co-deposition of all three molecules (producing a mixed ice), more CO than N_2 becomes trapped in H_2O ices (Notesco & Bar-Nun, 1996). However, no mention is made of the kinetics or binding energies in the paper, and as its focus was CO and N_2 in cometary systems, the ice surface was held at temperatures in excess of 40 - 50 K; not relevant to cold, pre-stellar cores.

It is known from observations that in many pre- and protostellar cores, up to 90% of the CO is frozen out in a distinct layer separated from the H_2O ice (Pontoppidan et al., 2003; Tielens et al., 1991). If N_2 freezes out subsequent to CO, it is likely to form an ice layer *above* the CO ice, creating segregated N_2/CO ices, or if CO continues to accrete to the grain, a mixed CO-N_2 ice. Consequently, the interplay between CO and N_2 during their desorption from binary CO-N_2 ice systems is equally relevant.

4.2 Experimental Procedure

The apparatus used here, CRYOPAD (CRYogenic Photoproducts Analysis Device) (van Broekhuizen et al. in prep.) is very similar to the other Leiden instrument, SURFRESIDE (SURface REaction SIMulation Device) described in detail elsewhere (Fraser & van Dishoeck, 2004). Briefly, the experiments were performed in an ultra-high vacuum (UHV) chamber, reaching base pressures lower than 1×10^{-10} mbar. At the center of the chamber is a gold-coated copper substrate, mounted in close thermal contact with a closed cycle He cryostat, which cools the whole substrate to 12 K. The system temperature is monitored with two thermocouples, one mounted on the substrate, the second by the heater element. Ices are grown *in situ*, by exposing the cold substrate to a steady flow of gas along the surface normal. Desorption is induced by linear heating of the substrate (and ice sample): during film growth or temperature programmed desorption (TPD), gases liberated from the surface are monitored using a quadrupole mass spectrometer (Pfeiffer Prisma). TPD is a well established method in surface science for determining surface-adsorbate binding energies (e.g., Attard & Barnes, 1998; Delchar, 1994).

Mixed (CO-N_2) and layered (N_2/CO) ice morphologies were studied. For completeness, control experiments were conducted on pure CO and pure N_2 ice films. Previous spectroscopic studies have shown that almost equal amounts of N_2 and CO could be frozen out onto interstellar grains without detectably affecting the line profile of the solid-CO vibrational band (Elsila et al., 1997). Therefore the three ice morphologies were studied in equimolar ratios. To enable the two molecules to be discriminated from each other (and the background signal) with mass spectrometry, isotopes of both molecules were used, i.e. ^{13}CO (Cambridge Isotopes Inc. 99 %), $m/e = 29$, and $^{15}\text{N}_2$ (Cambridge Isotopes Inc. 98 %), $m/e = 30$.

In the pure and layered ice morphologies, the gases were used as supplied;

to form the mixed ices a 1:1 gas mixture of ¹³CO:¹⁵N₂ was pre-prepared then mounted on the chamber. The dosing rate for ice-film growth was set prior to cooling the sample, by sequentially backfilling the chamber with the gas(es) of interest, to a pressure of around 1×10^{-8} mbar, equivalent to an ion reading on the mass spectrometer of 7.5×10^{-10} A for both ¹⁵N₂ and ¹³CO. After cooling the substrate to 12 K, the ice films were grown by opening the pre-set flow valve for exposure times equivalent to a dose of 40 L (Langmuir) per sample gas, (where $1 \text{ L} \approx 1 \times 10^{-6}$ Torr s), i.e. the number of molecules of each gas deposited on the surface is equivalent to the number of molecules in 40 monolayers of non-porous condensed solid, assuming 1×10^{15} molecules cm⁻² and a sticking probability of 1. The value of 40 L was chosen for two reasons; firstly it is the upper limit to the number of equivalent monolayers of pure CO ice condensed on grains on lines of sight to low mass stars, as determined by Pontoppidan et al. (2003); secondly, additional experiments (not shown here) indicate that at this ice thickness the behavior of the sample is substrate-independent (Bisschop et al. in prep.). Finally, the ice sample was heated from 12 to 80 K at a rate of 0.1 K min⁻¹ whilst the desorbing gases were monitored using the mass spectrometer.

4.3 Results

The TPD spectra from each of the ice systems are shown in Fig. 4.1. Equal amounts of either N₂ (grey traces) or CO (black traces) contribute to the TPD signal such that the integrated area under each TPD curve is constant to within $\pm 5\%$, and the desorption characteristics of the different ice morphologies can be compared directly.

Pure Ices: In Fig. 4.1a the data from 40 L exposure pure CO and N₂ ices are overlaid. It is clear that N₂ desorbs at lower temperatures than CO. TPD data from layers of higher and lower exposures (not shown) confirm that, at 40 L exposure, the desorption kinetics of N₂ and CO are zeroth order, like those of H₂O, i.e. the pre-exponential factor will typically have a value between 10^{28} to 10^{32} molecule cm⁻² s⁻¹ (Collings et al., 2003a; Fraser et al., 2001), and the desorption rate is independent of the amount of CO or N₂ adsorbed at the surface. Assuming that the enthalpy of adsorption and desorption in these systems are equal, the mean desorption energies (in K) are equivalent to the mean binding energy and can be approximately estimated from the TPD peak position ($E_b = T_{\text{peak}} \times 30.1$, Attard & Barnes, 1998). This gives $E_b(\text{N}_2\text{-N}_2) = 790 \pm 25$ K and $E_b(\text{CO-CO}) = 855 \pm 25$ K respectively, resulting in a ratio of binding energies $R_{\text{BE}} = 0.923 \pm 0.003$. The error bars on E_b arise from a conservative estimate of the range in which T_{peak} actually lies, given that in zeroth order desorption the TPD peak position shifts to higher temperatures and higher intensities as the surface coverage increases. It should be stressed that the mean desorption energies quoted throughout this paper are **estimates**, and the absolute values of E_b can only be accurately determined from kinetic models of the system, subject of a future publication. Consequently, the error bars are larger than those obtained from the TPD peak positions alone, which can be read more precisely and are re-

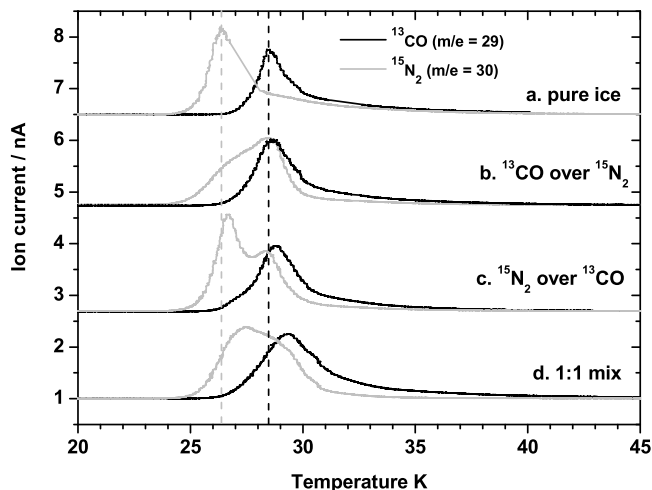


Figure 4.1: Temperature Programmed Desorption (TPD) spectra of (a) pure CO (40 L) and N₂ (40 L); (b) a CO layer (40 L) over a N₂ layer (40 L); (c) a N₂ layer (40 L) over a CO layer (40 L); and (d) an intimately mixed equimolar CO-N₂ ice (80 L total exposure). ¹³CO ($m/e = 29$) traces are in black; ¹⁵N₂ ($m/e = 30$) traces are in grey. The heating rate is 0.1 K min⁻¹. Two dashed lines are superposed on the plot to show the positions of the desorption peaks of the 40 L pure samples of N₂ (grey) and CO (black). Curves (a)–(d) are offset for clarity.

producible to ± 0.05 K for identical surface coverages. Within this experimental error, our $E_b(\text{CO-CO})$ is consistent with that reported by Collings et al. (2003a) of 830 ± 20 K. Our values are also close to the sublimation enthalpies of N₂ and CO determined from IUPAC accredited data (Lide, 2001), i.e. 756 ± 5 K and 826 ± 5 K respectively, giving a ratio $R_{BE} = 0.915$ (upper limit = 0.923, lower limit = 0.903).

Layered Ices: In Fig. 4.1b and c, TPD data from layered CO-N₂ ices are shown. As with the pure CO ice samples, the onset of CO desorption occurs at around 26 K, and over 95% of the CO has desorbed by 31–32 K. It seems that CO only desorbs from a CO dominated environment, although in comparison to the pure CO sample the presence of N₂ may result in a small increase in the range of binding sites from which desorption occurs, accounting for the slight broadening of the TPD profile. The mean desorption energy of CO molecules from the ice, $E_b(\text{CO-CO})$, is 855 ± 25 K, and like the pure CO ice, the desorption kinetics of CO in layered CO-N₂ ice systems follow zeroth order kinetics.

Although a significant fraction of the N₂ desorbs at lower temperatures than CO, i.e. 24–27.5 K, a second peak is clearly visible in the desorption profile of the layered ices, corresponding to N₂ co-desorbing with CO. This is interpreted as some fraction of the N₂ molecules becoming mobile and diffusing into the CO ice, where they become mixed. To establish the relative fractions of N₂ desorb-

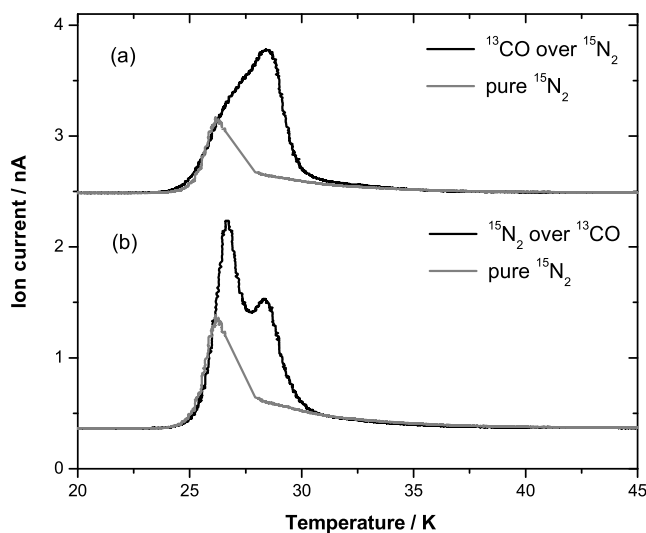


Figure 4.2: TPD spectra of ¹⁵N₂ (black) from (a) a CO layer (40 L) over a N₂ layer (40 L), and (b) a N₂ layer (40 L) over a CO layer (40 L) (Fig 4.1), shown together with the TPD spectra of pure ¹⁵N₂ (grey), scaled to fit their leading edges (see text for details). Curves (a) and (b) are offset for clarity.

ing from each environment a simple analysis was undertaken. The pure N₂ TPD trace (Fig. 4.1a) was scaled to fit the leading edge of each of the other N₂ TPD traces (Fig. 4.1b-d), then subtracted. This is illustrated for the two layered CO-N₂ systems in Fig. 4.2. The integrated area under the scaled, pure-N₂ trace was then attributed to N₂ molecules desorbing from a pure ice environment, and the integrated area under the remaining curve to a mixed ice environment, assuming that each TPD trace is a linear combination of these two contributions. The results of this analysis are shown in Fig. 4.3, where the error bars arise from the uncertainty in the initial scaling of the pure N₂ trace. The fraction of N₂ desorbing from the pure and mixed ice environments depends intrinsically on the initial morphology of the ice system. If N₂ is deposited above an existing CO ice layer, the majority of N₂ molecules do desorb prior to CO, whereas when N₂ is deposited below a CO layer about 50% of the N₂ molecules co-desorb with the CO. This implies that the desorption kinetics are unchanged between layered and pure ice systems (i.e. still zeroth order) and R_{BE} is unaltered, i.e. $R_{BE} = 0.923 \pm 0.003$. $E_b(\text{CO-N}_2)$ is determined from the co-desorbing fraction of N₂, i.e. $\approx 855 \pm 25$ K, i.e. $R_{BE} = 1$, although further differential N₂ exposure experiments are required to confirm this value.

CO-N₂ Ice Mixture: In Fig. 4.1d, the mixed-ice CO TPD traces are broadened and shifted to higher temperatures in comparison to the pure CO ice or layered ice systems. From the leading edge of the CO TPD trace, it appears that the CO desorption is hindered by the presence of N₂. This results in a small shift in the

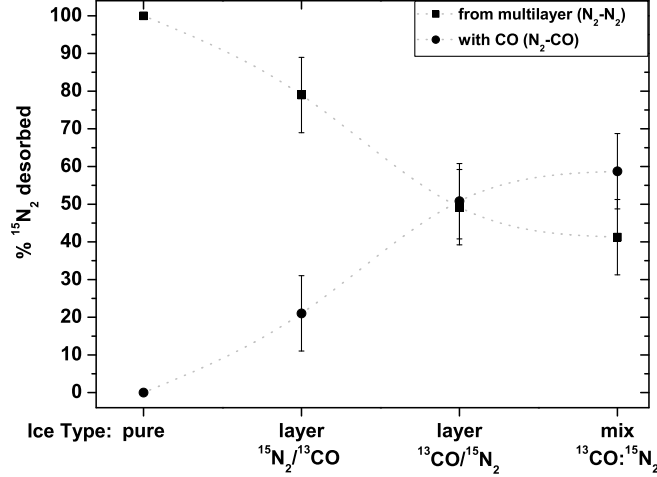


Figure 4.3: Fraction of N_2 desorbing from pure and mixed ice environments in each of the ice systems studied as a percentage of the total N_2 desorbed at the end of each experiment. See text for details.

TPD peak position, commensurate with a rise in the mean desorption energy of the CO molecules, i.e., $E_b(\text{CO-CO}) = 885 \pm 25$ K. This implies that the majority of the CO molecules in a mixed ice desorb from slightly different binding environments compared to those from which desorption occurs in pure and layered ice systems. Fig. 4.3 shows that at least 50% of the N_2 originally deposited in the mixture actually co-desorbs with the CO. The remaining N_2 desorbs from an environment resembling a pure N_2 ice layer: it is therefore proposed that some N_2 becomes segregated in a layer separated from the remaining ice mixture upon heating. For this segregated fraction of N_2 , $R_{BE} = 0.893 \pm 0.003$, due to the rise in the mean desorption energy of CO; for the remainder of the N_2 , $R_{BE} = 1$.

4.4 Discussion

The results from these experiments, summarized in Fig 4.4, have a direct impact on the modelling of CO and N_2 desorption in pre-stellar and star-forming cores. First, as the desorption behavior of layered and mixed ices are not identical, the models must adopt the system that most suitably emulates the interstellar case. Second, the desorption kinetics of CO and N_2 should be modelled as zeroth and not first order processes, adopting rates independent of the surface concentration of the molecules, with pre-exponential factors in the rate constant of 10^{28} to 10^{32} molecule $\text{cm}^{-2} \text{s}^{-1}$ (Collings et al., 2003a; Fraser et al., 2001). Depending on the initial ice morphology and assuming that depleted molecules play no part in any grain-surface chemistry, some fraction of the N_2 originally frozen-out on interstellar grains will only desorb as the CO multilayers themselves desorb.

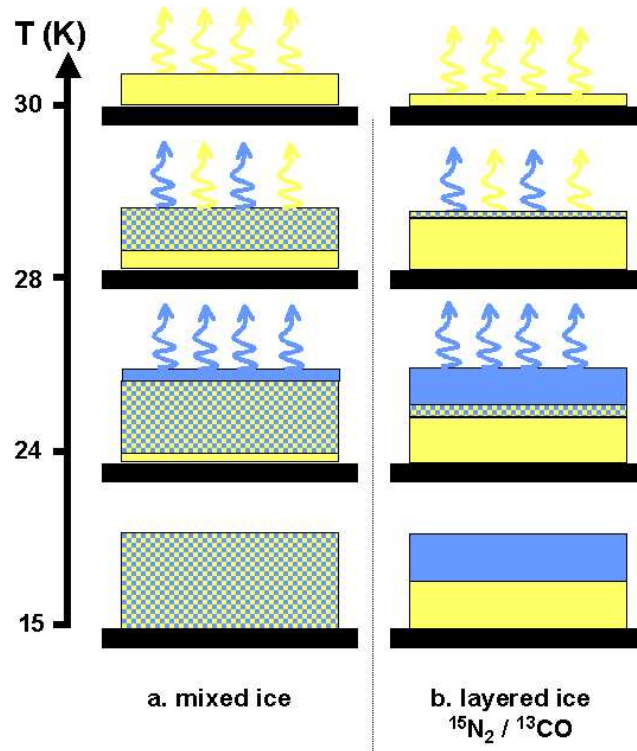


Figure 4.4: A summary of the desorption behavior of CO and N₂ within astrophysically relevant ice systems. Pure CO and N₂ are represented by light grey and dark grey shading respectively; mixed ice regions are chequered. Desorption is indicated by the wiggly arrows. (a) Mixed Ice: the ice components begin segregating as soon as the ice is heated, forming layers of CO and N₂, below and above the remaining ice mixture. Further heating leads to the onset of N₂ desorption from the segregated N₂ layer and then co-desorption of CO and N₂, until all the N₂ has desorbed. Finally, only CO is desorbing from the surface. (b) Layered Ice: as the N₂/CO layered ice is heated, the majority of N₂ molecules desorb directly from the upper surface of the N₂ multilayer. From ≈ 20 K, the diffusion of CO and / or N₂ across the layer interface leads to mixing between the two ice layers, and a fraction of the N₂ molecules subsequently co-desorb with the CO molecules.

Irrespective of the ice morphology, this work gives $E_b(\text{N}_2\text{-N}_2) = 790 \pm 25$ K and $E_b(\text{N}_2\text{-CO}) = 855 \pm 25$ K, except in the mixed ice, where $E_b(\text{CO-CO}) = 885 \pm 25$ K. Within experimental error, these values are consistent those obtained by Collings et al. (2003a), but significantly smaller than the $E_b(\text{CO-CO})$ value of 960 K (Sandford & Allamandola, 1990) used in BL97 or $E_b(\text{CO-SiO}_2)$ of 1210 K (Bergin et al., 2002). The latter value is closer to the experimentally determined value of $E_b(\text{CO-}$

H_2O) = 1180 ± 20 K (Collings et al., 2003b; Fraser et al., 2004). From the present reported values, therefore, the ratio between the binding energies of N_2 and CO, R_{BE} , is 0.923 ± 0.003 for all cases where N_2 desorbs from “pure” ice environments. However, $R_{\text{BE}} = 1$ for the fraction of N_2 that co-desorbs with CO. The lowest empirical value of R_{BE} , 0.893 ± 0.003 , is found in mixed ices, where the lower ratio reflects the rise in the mean value of $E_{\text{b}}(\text{CO-CO})$. Nevertheless, all these ratios are significantly greater than any of the values adopted by BL97, Bergin et al. (2002) or Aikawa et al. (2003). Such a situation mimics that explored at the end of BL97, where R_{BE} was set to 1, to study the effects of the N_2 binding energy on N_2H^+ depletion, which was then enhanced by two orders of magnitude. These new laboratory data, when applied to models of dense cores, will certainly decrease the anti-correlation between gas-phase CO and N_2H^+ abundances. The next step is clearly to address detailed modelling of the CO- N_2 desorption kinetics followed by empirical studies of the tertiary CO- N_2 - H_2O ice system.

Acknowledgements

We are grateful for comments by J. Jørgensen and T. Bergin and funding from NOVA, the Dutch Research School for Astronomy and a NWO Spinoza grant to EvD. KO is grateful to the summer undergraduate research fellowship (SURF) program at Caltech for sponsoring her visit to Leiden.

Bibliography

- Aikawa, Y., Ohashi, N., & Herbst, E. 2003, *ApJ*, 593, 906
- Attard, G. A. & Barnes, C. 1998, *Surfaces* (Oxford University Press Inc., New York)
- Belloche, A. & André, P. 2004, *A&A*, 419, L35
- Bergin, E. A., Alves, J., Huard, T., & Lada, C. J. 2002, *ApJL*, 570, L101
- Bergin, E. A., Ciardi, D. R., Lada, C. J., Alves, J., & Lada, E. A. 2001, *ApJ*, 557, 209
- Bergin, E. A. & Langer, W. D. 1997, *ApJ*, 486, 316
- Caselli, P., Walmsley, C. M., Tafalla, M., Dore, L., & Myers, P. C. 1999, *ApJL*, 523, L165
- Chiar, J. E., Gerakines, P. A., Whittet, D. C. B., et al. 1998, *ApJ*, 498, 716
- Collings, M. P., Dever, J. W., Fraser, H. J., & McCoustra, M. R. S. 2003a, *Ap&SS*, 285, 633
- Collings, M. P., Dever, J. W., Fraser, H. J., McCoustra, M. R. S., & Williams, D. A. 2003b, *ApJ*, 583, 1058
- Delchar, D. W. . T. 1994, *Modern Techniques of Surface Science*, 2nd ed. Chap. 9 (C.U.P., Cambridge)
- Di Francesco, J., André, P., & Myers, P. C. 2004, *ArXiv Astrophysics e-prints*
- Elsila, J., Allamandola, L. J., & Sandford, S. A. 1997, *ApJ*, 479, 818
- Fraser, H. J., Collings, M. P., Dever, J. W., & McCoustra, M. R. S. 2004, *MNRAS*, 353, 59
- Fraser, H. J., Collings, M. P., McCoustra, M. R. S., & Williams, D. A. 2001, *MNRAS*, 327, 1165
- Fraser, H. J. & van Dishoeck, E. F. 2004, *Advances in Space Research*, 33, 14
- Jørgensen, J. K. 2004, *A&A*, 424, 589
- Jørgensen, J. K., Schöier, F. L., & van Dishoeck, E. F. 2004, *A&A*, 416, 603
- Kramer, C., Alves, J., Lada, C. J., et al. 1999, *A&A*, 342, 257
- Lide, D. 2001, *Handbook of Chemistry and Physics*, 82nd ed. (CRC Press, Florida)
- Notesco, G. & Bar-Nun, A. 1996, *Icarus*, 122, 118
- Pagani, L., Pardo, J.-R., Apponi, A. J., Bacmann, A., & Cabrit, S. 2004, *A&A*, in press
- Pontoppidan, K. M., Fraser, H. J., Dartois, E., et al. 2003, *A&A*, 408, 981
- Sadlej, J., Rowland, B., Devlin, J. P., & Buch, V. 2003, *J. Chem. Phys.*, 102, 4804
- Sandford, S. A. & Allamandola, L. J. 1990, *Icarus*, 87, 188
- Sandford, S. A., Bernstein, M. P., Allamandola, L. J., Goorvitch, D., & Teixeira, T. C. V. S. 2001, *ApJ*, 548, 836
- Tafalla, M., Myers, P. C., Caselli, P., Walmsley, C. M., & Comito, C. 2002, *ApJ*, 569, 815

Bibliography

- Tielens, A. G. G. M., Tokunaga, A. T., Geballe, T. R., & Baas, F. 1991, *ApJ*, 381, 181
Walmsley, C. M., Flower, D. R., & Pineau des Forêts, G. 2004, *A&A*, 418, 1035
Whittet, D. C. B., Gerakines, P. A., Tielens, A. G. G. M., et al. 1998, *ApJL*, 498, L159

Chapter 5

Photodesorption of solid CO

First results from CRYOPAD

Abstract

*The photodesorption of CO from solid CO by UV-photons from a H₂-discharge source has been studied as a function of surface coverage and temperature. This is the first study conducted in the cryogenic photoproduct analysis device, CRYOPAD, a new ultra high vacuum apparatus dedicated to study photon-induced processes of condensed molecules of astronomical interest. A grazing angle FT-RAIRS system sensitive to 0.1–0.01 ML of CO, and a quadrupole mass spectrometer with a CO detection limit of $\sim 5 \times 10^9$ molec. s⁻¹, allow for simultaneously monitoring UV-induced reactions in the solid and the photodesorption of reactants and photoproducts into the gas phase. The results indicate that the CO photodesorption depends on the coverage and the temperature but show no evidence for any instantaneous desorption at $t = 0$ beyond the detection limit of the quadrupole mass spectrometer. This sets an upper limit on the photodesorption probability per photon of 1.9×10^{-5} . Consequently, a similar upper limit can be expected under interstellar conditions, although preliminary results on the UV-photolysis of solid CO₂ provide evidence for direct CO-desorption as a result of photochemical reactions. In contrast, the data show that the CO-desorption from the pure solid depends strongly on the photon dose and most probably involves processes induced in the underlying substrate surface. These can increase the maximum yield to about 1.4×10^{-4} molec. photon⁻¹ and may also arise in interstellar space due to the photoelectric effect liberating electrons from interstellar grains, although probably with a different efficiency. The first results presented demonstrate that CRYOPAD can derive qualitative and quantitative information about photon induced processes of condensed molecules, which will add to the current understanding of these processes under interstellar conditions.*¹

5.1 Introduction

Ever since the first observational indication that complex chemistry could be occurring in interstellar ice mantles (Soifer et al., 1979), it has been proposed that

¹F.A. van Broekhuizen, H.J. Fraser, E.F. van Dishoeck, and S.Schlemmer

irradiative processes induced by cosmic-rays, energetic particles or UV-photons may be key in the formation of molecules in dense molecular clouds (e.g. Gerakines et al., 1996; Hudson & Moore, 1993; Muñoz Caro et al., 2004). Similarly, molecules in cometary ices have been exposed to irradiation during the lifetime of the solar system (e.g. Brooke et al., 1996; Cottin et al., 2003; Elsila et al., 1997; Mumma et al., 1996; Wu et al., 2002). Although the contribution of UV-photons to the chemical evolution in dense clouds is still under discussion due to the low fluxes present in those environments (Bourdon et al., 1982; d’Hendecourt et al., 1982; Gerakines et al., 1999; Tielens & Hagen, 1982; van Broekhuizen et al., 2004), they are expected to play an important role in the (clumpy) photon dominated regions (PDR’s) (Bergin et al., 1995; Gorti & Hollenbach, 2002; Störzer & Hollenbach, 1999; Turner, 2000), in the upper layers of protoplanetary disks (Aikawa et al., 2002; van Zadelhoff et al., 2003; Willacy & Langer, 2000) and clumps, and in diffuse interstellar clouds (Shen et al., 2004).

Chemical models of these regions show that UV-photodesorption can be an effective means to return physisorbed molecules from interstellar grains to the gas phase in those parts, where there is major freeze-out due to high densities and low temperatures. This process should, however, have a relatively large yield of $\geq 10^{-3}$ molec. photon⁻¹ in order to be efficient in returning condensed molecules to the gas phase (Watson & Salpeter, 1972a,b; Willacy & Langer, 2000).

Photodesorption is the process in which the absorption of a photon by a molecule leads to the ejection of this molecule from the solid into the gas phase. Although much research has been done on the photodesorption properties of molecules from a large variety of surfaces in many different laboratories (e.g. Anashin et al., 1998; Fukutani et al., 1995; Hussia & Viswanathan, 1985; Lange, 1965; Mesawari & Ignatiev, 1988; Yoshinobu et al., 1991), only little is known about the photodesorption efficiency of physisorbed molecules under simulated interstellar conditions. Early experimental work by Greenberg (1973) studied this efficiency for CO, CO₂ and H₂O and concluded that the observed yield per photon (10^{-5} molec. photon⁻¹ at $\lambda_{UV} = 200\text{--}275$ nm) should be large enough to explain the observed gas-to-solid molecular abundance ratios in interstellar clouds of moderate density ($n_H = 10^3$ cm⁻³). However, this was questioned by Bourdon et al. (1982), who argued that their results should have been $10^3 \times$ smaller. This would make photodesorption inefficient under interstellar conditions. Nevertheless, more recent work by Westley et al. (1995a,b) claims that photodesorption by Ly α photons can indeed be significant for H₂O-ice, 3.5×10^{-3} molec. photon⁻¹. Given that these controversial conclusions are based on a limited amount of available data, more work is required to add to the understanding of photon-induced desorption processes and their importance for the chemical and physical evolution of the various environments in space.

For this and other reasons, we have recently developed a new ultra high vacuum apparatus, the Cryogenic Photoproduct Analysis Device (CRYOPAD), which is specifically designed to study quantitatively photon-induced reactions of volatile molecules of astrophysical relevance in the solid state. CRYOPAD improves upon the experimental systems available to date in most astronomically oriented laboratories, in which the photochemistry of condensed molecules has been extensively

studied under high-vacuum (HV, typically 10^{-7} Torr) conditions (e.g. Baratta et al., 2004; Cottin et al., 2003; Gerakines et al., 1996; Hudson & Moore, 2004; Palumbo, 1997). Due to the HV, these experiments suffer from the constant background accretion of H_2O (on the order of 100 monolayers hr^{-1}) so that only reasonably thick matrices (i.e. $\gg 100$ monolayers) can be studied. In contrast, the base pressure of $\sim 1 \times 10^{-10}$ Torr of CRYOPAD allows us to accurately study matrices of less than 40–100 monolayers (ML), the maximum grain-mantle thickness appropriate for dense molecular clouds (Pontoppidan et al., 2003). In addition, photodesorption products which may form a significant part of reactions can be monitored. Comparable instruments do exist (e.g. Chakarov et al., 1995; Kay et al., 1989; Petrik & Kimmel, 2004; Picq & Balanzat, 1999; Roser et al., 2002; Sack et al., 1993; Shi et al., 1995). However, CRYOPAD is unique in that it combines a calibrated UV-irradiation source with Fourier Transform reflection absorption infrared spectroscopy (FT-RAIRS) and quadrupole mass spectrometry (QMS) to study the UV-induced processes in the condensed- and the gas phase simultaneously. These analysis techniques are only used in this combination by Watanabe et al. (2000) to study UV-induced reactions in a solid.

A detailed outline of CRYOPAD is given in Sect. 5.2.1, followed by an explanation about its characteristics and principles of operation in Sect. 5.2.2. In Sect. 5.3, this is demonstrated by the first study conducted in CRYOPAD on the photodesorption of solid CO , using all different experimental options available. In Sect. 5.4, the underlying mechanisms of this photodesorption will be discussed and an application to a more complex system of the photodissociation and desorption of solid CO_2 is given. Some concluding remarks concerning the consequences for the importance of photodesorption under interstellar conditions will be given in Sect. 5.5.

5.2 CRYOPAD

The outline and principles of operation of the UHV apparatus CRYOPAD are described in Sect. 5.2.1. In Sect. 5.2.2, the two analysis techniques, quadrupole mass spectrometry (QMS) and Fourier Transform reflection infrared spectrometry (FT-RAIRS), adopted to study the physical and chemical interactions between molecules in the solid state in parallel to photodesorption, will be explained.

5.2.1 Description of the apparatus

Fig. 5.1 presents a cross sectional view of the reaction chamber on CRYOPAD in the plane of rotation of the substrate, situated at the centre of the chamber, and perpendicular to its surface, shown as a photograph in Fig. 5.2. The reaction chamber has a total volume of approximately 1 l. The substrate is made of oxygen-free high conductivity copper (OFHC) and coated with a thin vacuum-vapour deposited Au-layer of $\sim 0.1 \mu\text{m}$ thickness. This is mounted in close thermal contact with a closed cycle He cryostat (ARC cryogenics, DE202N). The cryostat is supported by a differentially pumped rotational feedthrough (Thermionics), which

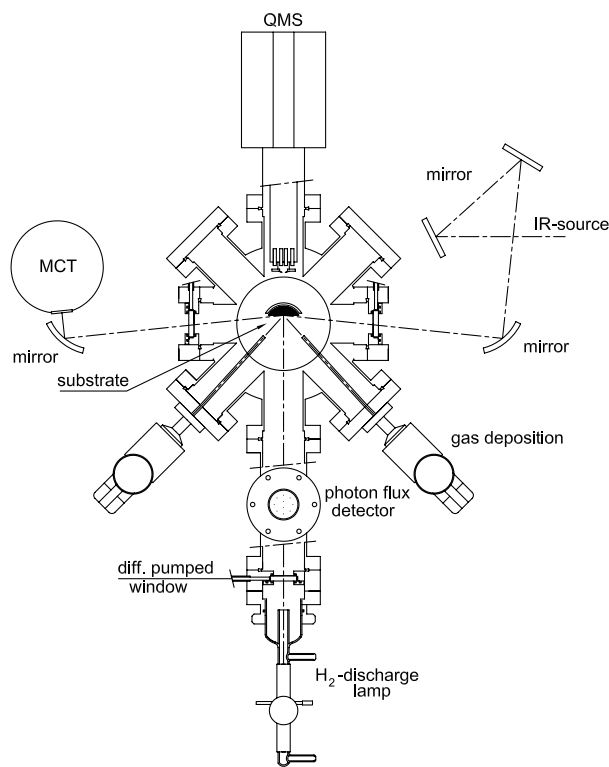


Figure 5.1: Cross sectional top view of the reaction chamber on CRYOPAD, perpendicular to the substrate surface and in the plane of rotation of the substrate. The key elements for detection are the FT-RAIRS system, consisting of two planar mirrors, an off-axis parabola and one ellipsoid, the QMS, and the photon flux detector to monitor the UV-photons produced at the H₂-discharge lamp. The two leak-valves for gas deposition are shown. All elements in the scheme are drawn on scale with the 14 cm outer-diameter of the reaction chamber as a reference.

allows for a 360° degrees rotation of the substrate. The irregular Au-surface of the substrate has a dimension of 12.5 × 10 mm and is 8 mm offset from the centre of rotation. The cryostat and the backside of the surface are shielded by a Ni-coated cryo-shield to minimise any external radiative heat load.

The temperature of the surface can be varied between 11–250 K using resistive heating, controlled by a LakeShore 340M temperature-control unit. Two Fe-Au (0.07%) versus chromel thermocouples (LakeShore), attached to the coldest spot of the cryostat close to the heater element and to the centre of the backside of the surface, are used to measure the temperature with a relative accuracy of ± 0.02 K. The absolute temperature, calibrated at 24 and 77 K using a standard silicon diode (LakeShore DT-670-CU), is accurate within ± 0.2 K.

The pressure in the chamber is monitored right below the photon flux detector in Fig. 5.1 by a Nude ion-gauge (DeMaco), equipped with a Thoriated Iridium

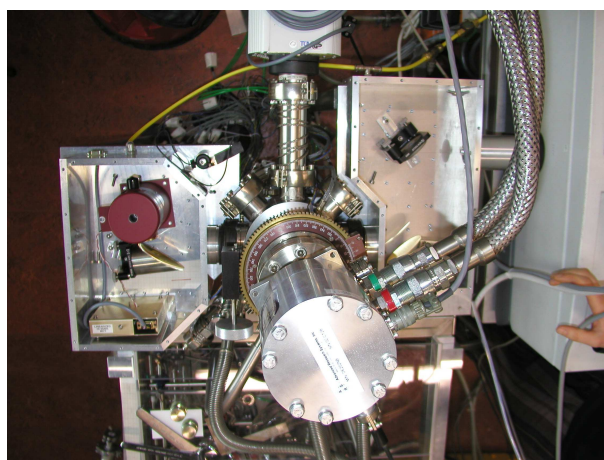


Figure 5.2: A top view photograph of the reaction chamber on CRYOPAD sketched in Fig. 5.1, showing the QMS (in the middle at the top) and the FT-RAIRS system where the IR-beam is going via an optics path from the right (source) to the left (detector).

filament, using a Perkin-Elmer pressure-gauge controller, accurate within 10%. The pressure was calibrated from the vapor pressure of Ar(s), using the Clausius-Clapeyron equation for various temperatures. In addition, the response of the ion-gauge to Ar was tested from the current output of the ion-gauge measured by a Keithley 610 CR as a function of the pressure read by the controller, assuming that the gauge-sensitivity for Ar is similar to that for N₂ (25 Torr⁻¹). At room temperature (RT), the pressure is better than 1×10^{-10} Torr with H₂ as the dominant gas-constituent. This base pressure is reached using a Leybold Turbo-340 MC magnetic bearing pump (pump speed for N₂ = 250 l s⁻¹), positioned right underneath the substrate, one level below the ion-gauge, backed by a Rotary-vane pump (Leybold). If the cryostat is in operation, the pressure in the chamber drops as a consequence of additional cryo-pumping. In case of CO, this cryo-pumping increases the total pump speed (S_{tot}) by a factor of 4.8. This effect will become important for the quantitative analysis of desorption processes in Sects. 5.2.2 and 5.3.

UV-source

The H₂-discharge lamp, shown in Fig. 5.1, has been previously used in various laboratories to simulate the interstellar UV in dense molecular cloud environments. The H₂ plasma is generated by a Sairem Microwave-generator (250 MHz), using a tunable microwave cavity to optimise the applied forward versus reflected power to typical values of 100 and 6 Watt, respectively. The H₂ pressure was kept constant between 0.4 and 0.5 mbar. The characteristics of this lamp have been described in detail by Cottin et al. (2003) and a typical UV-lamp spectrum, recorded using a home-built UV-spectrometer and a NIST calibrated silicon photo-diode

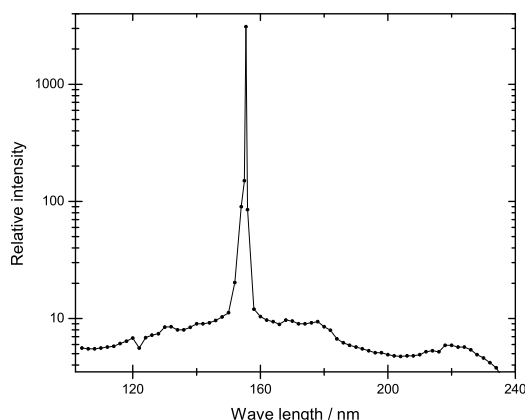


Figure 5.3: Spectrum of the H_2 -discharge lamp, recorded for $p(H_2) = 0.5$ mbar, and a forward and reflected power of 100 and 6 Watt, respectively.

($\lambda_{UV} = 52\text{--}254$ nm), is shown in Fig. 5.3.

The source is separated from the UHV-chamber by a MgF differentially-pumped window (5 mm thickness; van Loenen Instruments, Tobin et al., 1994) at a distance of 23 cm from the surface of the substrate. The resulting photon flux (ϕ_{UV}), which is illuminating this surface, is continuously monitored by a photon flux detector (Fig. 5.4), placed in the middle of the beam. The detector is made of a Au-wire (95 % purity) of 0.125 mm diameter connected to a 10-pins electrical UHV-compatible feed-through, from which the photon-induced electron current was measured by a Keithley 610CR pico-ampere meter. The Au-wire is centred between two stainless steel orifices, which block the UV-beam except for the 5 mm central hole, creating a semi-collimated beam of ~ 0.2 cm² to the surface of the substrate. Both these plates are put at a 250 V potential to prevent photo-electrons induced at the plates to interfere with those induced in the Au-wire. The response of this photon flux detector is linearly proportional to the total ϕ_{UV} irradiating the surface of the substrate (Fig. 5.5). The typical ϕ_{UV} is approximately 10 orders of magnitude higher than the estimated cosmic ray induced UV-field in dense molecular clouds (i.e. $2 \times 10^3\text{--}5 \times 10^4$ photons cm⁻² s⁻¹, Shen et al., 2004). The source is stable within 10 % during an individual experiment of typically 1 hr, as measured by the photo-electron current induced in the Au-wire. However, the flux intensity could vary by up to a factor of 2 between different irradiation sessions.

Gas handling system

Not shown in Fig. 5.1, but built as an integrated part of CRYOPAD, is a gas handling system, specifically designed to mix and store gases that are used to grow the condensed layers of molecules studied. This integrated system reduces the chances of contaminating the gases, which is an advantage over preparing the

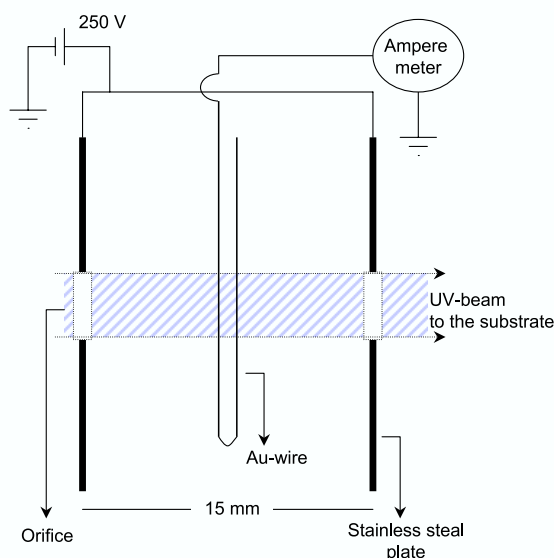


Figure 5.4: Cross sectional side view of the photon flux detector, parallel to the UV-beam. The schematic shows two stainless-steel metal plates put at a +250 V potential, blocking all of the UV-beam except for the fraction allowed to pass by a 5 mm diameter central orifice. In between is a 0.125 mm diameter Au-wire, placed in the middle of the through-coming UV-beam and connected to a pico-ampère meter. Both plates and the Au-wire are mounted to the electronic feed-through shown from the top in Fig. 5.1.

gases in a separated system. The system consists of a central glass-line to which two different lecture bottles containing pressurised gases can be coupled. In addition, the line connects to two separated 1 l glass bulbs that allow for the storage of gases and are connected via a dosing line to two UHV-needle valves that control the dosing rate of the stored gases into the UHV-chamber within an uncertainty of 5%. The two separated dosing lines allow for sequential dosing to prepare layers of distinct molecules, or for *in situ* mixing of various molecules at the surface applying a simultaneous deposition.

This whole gas handling system is pumped to a base pressure of 3×10^{-6} Torr (mini ion-gauge, DeMaCo) by a TV 301 Navigator pump (Varian) and a membrane pump (Leybold). The volume of the central glass-line can be used to prepare mixtures of gases prior to deposition. The gas-pressure applied to a bulb, or that used for mixing, is measured by a DIAVAC DV 100 with an uncertainty of ± 1 Torr in the normal operation range from 1–10 Torr (Leybold).

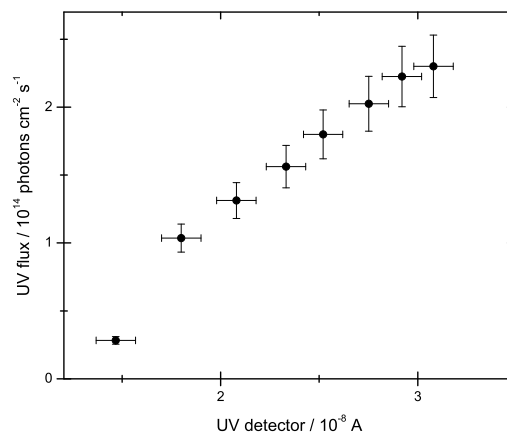


Figure 5.5: The photon flux at the surface of the substrate, determined using the NIST calibrated silicon photo-diode, is shown as a function of the photo-electron current measured by the UV detector.

5.2.2 Analysis techniques

The two key analysis techniques to study UV induced processes of solid state molecules, quadrupole mass spectrometry (QMS) and Fourier Transform reflection absorption infrared spectroscopy (FT-RAIRS), are operating in the plane perpendicular to the surface (Fig. 5.1).

The quadrupole mass spectrometer

The quadrupole mass spectrometer (Prisma200, Pfeiffer) is attached directly opposite to the H_2 -discharge lamp (Fig. 5.1). This instrument continuously analyses the composition of the gas phase mass-selectively, and can therefore be used to obtain information about desorption processes of infrared (IR) active and inactive condensed molecules. Hence, it finds two different applications to study UV-induced reactions in a solid. First, it can detect any photodesorbing reactant or photoproduct, and second, it allows to study the physical interactions between the molecules in the solid by recording their desorption characteristics as a function of temperature using a technique called temperature programmed desorption (TPD, Attard & Barnes, 1998).

The Prisma200 is sensitive to molecules in the mass-to-induced charge (m/z) range from 1–200, and detects them as an induced ion current, $I(t)$, which is proportional to the gas phase concentration. The current system supports a TPD ramp-rate that is linear between 0.1–20 K min^{-1} . $I(t)$ has a noise level of $1.2 \pm 0.2 \times 10^{-14}$ A. Hence the 3σ detection limit for any gas phase molecule is on the order of 3.5×10^{-14} A. This current can be converted to a concentration, i.e. a gas pressure, when the ionisation efficiency (ε_{ion} in A Torr^{-1}) for a specific molecule is known. Here, this value has been determined for CO and CO_2 , $\varepsilon_{\text{ion}}(\text{CO})$ is

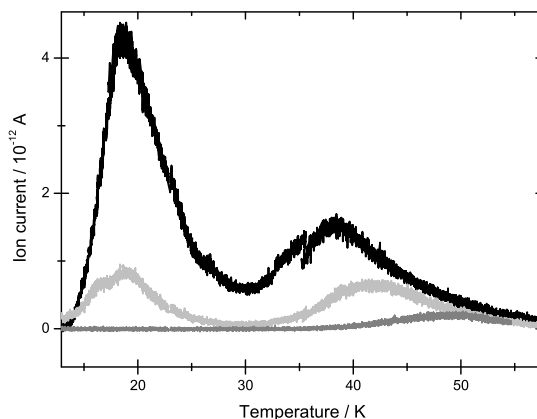


Figure 5.6: TPD spectra of ^{13}CO at sub-monolayer (ML) coverages deposited at 12 K using a dosing pressure of 1×10^{-8} Torr, and recorded at TPD-ramp rate of 0.6 K min^{-1} . The different curves refer to 0.76 ML (black), 0.21 ML (light grey) and 0.03 ML (grey). Coverages are derived from integrating the TPD spectra from 12–60 K in the time domain.

$0.272 \pm 0.003 \text{ A Torr}^{-1}$ and $\varepsilon_{\text{ion}}(\text{CO}_2)$ is $0.1859 \pm 0.004 \text{ A Torr}^{-1}$. Consequently, the total amount of desorbing molecules per unit time, $N_{\text{des}}(t)$, in a typical desorption experiment (either thermal or UV-induced) can be derived from $I(t)$ using the relation

$$N_{\text{des}}(t) = 3.5 \times 10^{19} \frac{I(t) S_{\text{tot}}}{\varepsilon_{\text{ion}}} \quad (\text{molec. s}^{-1}) \quad (5.1)$$

In this equation S_{tot} is the total pump speed and 3.5×10^{19} is derived assuming that $1.7 \times 10^4 \text{ Torr l} \equiv 6 \times 10^{23}$ molecules. Under the assumption that the effective pump speed at room temperature is similar to that for N_2 , such that $S_{\text{tot}} = 1200 \text{ l s}^{-1}$ (see Sect. 5.2.1), this detection limit is $5.4 \times 10^9 \text{ molec. s}^{-1}$. Consequently, in a typical UV-irradiation experiment of a pure solid of 40 ML, it is possible to detect any photoproduct formed in the matrix down to $\sim 10^{-3} \%$ of the reactant (adopting $\varepsilon_{\text{ion}}(\text{CO})$ and assuming a coverage of $1 \times 10^{15} \text{ molec. cm}^{-2}$ per ML, McElhiney & Pritchard, 1976).

The total amount of molecules desorbing over a certain time interval can be derived from integrating $I(t)$ over time, i.e. integrating $N_{\text{des}}(t)$ over time. Similarly, one can derive the total amount of molecules condensed at the surface of the substrate from integrating the full TPD spectrum in the time domain. This amount can then be converted to the approximate number of MLs at the surface.

Fig. 5.6 shows an example of typical TPD spectra of ^{13}CO deposited at sub-monolayer coverage. The total coverage has been derived using the analysis method explained above. The profiles of the spectra show clear indications of a range of different CO binding sites at around 45–50 K and at around 29 K. At the

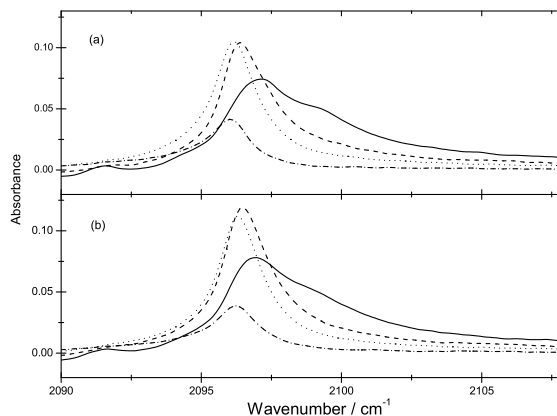


Figure 5.7: FT-RAIRS spectra of the CO-stretching mode of solid ^{13}CO for different coverages equivalent to 80 L (solid), 40 L (dashed), 20 L (dotted) and 5 L (dash-dotted). (a) CO as deposited at 15 K, i.e. before UV-irradiation, and (b) the resulting spectra after 20 min of UV exposure.

lowest coverage, CO exhibits only one desorption peak between 45–50 K, which is clearly distinct from the lower temperature one appearing at the higher coverages. It is therefore proposed that the desorption at around 45–50 K is due to CO adsorbed directly onto the Au-surface. In contrast, the fraction of CO that desorbs around 29 K is related to CO desorbing from a more CO dominated environment. This interpretation is in agreement with the TPD spectra of multi-layer coverages of CO that will be discussed in Sect. 5.3, and previous data presented by Collings et al. (2004) and Öberg et al. (2005).

The FT-RAIRS system

The FT-RAIRS system (Fig. 5.1) has been setup to record the IR absorption characteristics of condensed molecules and is able to monitor spectral changes (or the absence thereof) that are induced during UV-irradiation or thermal warming. The optical path consists of two planar mirrors (Aero Research Associates, ARA), which direct the parallel IR-beam from the source (BioRad, Excalibur FTS 3000) to a 90° off-axis paraboloid (ARA). This paraboloid focuses the beam under a 6° degrees angle to the centre of the surface through a differentially pumped, 5 mm thick ZnSe window (van Loenen Instruments, Tobin et al., 1994). The reflected beam exits the UHV-chamber through a second identical ZnSe window and is focused onto a linearised high sensitivity Mercury-Cadmium-Telluride (MCT) detector (BioRad) by a 90° off-axis Ellipsoid (ARA). The part of the optical path outside the UHV is enclosed by two boxes, one for each side of the reaction chamber, that are continuously purged with dry air.

The maximum IR-signal intensity obtained at the MCT detector at an aperture of 0.5 cm^{-1} after a full system alignment using a HeNe-laser, has an interferogram output that is $\sim 30\%$ of the total beam intensity at the source, which is mainly due to the limited transparency ($\sim 70\%$ each) of the ZnSe windows between $500\text{--}4000\text{ cm}^{-1}$.

Fig. 5.7 presents an example of typical FT-RAIRS spectra of the CO-stretching mode of ^{13}CO , recorded at 0.5 cm^{-1} resolution and adopting a 64 scans average (see Sect. 5.3.1 for the experimental details). Only minimum changes are induced in the band profile due to UV-irradiation, as seen from the similarity of Fig. 5.7a and Fig. 5.7b. In this setting, the noise level is of the order of 0.001. The surface coverages have been derived from their corresponding TPD spectra (see Sect. 5.3.3, Table 5.1) using the analysis method described in Sect. 5.2.2. Given the intensities at the band maximum, i.e. at around 2096 cm^{-1} (Table 5.2) and the derived monolayer coverages, the FT-RAIRS detection limit lies between $0.1\text{--}0.01\text{ ML}$ of CO condensed at the surface (i.e. $10^{13}\text{--}10^{14}\text{ molec. cm}^{-2}$). The further analysis of these spectra can be found in Sect. 5.3.3.

5.3 First Results of CRYOPAD: CO Photodesorption

As a first system that requires the use of all analysis techniques available on CRYOPAD, we have studied the UV-induced desorption of solid CO as a function of the layer thickness and the temperature. This is probably one of the simplest systems to explore the full operation of CRYOPAD since CO is not photodissociated by the UV-photons in the present energy range, it has an IR-active vibrational mode, and it is relatively well studied in other laboratories. Sect. 5.3.1 describes the experimental procedures followed, leading to the results presented in Sects. 5.3.3 and 5.3.4. Sect. 5.3.2 discusses the model that is proposed to explain the characteristics of the observed CO-photodesorption. This model is used in the discussion to assist in the understanding of possible underlying desorption mechanisms in Sect. 5.4.

5.3.1 Experimental procedure

All experiments presented here were conducted under UHV conditions in CRYOPAD, described in detail in Sect. 5.2. $^{13}\text{C}^{16}\text{O}$ (Cambridge Isotope Laboratories 99% purity), $^{12}\text{C}^{18}\text{O}$ (ICON Isotopes 98% purity) and $^{13}\text{C}^{16}\text{O}_2$ (Cambridge Isotope Laboratories 99% purity) were condensed via effusive dosing normal to the surface at a typical pressure of $1 \times 10^{-8}\text{ Torr}$, equivalent to a dosing rate of $0.01\text{ Langmuir s}^{-1}$ (L s^{-1}). In the case of CO, solid layers were grown at 15 K , whereas CO_2 was deposited at 11 K . In addition to the true deposition to form the solid layers, a similar deposition at room temperature was recorded by the QMS. This allowed to compare the amount of molecules admitted to the UHV, and that obtained from the corresponding TPD of the layer condensed at 11 or 15 K . These two measurements agreed within 30% .

Those solids that were to be irradiated at 15 K were left for 55 min before irradiation was started, to allow for the pressure of the system to return to the base

pressure. At 30 min after deposition, those solids that were to be irradiated at 19 and 24 K, respectively, were heated to their respective temperatures with a rate of 10 K min^{-1} and irradiated after another 25 min. The one exception is an experiment in which the effect of thermal annealing on the UV-induced desorption was tested. There, solid CO was grown at 15 K, warmed to 40 K and left at that temperature for 3 h in total. Then the solid was cooled back down to 15 K and after an additional 55 min exposed to 60 min of UV-irradiation. Typical exposure times ranged from 20 to 60 min. During irradiation, the photon flux was continuously monitored by the photon flux detector (Sect. 6.4.1). The TPD measurement of an irradiated solid was started one hour after finishing irradiation. In the absence of irradiation, the TPD was started 75 min after deposition. TPD spectra were recorded at a linear ramp rate of 1.0 K min^{-1} for CO, and 0.6 K min^{-1} for $^{13}\text{CO}_2$, starting all at 10 K.

FT-RAIRS spectra (64 scans, 0.5 cm^{-1} resolution, zero-filling factor of 4, sensitivity of 1) were recorded isothermally between $400\text{--}4000\text{ cm}^{-1}$ before and after deposition, and every 3 min during irradiation. The typical acquisition time per spectrum took about 2.5 min. All FT-RAIRS spectra are background subtracted, applying a linear baseline fit using the spectral regions between $1200\text{--}1300\text{ cm}^{-1}$ and $2500\text{--}3000\text{ cm}^{-1}$. Spectral changes induced by thermal warming were irreversible upon subsequent cooling.

The quadrupole mass spectrometer scanned mass selectively for m/z ratios of 14, 17, 18, 28, 29, 30, 32, 44, 45, 46 and 48 during deposition, irradiation and the final thermal desorption (TPD). The typical time for such a m/z cycle was about 2.5 s. All these measurements are background corrected. In case of the UV-induced desorption, the noise on the signal was reduced using a three-point adjacent averaging. The photon flux measured by the photon flux detector was stable within 10% during an individual experiment, but was seen to vary by a factor of 2 (at most) between different irradiation experiments. Therefore, to compare the different photodesorption rates obtained from these experiments, it was assumed that to a first approximation the photodesorption rate $I(t)$ is linearly dependent on the incident photon flux. Hence, all photodesorption measurements were scaled to a similar flux corresponding to a current of $1.4 \times 10^{-7}\text{ A}$ measured by the photon flux detector. The resulting photodesorption curves, shown in Figs. 5.9, 5.12 and 5.13, contain only 10–20% of all measured points. However, the model-fit to the data (see Sect. 5.3.2) was applied on all data points, and was conducted prior to any averaging of the data. The results obtained by the FT-RAIRS and the QMS were fully reproducible within reported uncertainties.

5.3.2 Model for UV-induced CO desorption

The most simple scenario for CO to desorb from the solid into the gas phase, $[\text{CO}_g]$, due to the interaction with a UV-photon, is that of direct ejection from the solid, $[\text{CO}_s]$, shown schematically in Fig. 5.8. In this scenario, the rate of desorption is proportional to the UV flux (ϕ_{uv}), to the amount of molecules at the surface and to the amount in the bulk of the solid (Lange, 1965). In those cases for which $[\text{CO}_g] \ll [\text{CO}_s]$, this scenario implies a constant photodesorption, independent of

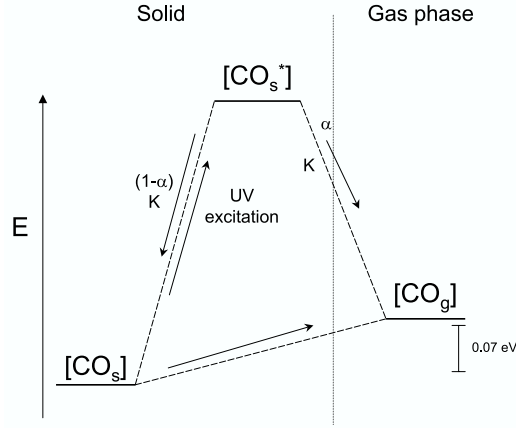


Figure 5.8: Two strongly simplified models for the photodesorption of CO, showing the scenario for photon-induced CO-desorption of solid CO, $[CO_s]$, directly into the gas phase, $[CO_g]$, and that involving an intermediate excited state, $[CO_s^*]$ (see text for details). The energy axis is non-linear and the difference in energy between CO_s and CO_s^* , and CO_s^* and CO_g is not on scale.

the irradiation time. As will be shown in Sects. 5.3.3 and 5.3.4, under the present experimental conditions in CRYOPAD, the UV-induced CO desorption is clearly a function of the irradiation time.

Under the assumption that $[CO_g] \ll [CO_s]$, these experimental data can be reproduced by a somewhat more involved model, introducing an intermediate excited state, $[CO_s^*]$. This is shown in Fig. 5.8 as the indirect mechanism. As the excitation mechanism is not known, the energy of $[CO_s^*]$ is uncertain, but could correspond to the solid-state equivalent of the $A-X$ transition in gas-phase CO ($\lambda_{UV} = 130-150$ nm, Eidelsberg et al., 1992) and is assumed to lie above the energy state in the gas phase. In that case, no extra energy is needed for an excited CO molecule to desorb. The rate equation system associated with this situation results in

$$\frac{d[CO_g]}{dt} = \alpha \varepsilon_{UV} \phi_{UV} [CO_s] (1 - \exp^{-Kt}) \quad (5.2)$$

The photodesorption rate is now given as a product of the photon flux, the excitation efficiency (ε_{UV}), and α , the efficiency to desorb into the gas phase from the excited state $[CO_s^*]$. Consequently, K is the rate at which the excited state relaxes. However, the measured desorption rate by the quadrupole mass spectrometer depends also on the pump speed, S_{tot} of CO_g and therefore the correct expression

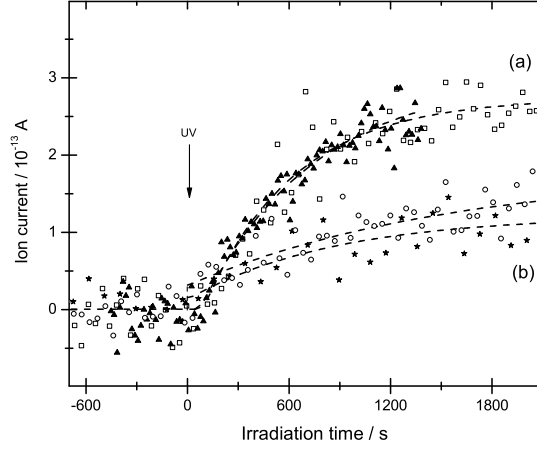


Figure 5.9: The ion current of gas phase ^{13}CO desorbing from solid ^{13}CO detected by the QMS prior to and during UV-irradiation as a function of the irradiation time for different coverages equivalent to 5 L (\star), 20 L (\circ), 40 L (filled \triangle) and 80 L (\diamond) at 15 K. Irradiation is started at $t=0$, as indicated by the arrow. The dashed lines show the fit by the model (see text for details). **(a)** and **(b)** indicate the two regimes observed for the photodesorption rate.

of the desorption rate as measured is

$$\frac{d[\text{CO}_g]}{dt}(\text{det}) = \alpha \varepsilon_{\text{UV}} \phi_{\text{UV}} [\text{CO}_s] (1 - \exp^{-Kt}) - [\text{CO}_g] S_{\text{tot}} \quad (5.3)$$

The fit of the experimental data in Sects. 5.3.3 and 5.3.4 is based on this relation, using the more simplified form

$$I(t) = I_1(1 - \exp^{-t/\tau}) + C \quad (5.4)$$

,which does not take the pump speed into account. Here, $I(t)$ is the photon-dose dependent ion current of CO as measured by the quadrupole mass spectrometer, I_1 is proportional to $\alpha \varepsilon_{\text{UV}} \phi_{\text{UV}} [\text{CO}_s]$, and C allows for a possible offset at $t=0$ due to direct photodesorption. Currently ongoing data analysis is investigating the effect of including the pump speed to the model of the photodesorption on the photodesorption rate.

5.3.3 Coverage dependence

The photodesorption of ^{13}CO from the pure solid at various coverages as a function of the irradiation time, is shown in Fig. 5.9. Starting at the onset of irradiation at $t=0$, none of the CO desorption curves show any evidence for instantaneous direct photodesorption (for which one would expect a step function). Consequently, the detected ion current by the quadrupole mass spectrometer at $t=0$

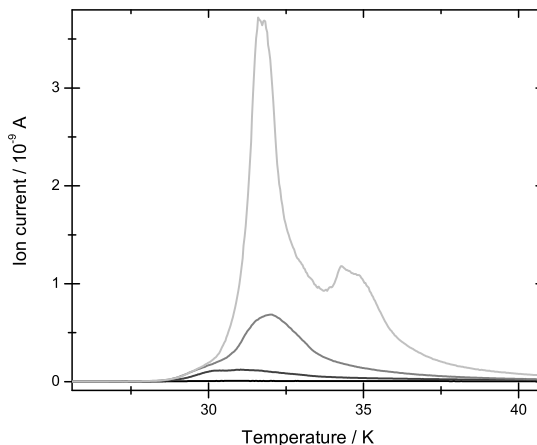


Figure 5.10: TPD spectra of ^{13}CO after the UV-irradiation at 15 K shown in Fig. 5.9 for the different exposures equivalent to 5 L (black), 20 L (dark grey), 40 L (grey) and 80 L (light grey) recorded at ramp rate of 1 K min^{-1} . The total UV-exposure was 20 min in the case of the 40 L matrix, and 40 min at all other coverages.

(i.e. the detection limit) is $\leq 3.5 \times 10^{-14}\text{ A}$ (see Sect. 5.2.2), or a photodesorption rate $N_{\text{des}}(t=0) \leq 5.4 \times 10^9\text{ molec. s}^{-1}$ applying Eq. 5.1. Given that $\phi_{\text{UV}} = 1.4 \times 10^{15}\text{ photons cm}^{-2}\text{ s}^{-1}$ and the irradiated surface area, $a_{\text{irr}} = 0.2\text{ cm}^2$, this corresponds to a maximum direct yield (Y_0) of $1.9 \times 10^{-5}\text{ molec. photon}^{-1}$.

In contrast to any direct desorption, the induced ion current of ^{13}CO , $I(t)$, increases gradually as a function of the irradiation time, until between 20–30 min $I(t)$ starts to reach a steady-state value. This maximum current ($I_{\text{max}}(t)$) and the corresponding maximum desorption yield (Y_{max}), are listed in Table 5.1. This behaviour is similar at each coverage studied and implies that the CO-desorption rate, $N_{\text{des}}(t)$ (derived from $I(t)$, Sect. 5.2.2), strongly depends on the UV-exposure time. In fact, all desorption curves can be fit to the model described in Sect. 5.3.2, where it is proposed that the desorption of solid CO to the gas phase proceeds via an excited intermediate state, $[\text{CO}_s^*]$. The fits of the data to this model are shown by the black dashed line overlying each of the desorption curves in Fig. 5.9; the fit parameters are summarised in Table 5.1. These will be discussed further in Sect. 5.4 when the different possible excitation mechanisms underlying the CO-desorption are considered.

It is evident from Fig. 5.9 (and Table 5.1) that the photodesorption rate is not only a function of the UV-exposure time, but that Y_{max} also depends strongly on the amount of CO at the substrate. Clearly, Y_{max} shows a jump when the CO deposit increases from 20 to 40 L, but is similar for 40 and 80 L (Fig. 5.9a), and for 5 and 20 L matrices (Fig. 5.9b). If the photodesorption is bulk dependent one would expect an increase with growing ice thickness. In contrast, if the process is domi-

nated by the photodesorption of surface CO molecules, it is reasonable to assume that only the total surface coverage influences the rate observed. Since $I_{40L}(t)$ and $I_{80L}(t)$ are similar, but twice the values of $I_{5L}(t)$ and $I_{20L}(t)$, CO-desorption is unlikely to be only bulk-dependent. However, if the desorption is only surface dependent, this would imply that the surface coverage in Fig. 5.9a is twice that in Fig. 5.9b.

Fig. 5.10 shows the TPD spectra for ^{13}CO at the various ^{13}CO exposures studied, recorded after UV-irradiation. Although it is difficult to deduce if the 5, 20 and 40 L CO matrices exhibit different desorption characteristics, the 80 L CO matrix clearly does, indicating to the presence of different CO-environments at increasing amounts of CO at the substrate. The total amount of molecules in ML, residing at the surface after irradiation, has been derived from the $I(t)$ of the spectrum integrated in the time domain (see Sect. 5.2.2) and listed in Table 5.1. Since $\int_{\text{irr}} I(t)dt$ is always $\ll 1\%$ of $\int_{\text{TPD}} I(t)dt$, one may safely assume that the amount of molecules at the surface after irradiation, is approximately similar to the initial amount deposited, although this does require further investigation (see Sects. 5.3.4 and 5.4.4). Hence, it can be concluded that at 5 L, CO is still in the monolayer to sub-monolayer regime, whereas at 40 and 80 L respectively, the CO matrix is about 20 and 80 ML thick. It may therefore be possible that the 5 and 20 L matrices exhibit a non fully covered surface in contrast to the 40 and 80 L experiments.

In addition to the TPD data, also the FT-RAIRS spectra of the ^{13}CO -stretching mode recorded prior to irradiation (Fig. 5.7a and Table 5.2), show evidence that, in going from 5 to 80 L solids, the environment of CO in the matrix changes, an effect that has been observed for solid CO on NaCl(100) grown at increasing multilayer coverages (Heidberg et al., 1993). At 5 and 20 L, the absorbance at 2096 cm^{-1} increases with the increasing amount of CO at the surface, but the profiles remain very similar. However, at higher coverages, this trend changes: the band broadens, the peak-position shifts to larger wavenumber, and the integrated absorbance increases less than the ML coverage would suggest. In fact, the spectra of CO at 20 and 40 L are unexpectedly similar. The general trend of a peak-shift to larger wavenumber is consistent with the TPD spectra of CO presented in Fig. 5.6, showing a much stronger interaction between CO and the Au-surface than between two neighbouring CO molecules. As the small but significant peak-shift becomes most pronounced beyond 20 L, this suggests that probably only beyond a 20 L coverage, CO is losing contact with the underlying Au and starts to behave more and more like in a pure CO environment.

The effect of irradiation on the FT-RAIRS spectra of the CO matrix is shown in Fig. 5.7b and Table 5.2. Overall, UV-irradiation induces an increase in the integrated absorbance of the CO-stretching band and a narrowing of its FWHM, except for the lowest coverage of 5 L. There, UV-irradiation seems to have the inverse effect. In general, any band narrowing and intensity increase is indicative of the formation of a more ordered matrix structure and hints that the energy input of the photons may induce some increasing degree of crystallinity for those matrices that are thicker than 1 ML. In the case of the 5 L matrix, irradiation of CO may result in a changing orientation with respect to the Au-surface. This could explain both the increased FWHM as well as the small decrease in the integrated

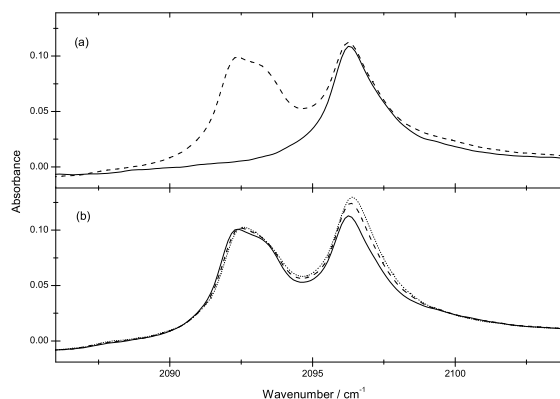


Figure 5.11: The FT-RAIRS spectra of the CO-stretching mode region of a bi-layered system of 40 L of ^{13}CO underneath 40 L of C^{18}O at 15 K. **(a)** The spectra of solid ^{13}CO only (solid), and that of 40 L of C^{18}O deposited on top (dashed). **(b)** The spectra of the bi-layered system shown after 0 (solid), 30 (dashed) and 60 (dotted) min of UV-exposure.

band area, if a fraction of the CO is induced to a more side-on orientation with respect to the surface (Attard & Barnes, 1998; McElhiney & Pritchard, 1976).

A bi-layered ice of CO-isotopes

More insight in the process of desorption and the effect of UV-photons on the CO matrix was obtained by studying the irradiation of a bi-layered system of C^{18}O on top of ^{13}CO . Fig. 5.11a shows the spectra of the CO-stretching mode region at 15 K for the first 40 L of ^{13}CO (solid line) and for the bi-layered system after subsequently adding 40 L of C^{18}O on top (dashed line). The spectral characteristics are summarised in Table 5.2. The band profile of C^{18}O is obtained after subtraction of the ^{13}CO spectrum from the spectrum of the bi-layered system. It is interesting to note that this profile is significantly broader and less intense than that of the underlying ^{13}CO . This is consistent with the spectral changes observed for increasing coverages at 40 and 80 L of pure ^{13}CO , and supports the idea of a changing CO matrix structure.

Fig. 5.12 shows the photodesorption of CO from this bi-layered system. Clearly, C^{18}O exhibits a higher desorption rate than ^{13}CO (also listed in Table 5.1). This is a strong indication that indeed the observed CO-desorption predominantly originates from the upper most layers. However, the contribution of ^{13}CO to the desorption is significant and accounts for about 24% of the total. This suggests that although surface desorption dominates, a fraction of CO may diffuse prior to desorption, or that alternatively, the CO matrix may contain substantial cracks and pores via which the underlayer of ^{13}CO is in direct contact with the solid-to-

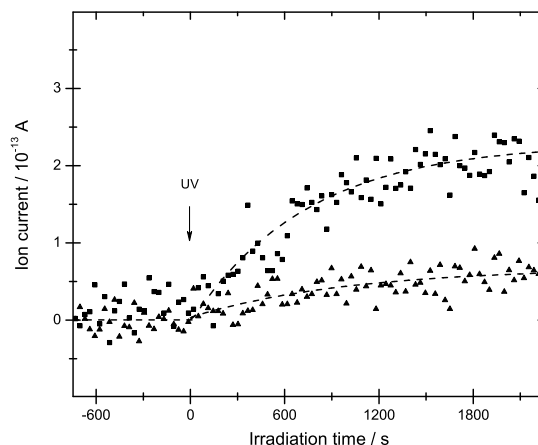


Figure 5.12: The ion current of gas phase $C^{18}O$ (filled \diamond) and ^{13}CO (filled \triangle) desorbing from a bi-layered system of 40 L of ^{13}CO underneath 40 L of $C^{18}O$ detected by the QMS prior to and during UV-irradiation as a function of the irradiation time at 15 K. Irradiation is started at $t=0$, indicated by the arrow. The dashed lines show the fit by the model (see text for details).

vacuum interface. The desorption behaviour of both CO isotopes in the layered structure is very similar to that observed in case of a mono-isotopic layer (compare Fig. 5.12 to Fig. 5.9) and has been fit similarly by the photodesorption model proposed in Sect. 5.3.2, shown in Fig. 5.12 by the dashed lines.

In contrast to the photodesorption data of the bi-layer, which seem to indicate that the top layers of $C^{18}O$ are those most affected by the UV, the FT-RAIRS spectra of this irradiated system show a somewhat different picture. Fig. 5.11b shows the spectra after 0, 30 and 60 min of UV-exposure. It is clearly seen that UV-irradiation induces the most pronounced changes in the band profile of ^{13}CO , i.e. the layer in closest contact with the underlying Au-surface. Both the integrated absorbance and the FWHM of the ^{13}CO band increase significantly with respect to the non-irradiated profile (Table 5.2), whereas almost no change is observed in the spectra of $C^{18}O$.

5.3.4 Temperature dependence

The results presented in Sect. 5.3.3 show that CO desorption is an activated process which may involve translational excitation of the molecule, so it can be expected that this is strongly dependent on the temperature of the CO matrix. Hence, in addition to the coverage dependence, the desorption of CO has been studied as a function of temperature for 40 L thick matrices at 15, 19 and 24 K.

Fig. 5.13 shows the UV-induced desorption of ^{13}CO at these various temperatures as a function of the irradiation time. Indeed, the maximum photodesorption of CO increases significantly when the temperature is raised from 15 to 24 K (see

Table 5.1: Induced CO desorption at 15K

Coverage ^a L	$I(t)_{max}$ ^b 10^{-13} A	Yield ^c 10^{-4} molec. photon ⁻¹	$\int_{irr} I(t) dt$ ^d 10^{-10} C	$\int_{TPD} I(t) dt$ ^e 10^{-7} C	ML ^f	C ^g 10^{-14} A	I_1 ^g 10^{-13} A	τ ^{g,h} s
80	2.6±0.2	1.44	1.86	5.52	78	2.1±0.5	2.74±0.03	538±20
40	2.4±0.2	1.34	1.83	1.52	20	3.2±0.5	3.01±0.06	677±29
20	1.2±0.2	0.66	0.69	0.48	6.6	1.3±0.4	1.22±0.05	860±99
5	1.4±0.2	0.78	0.89	0.06	0.9	3.1±1.0	1.78±0.12	1526±228
C ¹⁸ O on top of ¹³ CO								
40 C ¹⁸ O	1.9±0.2	1.06	1.36	1.91	24	0.3±0.3	2.29±0.03	737±30
40 ¹³ CO	0.6±0.2	0.34	0.44	1.83	23	0.3±0.3	0.68±0.30	1014±127

^a 1 L $\equiv 10^{15}$ molec. cm⁻² of ¹³CO, unless otherwise stated. ^b Ion current at 20 min of irradiation. ^c Yield = $N_{des}(t)/\phi_{UV} \times a_{irr}$, with $a_{irr} = 0.2$ cm² and $\phi_{UV} = 1.4 \times 10^{15}$ photons cm⁻² s⁻¹. ^d Integrated ion current from 0–20 min of irradiation in Coulomb. ^e Integrated ion current of the TPD curve of the irradiated solid CO between 15 and 60 K. ^f Derived from $\int_{TPD} I(t) dt$ using Eq. 5.1 for a total surface area $a = 1.25$ cm². ^g As derived from Eq. 5.4. ^h $\tau = 1/K_{relax}$

Table 5.2: The FT-RAIRS characteristics of the solid CO-stretching mode

Cov. ^b	T L K	Non-irradiated				Irradiated ^a			
		Peak centre cm ⁻¹	FWHM cm ⁻¹	Abs.	∫ Abs. ^c cm ⁻¹	Peak centre cm ⁻¹	FWHM cm ⁻¹	Abs.	∫ Abs. ^c cm ⁻¹
80	15	2097.18±0.05	4.65±0.05	0.075±0.001	0.438	2096.91±0.05	4.58±0.05	0.078±0.001	0.449
40	15	2096.36±0.02	2.25±0.03	0.104±0.001	0.391	2096.48±0.02	2.14±0.02	0.119±0.001	0.433
20	15	2096.21±0.01	2.14±0.03	0.108±0.001	0.358	2096.31±0.02	2.01±0.02	0.110±0.001	0.367
5	15	2096.02±0.01	1.98±0.04	0.041±0.001	0.141	2096.25±0.04	2.13±0.04	0.038±0.001	0.139
40	19	2096.35±0.05	2.44±0.03	0.092±0.001	0.325	2096.43±0.05	2.33±0.06	0.102±0.001	0.348
40	24	2096.42±0.05	2.91±0.08	0.071±0.001	0.272	2096.38±0.03	2.46±0.07	0.091±0.001	0.314
40 ML of C ¹⁸ O on top of 40 ML of ¹³ CO									
C ¹⁸ O	15	2092.36±0.03	2.44±0.03	0.094±0.001	0.294	2092.55±0.03	2.45±0.03	0.096±0.001	0.294
¹³ CO	15	2096.25±0.05	1.95±0.03	0.108±0.001	0.384	2096.41±0.05	2.15±0.03	0.127±0.001	0.423

^a Band profile characteristics after 20 min of irradiation, except for the isotopically layered experiment where the band profiles were analysed after 60 min of irradiation. ^b ¹³CO, unless otherwise stated. ^c The integrated absorbance between 2090–2105 cm⁻¹ for ¹³CO, and between 2085–2100 cm⁻¹ for C¹⁸O.

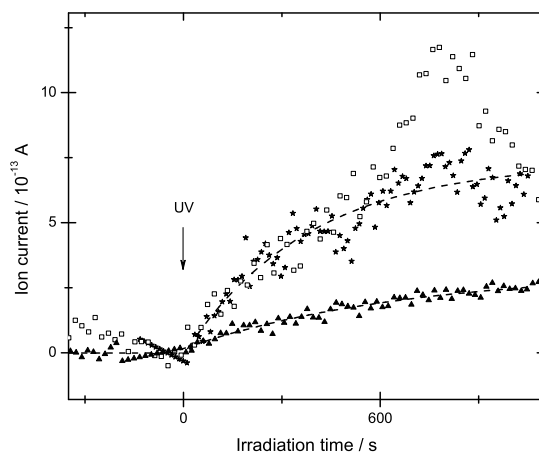


Figure 5.13: The ion current of gas phase ^{13}CO desorbing from solid ^{13}CO detected by the QMS prior to, and during UV-irradiation of 40 L matrices at 15 K (filled \triangle), 19 K ($*$) and 24 K (\diamond) as a function of the irradiation time. Irradiation started at $t=0$. The dashed lines show the fit by the model (see text for details).

Table 5.3). Again, none of the desorption curves show any evidence for direct photodesorption at the onset of irradiation at $t=0$. Instead, the desorption rate increases gradually, as observed for CO from the various coverages at 15 K. The fit to the 15 and 19 K desorption curves by the model proposed to describe this desorption in Sect. 5.3.2 is shown by the black dashed lines. However, in contrast to these two systems, at 24 K the desorption does not reach a steady-state but the rate shoots up after 10 min of UV-exposure and then suddenly drops again after a total of 13 min of irradiation. This behaviour was fully reproducible and special care was taken to make sure that the photon flux remained constant. $I_{\text{max}}(t)$ for the various temperatures is listed in Table 5.3 and is determined at ~ 13 min (760 s) of irradiation for 19 and 24 K.

Additional experiments (not shown here) suggest that this sudden drop of the desorption rate at 24 K is related to thermally induced structural changes in the CO ice, which depend on the time of annealing. This was tested by growing a 40 L ^{13}CO matrix at 15 K, which was warmed to 24 K and left to anneal for a total of 3 hours. Then, the matrix was cooled down again to 15 K and irradiated at that temperature. Interestingly, under these conditions no evidence was found for any induced desorption. Hence, it is likely that at 24 K thermally induced changes in the CO matrix will eventually inhibit CO desorption. Whether or not the actual process of UV-irradiation adds any significant contribution to this inhibition could not be resolved from the current data. However, within a total of 60 min of irradiation at either 15 or 19 K, no such effect was observed.

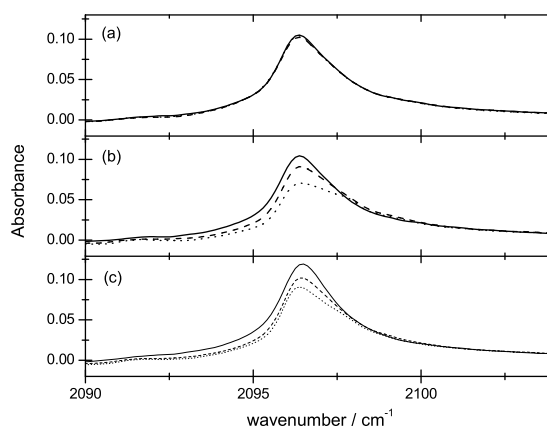


Figure 5.14: FT-RAIRS spectra of the CO-stretching mode of ^{13}CO of the three 40 L matrices irradiated in Fig. 5.13. (a) The spectra as deposited at 15 K, (b) the spectra after changing the temperature to 15 K (solid), 19 K (dashed) and 24 K (dotted) respectively, before the start of UV-irradiation, and (c) the resulting spectra after 20 min of UV-irradiation at the different temperatures.

Evidence for thermally induced matrix rearrangements is found in the FT-RAIRS spectra shown in Fig. 5.14 (and Table 5.2). Fig. 5.14a shows the ^{13}CO -stretching band of the three 40 L matrices directly after their deposition at 15 K. Note that all spectra are fully overlapping. Fig. 5.14b shows these same spectra but now after the temperature remained constant at 15 K (for one), and was raised to 19 and 24 K (for the two others), respectively. The band profile of the matrix at 24 K changes most significantly. However, the essentially similar TPD integrals of the three CO matrices after irradiation (Fig. 5.15 and Table 5.3) provide a clear indication that the spectral changes observed in the FT-RAIRS spectra in Fig. 5.14b are due to changes in the matrix structure. This temperature effect is less pronounced at 19 K and not observed at 15 K, implying that the reorganisation rate is temperature dependent. In contrast to thermal warming, UV-irradiation (Fig. 5.14c) induces a narrowing of the FWHM and an increase in integrated absorbance of the band. Apparently, UV-irradiation and thermal warming have a different effect on the profile of the ^{13}CO -stretching mode and consequently influence the matrix structure differently.

The TPD spectra in Fig. 5.15, provide some more insight into the structural rearrangements induced by the UV-photons. At all temperatures the profiles of the TPD spectra are similar. However, compared to a 15 K non-irradiated CO matrix, the profiles are very different. All the maxima of the TPD spectra of the irradiated matrices are shifted to higher temperatures (~ 32 K) with respect to the non-irradiated one (~ 31 K), which can be interpreted as being due to the formation of a more strongly bound CO ice structure, suggesting that the degree of

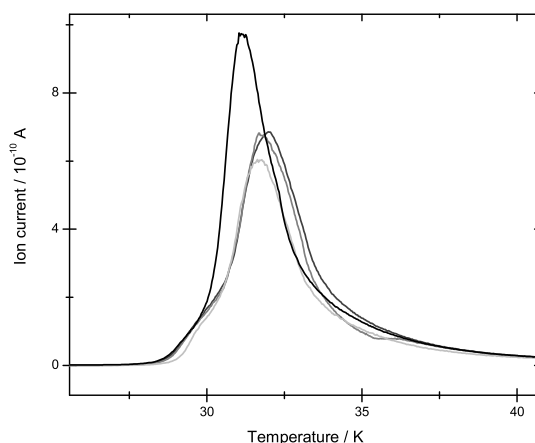


Figure 5.15: TPD spectra of a non-irradiated 40 L ^{13}CO matrix (black) deposited at 15 K, and those after UV-irradiation at 15 K (dark grey), 19 K (grey) and 24 K (light grey) at a TPD-ramp rate of 1 K min^{-1} . Each matrix has been irradiated for 20 min in total.

crystallisation of the CO matrix increases due to irradiation. This is supported by the observation of a shoulder at approximately 30 K on the leading edge of the desorption curves for all irradiated profiles. One interpretation of such a profile is that of an amorphous ice matrix crystallising during the temperature ramp of the TPD. This interpretation is in line with the UV induced band narrowing in the FT-RAIRS spectra in Fig. 5.14c, and with those in Figs. 5.7b and 5.11b.

A remarkable difference between the non-irradiated TPD spectrum and those of the different irradiated ices, is also the total integrated ionisation current under the spectrum, which is 10–30% less in case of irradiation (Table 5.3). This would suggest that in fact 10–30% of all CO is photodesorbed after 20 min of irradiation, which is much larger than is inferred from the integrated $I(t)$ over the time of irradiation (Table 5.3) and than is expected from the FT-RAIRS spectra (Table 5.2). If the discrepancy between $\int_{\text{TPD}} I(t) dt$ and $\int_{\text{irr}} I(t) dt$ is induced by a difference in pump speed due to a stronger cryo-pump present during irradiation, this may account for a maximum difference of a factor of 4.8 (see Sect. 5.2.1). Consequently, this observed effect should be further investigated.

5.4 Discussion

The results presented in Sects. 5.3.3 and 5.3.4 on the photodesorption of solid CO have shown clear evidence that these processes depend on the temperature of the adsorbate, its surface coverage and the total photon-dose. Here, we will discuss

Table 5.3: Induced CO desorption at various temperatures

T^a K	$I(t)_{max}^b$ 10^{-13} A	Yield ^c 10^{-4} molec. photon ⁻¹	$\int_{irr} I(t) dt^d$ 10^{-10} C	$\int_{TPD} I(t) dt^e$ 10^{-7} C	ML ^f	C^g 10^{-14} A	I_1^g 10^{-13} A	$\tau^{g,h}$ s
15	2.4±0.2	1.34	1.1	1.52	20	3.2±0.5	3.01±0.06	677±29
19	6.1±0.2	3.39	3.3	1.40	17	1.1±1.1	7.33±0.12	378±18
24	11.1±0.2	6.17	4.0	1.22	15	-	-	-
15				1.71 ⁱ	22			

^a Coverage of 40 L $\equiv 40 \times 10^{15}$ molec. cm^{-2} of ^{13}CO , condensed at 15 K and irradiated at the indicated temperatures. ^b Maximum ion current (at 13 min of irradiation for 24 K). ^c Yield = $N(t)/\phi_{UV} \times a_{irr}$, with $a_{irr} = 0.2 \text{ cm}^2$ and $\phi_{UV} = 1.4 \times 10^{15} \text{ photons cm}^{-2} \text{ s}^{-1}$. ^d Integrated ion current from 0–13 min of irradiation in Coulomb. ^e Integrated ion current of the TPD curve of the irradiated solid CO between 15 and 60 K. ^f Derived from $\int_{TPD} I(t) dt$ using Eq. 5.1 for a total surface area $a = 1.25 \text{ cm}^2$. ^g As derived from Eq. 5.4. ^h $\tau = 1/K_{relax}$. ⁱ Integrated TPD of non-irradiated solid CO.

these results in terms of possible desorption mechanisms underlying the experimental observations, and show that although further work is needed to fully resolve these mechanisms, the present data can already put some constraints on the different possible scenarios.

The present data contain no evidence for any direct photodesorption at the onset of irradiation beyond the detection limit of the quadrupole mass spectrometer (equivalent to $Y_0(\text{CO}) \leq 1.9 \times 10^{-5}$ molec. photon⁻¹). This result does not depend on the matrix temperature, nor on the surface coverage of CO, and suggests that UV-photons do not eject solid CO into the gas phase via a direct mechanism as proposed in Fig. 5.8. In contrast, evidence for an indirect desorption mechanism is observed from the data. Independent of temperature or surface coverage, the rate of photodesorption is seen to gradually increase as a function of the UV-exposure time, indicative of a dose dependent process (Figs. 5.9, 5.12 and 5.13). From the comparison of these data, it is clear that photodesorption is affected by the coverage showing two distinct regimes (Figs. 5.9a and 5.9b), and that the rate of desorption is strongly sensitive to the matrix temperature (Fig. 5.13).

5.4.1 Photodesorption model

In order to describe the observed desorption behaviour in Figs. 5.9, 5.12 and 5.13, a model was constructed in which a CO molecule gets ejected from the solid into the gas phase via an intermediate excited state, $[\text{CO}_s^*]$ (see Sect. 5.3.2 and Fig. 5.8). All the data were fit according to this model, shown by the dashed lines in Figs. 5.9, 5.12 and 5.13. The numerical results have been presented in Tables 5.1 and 5.3.

Although the model seems to nicely reproduce the data, the nature of the proposed intermediate $[\text{CO}_s^*]$ is unclear. One possibility might be the solid-state equivalent of the $A-X$ transition in gas-phase CO, which has a gas-phase cross section of $\sim 10^{-15}$ – 10^{-16} cm² nm between 130–150 nm (Eidelsberg et al., 1992). However, most interesting information about CO_s^* is derived from the relaxation constant K , or $1/\tau$, of the irradiated system determined by the fit. The value of this constant is generally of the order of 10^{-3} s⁻¹, implying a typical lifetime of an excited state of 500–1000s. This is unusually long for an excited state in a solid, which is typically orders of magnitude smaller (Corcelli & Tully, 2002; Dubost & Legay, 1989, and references therein). Its nature is therefore not directly apparent, although an obvious explanation could be the presence of an activation barrier, situated between CO_s^* and CO_s , and between CO_s^* and CO_g . Possible barrier heights are hard to predict from the present results not knowing the excitation mechanism, although it should be possible to study them in more detail from the decay of CO_s^* after switching off the UV-source.

5.4.2 Photodesorption mechanisms

Key insight into the underlying mechanism for desorption is derived from the data obtained by studying the CO-desorption from a bi-layered system of two different isotopes: C¹⁸O deposited on top of ¹³CO (Sect. 5.3.3). The photodesorption characteristics (Fig. 5.12) show that the dominant fraction (about 76 %) of all

solid CO desorbs from the upper most layers of the matrix, i.e from the C¹⁸O-deposit. However, the FT-RAIRS spectra of this system provide strong evidence that the supporting Au-surface plays a substantial role in the photodesorption process. UV-irradiation induces the attenuation of the integrated absorbance of the ¹³CO-stretching mode, indicative of a reorganisation of the CO-matrix. If this would involve the whole matrix, one would expect the intensity increase during irradiation and the matrix thickness to be proportional, which is not what is observed for solid ¹³CO at various coverages (Table 5.2).

Consequently, this suggests that we probe changes in the CO environment in close contact with the Au-surface. Those molecules adsorbed in a perpendicular orientation at the Au-surface will give rise to an absorption signal which is significantly stronger than that of molecules adsorbed parallel or situated several MLs away from the surface due to the creation of a mirror image of their oscillating dipole in the Au (Attard & Barnes, 1998). Hence, the observed spectral effects may be explained from differences arising in the orientation of CO at the CO-Au interface, which could change as a function of coverage as is observed for CO on NaCl (e.g. Heidberg et al., 1992, 1993). Given the fact that the present Au-surface is strongly irregular and that CO exhibits island growth (Bisschop et al. in prep.), it is possible that at 5 L, the surface is not fully covered. As such, UV-irradiation may induce some perpendicularly oriented CO to tilt with respect to the surface, giving rise to a decreasing integrated absorption, whereas at 20 L, when a larger fraction of the surface is covered, this effect may be different. One can imagine that the directing effect of the Au-surface on the orientation of CO in the matrix decreases over several monolayers, suggesting that the matrix structure changes with increasing distance to the Au. Such an effect is for example observed for CO on NaCl, showing indications of cluster growth and a changing structure of the first mono-layer due to multi-layer deposition (Heidberg et al., 1993). It seems that UV-irradiation can induce longer range ordering in the case of a 40 L matrix as the integrated absorbance increases and the FWHM becomes more narrow (Table 5.2). However, these effects are much less pronounced at 80 L, which might be caused by the increased amount of CO environments that are clearly present from the spectra (Fig. 5.7).

This surface selection may arise due to the photoelectric effect of Au. As the work-function of Au (4.8–5.6 eV, McElhiney & Pritchard, 1976; Potter & Blakeley, 1975) is typically much smaller than the average energy of the UV-photons from the H₂-discharge lamp (8–7 eV), it is likely that an electron-hole pair gets created in the Au-surface. This electron-hole pair then mediates in the excitation and re-orientation of solid CO via a photo-electron induced mechanism. Assuming such a scenario, one can imagine that, given the present relaxation times, more and more excited states are produced in the solid as the photon-dose increases. Consequently, these states will start to interact more strongly at increasing concentrations and repel each other, which logically gives rise to a higher desorption rate. This process will continue until the excitation of CO_s equals the relaxation of [CO_s*].

An electron induced mechanism involving the Au-surface is consistent with the different photodesorption rates observed as a function of coverage (Table 5.1).

We propose that the reduced desorption observed for the 5 and 20 L deposits, is due to the electronic coupling of CO to the underlying Au-surface (McElhiney & Pritchard, 1976), which may lower the barrier for relaxation of $[\text{CO}_s^*]$ back to the ground-state. The TPD spectra of CO in Fig. 5.6, showing that CO is more strongly bound to Au than to an adjacent CO molecule. It nevertheless requires for such an electronic coupling to be efficient over a distance of several monolayers.

The similar FT-RAIRS spectra of the 5 and 20 L deposits (Fig. 5.7a) prior to irradiation, and the changes that appear in the profiles of 40 and 80 L of CO, may hint that an electronic coupling over several monolayers could indeed be present. However, these spectra could also imply that a difference in matrix structure at 5 and 20 L, and 40 and 80 L of CO causes the distinct rate of CO photodesorption observed. The spectral similarities between the 5 and 20 L matrix may indicate that the CO structure formed for the first layer, is largely maintained throughout the subsequent 6 layers in the 20 L deposit. Based on the FWHM, the CO ice structure of the 20 L deposit is probably already somewhat more disordered than at 5 L. At 40 and 80 L, this disorder enhances, leading to a band shift that may be due to increasing dipole-dipole interaction between adjacent CO molecules in the solid or the formation of CO-aggregates (Heidberg et al., 1993; Persson & Ryberg, 1981). It might be the case that in the latter two matrices, the amount of CO available for desorption is therefore higher.

5.4.3 Temperature dependence

The temperature dependence of the photodesorption (Table 5.3) is obviously related to the probability to overcome any activation barrier. Consequently, it is not surprising that the desorption rate increases at higher temperatures. However, the FT-RAIRS spectra of non-irradiated CO have shown that its matrix structure formed at 15 K is thermally unstable at 24 K (Fig. 5.14). The thermally induced changes in the band profile suggest that the matrix becomes more disorganised. We propose that this disorganisation eventually inhibits any photodesorption. From the CO-desorption induced in the isotopic layered system (Fig. 5.12) it can be derived that, although most CO (up to 76 % of the total) desorbs from the top layers of the solid, a significant fraction of excited CO diffuses to the surface prior to desorption. This fraction is at least 24 % of all photodesorbing CO, i.e. the contribution of ^{13}CO to the total CO-desorption rate. Because this is such a large fraction, it is proposed that most of the CO_s^* population is formed closer to the Au-surface. These excited states then must find their way to the CO-to-vacuum surface, either via relaxation due to coupling with an adjacent CO molecule, or via diffusion. It is obvious that these properties are related to the matrix structure, effecting the relaxation time and the efficiency with which CO desorbs into the gas phase.

5.4.4 Future experiments

The different processes proposed (Sect. 5.4) that could be involved in the photodesorption of solid CO, call for dedicated experiments to test their validity. To

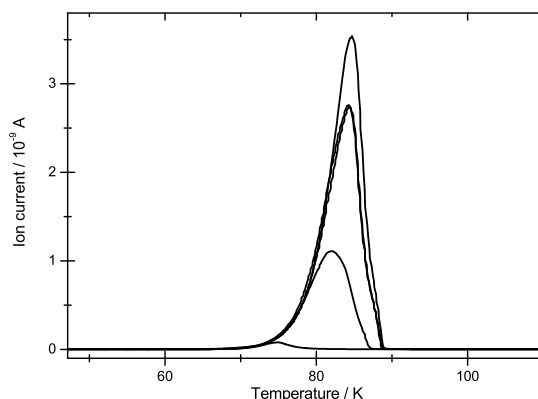


Figure 5.16: TPD spectra of $^{13}\text{CO}_2$ at coverages of 0.5, 25, 100, 100, and 125 ML deposited at 12 K. The TPD-ramp rate used is 6 K min^{-1} . Coverages were derived from integrating the TPD spectra from 12–110 K in the time domain.

summarise, the photodesorption can be a function of processes induced by direct UV excitation of solid CO (probably of minor influence since direct desorption is not observed), or of processes induced in the underlying Au-surface. These processes may in turn depend on the photon flux, the photon dose and the CO matrix structure, and possibly also involve CO diffusion.

More insight in the mechanism of the photodesorption can be derived from a more detailed study of the photodesorption rate as a function of ϕ_{UV} and $\int \phi_{\text{UV}} dt$. The relationship between ϕ_{UV} and the photodesorption rate will provide key information on the order of the reaction of the underlying mechanism. Furthermore, the dose dependence of the photodesorption will indicate if the established steady-state observed is due to the accumulation of $[\text{CO}_s^*]$ reaching equilibrium conditions, or due to ‘permanent’ UV-induced changes in the matrix that get saturated. By designing an experiment in which solid CO is irradiated for some time, then is left to relax, and subsequently is irradiated again, one can explore both this dose dependence and the influence of ϕ_{UV} .

The contribution of the photo-electric effect induced in the Au-surface to the CO-photodesorption, can be studied by replacing this surface by some material of which the workfunction is higher than the energy of the UV-photons (possibly quartz). This will yield direct information about the influence of Au, but has the disadvantage that a new surface will introduce a different experimental environment. Therefore, care should be taken with the surface adopted. Alternatively, one could study the CO-desorption as a function of the coverage, assuming that the photo-effect will decrease at sufficiently thick CO deposits.

However, as the present FT-RAIRS data suggest a transition in the matrix structure between 20 and 40 L, which goes in parallel with a change in the maximum

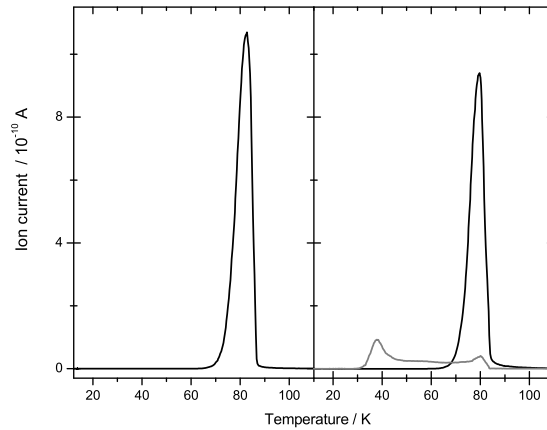


Figure 5.17: TPD spectra of $^{13}\text{CO}_2$ (black) deposited at 12 K at a coverage of 25 L, using a 6 K min^{-1} ramp rate, before (left panel) and after (right panel) 15 min of UV-irradiation. Photo-produced ^{13}CO is shown in grey and is corrected for the contribution of the ^{13}CO -ion fragment of $^{13}\text{CO}_2$ produced in the quadrupole mass spectrometer.

photodesorption rate, the matrix structure could affect the photodesorption. This possibility should therefore be investigated, especially in the critical range from 1–200 L. Here, using layers of variable thickness of different CO isotopes has several advantages over a mono-isotopic layer, and will provide extra information on the photodesorption system. First, the different isotopes will allow to distinguish between the contribution of bulk- and surface processes to the total desorption rate. In addition, one can become more quantitative about the total amount of photodesorbed CO by combining the information on the photodesorption rate of each isotope with the differences between the integrated areas under their TPD spectra prior and subsequent to irradiation.

Further investigation of the photodesorption mechanism, which is specially interesting for the interstellar case, involves the study of the CO photodesorption as a function of the photon energy. The photons used at present are probably energetic enough to excite solid CO (Sect. 5.3.2), and break a CO-CO bond once their energy finds a way into the solid. However, in addition to these photons, the interstellar UV field often also contains the more energetic Ly α radiation. Depending on the mechanisms at work, Ly α radiation might affect the desorption rate differently.

Table 5.4: Photolysis of CO₂ at 12 K

Molec. ^a	$I_{(t=0)}$ ^b 10 ⁻¹³ A	Yield _(t=0) ^c 10 ⁻⁵ molec. photon ⁻¹	$\int_{\text{irr}} I(t) dt$ ^d 10 ⁻¹⁰ C	$\int_{\text{TPD}} I(t) dt$ ^e 10 ⁻⁸ C	ML ^f	$I_{t=0}$ ^g 10 ⁻¹³ A	I_1 ^g 10 ⁻¹³ A	τ ^{g,h} s
¹³ CO ₂				8.4 ⁱ	15			
¹³ CO ₂	0.6±0.4	1	1.14	7.0	12	0.6±0.1	1.4	490±200
¹³ CO	2.8±0.4	3	5.06	1.7	2.1	3.2±0.2	9±1	1350±200

^a Initial dosing of 25 L of ¹³CO₂. ^b Prompt ion current at the start of irradiation as measured. ^c Yield = $N(t)/\phi_{\text{UV}} \times a_{\text{irr}}$, with $a_{\text{irr}} = 1.25 \text{ cm}^2$ and assuming $\phi_{\text{UV}} = 1.4 \times 10^{15} \text{ photons cm}^{-2} \text{ s}^{-1}$. ^d Integrated ion current from 0–15 min of irradiation. ^e Integrated ion current of the TPD curve after 15 min of irradiation between 12 and 100 K, unless otherwise stated. ^f Derived from $\int_{\text{TPD}} I(t) dt$ using Eq. 5.1 for a total surface area $a = 1.25 \text{ cm}^2$. ^g As derived from Eq. 5.4. ^h $\tau = 1/K_{\text{relax}}$. ⁱ Integrated TPD curve of non-irradiated solid ¹³CO₂.

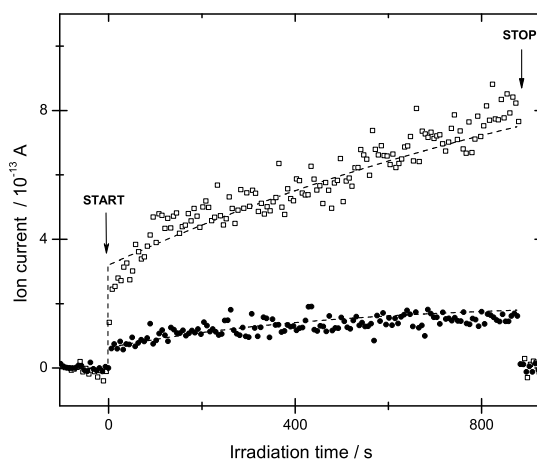


Figure 5.18: The ion current of gas phase $^{13}\text{CO}_2$ (filled \circ) and ^{13}CO (\diamond) desorbing from solid $^{13}\text{CO}_2$ detected by the QMS prior to, and during UV-irradiation of a 25 L matrix at 12 K as a function of the irradiation time. Irradiation started at $t = 0$ and covered the full surface of the substrate. The dashed lines show the fit by the model (see text for details).

5.4.5 CO_2 photolysis and photodesorption

The results obtained for the photodesorption of CO from a pure solid can be applied to improve the understanding about its desorption in more complex systems such as the photolysis of CO_2 forming CO. This process has been extensively studied in various laboratories (Cottin et al., 2003; Gerakines et al., 2000, 1996; Slinger et al., 1977). However, with few exceptions (e.g. Anashin et al., 1998), the desorption of CO in the process of its formation has been not addressed. Fig. 5.16 presents a set of typical TPD spectra of CO_2 obtained in CRYOPAD for various coverages, showing zeroth-order desorption characteristic, typical for pure matrices at multi-layer coverage. In Fig. 5.17, a similar the TPD of CO_2 , prior to irradiation (left panel), and that after 15 min of UV-exposure (right panel) is shown. In addition, the right panel of Fig. 5.17 includes the TPD of CO, produced in the solid during this 15 min of irradiation. From the shape of the TPD curve it is obvious that the formed CO desorbs from a range of different environments. The quantitative analysis of these TPD spectra is summarised in Table 5.4. It indicates that about 15% of all CO_2 that was initially at the surface, gets converted into CO.

The photodesorption of CO from the initially pure CO_2 layer, shown in Fig. 5.18, is in strong contrast with the desorption observed for a pure CO system. Clearly, in this case both CO and CO_2 do show evidence for direct desorption ($I_{t=0}$) at the immediate onset of UV-irradiation, which accounts for a yield of about 1×10^{-5} and $3 \times 10^{-5} \text{ molec. photon}^{-1}$ for CO_2 and CO respectively. These initial values

lie in the same range as those derived by Anashin et al. (1998). However, again the desorption seems photon-dose dependent and is reasonably well fitted by the model that was proposed for pure solid CO starting with a $I_{t=0}$ offset. In Fig. 5.18, this fit is shown by the black dashed line. Both the experimental and the fit values are summarised in Table 5.4. From the comparison between the integrated TPD and the integrated photodesorption, it can be derived that around 3% of all CO formed is directly desorbing, whereas only about 0.2% of CO₂ photodesorbs in the process. These preliminary results are a nice illustration how CRYOPAD can be used to study photodesorption yields and reaction efficiencies in more complex systems than pure CO.

5.5 Concluding Remarks

The work presented here on the photodesorption of solid CO, and the preliminary results on solid CO₂, demonstrate that CRYOPAD can derive both qualitative and quantitative information about photon-induced processes of solid-state molecules. Using the combination of FT-RAIRS and QMS has proved valuable to study UV-induced reactions in the solid, structural changes of the matrix and the photodesorption of both reactants and products. Furthermore, CRYOPAD has sufficient sensitivity to distinguish between direct and indirect desorption processes.

In case of pure solid CO, there is no evidence for any direct photodesorption beyond an upper limit yield (Y_0) of 1.9×10^{-5} molec. photon⁻¹. The secondary effects observed for the desorption of CO are similar to those observed for the photodesorption of H₂O from pure H₂O-ice (Westley et al., 1995a,b). In the case of H₂O, these were ascribed to an incubation period of bond-breaking, and the diffusion of formed radicals prior to desorption. However, we find evidence that for solid CO, these secondary desorption effects may arise due to the underlying Au-surface. Under astronomical conditions therefore, at least some CO-desorption can be expected due to the formation of electron-hole pairs induced by UV-photons in the underlying silicate or carbonaceous grain surface (Bakes & Tielens, 1994; Dwek & Smith, 1996; Watson, 1972), although those photodesorption yields cannot be directly derived from the present laboratory data. Alternatively, desorption may occur as a result of UV-induced photochemistry. For example, from the preliminary work conducted on ¹³CO₂, we do find evidence for direct photodesorption of CO during the CO₂-photolysis on the order of 3×10^{-5} molec. photon⁻¹. Hence, an active role for UV-induced grain-chemistry may be suggested as a possible mechanism to 'return' condensed molecules to the gas phase when modelling the observed gas-to-solid ratios of molecules in various astronomical environments. Future work, including a more detailed study of the photodose dependence of this process from surfaces with a work function higher than the maximum energy of the photons, such as quartz (Lange, 1965), is required to definitively distinguish between these desorption effects, being due to processes induced by UV-photons in the CO matrix, and those induced by electron-hole pairs from the underlying Au-surface. Furthermore, it will be most

important for the understanding of the photodesorption mechanisms at work to study the correlation between the photon-flux and the desorption rate, and / or alternatively study the time dependence of the photodesorption rate when irradiation is stopped. From such experiments it can be derived whether a second photon is necessary to overcome the barrier between CO_s^* and CO_g (or not).

Acknowledgements

This research was financially supported by the Netherlands Research School for Astronomy (NOVA) and a NWO Spinoza grant. The authors would like to thank E. de Kuyper, J. F. Benning and L. van As for building CRYOPAD and W. A. Schutte for initiating its construction. Furthermore, the authors would like to thank O. Berg, E. H. G. Backus, M. Bonn, S. Bisschop and G. Fuchs for useful discussions and valuable suggestions on the experiments.

Bibliography

- Öberg, K. I., van Broekhuizen, F., Fraser, H. J., et al. 2005, *ApJL*, 621, L33
- Aikawa, Y., van Zadelhoff, G. J., van Dishoeck, E. F., & Herbst, E. 2002, *A&A*, 386, 622
- Anashin, V. V., Malyshev, O. B., Calder, R. Gröbner, O., & Mathewson, A. 1998, *Nucl. Instr. and Meth. in Phys. Res. A*, 405, 258
- Attard, G. A. & Barnes, C. 1998, *Surfaces* (Oxford University Press Inc., New York)
- Bakes, E. L. O. & Tielens, A. G. G. M. 1994, *ApJ*, 427, 822
- Baratta, G. A., Brunetto, R., Leto, G., et al. 2004, *Memorie della Societa Astronomica Italiana Supplement*, 5, 33
- Bergin, E. A., Langer, W. D., & Goldsmith, P. F. 1995, *ApJ*, 441, 222
- Bourdon, E. B., Prince, R. H., & Duley, 1982, *ApJ*, 260, 909
- Brooke, T. Y., Tokunaga, A. T., Weaver, H. A., et al. 1996, *Bulletin of the American Astronomical Society*, 28, 1091
- Chakarov, D. V., Österlund, L., & Kasemo, B. 1995, *Vacuum*, 46, 1109
- Collings, M. P., Anderson, M. A., Chen, R., et al. 2004, *MNRAS*, 354, 1133
- Corcelli, S. A. & Tully, J. C. 2002, *J. Phys. Chem. A*, 106, 10849
- Cottin, H., Moore, M. H., & Bénilan, Y. 2003, *ApJ*, 590, 874
- d'Hendecourt, L. B., Allamandola, L. J., Baas, F., & Greenberg, J. M. 1982, *A&A*, 152, L12
- Dubost, H. & Legay, F. 1989, *Chemistry and Physics of Martix-Isolated Species* (Elsevier Science Publishers B.V., North Holland)
- Dwek, E. & Smith, R. K. 1996, *ApJ*, 459, 686
- Eidelsberg, M., Rostas, F., Breton, J., & Thieblemont, B. 1992, *J. Chem. Phys.*, 96, 5585
- Elsila, J., Allamandola, L. J., & Sandford, S. A. 1997, *ApJ*, 479, 818
- Fukutani, K., Song, M. B., & Murata, Y. 1995, *J. Chem. Phys.*, 103, 2221
- Gerakines, P. A., Moore, M. H., & Hudson, R. L. 2000, *A&A*, 357, 793
- Gerakines, P. A., Schutte, W. A., & Ehrenfreund, P. 1996, *A&A*, 312, 289
- Gerakines, P. A., Whittet, D. C. B., Ehrenfreund, P., et al. 1999, *ApJ*, 522, 357
- Gorti, U. & Hollenbach, D. 2002, *ApJ*, 573, 215
- Greenberg, L. T. 1973, in *IAU Symp. 52: Interstellar Dust and Related Topics*, 413
- Heidberg, J., Kampshoff, E., Kühnemuth, R., Suhren, M., & Weiss, H. 1992, *Surf. Sci.*, 269, 128
- Heidberg, J., Suhren, M., & Weiss, H. 1993, *J. Electr. Spec. Rel. Phenom.*, 64, 227

Bibliography

- Hudson, R. L. & Moore, M. H. 1993, *ApJL*, 404, L29
- Hudson, R. L. & Moore, M. H. 2004, *Icarus*, 172, 466
- Hussia, I. & Viswanathan, R. 1985, *J. Vac. Sci. Technol. B*, 3, 1520
- Kay, B. D., Lykke, L. H., Creighton, J. R., & Ward, S. J. 1989, *J. Chem. Phys.*, 91, 5120
- Lange, W. J. 1965, *J. Vac. Sci. Technol. A*, 2, 74
- McElhiney, G. M. & Pritchard, J. 1976, *Surf. Sci.*, 60, 397
- Mesawari, A. & Ignatiev, A. 1988, *J. Vac. Sci. Technol. A*, 6, 3140
- Muñoz Caro, G. M., Meierhenrich, U., Schutte, W. A., Thiemann, W. H.-P., & Greenberg, J. M. 2004, *A&A*, 413, 209
- Mumma, M. J., Disanti, M. A., dello Russo, N., et al. 1996, *Science*, 272, 1310
- Palumbo, M. E. 1997, *Advances in Space Research*, 20, 1637
- Persson, B. N. J. & Ryberg, R. 1981, *Phys. Rev. B*, 24, 6954
- Petrik, N. G. & Kimmel, G. 2004, *J. Chem. Phys.*, 121, 3736
- Picq, V. & Balanzat, E. 1999, *Nucl. Instr. Meth. Phys. Res. B*, 151, 76
- Pontoppidan, K. M., Fraser, H. J., Dartois, E., et al. 2003, *A&A*, 408, 981
- Potter, H. C. & Blakeley, J. M. 1975, *J. Vac. Sci. Technol.*, 12, 635
- Roser, J. E., Manicò, G., Pirronello, V., & Vidali, G. 2002, *ApJ*, 581, 276
- Sack, N. J., Baragiola, R. A., & Johnson, R. E. 1993, *Icarus*, 104, 152
- Shen, C. J., Greenberg, J. M., Schutte, W. A., & van Dishoeck, E. F. 2004, *A&A*, 415, 203
- Shi, M., Grosjean, D. E., Schou, J., & Baragiola, R. 1995, *Nucl. Instr. Meth. Phys. Res. B*, 96, 524
- Slanger, T. G., Sharpless, R. L., & Black, G. 1977, *J. Chem. Phys.*, 67, 5317
- Soifer, B. T., Puetter, R. C., Russell, R. W., et al. 1979, *ApJL*, 232, L53
- Störzer, H. & Hollenbach, D. 1999, *ApJ*, 515, 669
- Tielens, A. G. G. M. & Hagen, W. 1982, *A&A*, 114, 245
- Tobin, R. G., Chung, C., & Luo, J. S. 1994, *J. Vac. Sci. Technol. A*, 12, 264
- Turner, B. E. 2000, *ApJ*, 542, 837
- van Broekhuizen, F. A., Keane, J. V., & Schutte, W. A. 2004, *A&A*, 415, 425
- van Zadelhoff, G.-J., Aikawa, Y., Hogerheijde, M. R., & van Dishoeck, E. F. 2003, *A&A*, 397, 789
- Watanabe, N., Horii, T., & Kouchi, A. 2000, *ApJ*, 541, 772
- Watson, W. D. 1972, *ApJ*, 176, 103
- Watson, W. D. & Salpeter, E. E. 1972a, *ApJ*, 174, 321
- Watson, W. D. & Salpeter, E. E. 1972b, *ApJ*, 175, 659
- Westley, M. S., Baragiola, R. A., Johnson, R. E., & Baratta, G. A. 1995a, *Nature*, 373, 405
- Westley, M. S., Baragiola, R. A., Johnson, R. E., & Baratta, G. A. 1995b, *Planetary Space Sci.*, 43, 1311
- Willacy, K. & Langer, W. D. 2000, *ApJ*, 544, 903

Wu, C. Y., Judge, D. L., Cheng, B., et al. 2002, *Icarus*, 156, 456

Yoshinobu, J., Guo, X., & Yates, J. T. J. 1991, *J. Vac. Sci. Technol. A*, 3, 1726

Bibliography

Chapter 6

A quantitative analysis of OCN^- formation in interstellar ice analogs

Abstract

The $4.62\ \mu\text{m}$ absorption band, observed along the line-of-sight towards various young stellar objects, is generally used as a qualitative indicator for energetic processing of interstellar ice mantles. This interpretation is based on the excellent fit with OCN^- , which is readily formed by ultraviolet (UV) or ion-irradiation of ices containing H_2O , CO and NH_3 . However, the assignment requires both a qualitative and quantitative agreement in terms of the efficiency of formation as well as the formation of additional products. Here, we present the first quantitative results on the efficiency of laboratory formation of OCN^- from ices composed of different combinations of H_2O , CO , CH_3OH , HNCO and NH_3 by UV- and thermally-mediated solid state chemistry. Our results show large implications for the use of the $4.62\ \mu\text{m}$ feature as a diagnostic for energetic ice-processing. UV-mediated formation of OCN^- from $\text{H}_2\text{O}/\text{CO}/\text{NH}_3$ ice matrices falls short in reproducing the highest observed interstellar abundances. In this case, at most 2.7% OCN^- is formed with respect to H_2O under conditions that no longer apply to a molecular cloud environment. On the other hand, photoprocessing and in particular thermal processing of solid HNCO in the presence of NH_3 are very efficient OCN^- formation mechanisms, converting 60%–85% and $\sim 100\%$, respectively of the original HNCO . We propose that OCN^- is most likely formed thermally from HNCO given the ease and efficiency of this mechanism. Upper limits on solid HNCO and the inferred interstellar ice temperatures are in agreement with this scenario.¹

6.1 Introduction

The chemical composition of interstellar ices acts as a tracer of the chemical and physical history of molecular clouds. Based on spectral absorption features in the $2\text{--}16\ \mu\text{m}$ region, the ices are found to consist of simple neutral molecules. In addition, observational evidence now exists for the presence of ions such as OCN^- , HCOO^- and NH_4^+ (Allamandola et al., 1999; Grim et al., 1989; Novozamsky et al.,

¹F.A. van Broekhuizen, J.V. Keane, and W.A. Schutte

2001; Schutte & Khanna, 2003). The formation mechanisms underlying their presence, however, are still uncertain for most species. Understanding these processes is of key importance to improve our knowledge of the ice history and the evolution of molecular clouds.

The 4.62 μm (2165 cm^{-1}) laboratory feature of OCN⁻ matches well an interstellar absorption band, observed towards various young stellar objects (YSO's). Ever since its first detection in the infrared spectrum of W 33 A by Soifer et al. (1979), its assignment has remained controversial. First laboratory studies by Moore et al. (1983) reproduced the interstellar feature by proton irradiation of interstellar ice analogs composed of H₂O, CO and NH₃. Subsequently, Lacy et al. (1984) produced a similar feature by Vacuum ultraviolet (VUV) photoprocessing of CO/NH₃ ice. This 'XCN' feature was assigned to OCN⁻ by Grim & Greenberg (1987), and Schutte & Greenberg (1997) strengthened the hypothesis by looking at the band shift using different isotopes. In addition, Demyk et al. (1998) showed that OCN⁻ could also form from HNCO by simple acid-base chemistry with NH₃, serving as a proton acceptor. This process has recently been studied in more detail by Raunier et al. (2003a,b). Although HNCO has not been identified directly in interstellar ices, it is observed in 'hot cores' surrounding massive protostars and is a likely precursor of OCN⁻. In spite of the strong case for assigning the interstellar 4.62 μm feature to OCN⁻, many other carriers were proposed. A summary is given by Pendleton et al. (1999). Some carriers, like silanes, thiocyanates, isothiocyanates and ketenes, cannot be excluded but to date none of these present serious candidates.

The ease with which the interstellar 4.62 μm feature can be reproduced in the laboratory by the energetic processing of simple ices led to the direct association of this band in interstellar spectra with the presence of energetic processes. This is, however, a tentative assumption. A careful interpretation of interstellar data requires a thorough quantitative study of the efficiency of the OCN⁻ formation together with an exhaustive investigation of the formation of additional products. Moreover, renewed interest has stemmed from the possibility that CN-bearing species may get included in protoplanetary discs to become an important component of prebiotic matter. This adds to the importance in the quest to understand the underlying formation mechanism of one of its simplest compounds, OCN⁻ (Pendleton et al., 1999; Tegler et al., 1995; Whittet et al., 2001).

This study will look in detail at the formation efficiency of OCN⁻ by UV- and thermal processing of interstellar ice analogs and the evolution of additional products under laboratory conditions. The outline of the paper is as follows. Sect. 6.2 describes the experimental procedure, leading to the results in Sect. 7.5. The initial precursor abundance and the influence of photon-energy distribution and ice-thickness on the efficiency of OCN⁻ formation are addressed. Also alternative C- or N-sources to form OCN⁻ other than CO or NH₃ are considered, namely, H₂CO, CH₄ and N₂. Special attention is paid to the formation of OCN⁻ from HNCO or CH₃OH. Sect. 6.4 discusses the astrophysical implications of the results in relation to the 4.62 μm 'XCN' feature observed in ices towards various YSO's and aims to provide a more solid base for the use of this feature as a potential diagnostic of energetic processing of ices in space.

6.2 Experimental Methods

All experiments were performed under high vacuum (10^{-8} mbar) conditions using Fourier Transform Infrared spectroscopy (FTIR) over the $4000\text{--}400\text{ cm}^{-1}$ spectral range at 2 cm^{-1} resolution. Ice matrices were grown at 15 K on a CsI window following the general procedure as described by Gerakines et al. (1996, 1995). To obtain a particular ice composition, constituent gases were mixed in a glass vacuum manifold (typical base pressure 2×10^{-4} mbar) to their initial relative ice abundances. Unless stated otherwise, the ices were grown as heterogeneous mixtures.

Cyanic acid, HNCO, was produced as described by Novozamsky et al. (2001). In addition to their protocol, the collection of volatile HNCO was started at a cracking temperature of 343 K using a liquid nitrogen cool-trap and continued for 5 min. after completion of cracking. Infrared analysis of the volatile products at 216 K showed HNCO and CO_2 together with some very weak unidentified features. HNCO was purified by vacuum freeze-thaw using a n-octane and an isopentane slush at 216 K and 154 K, respectively. The purity of the HNCO was always $> 99.5\%$ relative to CO_2 . The contamination level of the residual products is probably less than 50% of the CO_2 impurity and is thus thought to have a minor influence on the experimental results of HNCO in astrophysically relevant ice matrices. Therefore no further purification was applied.

The thermal formation of OCN^- was studied by raising the temperature of the ice matrix in steps of 5–20 K. The actual warmup was fast relative to the time of the typical experiment such that no reaction rate constants could be determined.

Photoprocessing of optically thin ices used a microwave H_2 -discharge lamp equipped with a MgF_2 window (Gerakines et al., 1996) to obtain the standard ‘hard’ UV with an overall UV flux of $\sim 5 \times 10^{14}$ photons $\text{cm}^{-2} \text{s}^{-1}$ ($E_{\text{photon}} \geq 6$ eV). These conditions simulate best clouds located near hot stars (~ 20000 K) or cosmic-ray induced UV photons inside a molecular cloud. A less energetic ‘soft’ UV source with a $\sim 5 \times$ lower UV flux was produced by using a fused silica window (Janos technology ICC.). Fused silica becomes opaque below 140 nm. The transmitted photons are therefore lower in energy, typically $E_{\text{photon}} \leq 8.8$ eV. Astrophysically, this less energetic photon source can be viewed as a rough simulation of the UV impinging on ices that reside in more shielded regions around YSO’s where the higher energy photons have been absorbed by dust. Both hard and soft energy spectra are extensively described by Muñoz Caro & Schutte (2003).

Any astrophysical implications, based on efficiencies found in the laboratory must be treated with care. In the laboratory the ice is grown on a CsI-substrate. CsI can give rise to surface directed chemistry which can be different from interstellar grains. This effect is assumed to play a minor role within ice-thicknesses studied here. Also, differences in surface area introduce changes such as UV induced heating effects. Local heating on grains predominantly influences the very small ones that account for only a minor part of the total population and are therefore assumed to introduce only a small error on the total results. One other important point to consider is the total UV-flux of a molecular cloud, translating to a total UV fluence seen by one individual grain. The laboratory UV-flux is kept

Table 6.1: Band strength of relevant features at 15 K

	ν (cm^{-1})	A (molec.cm^{-1}) ^a
H ₂ O dominated matrix: H ₂ O/NH ₃ /HNCO = 120/10/1		
HNCO	2260	7.2×10^{-17}
OCN ⁻	2170	1.3×10^{-16}
NH ₄ ⁺	1485	4.1×10^{-17}
H ₂ O poor matrix: NH ₃ /HNCO = 10/1		
HNCO	2260	7.8×10^{-17}
OCN ⁻	2160	1.3×10^{-16}
NH ₄ ⁺	1485	4.6×10^{-17}

a. Band strengths are determined with 20% accuracy

such that it predominantly induces single-photon processes. Still the flux in the laboratory is about 10 orders of magnitude larger than that inside a molecular cloud. UV-photons induce secondary electrons and can form metastable species that can react on different time scales than ion-molecule or radical-molecule reactions. These processes, when present, could lead to discrepancies between observations and laboratory results.

6.3 Results

6.3.1 Band strengths

The integrated band strength, A , was determined for the relevant HNCO, OCN⁻, and NH₄⁺ features and was derived from the optical depth, τ_ν , at a frequency ν by means of the following equations where N is the total amount of molecules.

$$A = \int \frac{\tau_\nu d(\nu)}{N} \quad (6.1)$$

$$A_{\text{new}} = A_{\text{known}} \frac{\tau_{\text{new}}}{\tau_{\text{known}}} \quad (6.2)$$

To determine A in a matrix of different molecules we used the umbrella mode of NH₃ at 1070 cm^{-1} ($A_{\text{NH}_3} = 1.7 \times 10^{-17} \text{ cm molecule}^{-1}$ (d'Hendecourt & Allaman-dola, 1986) at 15 K as the known reference and assumed the thermally induced acid-base reaction of HNCO and NH₃ to OCN⁻ and NH₄⁺, earlier described by Demyk et al. (1998), to be 100% efficient. Using exactly the same deposition parameters to compose the ice mixtures made it possible to correct for a change in the reference band strength of NH₃ due to the ice matrix composition. The obtained band strengths are listed in Table 6.1. Within the accuracy of our measurement, 20%, band strengths are in good agreement with those derived earlier (d'Hendecourt et al., 1986; Lowenthal et al., 2000; Schutte & Khanna, 2003; Tegler et al., 1995).

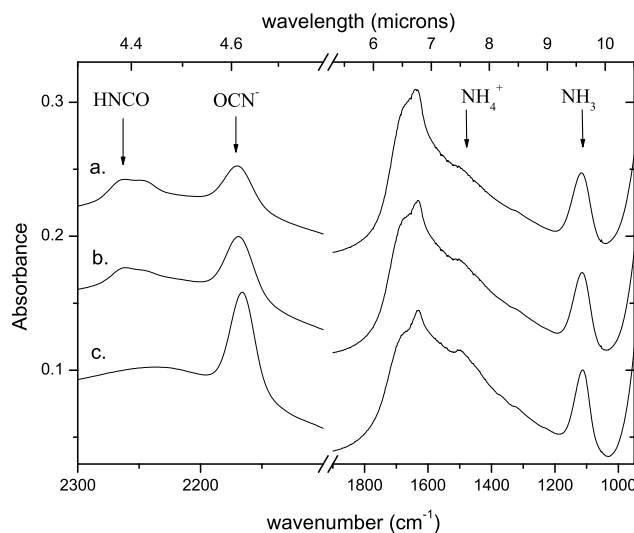


Figure 6.1: The thermal evolution of $\text{H}_2\text{O}/\text{NH}_3/\text{HNCO} = 120/10/1$ ice is shown qualitatively at a. $T = 15$ K, b. $T = 52$ K and c. $T = 122$ K in the spectral range of $2300\text{--}2100\text{ cm}^{-1}$ and $1850\text{--}990\text{ cm}^{-1}$. At 122 K OCN^- has reached maximum production.

6.3.2 Thermal formation of OCN^-

The acid-base like reaction mechanism in which HNCO donates a proton to NH_3 is the last step in the reaction towards OCN^- formation. As this process is likely thermally activated, OCN^- formation was studied qualitatively and quantitatively by thermal processing. Three different ice compositions were used to simulate interstellar abundances. The first sample has relative abundances such that they reflect column densities as observed towards W 33 A (Gibb et al., 2001). This ice is highly dominated by H_2O with a typical composition of $\text{H}_2\text{O}/\text{NH}_3/\text{HNCO} = 120/10/1$. Second, a matrix was composed that lacked H_2O , creating the most favourable extreme environment to form OCN^- from HNCO and NH_3 . Third, an in-between sample was taken with a reduced amount of H_2O , simulating a situation of high local HNCO and NH_3 abundances.

The thermal evolution of this acid-base reaction is shown qualitatively in Fig. 6.1, which contains spectral regions with the most distinctive features. The strong H_2O stretch vibration around 3300 cm^{-1} is left out for practical reasons. The unresolved double-peaked structure at 2265 cm^{-1} , extending to 2245 cm^{-1} , is assigned to HNCO (Novozamsky et al., 2001). As the temperature increases this structure evolves to a single peak at 2260 cm^{-1} which is consistent with the thermal behaviour of HNCO in a H_2O matrix (Raunier et al., 2003a). At 15 K OCN^- is already observed by its feature at 2169 cm^{-1} , supported by the counterion NH_4^+ that is seen as a shoulder at 1485 cm^{-1} on top of the broad H_2O bending

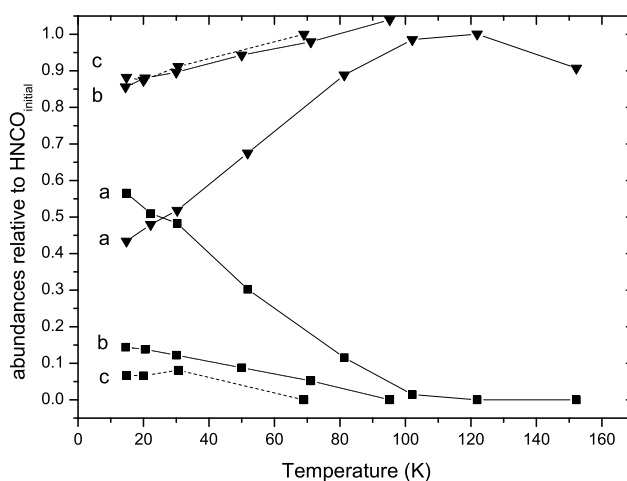
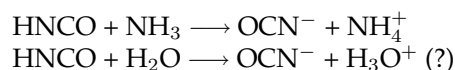
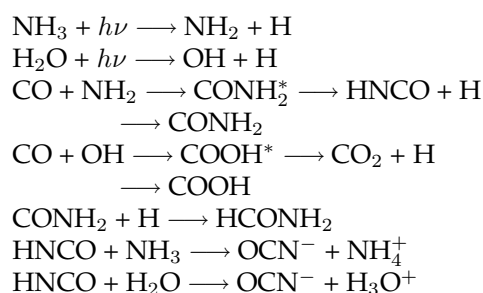


Figure 6.2: The conversion of HNCO to OCN^- as a function of temperature is shown quantitatively for a. $\text{H}_2\text{O}/\text{NH}_3/\text{HNCO} = 120/10/1$, b. $\text{H}_2\text{O}/\text{NH}_3/\text{HNCO} = 24/10/1$ and c. $\text{NH}_3/\text{HNCO} = 10/1$. Abundances are normalised to the initial HNCO abundance. OCN^- is marked by triangles while squares indicate HNCO . Conversions can exceed 100% due to an increased signal intensity of OCN^- at >70 K and a 20% accuracy of the measurements.

mode. This is in agreement with findings from Raunier et al. (2003b) who show that OCN^- forms from the interaction of HNCO with 4 NH_3 molecules by purely solvation-induced dissociative ionization at 10 K. The features of OCN^- and NH_4^+ continue to grow with temperature as the broad HNCO -structure at 2260 cm^{-1} and the NH_3 feature at 1070 cm^{-1} decrease, consistent with previous experiments by (Demyk et al., 1998). Furthermore, as the temperature rises the peak position of OCN^- shifts from 2170.8 cm^{-1} at 15 K to 2166.0 cm^{-1} at 120 K.

A quantitative analysis is shown in Fig. 6.2 for the three ices under study. The initial conversion at 15 K is influenced by the relative concentrations of HNCO and NH_3 and ranges from 40% in a H_2O -dominated matrix to a maximum of 90% in the absence of H_2O . A part of this initial conversion may be due to a local temperature rise when the molecules freeze out onto the surface. Studies by Raunier et al. (2003a,b) on the thermal reactivity of HNCO with H_2O and NH_3 individually show that dissociative ionization of HNCO in H_2O only occurs above 130 K but already at 10 K in the presence of NH_3 . The thermal deprotonation of HNCO in the only presence of H_2O (Raunier et al., 2003a), is not observed. This discrepancy may be due to the IR-analysis technique and the lower resolution used in the present study. The direct continuation of OCN^- formation observed in NH_3 containing ices when the temperature is only slightly raised, can be explained by an increasing mobility of NH_3 to facilitate the deprotonation of HNCO within

Table 6.2: Reactions responsible for OCN^- formation*reactions in thermally processed ices**reactions in photoprocessed ices*

the time of our experiment (~ 10 min.). Nevertheless is the temperature at which maximal conversion is achieved only slightly dependant on the H_2O dilution. All matrices show the expected conversion of $\sim 100\%$ for HNCO between 70–100 K that is irreversible upon cooling.

6.3.3 UV photoprocessing of HNCO-containing ices

The UV photoprocessing of HNCO-containing ices was performed to compare the efficiency of the UV-induced to the thermally induced chemistry discussed above. Similar ice mixtures were grown with compositions $\text{H}_2\text{O}/\text{NH}_3/\text{HNCO} = 140/8/1$ (hereafter mixture A), $\text{H}_2\text{O}/\text{NH}_3/\text{HNCO} = 20/8/1$, and $\text{H}_2\text{O}/\text{HNCO} = 14/1$.

The photoprocessing of mixture A at 15 K is shown qualitatively in Fig. 6.3. Only the $2300\text{--}2100\text{ cm}^{-1}$ and the $1850\text{--}950\text{ cm}^{-1}$ regions are shown. Part of the deposited HNCO reacts directly to OCN^- (see Sect. 6.3.2). UV irradiation causes the 2169 cm^{-1} and 1485 cm^{-1} features to increase further in intensity as the 2260 cm^{-1} and 1070 cm^{-1} bands decrease, showing the formation of OCN^- and NH_4^+ from HNCO and NH_3 (described by the reactions in Table 6.2). Apart from CO_2 no other photoproducts are seen to form based on the infrared spectroscopy. All nitrogen-bearing species disappear from the solid ice matrix at sufficiently high UV dose. This will be discussed in Sect. 6.3.4.

Fig. 6.4 shows the reaction of HNCO to OCN^- quantitatively as a function of UV dose for the three ices studied. Abundances are given in percentage of the initially deposited amount of HNCO. The maximal efficiency at which OCN^- can be produced depends on the H_2O dilution of the ice matrix. Higher concentrations of NH_3 and HNCO with respect to H_2O result in higher efficiencies of OCN^- for-

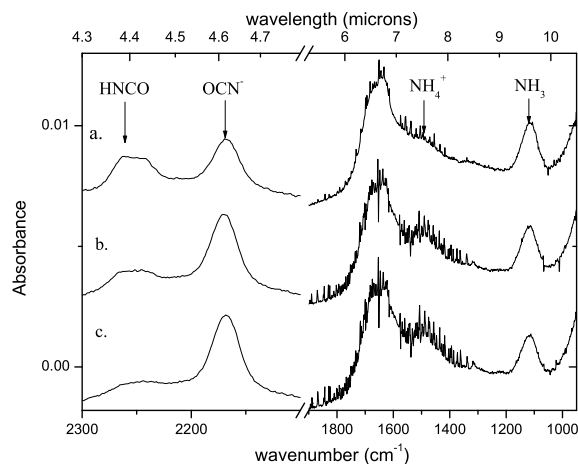


Figure 6.3: The deprotonation of HNCO, induced by ‘hard’ UV photons at 15 K, is shown qualitatively for $\text{H}_2\text{O}/\text{NH}_3/\text{HNCO} = 140/8/1$ for the spectral range of $2300\text{--}2100\text{ cm}^{-1}$ and $1850\text{--}990\text{ cm}^{-1}$ at a UV fluence of a. 0 photons cm^{-2} , b. $2.4 \times 10^{16}\text{ photons cm}^{-2}$ and c. $1.0 \times 10^{17}\text{ photons cm}^{-2}$, corresponding to the maximum OCN^- produced. CO_2 appears as the only observable by-product of OCN^- formation but is not shown for practical reasons.

mation. The efficiency ranges from 60% to 85% with respect to initial HNCO for the NH_3 containing matrices here studied and $\sim 18\%$ for $\text{H}_2\text{O}/\text{HNCO}$ ices. This indicates that NH_3 is not a priori required for the deprotonation of HNCO (Rauzier et al., 2003a). In the NH_3 containing matrices a maximal OCN^- abundance was obtained after a dose of $0.2\text{--}3.0 \times 10^{17}\text{ photons cm}^{-2}$. This is $\sim 10\times$ lower than the amount of photons needed to reach maximal abundances in $\text{H}_2\text{O}/\text{CO}/\text{NH}_3$ -precursor matrices (see section 3.4). At higher dose, OCN^- photodissociation dominates over its formation and after $\sim 2 \times 10^{18}\text{ photons cm}^{-2}$, OCN^- can no longer be detected for Figs. 6.4a and b. The thermal and UV processing have very similar effects in $\text{H}_2\text{O}/\text{NH}_3/\text{HNCO}$ matrices (compare Fig. 6.1 and 6.3). Photo-products, formed with a kinetic energy in excesses of the ambient ice temperature, will increase the effective ice temperature when they release this excess energy into the matrix phonon modes. It is therefore not possible to distinguish between these two routes.

6.3.4 UV photoprocessing of $\text{H}_2\text{O}/\text{CO}/\text{NH}_3$ ices

Previous work by Grim & Greenberg (1987) showed the formation of OCN^- by UV photoprocessing of ices composed of H_2O , CO and NH_3 . The resulting spectrum nicely fits the observed $4.62\text{ }\mu\text{m}$ feature toward various lines of sight. A careful interpretation of the interstellar data requires that the interstellar OCN^- feature is reproduced not only by shape but also in absolute intensity and that the

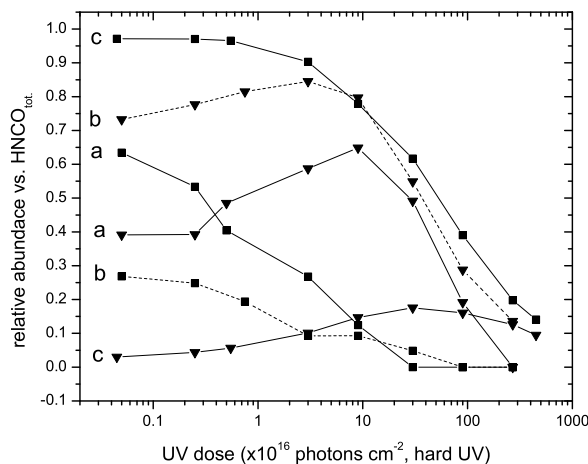


Figure 6.4: The deprotonation of HNCO at 15 K is shown quantitatively as a function of the fluence of ‘hard’ UV photons for *a.* $\text{H}_2\text{O}/\text{NH}_3/\text{HNCO} = 140/8/1$, *b.* $\text{H}_2\text{O}/\text{NH}_3/\text{HNCO} = 20/8/1$ and *c.* $\text{H}_2\text{O}/\text{HNCO} = 14/1$. Abundances are normalised to the initial HNCO abundance. Triangles and squares indicate OCN^- and HNCO, respectively. Maximal OCN^- abundances are obtained at a fluence of $0.2\text{--}3.0 \times 10^{17}$ photons cm^{-2} .

additional product formation in studied.

Apart from OCN^- , many products are formed by UV-photon induced reactions in a $\text{H}_2\text{O}/\text{CO}/\text{NH}_3$ ice matrix. The $2300\text{--}1000$ cm^{-1} spectral region in Fig. 6.5 shows the most distinctive features. Most products have been identified in earlier irradiation experiments of similar ices and are listed in Table 6.3 (d’Hendecourt et al., 1986; Grim et al., 1989; Hagen et al., 1983). The strong stretch vibration of CO_2 at 2340 cm^{-1} largely dominates the spectrum and is therefore not shown. A weak, broad, previously unidentified feature appears at 2260 cm^{-1} . This feature is partly blended with the 2278 cm^{-1} resonance of CO_2 and is identified as the ν_2 vibration of HNCO diluted in H_2O ice. None of the features, listed in Table 6.3, form an unique diagnostic for UV photoprocessing in this spectral region because they are either non-specific (CO_2) or have too weak band strengths to give constraints (H_2CO and HCONH_2).

Figure 6.6 shows the photolysis of CO and NH_3 in a H_2O dominated ice matrix together with the evolution of OCN^- . Using Equation (1), the derived abundances are normalised to the original H_2O ice content. For OCN^- the absolute integrated band strengths listed in Table 6.1 are used. CO_2 is formed almost instantly upon UV exposure. OCN^- , being a higher order product of irradiation, is detected only after prolonged irradiation and reaches a maximum abundance at a UV dose of $\sim 1 \times 10^{18}$ photons cm^{-2} . At higher UV doses it again decreases due to photodestruction. At the highest doses only CO_2 is seen to form. The nitrogen-

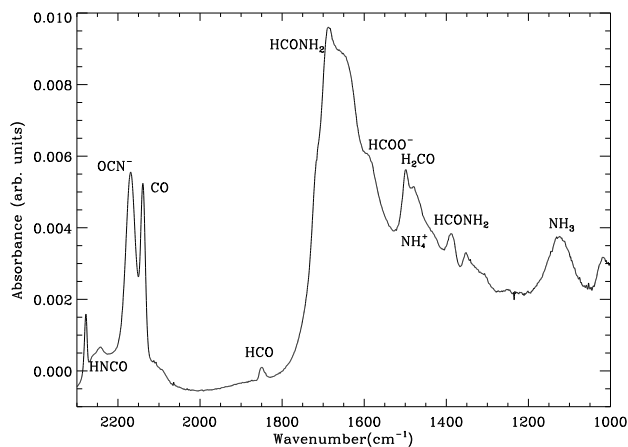


Figure 6.5: The $2300\text{--}1000\text{ cm}^{-1}$ spectral range of a standard $\text{H}_2\text{O}/\text{CO}/\text{NH}_3$ ice matrix after photoprocessing with ‘hard’ UV photons. The complete spectrum is dominated by the CO_2 stretch vibration at 2342 cm^{-1} , left out for practical reasons.

bearing species that were detected degrade and most likely form infrared-weak or -inactive molecules. Molecular nitrogen or complex large organics are suggested to form in this context (Agarwal et al., 1985; Bernstein et al., 1995; Muñoz Caro & Schutte, 2003).

Table 6.4 shows a summary of the ice matrices used to investigate the efficiency of the OCN^- formation. The repeatability of the listed values is typically of the order of 20%. The formation efficiency rises when the fraction of CO and NH_3 in the ice is increased, whereas the elimination of H_2O from the matrix shows no significant effect. In order to form OCN^- at the abundance observed towards W33 A, the minimum initial ice fraction of CO and NH_3 must be of the order of 30% or higher. No ice was found to form more than 2.7% OCN^- . On average the production efficiency ranges between 0.6% and 1.8%.

Standard experimental conditions used a ‘hard’ UV-irradiation source. The influence of the photon characteristics on the formation of OCN^- was tested with a less intense, less energetic ‘soft’ UV source that contains primarily photons of $\sim 160\text{ nm}$. ‘Soft’ processing is shown in Fig. 6.7. The photoproducts formed are similar as those due to ‘hard’ UV. However, due to the difference in energy distribution, products appear at different doses. Under ‘soft’ conditions, the maximum OCN^- formation occurs at a dose of $\sim 4 \times 10^{18}\text{ photons cm}^{-2}$, a factor of 4 higher than in the ‘hard’ environment, but its maximum abundance is hardly effected, 1.1% versus 0.8%. The destruction of CO and the formation of CO_2 decrease enormously with ‘soft’ UV but the evolution of NH_3 is almost unaltered: only 20% of its initial abundance is left when OCN^- reaches maximum abundance. This dependence on UV photon energy is consistent with the wavelength dependence of the photodissociation cross sections of these species, with CO being destroyed

Table 6.3: Peak assignment of a standard $H_2O/CO/NH_3$ ice after UV-photoprocessing.

Wavenumber (cm^{-1})	Assignment ^a	A ($cm^2 molec^{-1}$)
<i>Initial ice matrix</i>		
3290	H_2O	2.0×10^{-16d}
2139	CO	1.0×10^{-17d}
1127	NH_3	1.3×10^{-17d}
<i>Photoproducts</i>		
2342	CO_2	7.6×10^{-17e}
2278	$^{13}CO_2$	
2260	HNCO	7.2×10^{-17b}
2169	OCN^-	1.3×10^{-16b}
1849	HCO^c	
1720	H_2CO	
1690	$HCONH_2$	3.3×10^{-17i}
1580	$HCOO^-$	1.0×10^{-16h}
1499	H_2CO^2	3.9×10^{-18f}
1485	NH_4^+	4.1×10^{-17b}
1386	$HCONH_2$	2.8×10^{-18h}
1352	$HCOO^-$	1.7×10^{-17h}
1330	$HCONH_2$	
1020	CH_3OH	1.9×10^{-17g}
650	CO_2	

^a Assignment from Grim et al. (1989) unless otherwise noted; ^b This article; ^c d'Hendecourt et al. (1986); ^d d'Hendecourt & Allamandola (1986); ^e Gerakines et al. (1995); ^f Schutte et al. (1993); ^g Schutte & Greenberg (1991); ^h Schutte et al. (1999); ⁱ Wexler (1967)

only at $\lambda < 110$ nm (van Dishoeck 1988).

When a photoprocessed matrix is thermally annealed, the OCN^- production efficiency seems to increase. In Fig. 6.8 the dominant ice components of a photoprocessed $H_2O/CO/NH_3$ ice, plotted relative to the initial H_2O abundance shows an increase of the $4.62 \mu m$ signal intensity from 0.7–0.9% as a function of temperature up to 180 K. UV-photolysis experiments have shown that small amounts of HNCO form in the ice, contributing to an increasing signal by thermal conversion to OCN^- at temperatures of 70–100 K. However, since the increase is prominent only at higher temperatures while thermal deprotonation is already apparent below 70 K, it is more likely induced by changing interactions in the $OCN^- - NH_4^+$ salt-complex. NH_3 , CO and CO_2 evaporate in the laboratory between 120 K and 160 K when mixed in H_2O . OCN^- remains present in the condensed phase up to ~ 200 –240 K and the small strengthening of the $4.62 \mu m$ signal intensity is accompanied by the evaporation of the H_2O ice, motivating the argument of salt formation.

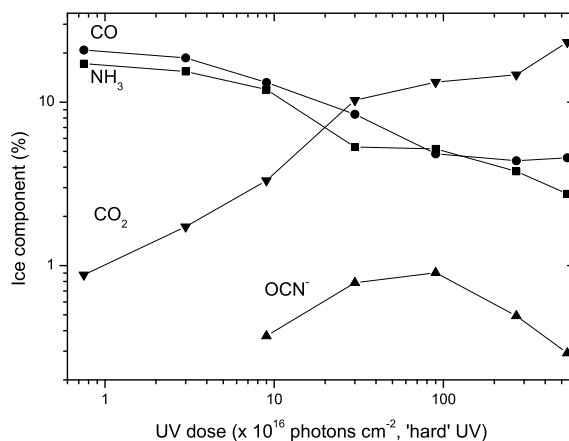


Figure 6.6: Photoprocessing of $\text{H}_2\text{O}/\text{CO}/\text{NH}_3 = 100/22/18$ ice with 'hard' UV photons. All ice components are shown as the percentage of the initial H_2O abundance.

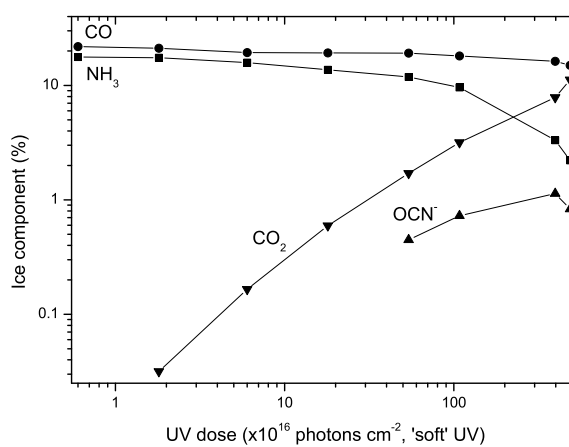


Figure 6.7: Photoprocessing of $\text{H}_2\text{O}/\text{CO}/\text{NH}_3 = 100/22/18$ ice with 'soft' UV photons. All ice components are shown in percentage of the initial H_2O abundance.

All the matrices studied were optically thin to UV radiation. Nevertheless, thicker ice layers are seen to support a higher OCN^- formation efficiency than thinner ones. The thicker the ice, the lower the ratio of photons/molecule needed to favor the processes involved in formation. A second, more plausible, explana-

Table 6.4: OCN^- peak abundances obtained by UV photoprocessing

Matrix composition			Layer thickness	OCN^- ^a
H ₂ O	CO	NH ₃	(μm)	(max.)
Variable layer thickness				
100	24	22	0.026	1.03
100	24	20	0.08	1.26
100	24	21	0.12	1.38
Variable NH ₃ abundance				
100	24	9	0.08	0.50
100	23	31	0.03	1.74
100	23	34	0.14	1.98
Variable CO abundance				
100	8	20	0.06	0.58
100	39	20	0.011	1.29
100	55	21	0.08	1.78
-	56	20	0.07	1.77
Variable NH ₃ at double CO abundance				
100	56	8	0.08	0.45
100	53	32	0.08	2.68
100	42	32	0.05	1.88
Variable NH ₃ at half CO abundance				
100	9	8	0.07	0.32
100	7	31	0.07	0.56
H ₂ O/CH ₃ OH/NH ₃				
100	22	9	0.09	1.1
100	35	11	0.07	1.6
100	15	15	0.10	1.2
100	28	40	0.07	1.6
Various				
100	24	20 ^b	0.07	0.96
100	25	20 ^c	0.10	1.05
100	50	20 ^d	0.016	0.41
100	-	18 ^e	0.12	1.00
-	24	- ^f	0.08	-
-	-	20 ^g	0.05	-
-	-	- ^h	0.06	-

All experiments are performed under standard conditions, $T = 15$ K and irradiation with 'hard' UV photons of 4×10^4 K, unless otherwise stated. Results are obtained with an accuracy of 20%; ^a abundance relative to the originally abundant H₂O in %; ^b $T = 50$ K; ^c Irradiation with a UV field of soft UV photons (1×10^4 K) at $T = 15$ K; ^d H₂O/NH₃ layer (0.01 μm) with a CO layer (0.006 μm) on top; ^e H₂CO (28%) substitutes CO; ^f N₂ (24%) substitutes NH₃; ^g CH₄ (20%) substitutes CO; ^h N₂ (24%) and CH₄ (20%) substitute NH₃ and CO.

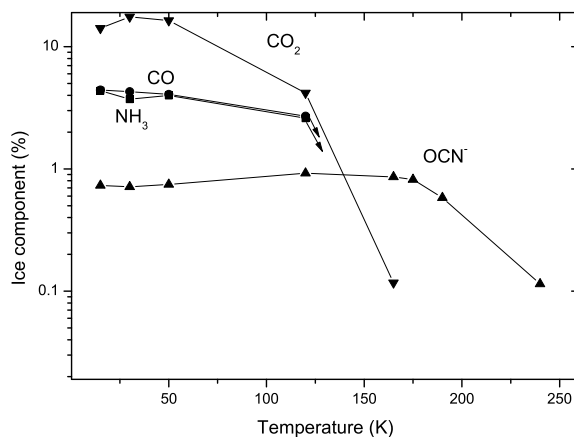


Figure 6.8: Thermal annealing of a photoprocessed $\text{H}_2\text{O}/\text{CO}/\text{NH}_3 = 100/22/18$ ice ('hard' UV). All ice components are shown in percentage of the initial H_2O abundance.

tion could be a caging effect that effectively slows down the dissociation of HNCO into $\text{NH} + \text{CO}$, making the reaction of $\text{H} + \text{NCO}$ more prominent. This is shown in noble gas matrices by Pettersson et al. (1999). Since the photoproduction of OCN^- is also likely to be matrix-assisted and the amorphous ice in which OCN^- is formed allows for some mobility of the photoproducts, the trapping of volatile intermediate products will be more effective in thicker ice layers and will result in a higher maximal OCN^- abundance. Our experiments are, however, not detailed enough to draw strong conclusions on the mechanisms involved.

Under 'Various' in Table 6.4 some experiments are listed that differ from the adopted standard conditions. Either the experimental conditions or the initial composition of the matrix is changed. UV processing of ice at elevated temperatures of 50 K results in a lower OCN^- production efficiency than at 15 K. The ice was grown under standard conditions at 15 K and then brought to 50 K for irradiation. Fig. 6.8 shows that CO and NH_3 slowly evaporate from such an ice matrix, which will cause a continuous decrease in concentration that in turn leads to a lower photoproduction of OCN^- . Alternatively, volatile intermediates evaporate more easily at higher temperatures, leading to lower production. This observation supports the argument above that increased product mobility in the ice lowers the maximum OCN^- formation efficiency.

A two phase model, in which CO is deposited on top of H_2O and NH_3 , shows that NH_3 and CO residing in different, adjoining, ice layers on a grain forms no restriction for OCN^- formation. The efficiency of formation is considerably lower than for mixed matrices but much higher than would be expected from a purely interface-based reaction and could be partly explained by CO grown on top of amorphous ice, making use of a much larger surface area to react. Also, UV pho-

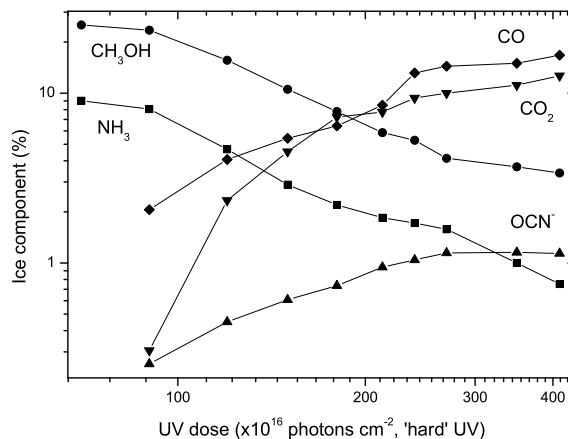


Figure 6.9: Photoprocessing of $\text{H}_2\text{O}/\text{CH}_3\text{OH}/\text{NH}_3 = 100/22/9$ ice with 'hard' UV photons. All ice components are shown in percentage of the initial H_2O abundance.

tons are likely to locally increase the effective temperature of the ice that increases diffusion and can lead to the mixing and trapping of CO, such as occurs upon thermal warming.

In analogy to CO, the more reduced species H_2CO , CH_3OH and CH_4 were also tested for their OCN^- production efficiency. H_2CO and CH_3OH showed favorable results and will be discussed in Sect. 6.3.5. CH_4 was found not to be an OCN^- precursor through UV photoprocessing. Also when NH_3 was substituted by N_2 no OCN^- formation was observed.

6.3.5 UV photoprocessing of $\text{H}_2\text{O}/\text{CH}_3\text{OH}/\text{NH}_3$ ice

In addition to the CO photolysis experiments, the OCN^- production has been examined in several ice matrices in which CO was replaced by more reduced analogs, e.g. H_2CO and CH_3OH . Methanol is the second most abundant molecule observed in interstellar ices for some lines of sight (Allamandola et al., 1992; Dartois et al., 1999b; Pontoppidan et al., 2003). Previous experiments by Bernstein et al. (1995) showed that photoprocessing of methanol in H_2O -ice produces similar oxygen-containing molecules as ices containing H_2O , CO and NH_3 . A further look into the production efficiency from CH_3OH at various relative abundances shows that less NH_3 is required in the starting ice-matrix to produce similar amounts of OCN^- as does a corresponding CO-containing ice matrix. Fig. 6.9 shows the photoprocessing of NH_3 and CH_3OH and the evolution of OCN^- . Compared to Fig. 6.6 both ices form similar quantities of OCN^- , however, in the presence of CH_3OH only half as much NH_3 is required initially to obtain the same amount of OCN^- (also Table 6.4). Notably, in this case, a higher ($\sim 3\times$) fluence

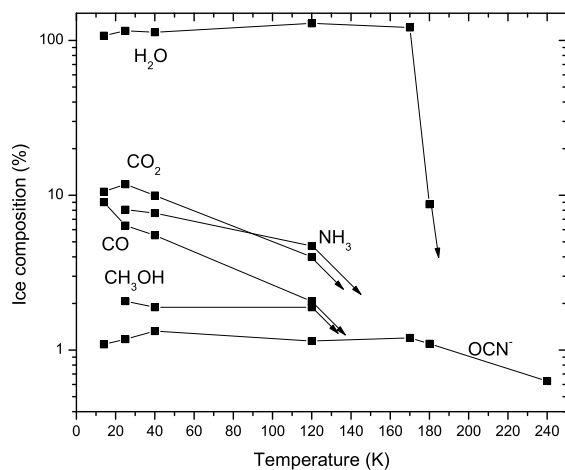


Figure 6.10: Thermal annealing of $\text{H}_2\text{O}/\text{CH}_3\text{OH}/\text{NH}_3 = 100/15/15$ ice. All species are in percentage relative to the initial H_2O abundance.

of $\sim 4 \times 10^{18}$ 'hard' UV-photons cm^{-2} is needed to reach maximum OCN^- abundance, resulting in higher NH_3 destruction.

The thermal processing of a photoprocessed $\text{H}_2\text{O}/\text{CH}_3\text{OH}/\text{NH}_3 = 100/15/15$ ice (initial composition) at maximal OCN^- production is shown in Fig. 6.10 and looks highly similar to the thermal processing of its irradiated CO-analog shown in Fig. 6.8. H_2O is included in this plot as a percentage of its own initial band strength to give an idea of the coexistence of H_2O -ice and solid OCN^- at different temperatures. It is important to realize that the H_2O -ice feature at $3 \mu\text{m}$ undergoes an enormous change around 120 K due to crystallisation and that this will directly effect the OCN^- matrix environment. It is also interesting to note that OCN^- evaporates at somewhat higher temperatures, 200–240 K, than H_2O but that the evaporation of H_2O is not accompanied by a major change in the infrared-feature at $4.62 \mu\text{m}$.

6.4 Astrophysical Implications

OCN^- is easily formed in the laboratory by energetic processing of interstellar ice analogs. Moreover, the fact that OCN^- can be readily produced by UV photolysis has led to the direct association of this interstellar feature with UV processing of ices in molecular clouds (Pendleton et al., 1999). The unambiguous interpretation of this feature as a diagnostic of photoprocessing, however, needs some in-depth analysis of the conditions under which OCN^- forms, its yield and the by-products of its formation. Hereby the caveat of Sect. 6.2 must be kept in mind when scaling laboratory data to the observations.

Detections and upper limits on the interstellar $4.62 \mu\text{m}$ feature observed to-

Table 6.5: Abundances and temperatures observed toward various sources

Source	A_v	H ₂ O (10 ¹⁸)	NH ₃ /H ₂ O (10 ⁻²)	CH ₃ OH/H ₂ O (10 ⁻²)	OCN ⁻ /H ₂ O (10 ⁻³)	CO _{total} $N \times 10^{17} \text{ cm}^{-2}$	CO ₂ -bend T (K)
W3 IRS5	144 ¹⁶	5.4 ¹	<3.5 ¹	≤ 2.96 ¹⁶	≤ 5.2 ³⁴	<1.7 ¹⁷	136 ¹
W 33 A	148 ¹⁴	12 ¹⁵	≤ 5 ³¹	15.4 ¹⁴	22.1 ¹⁵	3.9 ¹⁷	136 ¹ /50–90 ¹⁹
GL 2136	94.3 ³⁷	5 ¹	5.4 ²⁵	5.2 ²⁰	2.6 ²⁷	0.62 ²⁶	117 ¹
GL 2591	n.d.	1.7 ¹	n.d.	4.12 ¹	n.d.	<0.4 ²⁶	117 ¹
S140	75 ¹⁶	2.15 ¹	n.d.	≤ 2.79 ¹⁶	n.d.	n.d.	136 ¹
NGC 7538 IRS9	≥ 84 ¹⁶	8 ¹	8 ²⁵	6.06 ²³	5.8 ²⁷	9.6 ²⁶	119 ¹ /50–90 ¹⁹
AFGL 7009S	75 ¹⁴	12 ¹⁴	. ¹¹	29.5 ¹⁴	13.5 ²⁸	n.d.	85 ³
AFGL 961E	40 ¹⁴	4.2 ¹⁸	n.d.	≤ 4.76 ¹⁶	2.7 ²⁷	n.d.	n.d.
MonR2 IRS2	21 ¹⁷	5.9 ²	n.d.	2.20 ²⁰	6.5 ²⁷	n.d.	n.d.
IRAS 08448-4343	40 ⁵	7.8 ⁵	n.d.	0.84 ⁵	1.7 ⁵	n.d.	n.d.
L1551 IRS5	≥ 19 ¹⁰	3.5 ²⁹	n.d.	n.d.	14.1 ²⁹	3.0 ¹⁷	n.d.
RNO 91	≥ 10 ⁷	2.2 ²	n.d.	n.d.	≤ 13.1 ²	n.d.	n.d.
Elias 18	17 ⁶	1.5 ²	n.d.	5.33 ²¹	7.2 ³⁰	2.3 ¹²	20–30 ¹²
PV Cep	19 ³²	7.4 ²	n.d.	n.d.	≤ 0.8 ²	n.d.	n.d.
Elias 1-12	10 ⁶	1.1 ²	n.d.	n.d.	≤ 5.6 ²	n.d.	n.d.
HL Tau	22 ²²	1.4 ²	n.d.	n.d.	≤ 5.1 ²¹	≤ 2.1 ²	n.d.
HH100-IR	25 ⁹	3.9 ¹⁴	5.6 ²⁵	≤ 6.15 ²⁴	3.4 ⁴	n.d.	10 ¹²
Elias 29	<23 ¹⁹	<1.1 ¹⁹	<13 ¹¹	≤ 2.5 ¹⁹	≤ 0.4 ¹⁹	1.7 ¹⁹	<40 ¹¹
Elias 16	21 ³²	2.5 ¹²	n.d.	≤ 2.9 ²¹	≤ 23.1 ⁴	6.1 ⁹⁵	10 ¹
GC:IRS19	n.d.	3.6 ⁸	5 ³⁵	n.d.	32.1 ⁸	1.4 ¹³	10–40 ⁸ (H ₂ O 3.0 μm)
SgrA*	~31 ³⁶	1.24 ³⁵	≤5 ¹	<4 ³⁵	20 ³³	<1.5 ³⁵	10–15 ³⁵ (H ₂ O 3.0 μm)
NGC 4945	n.d.	3.5–4.3 ³³	n.d.	n.d.	38–46 ³³	9.7 ³³	≤90 ³³

n.d. indicates measures that have not yet been determined; ¹ Gerakines et al. (1999); ² Keane et al. (2001); ³ Dartois et al. (1999b); ⁴ Whittet et al. (2001); ⁵ Thi et al. (2002); ⁶ Whittet et al. (1985); ⁷ Weintraub et al. (1991); ⁸ Chiar et al. (2002); ⁹ Whittet et al. (1996); ¹⁰ Cohen (1975); Davidson & Jaffe (1984); ¹¹ Boogert et al. (2000b); ¹² Nummelin et al. (2001, Temperature determination by fitting of the 4.27 μm feature of CO₂); ¹³ Moneti et al. (2001, Temperature is determined towards Sgr A* from CO gas lines); ¹⁴ Dartois et al. (1999a); ¹⁵ Gibb et al. (2000); ¹⁶ Brooke et al. (1996); ¹⁷ Tielens et al. (1991); ¹⁸ Smith et al. (1989); ¹⁹ Boogert et al. (2000a); ²⁰ Brooke et al. (1999); ²¹ Chiar et al. (1996); ²² Stapelfeldt et al. (1995); ²³ Allamandola et al. (1992); ²⁴ Graham (1998); ²⁵ Gürtler et al. (2002); ²⁶ Sandford et al. (1988); ²⁷ Pendleton et al. (1999); ²⁸ Demyk et al. (1998); ²⁹ Tegler et al. (1993); ³⁰ Tegler et al. (1995); ³¹ Taban et al. (2003); ³² Whittet et al. (1988); ³³ Spoon et al. (2003); ³⁴ Lacy (1979); ³⁵ Chiar et al. (2000); ³⁶ Rieke et al. (1989, and references therein); ³⁷ Willner et al. (1982)

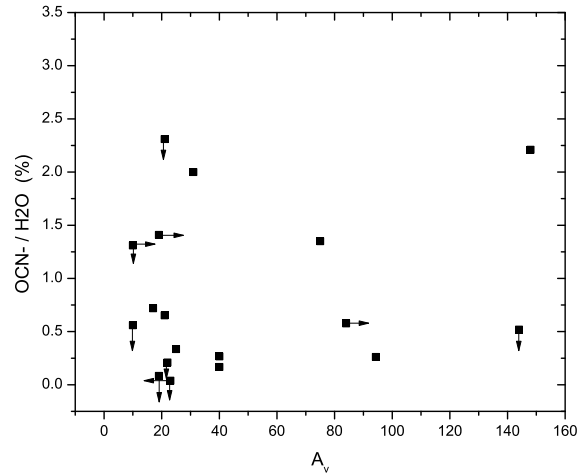


Figure 6.11: Correlation diagram of OCN^- , shown in abundance relative to H_2O , with the visual extinction A_v . Upper limits are indicated by arrows.

wards a variety of lines-of-sight are summarised in Table 6.5. The top part of the table lists high-mass YSO's, the middle part low-mass YSO's and the bottom part background sources, GC sources and an external galaxy. Typical abundances with respect to H_2O range from 0.2%–0.8% for both high and low mass stars, with a few exceptions where the observed values increase up to 1.4%–2.2%. W 33 A, by far the best studied object, shows the highest OCN^- content (2.2% relative to H_2O) in our galaxy, making it best suited to constrain the possible OCN^- production mechanisms. Recently Chiar et al. (2002) detected an even higher abundance of 3.6% OCN^- toward GC:IRS 19, and Spoon et al. (2003) find 3.4%–3.9% OCN^- towards the central region of the starburst galaxy NGC 4945. Fig. 6.11 shows that there is no correlation with A_v , stressing that OCN^- is most likely inhomogeneously distributed over the line-of-sight.

The experiments presented in Sect. 7.5 clearly show that OCN^- can form from many different ices under various conditions. Its formation efficiency is found to depend on the energy distribution of the radiation source and on the thickness, the temperature and, above all, the composition of the ice. Here we assess the probability of the various formation routes under interstellar conditions as well as search for correlations with established interstellar parameters.

6.4.1 UV photoprocessing: CO

UV photoprocessed ice matrices, composed of H_2O , CO and NH_3 , are shown to match the interstellar $4.62 \mu\text{m}$ feature nicely but a quantitative analysis proves that this route is inefficient. A large amount of CO and NH_3 is needed to reproduce the observed abundances. This problem is most severe towards W 33 A.

Assuming that the 2.2% of OCN^- observed towards W 33 A corresponds to a local maximum, Table 6.4 shows that the initial ice matrix needs to have at least 25%–50% CO and 30% NH_3 at 15 K, relative to H_2O . Table 6.5 includes the observed solid CO and NH_3 abundances towards a variety of sources. CO ice is detected towards numerous lines-of-sight and sets no constraints on the production possibility of OCN^- . NH_3 is more controversial with upper limits of the order of 5% (Taban et al., 2003). Even when photodestruction and storage in NH_4^+ is taken into account this upper limit makes it unlikely that interstellar ices could contain abundances as high as 30%. On the other hand, Table 6.4 shows that typical abundances of 0.2%–0.8%, found for OCN^- towards a number of sources (Table 5), are produced from a realistic interstellar ice analog, initially containing $\sim 8\%$ NH_3 with respect to H_2O .

In addition to NH_3 , the presence of UV photons enforces a constraint on the photoproduction of OCN^- . In the laboratory, the UV fluence that produces the maximum amount of OCN^- corresponds to a molecular cloud at an age of $\sim 4 \times 10^7$ yr with a cosmic-ray induced UV-field of 1.4×10^4 photons $\text{cm}^{-2} \text{s}^{-1}$ (Prasad & Tarafdar, 1983). This timescale is quite long compared with that estimated for the dense pre-stellar and YSO phases where ices are produced. Regions which could have sufficient UV to form OCN^- include the outer regions of protoplanetary discs (Herbig & Goodrich, 1986) or clouds located close to bright O & B stars (Mathis et al., 1983). However, since the $4.62 \mu\text{m}$ absorption band is only observed in association with H_2O ice, which is generally not seen in regions with large UV intensity, this casts doubt on its formation in such regions as well (Whittet et al., 2001). Based on these arguments, UV photoprocessing of H_2O , CO and NH_3 containing ices alone cannot account for the OCN^- abundance observed towards W 33 A, GC:IRS19, SgrA* and NGC 4945.

6.4.2 UV photolysis: Methanol

Methanol is the second most abundant ice component towards W 33 A and AFGL 7009S (Dartois et al., 1999b) and is highly abundant in the line-of-sight towards many objects that also show OCN^- . Gibb et al. (2000) suggest a possible correlation between the extent of ice processing and the methanol abundance. CH_3OH is thought to form by the sequential hydrogenation of CO on grain surfaces (Tielens & Charnley, 1997), which is believed to include some endothermic reaction steps that could be facilitated, or exclusively occur, when the ice is energetically processed, either thermally or photochemically. If the origin of CH_3OH is somehow coupled to irradiation, then a correlation with OCN^- could be expected. Fig. 6.12 shows the abundances of CH_3OH and OCN^- , relative to H_2O . A tentative but weak trend can be observed to support this idea, but it is based on only a few clear detections and decidedly more upper limits. This figure does not yet include the new detections of CH_3OH in low-mass YSOs by Pontoppidan et al. (2003). It will be particularly interesting to check the OCN^- abundance in these objects.

Laboratory experiments on the photoprocessing of $\text{H}_2\text{O}/\text{CH}_3\text{OH}/\text{NH}_3$ ices, Table 6.4, show methanol to be a similarly effective precursor of OCN^- as CO. The high methanol abundances observed support this possible route of formation.

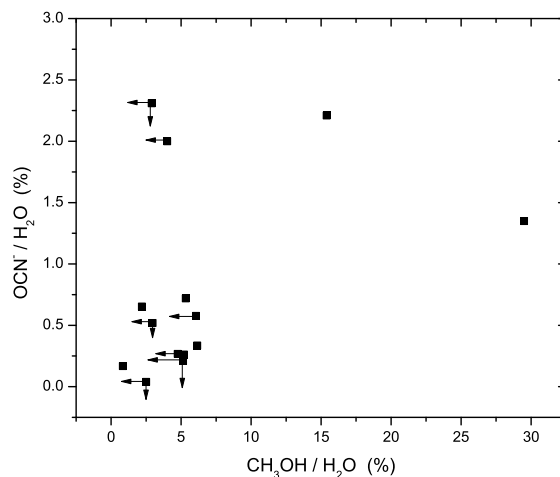


Figure 6.12: Correlation diagram of OCN^- and CH_3OH , both shown in abundance relative to H_2O . Upper limits are indicated by arrows.

Again a considerable initial abundance of NH_3 ice is required, although less than in CO mixtures. The UV fluence needed to produce OCN^- via CH_3OH , which is $\sim 3\times$ higher than for CO, results in a high degree of photodissociation of NH_3 , such that any remaining NH_3 could be consistent with the observed conservative upper limits (5% relative to H_2O towards W 33 A). However, such a high fluence is not expected to be present in the environments that show the $4.62\ \mu\text{m}$ feature which puts strong doubts on this formation mechanism (see discussion above).

6.4.3 UV photolysis or thermal processing: HNCO

The acid-base reaction that forms OCN^- in the condensed phase is efficiently mediated by thermal processing as well as by UV photoprocessing of HNCO-containing ice in the laboratory. How HNCO ices are formed on interstellar grains remains an unaddressed issue in this paper. HNCO is abundant in the gas phase in hot cores and regions associated with high mass star formation and shocked gas (Zinchenko et al., 2000, and references therein) but no HNCO has yet been detected in interstellar ices. One way to form HNCO is by grain-surface reactions in dense molecular clouds, which can lead to abundances of $\sim 3\%$ with respect to H_2O (Hasegawa & Herbst, 1993). In the gas phase, either an ion-molecule reaction mechanism or a neutral-neutral reaction pathway is suggested (Iglesias, 1977; Turner et al., 1999).

We determined upper limits on the HNCO ice abundance for NGC 7538 IRS9 ($\leq 0.5\%$), GL 2136 ($\leq 0.7\%$) and W 33 A ($\leq 0.5\%$). These allow for a minimal conversion to OCN^- of $\sim 50\%$, $\sim 50\%$ and $\sim 75\%$, respectively. NH_4^+ , detected toward various sources, is sufficiently abundant to balance the observed OCN^- (Keane

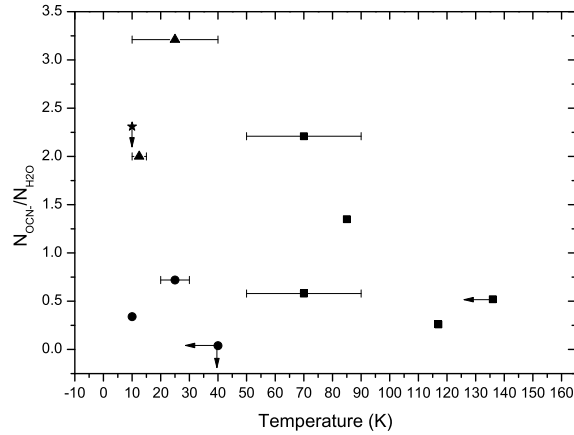


Figure 6.13: OCN^- abundance relative to H_2O , as a function of the ice temperature, observed towards YSOs. Upper limits are indicated by arrows.

et al., 2001; Schutte & Khanna, 2003). Induced by UV, this reaction mechanism would require a minimal fluence of $\sim 2 \times 10^{16}$ photons cm^{-2} (50% conversion) or 1×10^{17} photons cm^{-2} (75% conversion) of hard UV in the laboratory. In analogy to the discussion above on the presence of UV this very likely exceeds the acceptable fluence seen by a grain inside a cloud integrated over the lifetime of a molecular cloud.

Alternatively, a $\sim 75\%$ conversion can be thermally mediated at a temperature of 60–90 K in the laboratory, which is in good agreement with the temperatures found for the dominant part of the ice observed towards NGC 7538 IRS9, GL 2136 and W 33 A. Table 5 includes the (laboratory) temperature that best fits the solid CO_2 feature (Boogert et al., 2000a; Gerakines et al., 1999). Figure 6.13 shows the OCN^- abundance as a function of this temperature. No OCN^- is detected toward sources with CO_2 temperatures higher than 140 K but it seems randomly distributed at lower temperatures. Since its thermal formation starts at 15–20 K, this indirectly indicates an initially random HNC/O distribution. However, such a conclusion is premature since the presence or absence of other sources of energetic processing will highly influence any relation.

The combination of the efficiency of this process ($\sim 100\%$), the low NH_3 requirement, the low temperature formation route and the detection of NH_4^+ towards W 33 A make thermal processing of HNC/O the most favorable production mechanism for OCN^- .

6.5 Conclusion

We have presented a laboratory study on the efficiency of thermal versus UV-mediated OCN⁻ formation to qualitatively investigate the interstellar 4.62 μm feature. OCN⁻ is easily formed by UV-photolysis of an ice matrix of H₂O/CO/NH₃ and also when CO is replaced by CH₃OH or HNCO. Nevertheless, it remains questionable whether sufficient UV-photons are present inside dense clouds. UV photolysis also requires high initial abundances of NH₃ to reproduce the optical depth of the 4.62 μm feature, particularly towards YSO's where observed OCN⁻ abundances exceed 1.2% with respect to H₂O. Moreover, when starting from a CO ice mixture, the amount of NH₃ remaining in the ice after photoprocessing is too high to be consistent with the conservative upper limit of 5% determined toward W 33 A. In a CH₃OH ice mixture a lower NH₃ content is needed but the UV fluence required is approximately 3 \times higher with respect to a CO-containing ice. The most favorable OCN⁻ formation route emerging from this study is the thermal processing of HNCO-containing ices. Provided that HNCO is present in interstellar ices, thermal processing is \sim 100% efficient and is consistent with the data in particular toward W 33 A, NGC 7538 IRS9 and GL 2136. Also the inferred interstellar ice temperatures along the line-of-sight towards other OCN⁻-containing YSO's are in agreement with this route of formation.

In the case of sources for which OCN⁻ has not been detected, little insight can be gained about its formation mechanism. They could be either too young (too little UV exposure) or colder than 10 K. In these cases, HNCO can be present but only in H₂O-rich ices at temperatures below 10 K. At higher temperatures, the presence of sufficient amounts of proton acceptors like NH₃ rapidly induces OCN⁻ formation. A non-detection for OCN⁻ would in that case indicate lack of HNCO or NH₃ formation. Future searches for weak OCN⁻, NH₃ and HNCO features are needed to further constrain these chemical routes.

Acknowledgements

The authors wish to thank Helen Fraser and Klaus Pontoppidan for interesting discussions and Ewine van Dishoeck for many helpful comments on the paper. This research was financially supported by the Netherlands Research School for Astronomy (NOVA) and a NWO Spinoza grant.

Bibliography

- Agarwal, V. K., Schutte, W., Greenberg, J. M., et al. 1985, *Origins of Life*, 16, 21
- Allamandola, L. J., Bernstein, M. P., Sandford, S. A., & Walker, R. L. 1999, *Space Science Reviews*, 90, 219
- Allamandola, L. J., Sandford, S. A., Tielens, A. G. G. M., & Herbst, T. M. 1992, *ApJ*, 399, 134
- Bernstein, M. P., Sandford, S. A., Allamandola, L. J., Chang, S., & Scharberg, M. A. 1995, *ApJ*, 454, 327
- Boogert, A. C. A., Ehrenfreund, P., Gerakines, P. A., et al. 2000a, *A&A*, 353, 349
- Boogert, A. C. A., Tielens, A. G. G. M., Ceccarelli, C., et al. 2000b, *A&A*, 360, 683
- Brooke, T. Y., Sellgren, K., & Geballe, T. R. 1999, *ApJ*, 517, 883
- Brooke, T. Y., Sellgren, K., & Smith, R. G. 1996, *ApJ*, 459, 209
- Chiar, J. E., Adamson, A. J., Pendleton, Y. J., et al. 2002, *ApJ*, 570, 198
- Chiar, J. E., Adamson, A. J., & Whittet, D. C. B. 1996, *ApJ*, 472, 665
- Chiar, J. E., Tielens, A. G. G. M., Whittet, D. C. B., et al. 2000, *ApJ*, 537, 749
- Cohen, M. 1975, *MNRAS*, 173, 279
- Dartois, E., Demyk, K., d'Hendecourt, L., & Ehrenfreund, P. 1999a, *A&A*, 351, 1066
- Dartois, E., Schutte, W., Geballe, T. R., et al. 1999b, *A&A*, 342, L32
- Davidson, J. A. & Jaffe, D. T. 1984, *ApJL*, 277, L13
- Demyk, K., Dartois, E., D'Hendecourt, L., et al. 1998, *A&A*, 339, 553
- d'Hendecourt, L. B. & Allamandola, L. J. 1986, *A&AS*, 64, 453
- d'Hendecourt, L. B., Allamandola, L. J., Grim, R. J. A., & Greenberg, J. M. 1986, *A&A*, 158, 119
- Gürtler, J., Klaas, U., Henning, T., et al. 2002, *A&A*, 390, 1075
- Gerakines, P. A., Schutte, W. A., & Ehrenfreund, P. 1996, *A&A*, 312, 289
- Gerakines, P. A., Schutte, W. A., Greenberg, J. M., & van Dishoeck, E. F. 1995, *A&A*, 296, 810
- Gerakines, P. A., Whittet, D. C. B., Ehrenfreund, P., et al. 1999, *ApJ*, 522, 357
- Gibb, E. L., Whittet, D. C. B., & Chiar, J. E. 2001, *ApJ*, 558, 702
- Gibb, E. L., Whittet, D. C. B., Schutte, W. A., et al. 2000, *ApJ*, 536, 347
- Graham, J. A. 1998, *ApJ*, 492, 213
- Grim, R. J. A. & Greenberg, J. M. 1987, *ApJL*, 321, L91
- Grim, R. J. A., Greenberg, J. M., de Groot, M. S., et al. 1989, *A&AS*, 78, 161
- Hagen, W., Greenberg, J. M., & Tielens, A. G. G. M. 1983, *A&AS*, 51, 389

Bibliography

- Hasegawa, T. I. & Herbst, E. 1993, *MNRAS*, 263, 589
- Herbig, G. H. & Goodrich, R. W. 1986, *ApJ*, 309, 294
- Iglesias, E. 1977, *ApJ*, 218, 697
- Keane, J. V., Tielens, A. G. G. M., Boogert, A. C. A., Schutte, W. A., & Whittet, D. C. B. 2001, *A&A*, 376, 254
- Lacy, J. H. 1979, Ph.D. Thesis
- Lacy, J. H., Baas, F., Allamandola, L. J., et al. 1984, *ApJ*, 276, 533
- Lowenthal, M. S., Khanna, R. K., & Moore, M. H. 2000, *Bulletin of the American Astronomical Society*, 32, 1108
- Mathis, J. S., Mezger, P. G., & Panagia, N. 1983, *A&A*, 128, 212
- Moneti, A., Cernicharo, J., & Pardo, J. R. 2001, *ApJL*, 549, L203
- Moore, M. H., Donn, B., Khanna, R., & A'Hearn, M. F. 1983, *Icarus*, 54, 388
- Muñoz Caro, G. M. & Schutte, W. A. 2003, *A&A*, 412, 121
- Novozamsky, J. H., Schutte, W. A., & Keane, J. V. 2001, *A&A*, 379, 588
- Nummelin, A., Whittet, D. C. B., Gibb, E. L., Gerakines, P. A., & Chiar, J. E. 2001, *ApJ*, 558, 185
- Pendleton, Y. J., Tielens, A. G. G. M., Tokunaga, A. T., & Bernstein, M. P. 1999, *ApJ*, 513, 294
- Pettersson, M., Khriachtchev, L., & Jolkkonen, S. 1999, *Phys. Chem. A*, 103, 9154
- Pontoppidan, K. M., Dartois, E., van Dishoeck, E. F., Thi, W.-F., & d'Hendecourt, L. 2003, *A&A*, 404, L17
- Prasad, S. S. & Tarafdar, S. P. 1983, *ApJ*, 267, 603
- Raunier, S., Chiavassa, T., Allouche, A., Marinelli, F., & Aycard, J. P. 2003a, *Chem. Phys.*, 288, 197
- Raunier, S., Chiavassa, T., Marinelli, F., Allouche, A., & Aycard, J. P. 2003b, *Chem. Phys. Lett.*, 368, 594
- Rieke, G. H., Rieke, M. J., & Paul, A. E. 1989, *ApJ*, 336, 752
- Sandford, S. A., Allamandola, L. J., Tielens, A. G. G. M., & Valero, G. J. 1988, *ApJ*, 329, 498
- Schutte, W. A., Allamandola, L. J., & Sandford, S. A. 1993, *Icarus*, 104, 118
- Schutte, W. A., Boogert, A. C. A., Tielens, A. G. G. M., et al. 1999, *A&A*, 343, 966
- Schutte, W. A. & Greenberg, J. M. 1991, *A&A*, 244, 190
- Schutte, W. A. & Greenberg, J. M. 1997, *A&A*, 317, L43
- Schutte, W. A. & Khanna, R. K. 2003, *A&A*, 398, 1049
- Smith, R. G., Sellgren, K., & Tokunaga, A. T. 1989, *ApJ*, 344, 413
- Soifer, B. T., Puetter, R. C., Russell, R. W., et al. 1979, *ApJL*, 232, L53
- Spoon, H. W. W., Moorwood, A. F. M., Pontoppidan, K. M., et al. 2003, *A&A*, 402, 499
- Stapelfeldt, K. R., Burrows, C. J., Krist, J. E., et al. 1995, *ApJ*, 449, 888
- Taban, I. M., Schutte, W. A., Pontoppidan, K. M., & van Dishoeck, E. F. 2003, *A&A*, 399, 169
- Tegler, S. C., Weintraub, D. A., Allamandola, L. J., et al. 1993, *ApJ*, 411, 260
- Tegler, S. C., Weintraub, D. A., Rettig, T. W., et al. 1995, *ApJ*, 439, 279

- Thi, W. F., Pontoppidan, K. M., van Dishoeck, E. F., Dartois, E., & d'Hendecourt, L. 2002, *A&A*, 394, L27
- Tielens, A. G. G. M. & Charnley, S. B. 1997, *Origins of Life and Evolution of the Biosphere*, 27, 23
- Tielens, A. G. G. M., Tokunaga, A. T., Geballe, T. R., & Baas, F. 1991, *ApJ*, 381, 181
- Turner, B. E., Terzieva, R., & Herbst, E. 1999, *ApJ*, 518, 699
- Weintraub, D. A., Sandell, G., & Duncan, W. D. 1991, *ApJ*, 382, 270
- Wexler, S. P. 1967, *Appl. Spectr. Rev.*, 1, 29
- Whittet, D. C. B., Bode, M. F., Longmore, A. J., et al. 1988, *MNRAS*, 233, 321
- Whittet, D. C. B., McFadzean, A. D., & Longmore, A. J. 1985, *MNRAS*, 216, 45P
- Whittet, D. C. B., Pendleton, Y. J., Gibb, E. L., et al. 2001, *ApJ*, 550, 793
- Whittet, D. C. B., Smith, R. G., Adamson, A. J., et al. 1996, *ApJ*, 458, 363
- Willner, S. P., Gillett, F. C., Herter, T. L., et al. 1982, *ApJ*, 253, 174
- Zinchenko, I., Henkel, C., & Mao, R. Q. 2000, *A&A*, 361, 1079

Bibliography

Chapter 7

A 3-5 μ m VLT spectroscopic survey of young low mass stars II: solid OCN⁻

Abstract

The 4.62 μ m (2164.5 cm⁻¹) 'XCN' band has been detected in the M-band spectra of 34 deeply embedded young stellar objects (YSO's), observed with high signal-to-noise and high spectral resolution with the VLT-ISAAC spectrometer, providing the first opportunity to study the solid OCN⁻ abundance toward a large number of low-mass YSO's. It is shown unequivocally that at least two components, centred at 2165.7 cm⁻¹ (FWHM = 26 cm⁻¹) and 2175.4 cm⁻¹ (FWHM = 15 cm⁻¹), underlie the XCN band. Only the 2165.7-component can be ascribed to OCN⁻, embedded in a strongly hydrogen-bonding, and possibly thermally annealed, ice environment based on laboratory OCN⁻ spectra. In order to correct for the contribution of the 2175.4-component to the XCN band, a phenomenological decomposition into the 2165.7- and the 2175.4-components is used to fit the full band profile and derive the OCN⁻ abundance for each line-of-sight. The same analysis is performed for 5 high-mass YSO's taken from the ISO-SWS data archive. Inferred OCN⁻ abundances are $\leq 0.85\%$ toward low-mass YSO's and $\leq 1\%$ toward high-mass YSO's, except for W33 A. Abundances are found to vary by at least a factor of 10–20 and large source-to-source abundance variations are observed within the same star-forming cloud complex on scales down to 400 AU, indicating that the OCN⁻ formation mechanism is sensitive to local conditions. The inferred abundances allow quantitatively for photochemical formation of OCN⁻, but the large abundance variations are not easily explained in this scenario unless local radiation sources or special geometries are invoked. Surface chemistry should therefore be considered as an alternative formation mechanism. ^{1 2}

¹F.A. van Broekhuizen, K.M. Pontoppidan, H.J. Fraser, and E.F. van Dishoeck

²Based on observations obtained at the European Southern Observatory, Paranal, Chile, within the observing programs 164.I-0605 and 69.C-0441. ISO is an ESA project with instruments funded by ESA Member States (especially the PI countries: France, Germany, The Netherlands and the UK), and with the participation of ISAS and NASA.

7.1 Introduction

The 4.62 μ m (2165 cm^{-1}) feature, commonly referred to as the XCN band, was first detected toward the massive protostar W 33A by Soifer et al. (1979). Its presence was the first observational indication that complex chemistry could be occurring in interstellar ice mantles. Subsequently, a similar feature was observed around a number of other sources, mostly high-mass young stellar objects (YSO's) (Demyk et al., 1998; Gibb et al., 2000; Keane et al., 2001; Pendleton et al., 1999; Tegler et al., 1993, 1995; Whittet et al., 2001), one field star (Tegler et al., 1995) and several galactic centre sources (Chiar et al., 2002; Spoon et al., 2003).

Pontoppidan et al. (2003) (henceforth referred to as Paper I) have recently presented M -band spectra of 44 YSO's, 31 of which are low-mass sources ($\leq 2 M_{\odot}$, $< 50 L_{\odot}$). Most of these sources are deeply embedded in dark clouds, with few external sources of ultraviolet radiation, offering a unique opportunity to study the chemical characteristics of ice mantles in low-mass star-forming environments. In addition to the strong CO-ice band, observed on most lines of sight, Paper I reported the detection of a weaker band in 34 of the spectra (27 of which were low-mass objects). This band was labelled the 2175 cm^{-1} band because its peak-centre position ranged from 2162-2194 cm^{-1} , with an average value of 2175 cm^{-1} . These were the first reported detections toward a large number of low-mass YSO's of a feature similar to the XCN band.

The XCN band has been studied extensively in the laboratory where it is easily reproduced by proton irradiation (Moore et al., 1983), vacuum ultraviolet photolysis (Demyk et al., 1998; Grim & Greenberg, 1987; Lacy et al., 1984), or thermal annealing (Raunier et al., 2003; van Broekhuizen et al., 2004) of interstellar ice analogues. Experimental studies using isotopic substitution proved unequivocally that the carrier of the laboratory feature is OCN⁻ (Bernstein et al., 2000; Novozamsky et al., 2001; Palumbo et al., 2000; Schutte & Greenberg, 1997). Despite this assignment, alternative identifications of the interstellar feature are still debated (Pendleton et al., 1999).

Here we present a detailed analysis of the 2175 cm^{-1} feature (henceforth described in this paper as the XCN band) for 34 of the YSO's from Paper I, plus 5 additional high-mass YSO's taken from the ISO-SWS data archive, i.e. AFGL 2136, NGC 7538 IRS1, RAFGL 7009S, AFGL 989 and W 33A. Our analysis suggests that two components are required to reproduce the observational line profiles of the XCN band, only one of which can be associated with OCN⁻. The carrier of the second component is not known but may be due to CO gas-grain interactions, as described in detail by Fraser et al. (2005).

In Sect. 2, the observational details are summarised, followed by an overview, in Sect. 3, of laboratory spectroscopy of OCN⁻ in interstellar ice analogues and studies of OCN⁻ formation mechanisms under interstellar conditions, focusing on UV- and thermally induced OCN⁻ formation. The fitting methods used for the XCN band analysis are described in Sect. 4, and the results presented in Sect. 5. In Sect. 6 OCN⁻ abundances are determined and the implications for the OCN⁻ formation mechanisms toward the low-mass YSO's studied here are discussed.

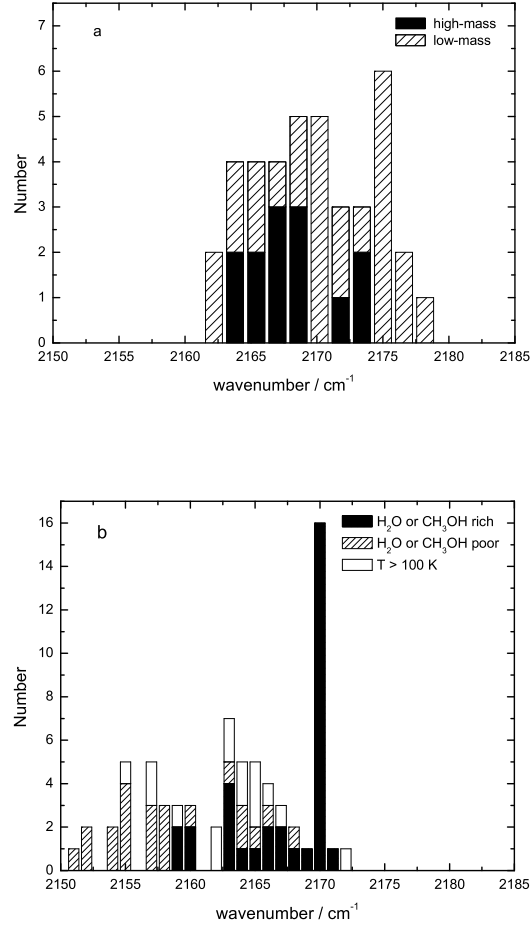


Figure 7.1: (a) Observed peak-centre positions of the XCN band toward all 39 low- and high-mass YSO's studied here. Bands originating in high-mass YSO spectra are represented in black, all other YSO's (dominated by low-mass objects) are hatched. Peak centres are binned at 1.6 cm^{-1} . (b) Peak-centre positions of laboratory spectra of the ν_3 vibrational band of solid OCN^- in a variety of interstellar ice analogues, also summarised in Tables 7.1 and 7.2. H_2O - and CH_3OH -rich ices are shown in black, H_2O - and CH_3OH -free ices are hatched, and those thermally annealed to $\geq 110 \text{ K}$ are white. These centre positions are rounded to the nearest integer wavenumber (cm^{-1}).

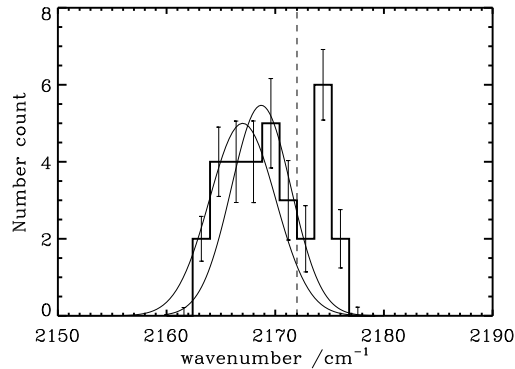


Figure 7.2: The distribution of centre positions of the XCN band toward the various lines-of-sight in bins of 1.6 cm^{-1} including the uncertainties derived from the Monte-Carlo simulations. The Gaussian at 2168.7 cm^{-1} is obtained from a single Gaussian fit to the full data set, that at 2166.9 cm^{-1} from a similar fit excluding all XCN band centres $\geq 2172 \text{ cm}^{-1}$. This analysis strengthens the conclusion that two components are present in the observational data. The dashed line indicates the maximum wavenumber beyond which no laboratory-based $\nu_3(\text{OCN}^-)$ feature has been found in interstellar ice analogues.

7.2 Observations

7.2.1 Observational details

This work uses the M -band spectra of a large sample of deeply embedded young stars, which were first presented in Paper I. The data are part of a 3–5 μm spectroscopic survey of low-mass embedded objects in the nearest star-forming clouds (ρ Oph, Serpens, Orion, Corona Australis, Chamaeleon, Vela, and Taurus) using the Infrared Spectrometer And Array Camera (ISAAC) mounted on UT1-Antu of the Very Large Telescope (VLT) (van Dishoeck et al., 2003). All sources have spectral energy distributions representative of Class I objects, with typical lifetimes of $\sim 10^5$ yr since cloud collapse. The M -band spectra were obtained in the 4.53–4.90 μm range using the medium resolution mode, resulting in a resolving power of $\lambda/\Delta\lambda = 5000$ -10000. The reduction of the spectra is described in detail in Paper I. In short, the spectra were corrected for telluric absorption, flux-calibrated relative to bright early-type standard stars, and wavelength-calibrated relative to telluric absorption lines in the standard star spectrum with an accuracy of $\sim 5 \text{ km s}^{-1}$. The final optical depth spectra were derived by fitting a black-body continuum to the 4.52-4.55 μm and 4.76-4.80 μm regions, where no features are expected, taking care to exclude known gas-phase lines from the fit. The short wavelength end of the spectra is more noisy due to the onset of the strong telluric CO_2 features. In addition, spectra of 5 high-mass sources taken from the ISO-SWS data archive, i.e. AFGL 2136, NGC 7538 IRS1, RAFGL 7009S, AFGL 989 and

W33A, were added to the sample.

7.2.2 The XCN band

In addition to the CO-ice band, a weak secondary feature was detected in a significant subset of the lines of sight. In Paper I this feature was reasonably well reproduced using a single Gaussian whose peak-centre position varied significantly (from 2162 to 2194 cm^{-1}) and Full Width Half Maxima (FWHM) ranged from 9 to 36 cm^{-1} . This distribution is summarised in Fig. 7.1a, where the peak-centres of all XCN bands in the observed sample are plotted, together with the data from the ISO sources.

Careful inspection of the XCN band shows that in some sources like W33 A the feature peaks at 2165.7 cm^{-1} whereas in other sources like Elias 32 and IRS 63 the feature is shifted much further to the blue, around 2175 cm^{-1} . This conclusion that two components underlie the XCN band is supported by a statistical analysis of the observed centre positions shown in Fig. 7.2. The uncertainties in the observed distribution were quantified using a Monte Carlo approach. Each Monte Carlo run varies the XCN band centre position of each source within a normal distribution with a standard deviation from peak-centre position as found in Paper I. This produces a perturbed distribution allowed within the uncertainties on the band positions. By calculating a large number (10^5) of perturbed distributions, an uncertainty on the number of sources within each wavenumber bin can be estimated by simply deriving the standard deviation for the set of perturbed distributions. A single Gaussian distribution centred at $2168.7 \pm 1.9 \text{ cm}^{-1}$ ($\chi^2 = 5.58$) is seen to give a poor fit. When all bands centred at $\geq 2172 \text{ cm}^{-1}$ are excluded from the fit, the centre of the Gaussian distribution shifts to $2166.9 \pm 1.5 \text{ cm}^{-1}$ ($\chi^2 = 1.57$). The converging χ^2 confirms that two components, i.e. one centred at around 2166 cm^{-1} and one at around 2175 cm^{-1} , provide a much better fit.

7.2.3 H₂O-ice column densities

In order to derive the OCN⁻ abundances, water ice column densities were estimated using *L*-band spectra (2.85–4.2 μm) from the same survey (Dartois et al., in prep.). Optical depth spectra of the H₂O-ice feature were obtained by fitting a blackbody spectrum to a *K*-band photometric point from the 2MASS point source catalogue and the available spectroscopic points in the *L*- and *M*-band spectra at wavelengths longer than 3.8 μm . Care was taken to exclude any hydrogen recombination lines from the fit. Estimated uncertainties in the water ice optical depths are $\sim 20\%$, mainly due to the variable near-infrared fluxes of embedded young stars (see e.g. Kaas, 1999). The optical depths were converted to column densities using a factor of $1.56 \times 10^{18} \text{ cm}^{-2}$. This factor was derived by integrating over a laboratory-based H₂O spectrum fitted to the highest quality water bands and scaling with a band strength of $2 \times 10^{-16} \text{ cm molec.}^{-1}$ (Gerakines et al., 1995).

Table 7.1: Laboratory experiments on the spectroscopy of $\nu_3(\text{OCN}^-)$ in interstellar ice analogues ($T = 10\text{-}100\text{K}$)^a

T (K)	Energetic processing	Ice composition (spectral res. where known / cm^{-1})	$\nu_3(\text{OCN}^-)$ (cm^{-1})	FWHM (cm^{-1})	ref.
10	ion (30keV)	$\text{H}_2\text{O}/\text{CH}_4/\text{NH}_3 = 5:4:2$ (2)	2170		1
10	thermal	$\text{HNCO}/\text{NH}_3 = 1:10$ (0.5)	2151		2
10	UV (at 10K)	$\text{H}_2\text{O}/\text{CO}/\text{CH}_4/\text{NH}_3 = 6:2:1:1$ (2)	2167	25	3
10	UV (at 10K)	$\text{CO}/\text{NH}_3 = 3:1$	2155		4
10	UV (at 10K)	$\text{H}_2\text{O}/\text{CO}/\text{CH}_3\text{OH}/\text{NH}_3 = 100:10:50:10$	2168		5
10	UV (at 10K)	$\text{H}_2\text{O}/\text{CO}/\text{CH}_3\text{OH}/\text{C}_n\text{H}_{2n+2}/\text{NH}_3 = 100:10:50:10:10$ (0.9)	2160		6
12	UV (at 12K)	$\text{HNCO}/\text{NH}_3 = 1:1$ (2)	2155		7
12	UV (at 12K)	$\text{HNCO}/\text{NH}_3 = 1:100$ (2)	2155		7
12	UV (at 10K)	$\text{CO}/\text{NH}_3 = 1:40$ (2)	2152		7
12	UV (at 30K)	$\text{CO}/\text{NH}_3 = 1:40$ (2)	2152		7
12	ion (60keV)	$\text{CO}_2/\text{N}_2 = 1:1$ (1)	2168		8
15	proton (0.8MeV)	$\text{H}_2\text{O}/\text{CO}/\text{NH}_3 = 5:1:1$ (4)	2167	26	9
15	proton (0.8MeV)	$\text{H}_2\text{O}/\text{CO}_2/\text{NH}_3 = 1:1:2$ (4)	2164	25	9
15	proton (0.8MeV)	$\text{H}_2\text{O}/\text{CH}_4/\text{NH}_3 = 1:1:1$ (4)	2159	23	9
15	proton (0.8MeV)	$\text{H}_2\text{O}/\text{CO}_2/\text{N}_2 = 5:1:1$ (4)	2170	25	9
15	proton (0.8MeV)	$\text{H}_2\text{O}/\text{CH}_4/\text{N}_2 = 1:1:1$ (4)	2159	27	9
15	proton (0.8MeV)	$\text{CO}/\text{NH}_3 = 1:1$ (4)	2164	27	9
15	proton (0.8MeV)	$\text{CO}_2/\text{NH}_3 = 1:2$ (4)	2158	26	9
15	proton (0.8MeV)	$\text{CO}/\text{N}_2 = 1:1$ (4)	2164	27	10
15	proton (0.8MeV)	$\text{CO}/\text{N}_2 = 1:2$ (4)	2158	26	10
15	UV (at 15K)	$\text{H}_2\text{O}/\text{HNCO}/\text{NH}_3 = 120:1:10$ (2)	2169	25	11
15	UV (at 15K)	$\text{H}_2\text{O}/\text{HNCO}/\text{NH}_3 = 120:1:10$ (2)	2171	25	11
15	UV (at 15K)	$\text{HNCO}/\text{NH}_3 = 1:10$ (2)	2160	20	11
15	UV (at 15K)	$\text{H}_2\text{O}/\text{HNCO}/\text{NH}_3 = 140:8:1$ (2)	2165	25	11
20	proton (1MeV)	$\text{H}_2\text{O}/\text{CH}_4/\text{NH}_3 = 1:2:3$	2170		12
20	proton (1MeV)	$\text{H}_2\text{O}/\text{CH}_4/\text{NH}_3 = 1:2:4$	2170		12
20	proton (1MeV)	$\text{H}_2\text{O}/\text{CH}_4/\text{NH}_3 = 2:4:7$	2170		12
20	proton (1MeV)	$\text{H}_2\text{O}/\text{CH}_4/\text{NH}_3 = 1:7:10$	2170		12
20	proton (1MeV)	$\text{H}_2\text{O}/\text{CH}_4/\text{NH}_3 = 1:3:6$	2170		12
20	proton (1MeV)	$\text{H}_2\text{O}/\text{CH}_4/\text{NH}_3 = 1:3:3$	2170		12
20	proton (1MeV)	$\text{H}_2\text{O}/\text{CH}_4/\text{NH}_3 = 1:4:3$	2170		12
20	proton (1MeV)	$\text{H}_2\text{O}/\text{CH}_4/\text{NH}_3 = 15:7:9$	2170		12
20	proton (1MeV)	$\text{H}_2\text{O}/\text{CH}_4/\text{N}_2 = 1:1:1$	2170		12
20	proton (1MeV)	$\text{H}_2\text{O}/\text{CO}/\text{N}_2 = 5:1:1$	2170		12
20	proton (1MeV)	$\text{H}_2\text{O}/\text{CO}/\text{NH}_3 = 2:2:1$	2170		12
20	proton (1MeV)	$\text{H}_2\text{O}/\text{CO}/\text{NH}_3 = 2:1:3$	2170		12
20	proton (1MeV)	$\text{H}_2\text{O}/\text{CO}/\text{NH}_3 = 5:1:10$	2170		12

7.3 Laboratory Experiments on OCN^- Pertinent to the Analysis of the XCN Band

7.3.1 Spectroscopy

The formation and infrared spectroscopy of solid OCN^- has been studied extensively in numerous laboratories. Its spectrum is dominated by the CN stretching-vibration (the ν_3 band), which can be well fitted by a single Gaussian profile (see for example Fig. 7.3). In Tables 7.1 and 7.2 an overview is given of all (to the best

7.3 Laboratory Experiments on OCN^- Pertinent to the Analysis of the XCN Band

Table 7.1: Laboratory experiments on the spectroscopy of $\nu_3(\text{OCN}^-)$ in interstellar ice analogues ($T = 10\text{-}100\text{ K}$)^a, cont'd.

T (K)	Energetic processing	Ice composition (spectral res. where known / cm^{-1})	$\nu_3(\text{OCN}^-)$ (cm^{-1})	FWHM (cm^{-1})	ref.
30	<i>UV (at 12K)</i>	<i>$\text{HNCO}/\text{NH}_3 = 1:100$</i>	2155		7
30	<i>thermal</i>	<i>$\text{HNCO}/\text{NH}_3/\text{Ar} = 2:2:1000 (0.125)$</i>	2157		2
30	UV (at 10K)	$\text{H}_2\text{O}/\text{CO}/\text{CH}_3\text{OH}/\text{C}_n\text{H}_{2n+2}/\text{NH}_3 = 100:10:50:10:10 (0.9)$	2163		6
35	<i>proton (0.8 MeV)</i>	<i>$\text{CO}/\text{CH}_4/\text{N}_2 = 1:1:100 (1)$</i>	2166	25	13
50	UV (at 12K)	$\text{HNCO}/\text{NH}_3 = 1:100 (2)$	2154		7
50	UV (at 37K)	$\text{CO}/\text{NH}_3 = 1:1 (2)$	2158		7
55	UV (at 10K)	$\text{H}_2\text{O}/\text{CO}/\text{CH}_3\text{OH}/\text{C}_n\text{H}_{2n+2}/\text{NH}_3 = 100:10:50:10:10 (0.9)$	2163		6
60	UV (at 12K)	$\text{HNCO}/\text{NH}_3 = 1:100 (2)$	2154		7
80	UV (at 12K)	$\text{CO}/\text{NH}_3 = 1:1 (4)$	2157		14
80	UV (at 12K)	$\text{H}_2\text{O}/\text{CO}/\text{NH}_3 = 1:1:1 (4)$	2160		14
80	UV (at 12K)	$\text{H}_2\text{O}/\text{CO}/\text{NH}_3 = 2:1:1 (4)$	2163		14
80	UV (at 12K)	$\text{H}_2\text{O}/\text{CO}/\text{NH}_3 = 3:1:1 (4)$	2166		14
100	UV (at 37K)	$\text{CO}/\text{NH}_3 = 1:1$	2163		15
100	UV (at 37K)	$\text{CO}/\text{NH}_3 = 1:1 (2)$	2157		7
100	<i>ion (60keV)</i>	<i>$\text{CO}_2/\text{N}_2 = 1:1 (1)$</i>	2165		8
100	UV (at 10K)	$\text{H}_2\text{O}/\text{CO}/\text{CH}_3\text{OH}/\text{NH}_3 = 100:10:50:10$	2166		5
100	UV (at 10K)	$\text{H}_2\text{O}/\text{CO}/\text{CH}_3\text{OH}/\text{C}_n\text{H}_{2n+2}/\text{NH}_3 = 100:10:50:10:10 (0.9)$	2163		6

^aExperiments in italics show ices that lack H_2O . All ν_3 peak-positions are rounded up or down to the nearest integer wavenumber. ¹ Strazzulla & Palumbo (1998), ² Raunier et al. (2003), ³ d'Hendecourt et al. (1986), ⁴ Lacy et al. (1984), ⁵ Tegler et al. (1993), ⁶ Allamandola et al. (1988), ⁷ Novozamsky et al. (2001), ⁸ Palumbo et al. (2000), ⁹ Hudson & Moore (2000), ¹⁰ Hudson et al. (2001), ¹¹ van Broekhuizen et al. (2004), ¹² Moore et al. (1983), ¹³ Moore & Hudson (2003), ¹⁴ Grim & Greenberg (1987), ¹⁵ Bernstein et al. (2000)

of our knowledge) published peak centres and FWHM of the ν_3 band of OCN^- , as measured in the laboratory under conditions relevant to the interstellar case, e.g. matrix-isolation studies have been excluded. In addition, information is tabulated on the initial ice composition, ice temperature and processing mechanism applied to the ice. With the exception of H_2O , CH_3OH and NH_3 , most of the other ice components have fully desorbed by 120 K under high-vacuum laboratory conditions but OCN^- remains in the solid state, stabilised by a counter ion (possibly NH_4^+ , Demyk et al., 1998; Taban et al., 2003). Hence, Table 7.1 contains those experiments in which the ice matrix is predominantly intact, whereas Table 7.2 summarises those in which most ice constituents have desorbed or are desorbing.

Fig. 7.1b shows the distribution of peak centres of the laboratory ν_3 of the OCN^- feature highlighting the initial ice environment, i.e. H_2O - or CH_3OH -rich (black), H_2O - and CH_3OH -lacking (hatched) and thermally annealed, i.e. those listed in Table 7.2 ($T \geq 110\text{ K}$, white). It is important to note that this histogram is significantly weighted by the parameter space investigated in the laboratory. Peak centres vary strongly with ice composition, ranging from 2151 to 2172 cm^{-1} . Within this range, $\nu_3(\text{OCN}^-)$ peaks at between 2151–2160 cm^{-1} in the absence of H_2O and CH_3OH (Grim & Greenberg, 1987; Hudson & Moore, 2000; Novozamsky

Table 7.2: Laboratory experiments on the spectroscopy of OCN⁻ in interstellar ice analogues ($T > 100$ K)^a

T (K)	Energetic processing	Ice composition (spectral res. where known /cm ⁻¹)	$\nu_3(\text{OCN}^-)$ (cm ⁻¹)	FWHM (cm ⁻¹)	ref.
110	thermal	H ₂ O/HNCO/Ar = 12:1:1000 (0.12)	2170		1
120	<i>UV (at 10K)</i>	<i>CO/NH₃ = 1:1</i>	2155		2
120	UV (at 15K)	H ₂ O/HNCO/NH ₃ = 120:1:10 (2)	2166	22	3
130	thermal	H ₂ O/HNCO = 10:1 (0.5)	2172		1
140	<i>UV (at 37K)</i>	<i>CO/NH₃ = 1:1 (2)</i>	2159		4
150	<i>ion (60keV)</i>	<i>CO₂/N₂ = 1:1 (1)</i>	2163		5
150	<i>UV (at 10K)</i>	<i>CO/NH₃ = 3:1</i>	2165		6
150	UV (at 10K)	H ₂ O/CO/CH ₃ OH/NH ₃ = 100:10:50:10	2162		7
160	<i>thermal</i>	<i>HNCO/NH₃ = 1:10 (0.5)</i>	2165		1
180	<i>UV (at 12K)</i>	<i>CO/NH₃ = 1:1 (4)</i>	2157		8
180	<i>UV (at 12K)</i>	<i>CO/NH₃ = 1:10 (4)</i>	2157		8
200	<i>ion (60keV)</i>	<i>CO₂/N₂ = 1:1 (1)</i>	2162		5
200	UV (at 10K)	H ₂ O/CO/CH ₄ /NH ₃ = 6:2:1:1 (2)	2167	25	9
200	UV (at 10K)	H ₂ O/CO/CH ₃ OH/NH ₃ = 100:10:50:10	2164		7
200	UV (at 10K)	H ₂ O/CO/CH ₃ OH/NH ₃ = 100:10:50:10 (0.9)	2165		10
200	UV (at 10K)	H ₂ O/CO/CH ₃ OH/C _n H _{2n+2} /NH ₃ = 100:10:50:10:10 (0.9)	2164		10
200	UV (at 10K)	H ₂ O/CO/CH ₃ OH/C _n H _{2n+2} /NH ₃ = 100:10:50:10:10 (0.9)	2163		10

^aExperiments in italics show ices that lack H₂O. All ν_3 peak-positions are rounded up or down to the nearest integer wavenumber. ¹ Raunier et al. (2003), ² Schutte & Greenberg (1997), ³ van Broekhuizen et al. (2004), ⁴ Novozamsky et al. (2001), ⁵ Palumbo et al. (2000), ⁶ Lacy et al. (1984), ⁷ Tegler et al. (1993), ⁸ Grim & Greenberg (1987) ⁹ d'Hendecourt et al. (1986), ¹⁰ Allamandola et al. (1988)

et al., 2001; Raunier et al., 2003), or at between 2160–2172 cm⁻¹ when associated with a strongly hydrogen-bonding environment, i.e. H₂O- or CH₃OH-rich ices (Grim & Greenberg, 1987). No trend is apparent in the data relating the actual formation mechanism of OCN⁻ to its band position.

From Fig. 7.1b is also clear that in warm ices ($T \geq 110$ K), $\nu_3(\text{OCN}^-)$ peaks at similar positions to the colder ices. However within a single ice matrix, thermal annealing beyond 100 K tends to shift the $\nu_3(\text{OCN}^-)$ peak to between 2155 and 2167 cm⁻¹ when OCN⁻ is stabilised by NH₄⁺ (Novozamsky et al., 2001; Palumbo et al., 2000). However, in the exclusive presence of H₂O (i.e. for H₂O/HNCO and H₂O/HNCO/Ar), $\nu_3(\text{OCN}^-)$ must be stabilised by water solvation (most plausibly H₃O⁺) and seems thermally unaffected, peaking at 2170 to 2172 cm⁻¹.

The spectral range of peak positions observed for laboratory $\nu_3(\text{OCN}^-)$ implies that only one component of the observed XCN-bands can be associated with OCN⁻. No laboratory $\nu_3(\text{OCN}^-)$ spectrum in Fig. 7.1b peaks beyond 2172 cm⁻¹, whereas a significant fraction of the astronomical spectra in Fig. 7.1a peaks around 2175 cm⁻¹. This is emphasised by the dashed line in Fig. 7.2, indicating that only those XCN-bands represented by the Gaussian fit to the left of the dashed line can be matched to a laboratory spectrum of OCN⁻. The peak centres of these XCN-bands can be explained by OCN⁻ residing in a strong hydrogen-bonding ice environment that may have been thermally annealed up to 200 K. OCN⁻ em-

7.3 Laboratory Experiments on OCN^- Pertinent to the Analysis of the XCN Band

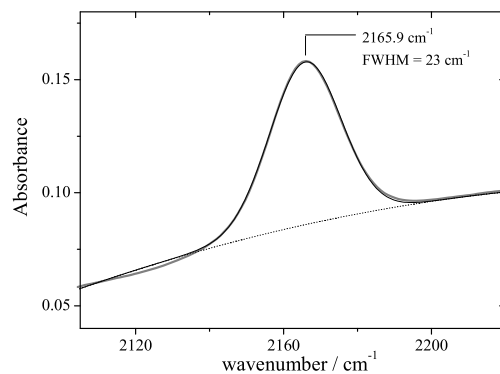


Figure 7.3: Example of a laboratory spectrum of $\nu_3(\text{OCN}^-)$, obtained after thermal annealing to 120K of an ice composed of $\text{H}_2\text{O}/\text{HNCO}/\text{NH}_3 = 120/1/10$ (grey curve). After accounting for the baseline (dotted line), an excellent fit to the laboratory data is obtained with a single Gaussian fit, centred at 2165.9 cm^{-1} , $\text{FWHM} = 23\text{ cm}^{-1}$ (black curve).

bedded in an ice that lacks a strong hydrogen-bonding network generally peaks red-wards of the XCN-bands observed, even after thermal annealing, causing this kind of ice to be an unlikely interstellar OCN^- environment.

7.3.2 Band strength

The reported value of the $\nu_3(\text{OCN}^-)$ band strength, A_{OCN^-} , varies considerably in the literature. Lacy et al. (1984) assumed $A_{\text{OCN}^-} \leq 1.0 \times 10^{-17}\text{ cm molec.}^{-1}$, based on the assumption that the cross section of a typical CN-stretching vibration is approximately 5 times less than that of a CO-stretch. d’Hendecourt et al. (1986) derived A_{OCN^-} from photolysis experiments to be $1.8\text{--}3.6 \times 10^{-17}\text{ cm molec.}^{-1}$, assuming a constant carbon budget per experiment, followed by Demyk et al. (1998), who assumed a constant oxygen budget to obtain $A_{\text{OCN}^-} \geq 4.3 \times 10^{-17}\text{ cm molec.}^{-1}$. Both studies probably underestimated the value of A_{OCN^-} due to the formation of infrared-weak or inactive photoproducts, and the neglect of photodesorption of volatile species like CO and CO_2 (van Broekhuizen et al. in prep).

More recently, van Broekhuizen et al. (2004) determined A_{OCN^-} from the thermal deprotonation of HNCO by NH_3 , using the NH_3 to NH_4^+ conversion as reference, giving $A_{\text{OCN}^-} = 1.3 \times 10^{-16}\text{ cm molec.}^{-1}$. In the present analysis of the XCN band, this value of A_{OCN^-} has been adopted because its determination is not influenced by any photodesorption or the formation of photo-products (both known and unknown), which may have affected the previously derived values. The adopted band strength does not affect any subsequent conclusions in this paper on the photo-production of OCN^- , since these reaction efficiencies were derived using the same value of the band strength. However, the adopted A_{OCN^-} value does impact on the conclusions drawn if OCN^- is thermally formed, because sig-

nificantly more HNCO will be required in the solid state if a smaller value of A_{OCN^-} were used.

7.3.3 Formation mechanisms

The presence of OCN⁻ in interstellar ices has become widely cited as a probe of energetic processing of the protostellar environment, in particular by ultraviolet (UV) photons. However, this assumption has been challenged on the basis of a quantitative set of laboratory experiments studying the efficiency of OCN⁻ photo-production, and the possibilities of forming OCN⁻ thermally (Raunier et al., 2003; van Broekhuizen et al., 2004). To assist the reader in following the subsequent discussions and conclusions of this paper, these two OCN⁻ formation mechanisms, and the regimes in which they apply, are summarised below.

In the laboratory, photochemical processes lead to the formation of OCN⁻ at abundances of (at most) 1.9% with respect to H₂O-ice, starting from an interstellar ice analogue containing H₂O, CO and NH₃ (van Broekhuizen et al., 2004). The initial amount of NH₃ in these experiments ranges from 8 to 40% with respect to H₂O ice. The abundance of interstellar NH₃ is uncertain, but is observed to be <5% toward W33 A (Taban et al., 2003). Including the constraint that the abundance of NH₃ ice after photolysis cannot be more than 5% lowers the maximum OCN⁻ photoproduction yield to 1.2% with respect to H₂O ice (see, for example, Figure 6 of van Broekhuizen et al., 2004).

From these experiments, the maximum yield for the photoproduction of interstellar OCN⁻ was constrained to an abundance of 1.2% with respect to H₂O-ice by assuming a maximum abundance for solid NH₃ of 5% with respect to H₂O-ice, as observed toward W 33A (Taban et al., 2003). If the cosmic ray induced UV-field (1.4×10^3 photons cm⁻² s⁻¹, Prasad & Tarafdar, 1983) is assumed to be the only source of UV-photons, this maximum 1.2% OCN⁻ abundance would be reached after a UV-fluence equivalent to a molecular cloud lifetime of 4×10^8 years. This is long compared to the assumed age of the YSO's studied in this paper ($\sim 10^5$ yr), even if a long pre-stellar phase of $\sim 10^7$ yr is included.

Alternatively, laboratory studies show that OCN⁻ can be formed via thermal heating of ices containing HNCO in the presence of NH₃ or H₂O with an efficiency of 15-100% (Demyk et al., 1998; Raunier et al., 2003; van Broekhuizen et al., 2004). Laboratory experiments and theoretical calculations show that this solvation process is even efficient at 15 K provided that HNCO is sufficiently diluted in NH₃ or H₂O-ice (Park & Woon, 2004; Raunier et al., 2003), for the proton transfer to occur.

7.4 Decomposition of the XCN Profile

Our analysis of the XCN band, containing two components (see Sect. 7.2.2), refines the results from Paper I where a single component fit was used. The component centred at ~ 2175 cm⁻¹ has been discussed in detail by Fraser et al. (2005) in terms of gas-surface interactions of CO with interstellar grains. Thus, in the remainder

Table 7.3: *Components adopted in the fit of the observed XCN bands*

	2165.7-component	2175.4-component
Line profile	Gaussian	Gaussian
Centre (cm^{-1})	2165.7	2175.4
FWHM (cm^{-1})	26	15

of this paper the discussion is focused on the carrier of the component of the XCN band centred at $\sim 2166 \text{ cm}^{-1}$, and simply uses a two component fit to correct for any contribution from the component centred at $\sim 2175 \text{ cm}^{-1}$.

The distribution of the $\sim 2166 \text{ cm}^{-1}$ component of the XCN band shows a broad spread of band centres, most probably related to source-to-source differences in the local ice-environment of the carrier of this component in the various lines-of-sight. A good ‘prototype’ for this component is the XCN band of W33 A, as it is also one of the most red-centred and strongest of the objects studied. It matches a Gaussian profile, peaking at $2165.7 \pm 0.1 \text{ cm}^{-1}$ (FWHM = $26 \pm 1 \text{ cm}^{-1}$), that is well reproduced by laboratory spectra of OCN^- (see Fig. 7.3). An initial analysis showed that this Gaussian profile also reproduces the red wing and component of the XCN band of all other YSO’s in this study. Consequently, the XCN band was analysed using a similar procedure to that employed for the $6.8 \mu\text{m}$ band by Keane et al. (2001), whereby the $6.8 \mu\text{m}$ band was also decomposed by using the most extreme source in the sample, Mon R2:IRS3, to fit all lines-of-sight together with a ‘rest-spectrum’ obtained after the initial fitting of the other sources. Here, the Gaussian fit to the W33 A XCN band is adopted (henceforth referred to as the 2165.7-component), and not the actual YSO spectrum, to avoid any contribution from the CO-ice band to the fit.

The component underlying the distribution of XCN bands centred at $\sim 2175 \text{ cm}^{-1}$ in Fig. 7.2 was determined empirically, in effect by fitting the residual of the XCN band after spectral subtraction of the contribution of the 2165.7-component. This resulted in a Gaussian, centred at $2175.4 \pm 3 \text{ cm}^{-1}$ (FWHM = $15 \pm 6 \text{ cm}^{-1}$). This feature will be referred to as the 2175.4-component. Adopting a different Gaussian for the 2165.7-component, i.e. one centred at 2166.9 or 2168.7 cm^{-1} , does not significantly affect these fit results, which indicates that the range of environments observed for the 2165.7-component do not introduce an error on the fit.

The fitting routine is based on the same IDL algorithms developed in Paper I. All spectra were fitted using the same 2165.7- and 2175.4-components, keeping the centre positions and FWHM constant. The optical depths of the two components are the only free parameters (see Table 7.3 for a summary). In addition, a full fit of the CO-ice feature was run in parallel to correct for possible overlap between the wing of the CO-ice feature and the XCN band (see Paper I and Fig. 4b for details on the CO-ice fit).

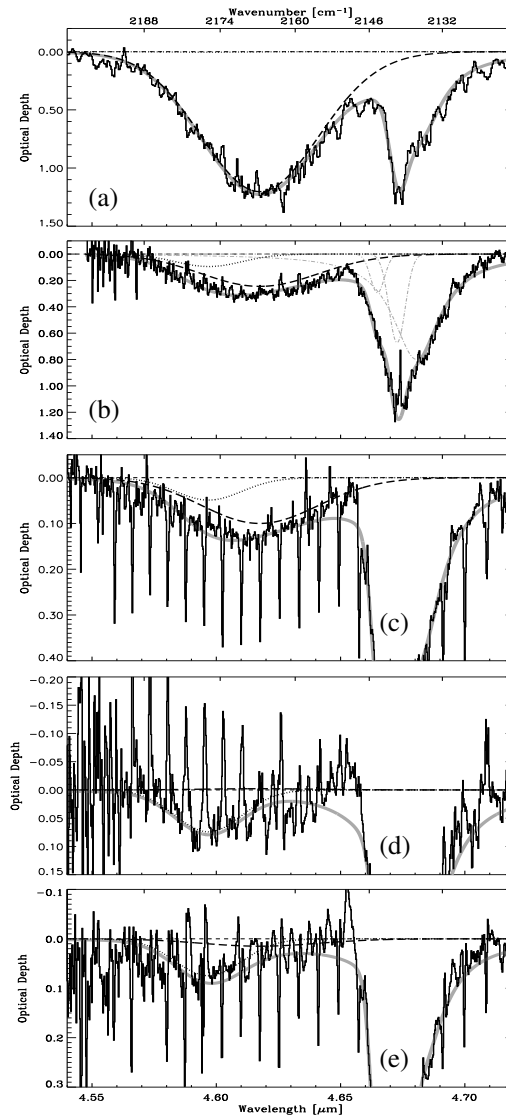


Figure 7.4: The XCN band as observed in the line-of-sight toward five YSO's, ordered from top to bottom from the most red-centred to the most blue-centred band, i.e. (a) W33 A, (b) HH 46, (c) Reipurth 50, (d) Elias 32 and (e) IRS 63. All spectra (black) are continuum subtracted (small-dashed line) and the total fit is shown (grey curve). The two components underlying the XCN band, i.e. the 2165.7-component (dashed curve) and the 2175.4-component (dotted curve) are shown. The three-component fit to the solid CO band at 4.67 μm (2139 cm^{-1}) is shown only in (b) by the three grey dash-dotted curves.

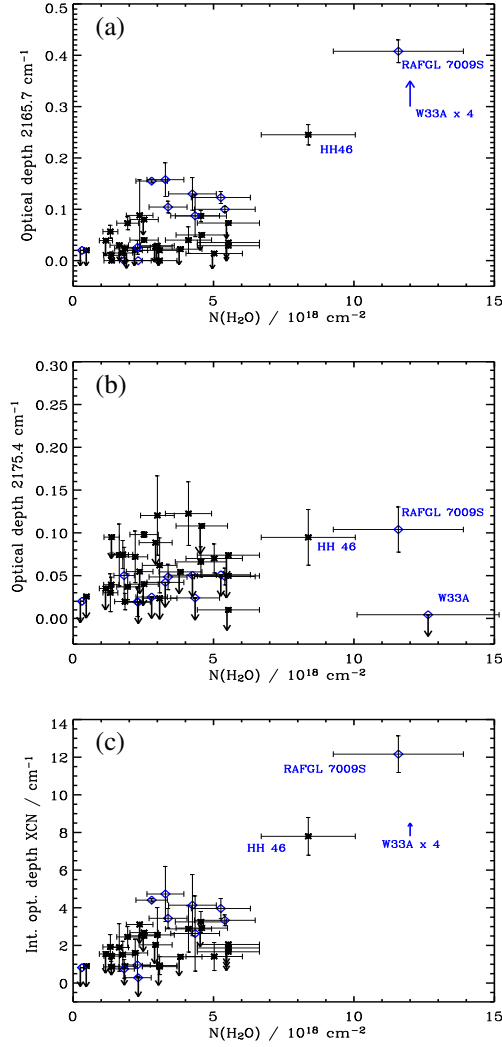


Figure 7.5: (a) The optical depth of the 2165.7-component, (b) the optical depth of the 2175.4-component, and (c) the total integrated area of the XCN band, as determined by Eq.1, are shown versus the H_2O ice column density, $N(\text{H}_2\text{O})$. High-mass objects are indicated by diamonds, all others, dominated by low-mass YSO's, by stars. 3σ uncertainties are given, or upper limits are indicated by arrows.

7.5 Results

7.5.1 Results of the fitting procedure

Fig. 7.4 shows the results of fitting the XCN band in five of the YSO's in our sample. These are presented from top to bottom in order of decreasing wavelength

of the XCN band centre position. The XCN band of W33 A (Fig. 7.4a) shows the excellent fit of the 2165.7-component with $\leq 1\%$ contribution by the 2175.4-component. In Fig. 7.4b, already some contribution to this band from the 2175.4-component is apparent. From Fig. 7.4b to e, the 2175.4-component contribution increases, blue-shifting the XCN band, until it dominates the XCN band toward Elias 32 and IRS 63. Table 7.4 summarises the derived optical depths. The χ^2 of the fit (not shown) generally varies between 0.3 and 10. The additional three-component fit of the solid CO feature (Paper I) is shown by the three grey dash-dotted curves in Fig. 7.4b only, but was applied to all fits.

7.5.2 Correlations with H₂O

In Fig. 7.5a, the optical depth of the 2165.7-component is plotted against the H₂O column density, $N(\text{H}_2\text{O})$. For all YSO's studied here, the derived optical depth of the 2165.7-component is ≤ 0.16 , except for HH 46, RAFGL 7009S and W33 A. No relationship with $N(\text{H}_2\text{O})$ is apparent. In fact, it seems that the optical depth value of the 2165.7-component toward high-mass YSO's is in most cases larger than toward lower mass YSO's, where the optical depth is typically ≤ 0.09 .

Fig. 7.5b presents the optical depth of the 2175.4-component plotted against $N(\text{H}_2\text{O})$. The optical depth of the 2175.4-component is ≤ 0.14 for all sources in this study and is not correlated to the H₂O column density. An interpretation of this feature is given by Fraser et al. (2005).

Comparing Figs. 7.5a and 7.5b shows that the 2165.7-component dominates the XCN band toward most high-mass YSO's, whereas the 2175.4-component contributes most to the XCN band in all other sources. Checks of a possible relationship between the optical depth of the two components (not shown) proved negative, indicating that the components do not trace the same feature.

In Fig. 7.5c the total integrated area of the XCN band is plotted against $N(\text{H}_2\text{O})$. The total integrated area of the XCN band is derived from the sum of the integrated areas of the individual components

$$\int \tau_{(\text{XCN})} d\nu = \int \tau_{2165.7} d\nu + \int \tau_{2175.4} d\nu \quad (7.1)$$

The XCN band is evenly distributed toward high- and low-mass YSO's and its total area tentatively increases with increasing $N(\text{H}_2\text{O})$.

7.5.3 Correlations with CO

The CO-ice band, observed at around 2140 cm⁻¹ toward all lines-of-sight here, has been analysed in detail in Paper I, using a phenomenological decomposition into 3 components to fit its band profile. The most red-centred component (rc) was attributed to CO in a hydrogen-bonded environment, although this cannot fully explain its extended red wing. It was suggested that the rc may evolve from pure CO-ice when thermal annealing of the ice induces CO to migrate into, and get trapped in, porous H₂O-ice. As such, this component may trace the thermal

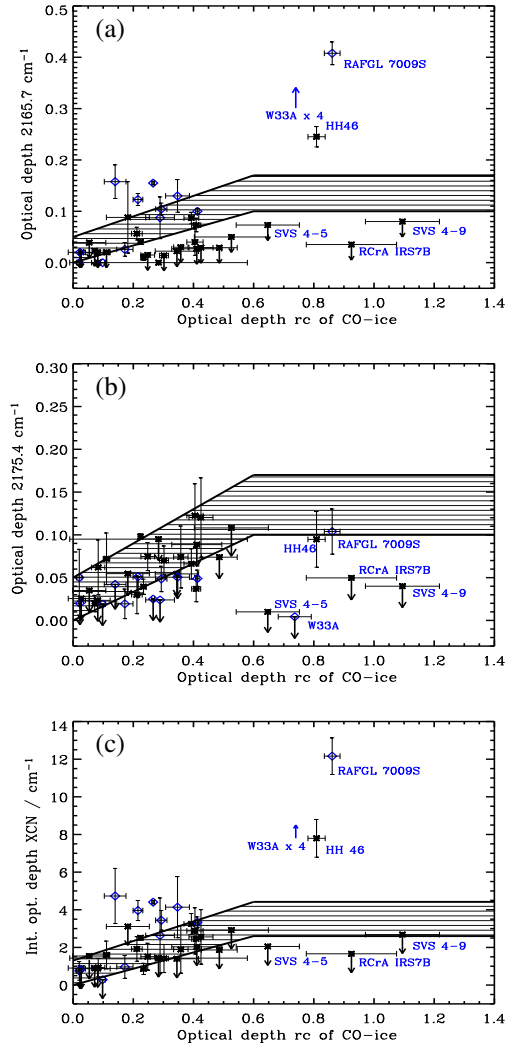


Figure 7.6: (a) The optical depth of the 2165.7-component, (b) the optical depth of the 2175.4-component, and (c) the total integrated area of the XCN band, as determined by Eq.1, are presented versus the optical depth of the red component (τ_{rc}) of CO-ice. High-mass objects are indicated by diamonds, all others, dominated by low-mass YSO's, by stars. 3σ uncertainties are given, or upper limits are indicated by arrows. The shaded area, shown in each plot, marks the correlation between the optical depth of the XCN band and the red component (τ_{rc}) of CO-ice as proposed by Paper I.

history of the interstellar ice mantle (Tielens et al., 1991, Paper I). Hence, the relationship between the optical depth of the τ_{rc} of CO-ice and the XCN band may

provide information on the thermal history of the XCN band as well. Paper I found a tentative correlation between this rc and the optical depth of the XCN band and suggested that this was actually due to a component of the XCN band, centred between 2170-2180 cm^{-1} .

Fig. 7.6a presents the optical depth of the 2165.7-component versus the optical depth of the rc of the CO-ice band, showing that this component and the rc of CO-ice are not correlated. The shaded area marks the correlation suggested by Paper I. However, those sources that show a strong 2165.7-component also tend to have a strong CO rc, but not the other way around.

In Fig. 7.6b the optical depth of the 2175.4-component is plotted against the optical depth of the rc of the CO-ice band. In contrast to the 2165.7-component, the 2175.4-component matches the correlation indicated by the shaded area much better, particularly at rc optical depths of below 0.6, corroborating the idea posed by Paper I. However, the YSO's with deep rc optical depths (and deep 2165.7-component optical depths) fall outside the correlation proposed by Paper I.

For completion, Fig. 7.6c illustrates the relation between the integrated area of the XCN band and the optical depth of the rc of CO-ice, showing that most low-mass YSO's match the correlation suggested by Paper I (shaded area) and reflecting that in these objects the 2175.4-component dominates the XCN band (see Sect. 7.5.2). Conversely, approximately half of the XCN bands observed toward high-mass YSO's clearly exhibit larger integrated areas than would be expected from that correlation.

7.6 Discussion

7.6.1 The OCN^- abundance

Based on the discussion in Sect. 7.3.1, only the 2165.7-component of the astronomical spectra can be confidently assigned to OCN^- . Thus, the OCN^- column density, $N(\text{OCN}^-)$, and its abundance with respect to H_2O , $[\text{OCN}^-]$, are derived from the optical depth of the 2165.7-component via:

$$[\text{OCN}^-] = \frac{N(\text{OCN}^-)}{N(\text{H}_2\text{O})} = \frac{\int \tau_{2165.7} d\nu \times A_{\text{OCN}^-}^{-1}}{N(\text{H}_2\text{O})} \quad (7.2)$$

where the FWHM of $\tau_{2165.7}$ is fixed at 26 cm^{-1} and A_{OCN^-} is 1.3×10^{-16} cm molec.^{-1} (van Broekhuizen et al., 2004, see Sect. 7.3.2 for a discussion on the value of A_{OCN^-}). The inferred $N(\text{OCN}^-)$ and $[\text{OCN}^-]$ are summarised in Table 7.4.

In Fig. 7.7 the OCN^- abundance with respect to $N(\text{H}_2\text{O})$, $[\text{OCN}^-]$, is plotted against $N(\text{H}_2\text{O})$. All sources studied here show abundances of $\leq 1.0\%$, except for W33 A. Excluding the high-mass stars, gives abundances of $\leq 0.85\%$. The high signal-to-noise of the spectra allows the detection of the XCN band down to optical depths of 0.01. As a result, very strict upper limits have been put on the OCN^- abundance along some lines of sight.

Table 7.4: Results of the XCN band fitting procedure

Source ^a	$\tau(2165.7)^b$ 2165.7 cm ⁻¹	$\tau(2175.4)^b$ 2175.4 cm ⁻¹	$N(\text{OCN}^-)^c$ $\times 10^{16}$ molec. cm ⁻²	$[\text{OCN}^-]^c$ %	$\tau(\text{H}_2\text{O})^d$
ρ Ophiuchus					
IRS42	≤ 0.023	0.020 ± 0.010	≤ 0.46	≤ 0.25	1.17
IRS43	≤ 0.02	0.072 ± 0.030	≤ 0.40	≤ 0.18	1.40
IRS44	≤ 0.02	≤ 0.024	≤ 0.40	≤ 0.13	1.95
IRS46	≤ 0.039	≤ 0.035	≤ 0.78	≤ 0.68	0.74
IRS51	0.073 ± 0.013	0.037 ± 0.015	1.46 ± 0.26	0.76 ± 0.12	1.23
IRS63	≤ 0.015	0.075 ± 0.016	≤ 0.3	≤ 0.17	1.12
WL12	-	0.062 ± 0.032	-	-	1.95
CRBR 2422.8	≤ 0.029	0.120 ± 0.045	≤ 0.58	≤ 0.19	1.90
Elias 32	≤ 0.030	0.074 ± 0.036	≤ 0.60	≤ 0.36	1.04
VSSG17	-	≤ 0.095	-	-	0.87
RNO 91	0.087 ± 0.010	0.066 ± 0.017	1.74 ± 0.2	0.40 ± 0.09	2.88
Serpens					
EC90 A	0.010 ± 0.006	0.039 ± 0.008	0.2 ± 0.12	0.15 ± 0.05	0.86
EC90 B	0.056 ± 0.012	0.030 ± 0.007	1.12 ± 0.24	0.86 ± 0.12	0.84
EC82	≤ 0.02	≤ 0.026	≤ 0.40	≤ 0.86	0.30
CK2	≤ 0.027	≤ 0.089	≤ 0.54	≤ 0.19	1.86 ± 0.19^e
SVS 4-9	≤ 0.08	≤ 0.04	≤ 1.60	≤ 0.64	1.6 ± 0.1^f
SVS 4-5	≤ 0.073	≤ 0.010	≤ 1.46	≤ 0.27	3.50 ± 0.30^f
Orion					
TPSC 78	0.155 ± 0.003	≤ 0.025	3.1 ± 0.06	1.12 ± 0.14	1.77
TPSC 1	0.158 ± 0.032	≤ 0.042	3.16 ± 0.64	0.97 ± 0.13	2.08
Reipurth 50	0.100 ± 0.005	0.049 ± 0.012	2.0 ± 0.1	0.38 ± 0.08	3.42
Corona Australis					
HH100 IRS	0.04 ± 0.002	0.098 ± 0.003	0.8 ± 0.04	0.32 ± 0.08	1.6
HH46	0.245 ± 0.019	0.095 ± 0.032	4.9 ± 0.38	0.59 ± 0.01	5.3 ± 3.0^g
RCrA IRS7A	≤ 0.029	≤ 0.074	≤ 0.58	≤ 0.11	3.5
RCrA IRS7B	≤ 0.035	≤ 0.050	≤ 0.70	≤ 0.13	3.5
RCrA IRS5A	0.040 ± 0.025	0.123 ± 0.036	0.80 ± 0.5	0.20 ± 0.06	2.60
RCrA IRS5B	≤ 0.022	≤ 0.054	≤ 0.44	≤ 0.12	2.42

Table 7.4: Results of the XCN band fitting procedure, cont'd.

Source ^a	$\tau(2165.7)^b$ 2165.7 cm ⁻¹	$\tau(2175.4)^b$ 2175.4 cm ⁻¹	$N(\text{OCN}^-)^c$ $\times 10^{16}$ molec. cm ⁻²	$[\text{OCN}^-]^c$ %	$\tau(\text{H}_2\text{O})^d$
Chamaeleon					
ChaIRN	0.088±0.069	≤0.055	1.76±1.38	0.75±0.12	1.5
ChaIRS 6A	≤0.05	≤0.108	≤1.0	≤0.22	2.90
Vela					
LLN17	0.104±0.011	0.048±0.014	2.08±0.22	0.62±0.11	2.14
LLN20	0.087±0.040	≤0.024	1.74±0.8	0.41±0.09	2.75
LLN33	0.130±0.032	≤0.051	2.6±0.64	0.62±0.11	2.69
LLN39	≤0.02	≤0.02	≤0.40	≤1.3	0.20
LLN47	-	0.050±0.033	-	-	1.15
Taurus					
LDN 1489 IRS	≤0.014	0.070±0.016	≤0.28	≤0.06	3.18
Additional sources ^h					
RAFGL 2136	0.123±0.011	≤0.051	2.46±0.22	0.47±0.09	3.33 ⁱ
NGC7538 IRS1	-	≤0.019	-	-	1.47
RAFGL 7009S	0.408±0.021	0.104±0.026	8.16±0.42	0.71±0.11	7.33 ^j
W33A	1.204±0.030	≤0.004	24.08±0.60	1.93±0.01	8.00±0.75 ^k
RAFGL 989	0.026±0.013	0.019±0.017	0.52±0.26	0.23±0.06	1.45

^a Source spectra taken from Paper I, unless otherwise stated. ^b 3σ uncertainties or upper limits are given. ^c Column densities and abundances derived from the 2165.7-component using Eq.2. ^d H₂O optical depths from Dartois et al. private communication, unless otherwise stated, and derived according to Sect. 7.2.1. Uncertainties are between 10 to 20%. ^e Eiroa & Hodapp (1989) ^f Pontoppidan et al. (2004) ^g Boogert et al. (2004) ^h ISO-data archive. ⁱ Gerakines et al. (1999) ^j Dartois et al. (1999) ^k Gibb et al. (2000)

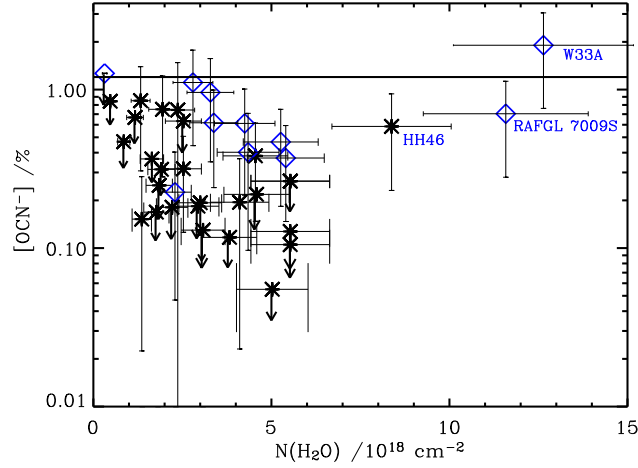


Figure 7.7: The OCN^- abundance, $[\text{OCN}^-]$, plotted with respect to the H_2O column density, $N(\text{H}_2\text{O})$. High-mass objects are indicated by diamonds, all others, dominated by low-mass YSO's, by stars. 3σ uncertainties are given, or upper limits are indicated by arrows. The black horizontal line marks the 1.2% maximum abundance of OCN^- that may be formed photochemically under interstellar conditions, as determined from laboratory studies.

7.6.2 OCN^- abundance variations

The sample of XCN observations presented here is large enough to obtain statistically significant information on the distribution of abundances and to compare between different classes of cloud environments, such as low- and high-mass star-forming regions. As seen in Fig. 7.7 and Table 7.4, the abundance of OCN^- is observed to vary by at least a factor of 10-20 among the lines of sight in the sample. This observed range of OCN^- abundances is larger than that of CH_3OH and second only to that of ice species whose abundances are sensitive to low-temperature freeze-out and evaporation, such as CO.

A particularly interesting point is that some of the observed lines of sight toward low-mass sources are located in close proximity to each other in the plane of the sky (100-10 000 AU). Such objects provide a direct probe of the physical size of regions with enhanced (or reduced) OCN^- abundances. In particular, several close binaries in the sample probe variations in abundances on scales of a few hundred AU, i.e. at the scale of circumstellar disks. Some of the best upper limits on the OCN^- abundance of $< 0.1\%$ are observed toward IRS 43 and IRS 44 in the ρ Ophiuchus star-forming cloud. These lines of sight are located approximately $4'$ or 30 000 AU from IRS 51, which has a measured OCN^- abundance of 0.8%. This shows that OCN^- is formed in localised regions even within the same low-mass star-forming cloud complex. The individual components of the close binary source EC 90A+B, which were observed separately, appear to have OCN^- abun-

dances varying by a factor of 6. Since the separation between the two components is only 1".6, corresponding to approximately 400 AU, this is an indication that processes occurring on the size scale of circumstellar disks may be required to form OCN⁻ in large quantities. Note, however, the spectrum observed toward EC 90B is complicated by complex emission and absorption from gaseous CO, so that the observed difference in OCN⁻ abundances for this binary requires further investigation. The two components in another close binary, RCrA IRS5, also show a tentative difference in OCN⁻ abundance of a factor of 2. Clearly, only slightly more sensitive observations of embedded close binaries will be able to confirm the observation of a varying OCN⁻ abundance on scales of a few hundred AU.

7.6.3 OCN⁻ formation toward low-mass YSOs

The observed abundances and their variations for our large sample of sources put important constraints on the formation mechanism of OCN⁻. All inferred OCN⁻ abundances presented here allow quantitatively for a photochemical formation mechanism (see Sect. 7.3.3). Only W33 A, an embedded O-type star with a luminosity of $10^5 L_{\odot}$ (Mueller et al., 2002) with an OCN⁻ abundance of $\sim 2\%$ is at the edge of the range, as are the Galactic center source GC:IRS19 and the external galaxy NGC 4945 presented elsewhere (see van Broekhuizen et al. 2004). If we define high- and intermediate mass YSO's as those more luminous than $50 L_{\odot}$, it is found that OCN⁻ abundances of order 0.85–1% are observed toward high-intermediate- and low-mass stars in our sample, but strict upper limit abundances of $< 0.2\%$ are observed only toward low-mass stars. This does indicate that some differences exist in the efficiency of OCN⁻ production between high- and low-mass star-forming regions, and may suggest that UV photons play a role. However, comparison with laboratory studies shows that the photon dose required to produce the highest OCN⁻ abundances (of $\sim 0.85\%$) detected here toward low-mass YSO's are $\sim 40 \times$ larger than can be accounted for by the cosmic ray induced photons that any ice might receive within the typical lifetime of the pre- and protostellar phases (see Sect. 7.3.3). Adopting the somewhat higher cosmic-ray induced photon fluxes estimated by Shen et al. (2004) would lower these timescales by an order of magnitude, and they could be further decreased by a factor of 2 if the initial NH₃ abundance were as high as 30%, but it remains difficult to fully reconcile the ages.

Another, perhaps more serious problem with the UV photoproduction scenario is that little variation in the OCN⁻ abundance from source to source is expected if the cosmic-ray induced photon flux is assumed to be the same everywhere. Thus, local sources of radiation—either UV from the young star or star-disk boundary—need to be invoked to explain the observed small-scale variations. A well-known concern is whether any of this UV radiation is able to reach the bulk of the ices because of the large extinctions involved. Spherically-symmetric models of YSO envelopes have been constructed, taking the variation of the density, dust temperature and UV radiation with depth into account (e.g. Jørgensen et al., 2002), and it has been shown that any UV from the star only reaches the inner few % of the envelope mass (e.g., Stäuber et al., 2004). Thus, special geometries are required

to allow the UV to escape and reach the bulk of the ice, such as outflow cavities or flaring turbulent disks in which the ices are cycled from the shielded midplane to the upper layers. One alternative option is UV radiation created by secondary electrons resulting from X-rays from the young star. Model calculations show that the X-rays, and thus the UV radiation, penetrate much deeper into the envelope than the UV from the star itself so that it can reach a larger fraction of the ices (Stäuber et al., 2004). It would be worthwhile to couple such models with an ice chemistry to check the OCN^- production quantitatively, but this is beyond the scope of this paper.

An alternative scenario for OCN^- formation is via thermal heating of HNCO in the presence of NH_3 - or H_2O -ices. Assuming a 15–100% efficiency of this mechanism as determined under laboratory conditions (see Sect. 7.3.3), the OCN^- abundances toward low-mass YSO's presented here imply that 0.85–5% HNCO should be present in the solid state prior to the formation of OCN^- to explain the highest observed abundances of $\sim 0.85\%$. To date, HNCO has been detected in interstellar gas associated with star-forming regions, with column densities in the range from $0.3\text{--}7.5 \times 10^{14} \text{ cm}^{-2}$ (Jackson et al., 1984; Kuan & Snyder, 1996; van Dishoeck et al., 1995; Wang et al., 2004; Zinchenko et al., 2000). This is a factor of 100 less than what is expected from the OCN^- column densities derived here, assuming all the OCN^- evaporates as HNCO. In the solid state, only HNCO upper limits, of the order of 0.5 to 0.7% with respect to H_2O -ice, are determined toward W 33A, NGC 7538 IRS9 and AFGL2136 (van Broekhuizen et al., 2004). Toward the low-mass YSO Elias 29, this is $\leq 0.3\%$ (derived from Boogert et al., 2002). The ease with which HNCO is deprotonated in a H_2O -rich environment implies that HNCO would be difficult to detect toward regions where the ice is warmer than 15 K, although its presence may be observable by means of its $4.42 \mu\text{m}$ feature toward the coldest regions where the ice temperature is close to 10 K. On the basis of τ_{OCN^-} derived here, and the band strength of HNCO (van Broekhuizen et al., 2004), τ_{HNCO} is expected to range from 0.001 to 0.08, a factor of 5 less than observed for OCN^- .

Chemical models predict that HNCO is formed on interstellar grains via grain-surface reactions with an abundance upper limit of $\leq 1\text{--}3\%$ with respect to H_2O -ice (Hasegawa & Herbst, 1993; Keane et al., 2001). Given the observed upper limits and model abundances for HNCO, thermal processing also has difficulties to explain the highest observed OCN^- abundances, but it is a serious alternative to UV-photoprocessing for the formation of at least a fraction of OCN^- in interstellar ices. The observed OCN^- abundance variations would in this scenario have to result from variations in the grain-surface chemistry rates forming the reactants that lead to OCN^- , for example due to temperature or availability of atomic N.

On the basis of its spectroscopy, it is not possible to draw a distinction between OCN^- formation via proton-, electron-, UV- or thermally induced processes, neither from laboratory spectra (Sect. 7.3.1), nor from astronomical observations of the 2165.7 cm^{-1} OCN^- band.

7.7 Conclusion

The XCN band has been observed toward 39 YSO's enabling the first detailed study of the OCN⁻ abundance in a large sample of low-mass YSO's. Statistical analysis of the band centre position distribution proves unequivocally that the band contains at least two components, of which only one (centred at 2165.7 cm⁻¹) can be associated with OCN⁻ as its carrier, based on laboratory OCN⁻ spectra. We conclude that in all cases the OCN⁻ is embedded in a strongly hydrogen-bonded, and possibly thermally annealed, ice environment. A phenomenological decomposition was undertaken to fit the full XCN band profile toward each line of sight using two components, centred at 2165.7 cm⁻¹ (FWHM = 26 cm⁻¹) and 2175.4 cm⁻¹ (FWHM = 15 cm⁻¹). OCN⁻ abundances were derived from the 2165.7-component of this fit.

Typically, OCN⁻ is detected toward the low-mass YSO's in our sample at abundances $\leq 0.85\%$ (with respect to the H₂O-ice column density) and $\leq 1.0\%$ toward high-mass YSO's, with the exception of W33 A. A large dynamic range of abundances is observed, varying by at least a factor of 10–20. Together with the variations in abundance observed between regions separated by only 400 AU, this provides a strong indication that OCN⁻ formation is a highly localised process. The inferred OCN⁻ abundances allow quantitatively for a photochemical formation mechanism, but the observed large variations are more difficult to explain unless local sources of UV radiation or X-rays are invoked which reach a large fraction of the ices. Alternatively, OCN⁻ can be formed in the bulk of the ice from the solvation of HNCO, which may have formed via surface reactions. Further diagnostics are required to be more conclusive about the chemistry leading to OCN⁻ formation in interstellar environments. These include the construction of more detailed physical models of the sources presented here to derive the effects of varying grain temperatures and UV radiation fields on the different formation mechanisms of OCN⁻, slightly more sensitive observations to probe OCN⁻ abundance variations on a 100 AU scale, and laboratory data on the formation of HNCO via surface reactions at various temperatures.

Acknowledgements

This research was financially supported by the Netherlands Research School for Astronomy (NOVA) and a NWO Spinoza grant. Thanks to F. Lahuis, E. Dartois, L. d'Hendecourt, A.G.G.M. Tielens, W.-F. Thi and S. Schlemmer for many useful discussions on the VLT program, and to an unknown referee for useful comments that led to considerable improvements to the article.

Bibliography

- Allamandola, L. J., Sandford, S. A., & Valero, G. J. 1988, *Icarus*, 76, 225
- Bernstein, M. P., Sandford, S. A., & Allamandola, L. J. 2000, *ApJ*, 542, 894
- Boogert, A. C. A., Hogerheijde, M. R., Ceccarelli, C., et al. 2002, *ApJ*, 570, 708
- Boogert, A. C. A., Pontoppidan, K. M., Lahuis, F., et al. 2004, *ApJS*, 154, 359
- Chiar, J. E., Adamson, A. J., Pendleton, Y. J., et al. 2002, *ApJ*, 570, 198
- Dartois, E., Schutte, W., Geballe, T. R., et al. 1999, *A&A*, 342, L32
- Demyk, K., Dartois, E., D'Hendecourt, L., et al. 1998, *A&A*, 339, 553
- d'Hendecourt, L. B., Allamandola, L. J., Grim, R. J. A., & Greenberg, J. M. 1986, *A&A*, 158, 119
- Eiroa, C. & Hodapp, K.-W. 1989, *A&A*, 210, 345
- Fraser, H. J., Bisschop, S. E., Pontoppidan, K. M., van Dishoeck, E. F., & Tielens, A. G. G. M. 2005, *MNRAS*, 356, 1283
- Gerakines, P. A., Schutte, W. A., Greenberg, J. M., & van Dishoeck, E. F. 1995, *A&A*, 296, 810
- Gerakines, P. A., Whittet, D. C. B., Ehrenfreund, P., et al. 1999, *ApJ*, 522, 357
- Gibb, E. L., Whittet, D. C. B., Schutte, W. A., et al. 2000, *ApJ*, 536, 347
- Grim, R. J. A. & Greenberg, J. M. 1987, *ApJL*, 321, L91
- Hasegawa, T. I. & Herbst, E. 1993, *MNRAS*, 263, 589
- Hudson, R. L. & Moore, M. H. 2000, *A&A*, 357, 787
- Hudson, R. L., Moore, M. H., & Gerakines, P. A. 2001, *ApJ*, 550, 1140
- Jackson, J. M., Armstrong, J. T., & Barrett, A. H. 1984, *ApJ*, 280, 608
- Jørgensen, J. K., Schöier, F. L., & van Dishoeck, E. F. 2002, *A&A*, 389, 908
- Kaas, A. A. 1999, *AJ*, 118, 558
- Keane, J. V., Tielens, A. G. G. M., Boogert, A. C. A., Schutte, W. A., & Whittet, D. C. B. 2001, *A&A*, 376, 254
- Kuan, Y. & Snyder, L. E. 1996, *ApJ*, 470, 981
- Lacy, J. H., Baas, F., Allamandola, L. J., et al. 1984, *ApJ*, 276, 533
- Moore, M. H., Donn, B., Khanna, R., & A'Hearn, M. F. 1983, *Icarus*, 54, 388
- Moore, M. H. & Hudson, R. L. 2003, *Icarus*, 161, 486
- Mueller, K. E., Shirley, Y. L., Evans, N. J., & Jacobson, H. R. 2002, *ApJS*, 143, 469
- Novozamsky, J. H., Schutte, W. A., & Keane, J. V. 2001, *A&A*, 379, 588
- Palumbo, M. E., Pendleton, Y. J., & Strazzulla, G. 2000, *ApJ*, 542, 890

Bibliography

- Park, J. & Woon, D. E. 2004, *ApJL*, 601, L63
- Pendleton, Y. J., Tielens, A. G. G. M., Tokunaga, A. T., & Bernstein, M. P. 1999, *ApJ*, 513, 294
- Pontoppidan, K. M., Fraser, H. J., Dartois, E., et al. 2003, *A&A*, 408, 981
- Pontoppidan, K. M., van Dishoeck, E. F., & Dartois, E. 2004, *A&A*, 426, 925
- Prasad, S. S. & Tarafdar, S. P. 1983, *ApJ*, 267, 603
- Raunier, S., Chiavassa, T., Marinelli, F., Allouche, A., & Aycard, J. P. 2003, *J. Phys. Chem. A*, 107, 9335
- Schutte, W. A. & Greenberg, J. M. 1997, *A&A*, 317, L43
- Shen, C. J., Greenberg, J. M., Schutte, W. A., & van Dishoeck, E. F. 2004, *A&A*, 415, 203
- Soifer, B. T., Puetter, R. C., Russell, R. W., et al. 1979, *ApJL*, 232, L53
- Spoon, H. W. W., Moorwood, A. F. M., Pontoppidan, K. M., et al. 2003, *A&A*, 402, 499
- Stäuber, P., Doty, S. D., van Dishoeck, E. F., Jørgensen, J. K., & Benz, A. O. 2004, *A&A*, 425, 577
- Strazzulla, G. & Palumbo, M. E. 1998, *Plan. Space Sci.*, 46, 1339
- Taban, I. M., Schutte, W. A., Pontoppidan, K. M., & van Dishoeck, E. F. 2003, *A&A*, 399, 169
- Tegler, S. C., Weintraub, D. A., Allamandola, L. J., et al. 1993, *ApJ*, 411, 260
- Tegler, S. C., Weintraub, D. A., Rettig, T. W., et al. 1995, *ApJ*, 439, 279
- Tielens, A. G. G. M., Tokunaga, A. T., Geballe, T. R., & Baas, F. 1991, *ApJ*, 381, 181
- van Broekhuizen, F. A., Keane, J. V., & Schutte, W. A. 2004, *A&A*, 415, 425
- van Dishoeck, E. F., Blake, G. A., Jansen, D. J., & Groesbeck, T. D. 1995, *ApJ*, 447, 760
- van Dishoeck, E. F., Dartois, E., Pontoppidan, K. M., et al. 2003, *The Messenger*, 113, 49
- Wang, M., Henkel, C., Chin, Y.-N., et al. 2004, *A&A*, 422, 883
- Whittet, D. C. B., Pendleton, Y. J., Gibb, E. L., et al. 2001, *ApJ*, 550, 793
- Zinchenko, I., Henkel, C., & Mao, R. Q. 2000, *A&A*, 361, 1079

Nederlandse samenvatting

Interstellair ijs

Wanneer je in alle vroegte op een winterse dag naar buiten kijkt, zie je soms de meest prachtige ijsbloemen op de ruit. Deze worden gevormd doordat water uit de lucht condenseert op het koude glasoppervlak. Op een zelfde manier ontstaan sneeuwvlokken hoog in de atmosfeer wanneer opstijgende lucht afkoelt zodat water condenseert rond kleine stofdeeltjes.

Ruimte-ijs, of wel interstellair ijs, ontstaat op soortgelijke wijze. Een verschil is echter dat de temperatuur in de ruimte veelal lager is dan op aarde waardoor dit ijs, naast water (H_2O), vaak ook aanzienlijke hoeveelheden moleculen zoals koolstofmonoxide (CO), koolstofdioxide (CO_2) en methanol (CH_3OH), en kleine beetjes stikstof (N_2) en ammonia (NH_3) bevat. De aan- of afwezigheid van deze ijsmoleculen hangt in grote mate af van de specifieke condities van de omgeving (temperatuur, druk en stralingsvelden). Andersom geldt dat de moleculen in een bepaald gebied in de ruimte invloed hebben op de verdere ontwikkeling van dit gebied. Je kunt dus stellen dat de chemische compositie van interstellair ijs waardevolle informatie kan verschaffen over de geschiedenis en de nabije toekomst van deze gebieden. Eén manier om deze informatie te extraheren is door dit ijs na te bootsen in laboratoria, en te kijken naar de fysische en chemische processen die kunnen plaatsvinden wanneer deze ijsanalogen worden blootgesteld aan gesimuleerde interstellaire omstandigheden zoals geleidelijke opwarming en ultraviolette (UV) straling.

In dit proefschrift wordt specifiek gekeken naar de interacties tussen moleculen in interstellaire ijsanalogen in het laboratorium als functie van temperatuur en van UV-straling. Tevens bevat het de beschrijving van een nieuwe experimentele ultra hoog vacuüm (UHV) proefopstelling ($\sim 10^{-10}$ mbar, ofwel $\sim 10^7$ moleculen cm^{-3} bij 50 K), "The Cryogenic Photoproduct Analysis Device" (CRYOPAD), die als onderdeel van deze promotie is ontwikkeld. CRYOPAD levert een betere simulatie van de interstellaire ijsomgeving, en maakt het mogelijk om de chemische en fysische interacties tussen ijsmoleculen zowel kwalitatief als kwantitatief te bestuderen. De combinatie van de twee analysetechnieken, Reflectie-absorptie infrarood spectroscopie (RAIRS) en quadrupool massa spectrometrie (QMS), waarover CRYOPAD beschikking heeft, maken dit instrument gevoelig voor kleine (fysische en chemische) veranderingen in het ijs en in de moleculaire compositie van de gasfase. Hiermee draagt CRYOPAD bij aan een verbetering van de bestaande experimentele methoden en aan een meer nauwkeurige analyse van interstellaire ijsanalogen.

Waarom interstellair ijsonderzoek?

Overall in het interstellair medium (ISM), de ruimte tussen de sterren, treft men moleculen aan. Deze variëren in complexiteit van twee-atomige moleculen zoals waterstof (H_2), en bekende moleculen zoals H_2O , CO , CO_2 , NH_3 , "lachgas" (N_2O), alcohol (CH_3CH_2OH) en polycyclische aromatische koolwaterstoffen (PAHs), tot exotische koolstofketens ("cyano-polyenen") zoals $HC_{11}N$. Telescopen nemen deze moleculen waar aan de hand van hun licht-emissie of absorptie karakteristieken. Emissiespectroscopie wordt voornamelijk gebruikt voor de waarnemingen van gasfasemoleculen, en berust op het detecteren van het lichtspectrum dat wordt uitgezonden wanneer energetisch aangeslagen moleculen ontspannen in een lagere energietoestand. Bij het waarnemen van moleculen in de vaste (ijs) fase wordt gekeken naar het specifieke lichtabsorptiespectrum tegen de achtergrondstraling van een verderweg gelegen jonge ster. Het absorptiespectrum van ijsmoleculen ligt typisch in het infrarood (IR) golflengtegebied van het elektromagnetische spectrum ($\lambda = 2-20 \mu m$).

Tot op heden wordt interstellair ijs gevonden in zogenaamde interstellair wolken, op satellieten in ons zonnestelsel, in ("stof") schijven rond jonge sterren, en in kometen. Echter, de grootste variëteit aan moleculen wordt (in de gasfase) aangetroffen in zogenaamde 'hot cores'. Deze gebieden worden geassocieerd met de vorming van veelal hoge massa sterren (meer dan $10\times$ zwaarder dan de zon) en maken onderdeel uit van de dichte interstellair wolken. Het idee is daarom dat een groot deel van deze hot core moleculen gevormd wordt uit het ijs dat oorspronkelijk in deze wolken aanwezig was. De ontwikkeling van een hot core gaat gepaard met hoge temperaturen (100–200 K) en intense stralingsvelden (waaronder UV-straling). Naar alle waarschijnlijkheid vormen deze factoren de bron van een weelde aan chemische reacties tussen de ijsmoleculen, welke kunnen leiden tot de productie van complexere moleculen zowel in de vaste- als in de gasfase wanneer het ijs verdampt. Dit maakt de studie van interstellair ijsanalogen een essentieel onderdeel in de zoektocht naar de opheldering van de chemische (en fysische) evolutie van het ISM.

Dit proefschrift

Het grootste gedeelte van dit proefschrift bestaat uit een laboratoriumstudie waarbij twee verschillende experimentele opstellingen zijn gebruikt. Het onderzoek beschreven in de hoofdstukken 2, 3, en 6 is uitgevoerd in een proefopstelling onder hoog vacuüm condities ($\sim 10^{-7}$ mbar) met behulp van de transmissie IR-spectroscopie analysetechniek. Hoofdstukken 4 en 5 beschrijven de eerste twee onderzoeken in de nieuw ontwikkelde UHV proefopstelling CRYOPAD. De hoofdstukken zijn geïndexed naar oplopende complexiteit van de geïnduceerde processen, beginnend met een studie naar het thermische effect op de interacties tussen CO en CO_2 , en eindigend met de kwantitatieve analyse van fotochemische processen zoals de productie van OCN^- . Hoofdstuk 7 presenteert de analyse van een grote verzameling van waarnemingen van een interstellair absorptieband rond een golflengte van $4.62 \mu m$ die (gedeeltelijk) kan worden toegeschreven aan het OCN^- ion dat is bestudeerd in Hoofdstuk 6.

In **Hoofdstuk 2** wordt gekeken naar de spectrale karakteristieken van de fysische interacties tussen CO en CO₂ in de vaste fase als functie van de temperatuur. Deze twee moleculen worden na H₂O het meest gevonden in interstellair ijs. Onder interstellaire condities wordt CO₂ naar alle waarschijnlijkheid gevormd uit CO-ijs. Dit kan gebeuren door middel van oppervlaktereacties of door reacties die geïnduceerd worden door straling (bijvoorbeeld UV) wanneer CO zich in een H₂O-rijke ijsomgeving bevindt. CO zelf wordt hoofdzakelijk gevormd in de gasfase, maar wordt tevens geregenereerd uit CO₂ door dezelfde stralingsprocessen die CO₂ opleveren. Het is dus waarschijnlijk dat CO en CO₂ ijs in elkaars nabijheid worden aangetroffen, wat zou moeten blijken uit hun interstellaire IR-spectrum. De vormingsszenario's voor CO₂ suggereren twee mogelijke 'modelstructuren' voor CO-CO₂ ijs: een lagensysteem als CO₂ wordt gevormd door middel van oppervlakte reacties, of een gemengd ijs wanneer stralingsprocessen de hoofdrol spelen. Systematisch onderzoek naar de temperatuursafhankelijkheid van de IR-spectra van deze twee systemen toont aan dat deze spectra zich significant verschillend gedragen. Het aantal mogelijke composities van het interstellaire CO-CO₂ ijs en haar thermische geschiedenis kan hierdoor aanzienlijk worden gereduceerd aan de hand van een combinatie van de aangetroffen spectrale patronen van CO en CO₂. Tevens suggereren de laboratoriumexperimenten dat wanneer interstellaire CO-CO₂ ijsspectra worden waargenomen, deze de oorspronkelijke vorming van CO₂ uit CO reflecteren. Deze resultaten zullen worden toegepast bij de analyse van de interstellaire spectra die momenteel worden verkregen met behulp van de recent gelanceerde ruimtetelescoop Spitzer.

In **Hoofdstuk 3** worden de laboratoriumresultaten uit Hoofdstuk 2 gebruikt om een algemeen geldend model te construeren dat de fysische interacties tussen CO en CO₂ in ijs onder interstellaire condities beschrijft. Dit model verbetert het fundamentele inzicht in het gedrag van CO-CO₂ ijssystemen, waardoor het mogelijk wordt om de interacties tussen deze moleculen te voorspellen in verschillende interstellaire ijsstructuren.

Hoofdstuk 4 beschrijft de eerste experimentele studie naar de thermisch geïnduceerde verdamping van CO en N₂ vanuit een gemengde of gelaagde ijstoestand. De accretie en desorptie van CO en N₂ in de beginstadia van de stervorming zijn een belangrijke maatstaf aan de hand waarvan astrochemische modellen deze vorming bestuderen. De modellen maken gebruik van gasfase-waarnemingen van C¹⁸O (een natuurlijke isotoop van CO) en N₂H⁺ om de accretie en desorptie van respectievelijk CO en N₂ te simuleren. Belangrijke parameters in deze modellen zijn de bindingsenergiën van CO en N₂ in het ijs. Hoewel de modellen in staat zijn de waarnemingen redelijk te reproduceren blijkt uit de beschreven experimenten dat de bindingsenergiën van CO en N₂ veel minder verschillen dan door de modellen wordt aangenomen. Onder interstellaire condities is het echter waarschijnlijker dat CO en N₂ verdampen vanaf een H₂O ijsoppervlak. Deze studie is daarom een eerste stap in het onderzoek naar dit complexere en astrofysisch meer relevante systeem waarin gekeken zal moeten worden naar de bindingsenergiën van CO en N₂ op H₂O-ijs.

Hoofdstuk 5 beschrijft de constructie en calibratie van de verschillende functies (RAIRS, QMS en UV-bestraling) van CRYOPAD aan de hand van een studie naar

de UV-geïnduceerde verdamping van dunne laagjes CO-ijs. Een eerste analyse van de resultaten wijst erop dat de directe fotodesorptie van CO weinig efficiënt is, maar wel significant kan zijn onder interstellaire condities als gevolg van processen die kunnen worden opgewekt in het onderliggende (ijs)oppervlak. Deze eerste resultaten laten zien dat CRYOPAD de potentie heeft om zowel kwalitatief als kwantitatief informatie te verschaffen over de chemische en fysische effecten van UV- en thermisch geïnduceerde processen in interstellaire ijsanalogen.

In **Hoofdstuk 6** wordt de efficiëntie van de UV-geïnduceerde productie van isocynaat (OCN^-) vergeleken met de thermisch geïnduceerde productie uit isocyanazuur (HNCO) in aanwezigheid van een protonacceptor (H_2O of NH_3). Het laboratoriumspectrum van het OCN^- ion vertoont grote gelijkenis met het interstellaire ijspectrum dat rond een golflengte van $4.62 \mu\text{m}$ wordt waargenomen. In eerste instantie werd dit spectrum alleen gezien in de richting van gebieden waar hoge massa sterren gevormd worden (sterren die typisch meer dan $10\times$ zwaarder zijn dan de zon). De vorming van dit soort sterren gaat veelal samen met de ontwikkeling van intense stralingsvelden. Aangezien verschillende soorten straling (zoals UV-straling of bombardering met hoog energetische deeltjes) in het laboratorium gemakkelijk OCN^- vormen uit ijs dat bestaat uit H_2O , CO en NH_3 , werd de $4.62 \mu\text{m}$ band geassocieerd met interstellair ijs dat zou zijn blootgesteld aan een intense stralingsbron. De resultaten die hier worden gepresenteerd laten echter zien dat de UV-geïnduceerde productie van OCN^- waarschijnlijk niet efficiënt genoeg is om de hoogst waargenomen concentraties in interstellair ijs te verklaren. De vorming uit HNCO middels een zuur-base reactie blijkt echter een goed alternatief. Derhalve wordt voorgesteld dat de productie van HNCO mogelijk voorafgaat aan de vorming van OCN^- , en dat OCN^- daardoor niet noodzakelijkerwijs een indicator voor de aanwezigheid van stralingsprocessen is.

Kort na publicatie van de resultaten beschreven in Hoofdstuk 6, werd er een $4.62 \mu\text{m}$ band waargenomen in spectra in de richting van 34 verschillende jonge lage massa sterren gelegen in donkere interstellaire wolken. Deze spectra waren de eerste aanwijzingen voor OCN^- rond een grote hoeveelheid lage massa sterren. **Hoofdstuk 7** geeft de resultaten van de analyse van deze spectra. Uit onderlinge vergelijking blijkt dat de $4.62 \mu\text{m}$ band bestaat uit twee spectrale componenten waarvan er maar één verklaard kan worden met een laboratoriumspectrum van OCN^- . Kwantitatief gezien is het mogelijk om de afgeleide OCN^- concentraties te produceren door middel van een fotochemisch vormingsmechanisme. Echter, het zwakkere stralingsveld van jonge lage massa sterren, de hoge dichtheid van de wolken die het ijs beschermen tegen externe stralingsvelden, en de plaatselijke concentratieverschillen, wijzen op een alternatief vormingsmechanisme, bijvoorbeeld het mechanisme voorgesteld in Hoofdstuk 6.

Curriculum Vitae

I was born on October 21, 1976 in Amsterdam, the Netherlands. During the last years of high school I became fascinated by the human brain functions, which was why, in 1995, I started the study of Chemistry at the University of Amsterdam aiming to resolve the mysteries of human intelligence and communication. I graduated in the Biocatalysis group of Prof. Dr. S.P.J. Albracht (UvA) on the conversion of H_2 into protons and electrons by a metallo-enzyme from the *C. vinosum* bacterium, using electron paramagnetic resonance spectroscopy and transmission absorption infrared spectroscopy to analyse the activation mechanism of the active site of the enzyme under anaërobie conditions.

Only by accident I found the Ph.D advertisement in the Astrochemistry group of Prof. Dr. Ewine F. van Dishoeck (Leiden University): a laboratory study towards the formation and evolution of the first molecules in the interstellar medium. More than anything I could imagine, this project touched on the basic chemical puzzles of the evolution of biological life forms. I started this project in October 2000, under the direct supervision of Dr. Willem A. Schutte in the Raymond and Beverly Sackler Laboratory for Astrophysics. An important part of the work in Leiden concerned the design and development of a novel ultra high vacuum experimental apparatus, which involved laboratory management and close collaboration with the glass- and mechanical workshops.

I have presented my work at various conferences in the Netherlands (Leiden and Dwingeloo), France (Les Houches), Canada (Waterloo, OT) and the US (Andover, NH). During my time in Leiden, I was involved in the organisation of the Dutch astronomers conference (NAC), a member of the advisory board of the computer committee and editor of the 'HOORT'. For two years, I taught the combined 1st year's experimental course for Physics-, Mathematics- and Astronomy students. In 2003–2004, I had the day-to-day supervision of a graduate student Irene M.N. Groot, working for nine months in the laboratory, whose work was key to Chapters 2 and 3 of this thesis.

Curriculum Vitae

Acknowledgements

Without the enormous love, support, and constructive criticism of my family, friends and colleagues, this thesis would never have been written. Het ontwerpen en opbouwen van CRYOPAD bleek een van de grootste struikelblokken. Vele handen maken licht(er) werk: Ewi, Koos, Arjen, Rafaël en Arie (Fijnmechanische dienst), Lou (LIS), Arno en René (Electronische dienst), en alle anderen die hebben bijgedragen aan het tot stand komen van deze proefopstelling, zonder jullie werk en gezelligheid was dit project nooit van de grond gekomen. Dit geldt ook voor de mensen uit de SurfCat-groep. I've always felt like you people adopted me and I consider myself just too lucky that you were there.

Dear Klaus, as a roommate you were wonderful for not minding my chaos (although my bike made an impression). Your thesis template saved me a lot of trouble and without your observations, Chapter 7 would have been a lot more difficult to write. "Cookies for coffee" appeared to be a way to buy myself into the network of the anonymous coffee suppliers next door. In the lab, Suzanne, Guido, Oskar, Edouard and Wassim made sure I got enough day-to-day peptalk and interesting discussions. Specially also Irene, ik heb veel van je geleerd. Je was een geweldige studente en het was heerlijk om met je samen te werken. Dear people from the the rest of the Astrochem group, although I didn't often join for lunch, nor participated in drinking festivities after work, it was great to be a part of you. Inge Loes, onze vrijdagmiddagssessies zijn een te snelle dood gestorven. Met pijn in mijn hart neem ik afscheid van je fietsje.

Mijn reistijd van en naar Leiden werd aanzienlijk veraangenaamd door de mobiele telefonie: lieve Untje, hoera voor de treinmomentjes! Hoera ook voor alle andere vrienden die geen genoeg leken te krijgen van verhalen over kapotte pompen en geweldige experimentele doorbraakjes. Lieve Pauline en Pieter jullie waren er altijd voor de juiste vraag op het juiste moment. Lieve Tijnie, eerlijkheid boven alles! Jij en Jiska konden zowel hartverwarmend enthousiast als heerlijk verontwaardigd zijn. Lieve Ab en Lux, wat een prachtige cover! Jullie zijn erin geslaagd een balans te vinden tussen mystiek en wetenschap binnen de dynamiek van het onderzoek, en wisten daarmee mijn dromen, fantasiën, onzekerheden, en groeiende kennis tijdens de promotie in beeld te vatten.

Bernard, zonder jou was mijn hoofd geëxplodeerd. Je krijgt een dikke kus.
SMAK!

Fleur, 2005

Acknowledgements
